Niemann-Pick type C disease: Pathogenesis and Therapy

Alexandria Nicole Colaço

A thesis presented for the degree of
Doctor of Philosophy

Department of Pharmacology
Somerville College
University of Oxford

Niemann-Pick type C disease: Pathogenesis and Therapy

Alexandria Nicole Colaço, Somerville College, D. Phil Thesis, Hilary Term 2016

Abstract

Niemann-Pick disease Type C is a rare, lysosomal storage disorder caused by defects in either *NPC1* (95% of cases) or *NPC2*, and characterized by progressive neurodegeneration that ultimately results in premature death. The function of the NPC1 protein still remains poorly understood and how the NPC1 or NPC2 proteins interact, or the functions of the pathways they regulate still remains unknown. We have found unexpected links between NPC and other human diseases - particularly Tangier disease, suggesting that the NPC cellular pathway is more broadly involved in human disease than previously suggested. To gain further insight into the function of NPC1 and proteins it interacts with we used the yeast orthologue, Ncr1p. I recreated the Δ*ncr1* mutant and characterized the mutant using an array of systematic screens to identify different processes and pathways that may play a role in NPC pathogenesis. The screen implicated mitochondrial dysfunction, defects in metal ion homeostasis and lipid trafficking, cytoskeleton dysfunction and nutrient sensing deficiencies. These screens were validated in the *Npc1*$^{-/-}$ mouse model, where the effects of modulating kinases also emerged as a potential therapeutic option. In addition to kinases, we examined the therapeutic potential of the FDA-approved hypertension drug, losartan. Losartan ameliorated the acidic store Ca^{2+} defect, which characterizes NPC, and all downstream pathologies as well as in combination with miglustat reduced levels of neuroinflammation in the mouse model. Furthermore, the cyclodextrin analogue Crysmeb was also examined as a novel therapy for NPC, and was found to have significant survival benefits as compared to HPβCD, the cyclodextrin compound currently in clinical trials. Taken together, in this thesis I have identified novel aspects of NPC pathogenesis, as well as mechanistic links between NPC and Tangier disease – which has led to miglustat treatment options for two patients at Addenbrooke's Hostpital, Cambridge. Additionally, taking advantage of the convergent disease mechanisms I have examined treatments (losartan/Crysmeb) that take advantage of the similarities and differences between these two disorders paving the way for potential clinical studies in the future.

Acknowledgements

I would like to express my upmost gratitude to my advisor Professor Fran Platt for her continuous support throughout my time here, as well as her enthusiasm and knowledge. I could not have imagined having a better advisor and mentor.

I would also like to thank all the members of the Platt lab, past and present: Kerri, James, Paul, Ecem, Doris, David, Danielle, Dave, Lauren, Mylene, Nick, Stephanie, Ralu, Elias, Martin, Duran, Maysa, Jo, Nada, Oscar, Claire, Rizwana, Gokhan, Alison, Ian and Wendy. Thank you for the science discussions, the not science discussions, the fun times at conferences as well as the pub! You made my time here so meaningful and never could have envisioned laughing and having as much fun while at work.

I am thankful to have been funded by both the EU Marie Curie ITN: SPHINGONET and the Niemann-Pick disease group UK. SPHINGONET was an incredibly fun and rewarding network to be involved with, and I thank all the fellows and advisers involved. Specifically, a special thanks to Dr Maya Schuldiner and her lab at the Weizmann Institute, where while I was only there for 6 weeks they welcomed me into the lab and helped me make the most out of my time in Israel.

Additional thanks to Christoph Poincilit at NPSuisse who mentioned losartan in the first place! As well as other collaborators at the John Radcliff Hospital who got me excited about mitochondria – Dr Jo Poulson, Dr Karl Morten, Dr Alan Diot, and Tiffany Lodge.

Big thanks to my family who has been so supportive of me despite being so far away from home, especially Keith who has been the inspiration from the beginning. As well as to those who helped make Oxford my home away from home – Monday night dinners will just never be the same. And Jamie, thanks for your love and support, its fine.

Table of Contents

Abbreviations

Δncr1 - NCR1 knockout mutant
17-DMAG - 17-Dimethylaminoethylamino-17-demethoxygeldanamycin
2-AA -Anthranilic acid
ABC - ATP binding cassette
ABCA1- ATP-binding cassette A1 transporter
AD - Alzheimer's Disease
ALS - Amyloid lateral sclerosis
Ang II - Angiotensin II
apoA1 - apolipoprotein A-1
ARB - Angiontensin II receptor blocker
Arg - Arginine
ASMase - Acid sphingomyelinase
AT-1 - Angiotensin II type 1 receptor
BBB - Blood brain barrier
BCA - Bicinchonic Acid
BODIPY-LacCer - BODIPY® FL C5 lactosylceramide
BSA - Bovine serum albumin
Ca2+ - Calcium
CaMKII - Ca2+/calmodulin-dependent protein kinase II
Can - Cavanine
CD - Cyclodextrin
CGase - Ceramide glycanase
CHO - Chinese hamster ovary
CNS - Central nervous system
CTxB - cholera toxin subunit B
ENU - Ethyl-nitrosaurea
ER - Endoplasmic reticulum
FACS - Fluorescence-activated cell sorting
FCS - Fetal calf serum
G418 KanR - Kanamycin resistance
Gb3 - Globotriaosylceramide
GBA - Glucocerebrosidase
GBA2 - β-glucosidase 2
GFP - Green fluorescent protein
GlcCerT - Ceramide glucosyl-transferase
GSLs - Glycosphingolipids
HDAC - Histone deacetylase
HDAC6 - Histone deacetylase 6
HDL - High density lipoprotein
His - Histodine
HMG-R - HMG-CoA reductase
HPLC - High performance liquid chromatography
HPβCD - Hydroxyl-propyl-β-cyclodextrin
HSF1 - Heat shock factor 1

HSP70 - Heat shock protein 70
HSP90 - Heat shock protein 90
HTS - High throughput screening
Hygror - Hygromycin B
ICV - Intracebralventricular
IN - Intranasal
IP - Intraperitoneal
IV- Intravenous
LC3- Microtubule-associated protein 1A/1B-light chain 3
LE/LY - Late endosome/lysosome
LRP1 - Low density lipoprotein receptor-related protein 1
LSDs - Lysosomal storage disorders
LXR - Liver-X-receptor
Lys - Lysine
MEFL - Molecules of equivalent fluorescence
mtDNA - Mitochondrial DNA
mTORC1 - Mammalian target of rapamycin complex 1
NAD - β-Nicotinamide adenine dinucleotide
Nat - Nourseothricin
Ncr1p - Niemann-Pick C related 1 protein
NPA - Niemann-Pick type A
NPB - Niemann-Pick type B
NPC - Niemann-Pick disease type C
NPC1 - Niemann-Pick type C 1 protein
NPC2 - Niemann-Pick type C2 protein
p7 - Post natal day 7
PBS-Tw - PBS containing 0.1% Tween-20
PEG - Polyethylene glycol
PI - Propidium iodide
PKC - Protein kinase C
PPARγ - Peroxisome proliferator-activating receptor gamma
PTC - Patched
RND - Resistance-nodulation cell division permeases
ROS - Reactive oxygen species
RT- Room temperature
RT-PCR - Real time polymerase chain reaction
RXR - Retinoid-X-receptors
SAEC - Thialysine
SIRT2 - Sirtuin 2
SREBP - Sterol-regulatory element binding protein
SRT - Substrate reduction therapy
SSD - Sterol sensing domain
TOM20 - Mitochondrial imiport receptor subunit TOM20
UT - Untreated
YPD - Yeast extract peptone dexrose
βCD - β-cyclodextrins

Chapter 1: Introduction

1 Introduction

1.1 Lysosomal Storage Disorders

Lysosomal storage disorders (LSDs) are a family of approximately 70 rare, inherited, metabolic disorders, and are caused by defects in lysosomal proteins, most commonly lysosomal enzymes (17, 18). These defects result in the characteristic accumulation of undigested, or partially digested, macromolecules in the lysosomes of cells (19). This accumulation leads to lysosomal and cellular dysfunction and the various clinical phenotypes observed in patients with these diseases (19). While individually rare, collectively LSDs have a combined incidence of 1:5000, and account for 14% of all inherited metabolic disease cases (20, 21). Specific disorders had originally been found to have a high prevalence in specific populations (i.e. Tay-Sachs historically was found at much higher rates in Ashkenazi Jewish population) although today we appreciate that these disorders are found in all ethnic groups across the world (22).

1.2 Niemann-Pick Disease Type C

Niemann-Pick disease type C (NPC) is a lysosomal storage disorder with a rate of incidence of approximately 1:120,000 live births, although recent data suggests it may be as high as 1:90,000 (1, 23).

1.2.1 Clinical Presentation

Patients classically present with symptoms in mid-childhood, however, infantile and late-onset adult forms of this disease also occur. The infantile, and most aggressive form of this disease, generally presents at birth as neonatal jaundice and liver disease (1, 24). The adult form is much more heterogeneous, with varied rates of disease progression, as the oldest known NPC patient to date is over 66 years old (25).

NPC patients generally have both neurological and systemic manifestations of the disease. One of the early symptoms is an impaired vertical gaze and vertical supranuclear gaze palsy followed by cognitive decline (24). The progressive neurological decline that characterizes this disease can also be accompanied by epileptic seizures, cerebellar ataxia and motor impairment **Figure 1.1** (24).

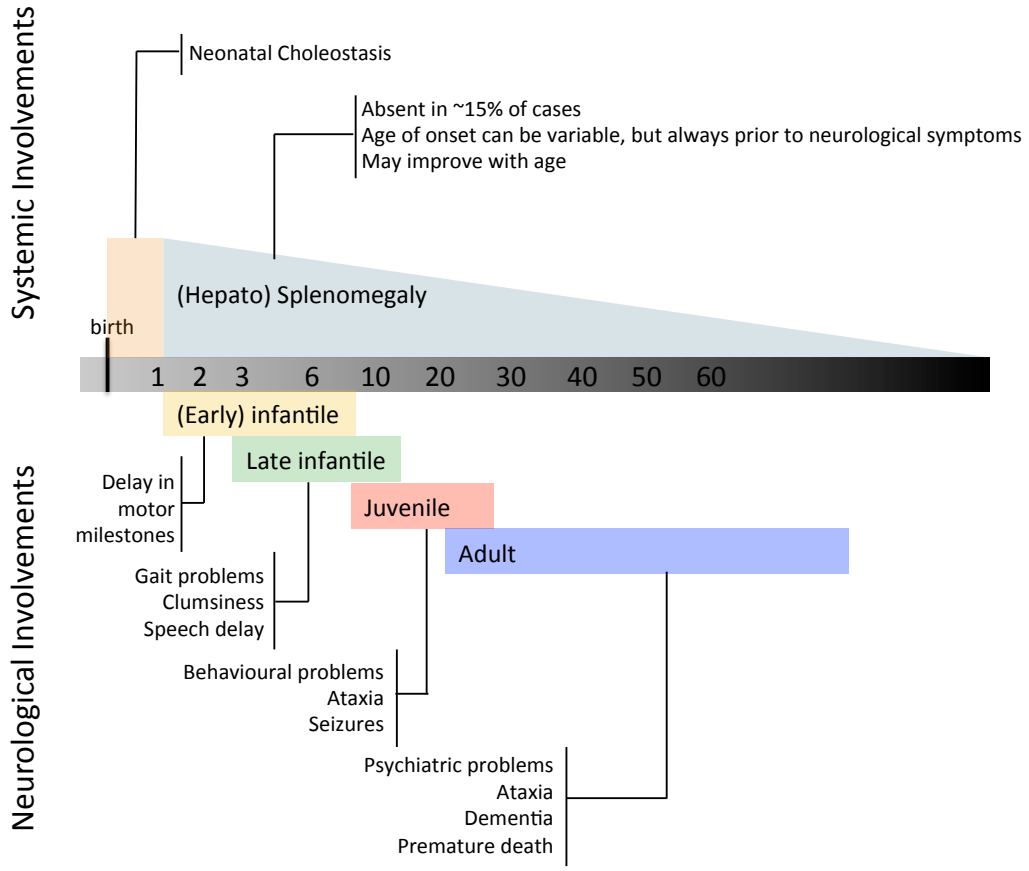

Figure 1.1. Representative time frame of systemic and neurological disease progression and onset variations in Niemann-Pick disease type C. With minor modifications from Vanier MT 2010 (1).

1.2.2 Genetic Basis of NPC

NPC is caused by a mutation in either the *NPC1* or the *NPC2* gene. The majority of patients have mutations in the *NPC1* gene (95%), but mutations in either gene results in identical clinical phenotypes (24). The *NPC1* gene maps to chromosome 18q11-12, and encodes a 1278 amino acid protein, NPC1 (26). The *NPC2* gene is located on chromosome 14q24.3 and was previously known as *HE1*, human epididymal secretory protein EI (27).

The Niemann-Pick disease type C2 (NPC2) protein structure and function has been fairly well characterized and is a small, soluble 132 amino-acid glycoprotein found in the lysosomal lumen containing a mannose-6-phosphate receptor binding domain (27). It has been shown that NPC2 can bind free cholesterol with a 1:1 stoichiometry, suggesting that cholesterol binding is integral to this protein's activity and function (28). Additionally, NPC2 specifically and efficiently transports cholesterol, and this transport can be stimulated by low pH or low sphingomyelin levels (29).

Cholesterol is the major lipid species of both the plasma membrane and the membranes of early endosomes, however, it is nearly absent in the inner lysosomal membranes (30). It has been suggested that NPC2 also functions to maintain correct sterol intercalation into the lysosomal membrane, particularly of cholesterol in the late endosome/lysosome (LE/Lys) membranes (30). It has been demonstrated that NPC2 can move inter-endosomal membrane cholesterol to Niemann-Pick disease type C1 protein (NPC1), where cholesterol is transferred through the glycocalyx and out of the LE/Lys system (31). This process is inhibited by the presence of sphingomyelin, thus the acid sphingomyelinase (ASMase) plays an important role in NPC2's activity, as the sphingomyelin derivative ceramide has been shown to the promote cholesterol transport via NPC2 (32). The LE/Lys acidic environment promotes the activity of ASMase which therefore enhances cholesterol transport and maintenance of LE/Ly low cholesterol membrane levels (30).

The structure of NPC1 was recently determined by cryo-electron microscopy and identified a cavity in the protein's sterol sensing domain (SSD), which was found to be large enough to accommodate a cholesterol molecule (33). The NPC1 protein's function as a putative cholesterol-transporting molecule, however, still remains controversial. Structurally, the NPC1 protein is large, 13-transmembrane protein localized to the late endosome/lysosome (34). It contains three luminal loops, a small cytoplasmic loops, and a C-terminal cytoplasmic tail (**Figure 1.2**)(34). The majority of the protein has no known shared homology with other mammalian proteins, however domains 3-7 do share homology with the morphogen receptor Patched (PTC), the SSD of HMG-R, and SREBP cleavage activating protein (26). This shared homology further suggests NPC1 may have a role in cholesterol sensing, as PTC is a signalling molecule for sonic hedgehog that contains a cholesterol moiety and the SSD of HMG-R acts a cholesterol level sensor (26). However, this has yet to be experimentally proven, and this domain's function remains unknown.

1.2.2.1 Conserved Structure

The topology of the NPC1 protein does, however, share multiple consensus sites with prokaryotic multi-transmembrane proteins. Specifically the bacterial resistance-nodulation-cell division (RND) permeases (26).

Additionally, the NPC1 protein also shares considerable homology with the *Psueodomonas aeruginosa* multidrug efflux pump, MexD (3). Comparisons of their topology suggests that NPC1 protein evolved through duplication, as the NPC1 protein duplicates the MexD structure exactly with an addition of a single N-terminus loop (3). This loop most likely had been acquired after the divergence of this protein from the ancestral RND permeases (**Figure 1.2**) (3). Additionally, further experimentation established NPC1 as a mammalian member of the RND family of permeases that can transport lipophilic molecules out of the LE/Lys systems (3). Transport studies in the bacterial *Escherichia coli* (E. *coli*) showed that NPC1 could transport fatty acids but not cholesterol or cholesterol esters (3), suggesting NPC1's conserved function may not have been a cholesterol transporting protein, at least in prokaryotic systems.

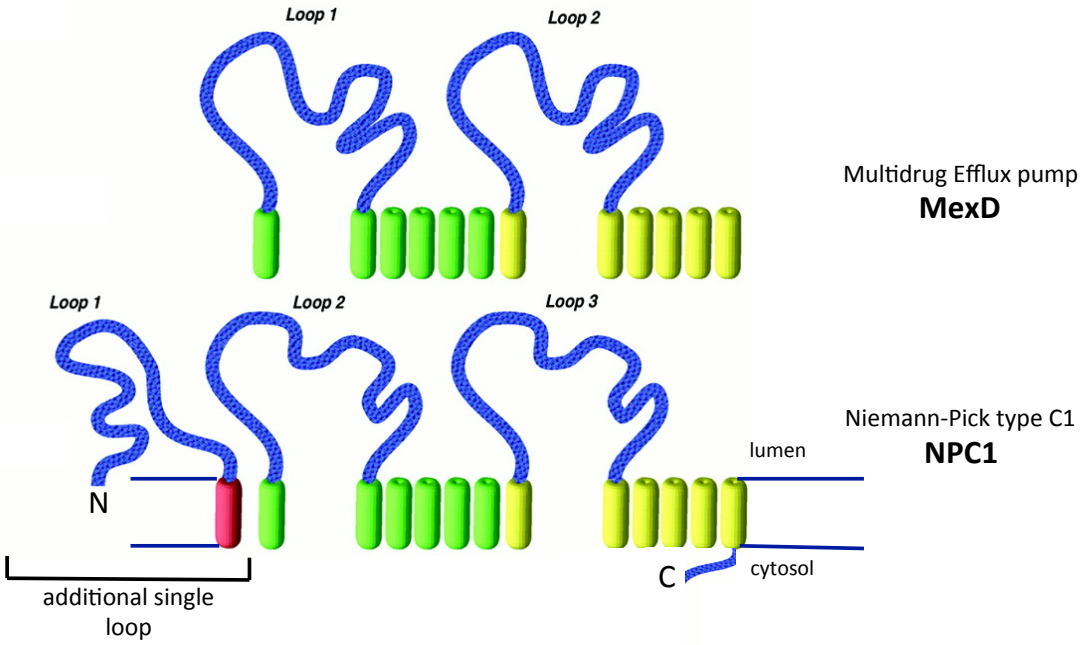

Figure 1.2. Structural homology between the bacterial multidrug efflux pump protein MexD and the human Niemann-Pick type C1 protein, NPC1. With minor modifications from Davies 2000 (3).

In addition to shared homology with bacterial effluxers, the NPC1 protein also has an orthologue in the yeast *Saccharomyces cerevisiae* (*S. cerevisiae*) called *NCR1. NCR1* encodes the protein Ncr1p [Niemann-Pick C related 1 protein] and has 42% amino acid sequence identity and 75% similarity at the protein level (35).

S. cerevisiae lack lipoprotein receptors and generally do not use exogenous sterols, so the presence of a protein that has been implicated in exogenous sterol transport is unexpected (35). Additionally, deletion of *NCR1* had no effect on sterol transport, suggesting that the function of the yeast *NCR1* gene may have been, like in the bacterial systems, not involved in sterol efflux (35).

This is interesting as the presence of the SSD in both the mammalian NPC1 and yeast orthologue Ncr1p protein suggests a role in cholesterol efflux, where at least in the case of the yeast it does not seem a major function. In fact, a dominant mutation in the SSD in the yeast Ncr1p led to increased sensitivity to sphingosine and C2-ceramide, rather than sterols (10). Additionally, there was a redistribution and accumulation of sphingolipids in the plasma membrane and vacuole in Ncr1p mutant colonies (10). It has been proposed that in yeast, the primary role of Ncr1p is to recycle sphingolipids, and in multicellular organisms NPC1's function has such evolved to also include the transport of cholesterol (10).

1.2.3 Sphingolipids and Sterol Regulation

The suggestion that in yeast the role of Ncr1p may be to recycle sphingolipids and in higher organisms the function has evolved to include transporting/sensing cholesterol is interesting in the context of the regulation of sphingolipid and sterol pathways. Recent evidence has suggested that sterols and sphingolipids function together, however, the data is conflicting on whether sterols regulate sphingolipids or vice versus (36).

The sterol biosynthesis pathway is highly conserved from yeast to humans, with the exception that ergosterols are the final end product in yeast rather than cholesterol (**Figure 1.3**). Erg26p is one of the four proteins in yeast involved in the conversion of ignosterol to zymosterol, one of the precursors in the ergosterol synthesis pathway (37). In Δ*Erg*26 the genes involved in sphingolipid biosynthesis were altered, and it has been proposed based on these studies that sterols may regulate sphingolipid metabolism, at least at the level of transcription (37).

In mammalian systems, however, studies have shown that cholesterol and sphingolipid trafficking appear to be dependent on each other, with perturbations to cholesterol homeostasis occurring secondary to sphingolipid accumulation (38). This has been examined particularly in the cases of spingolipidoses, where Fabry, Tay-Sachs, Sandhoff, Niemann-Pick disease type A (NPA), Niemann-Pick disease type B (NPB) and NPC were examined (39). Each of these disorder are caused by

defects in different lysosomal enzymes or proteins and result in an accumulation of various sphingolipids in the lysosome. Analysis of cholesterol levels and lipid endocytic trafficking in the different patient fibroblasts suggested that in the sphingolipidoses cholesterol homeostasis is disrupted, and this defect is secondary to the sphingolipid accumulation (39, 40).

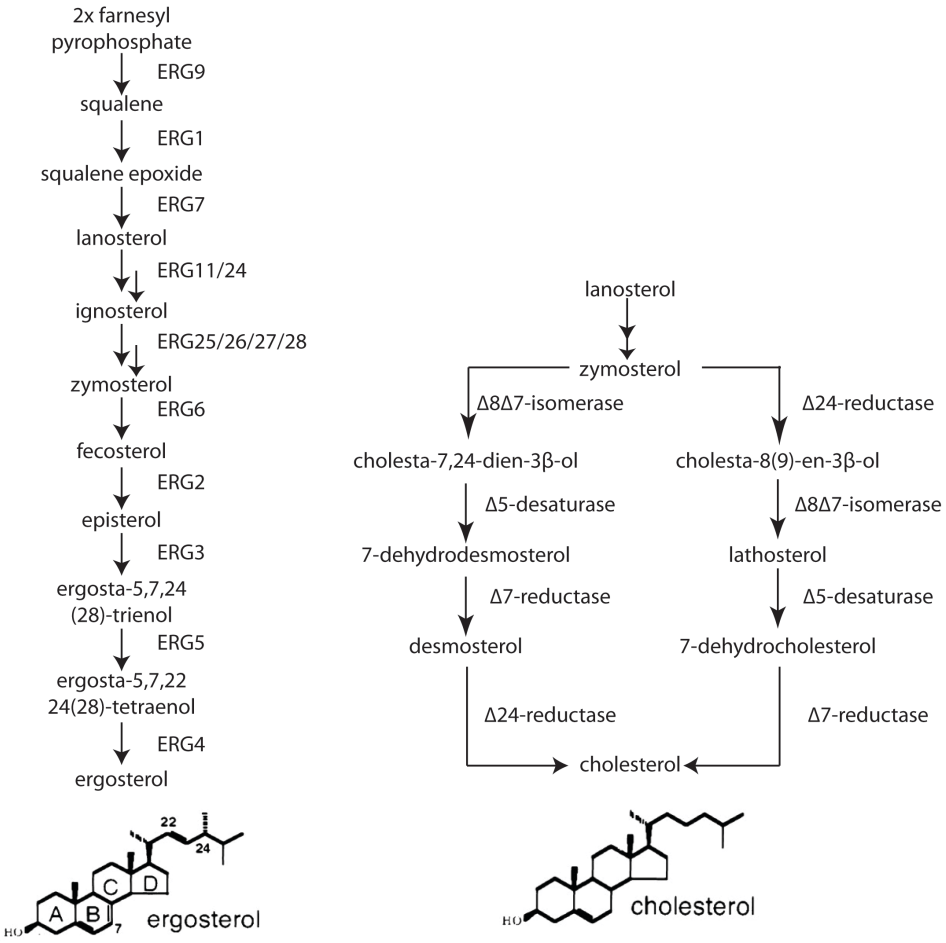

Figure 1.3. Sterol biosynthetic pathway in yeast and humans for the production of ergosterol and cholesterol. Modified from Eisenkolb et al. 2002 (7).

This may occur by an indirect mechanism in which sphingolipids stimulate the expression of proteins that regulate cholesterol, or by direct physical interaction of

the sphingolipids with cholesterol in the endocytic pathway (38). Neither sphingolipid nor cholesterol biosynthesis is controlled by a single regulator and regulation is most likely coordinated by a cross talk between their individual metabolic pathways (41).

Spingolipid biosynthesis has been shown to regulate the sterol-regulatory element binding protein (SREBP), a protein which regulates over 30 genes involved in cholesterol, fatty acid, and phospholipid synthesis (42). SREBP is then regulated by the presence of cholesterol/fatty acids and cholesterol synthesis in a negative feedback loop (43). Interestingly, the NPC1 protein has been shown to be transcriptionally regulated by SREBP, and that high levels of cholesterol/fatty acids and the consequent inhibition of the SREBP pathway leads to the down-regulation of *NPC1* (44). This is interesting in the context of the function of NPC1, if NPC1 acts as a sphingolipid transporting protein, then defects may result in the secondary accumulation of cholesterol and fatty acids. However, if it acts as a cholesterol transporter then the secondary accumulation of sphingolipids may occur due to endocytic trafficking defects due to elevated cholesterol storage (45). Further understanding of this protein's function may help elucidate some aspects of the regulation of sterols and sphingolipids.

1.2.4 Cellular and Biochemical Phenotypes

As was found in the mutant yeast colonies, mammalian NPC1 mutant cells also accumulate sphingolipids in the lysosome (13). Characterization of the cascade of events following inactivation of the NPC1 protein found the first lipid to accumulate in the lysosome was sphingosine (13). The rapid elevation in sphingosine coincided with a transient decrease in the signalling molecule sphingosine-1-phosphate, and a subsequent reduction in acidic store calcium (Ca^{2+}) levels (13). This reduction in acidic store Ca^{2+} seems to be caused specifically by sphingosine storage as exogenous addition of other lipids, including those stored in NPC disease, did not induce a Ca^{2+} defect (13, 46). It is not known, however, if it is through a direct inhibition of a specific acidic store Ca^{2+} filling protein or through a more indirect mechanism such as protein kinase C (PKC) inhibition (13). Or conversely, through an alteration to the Ca^{2+} leak channels leading to a lower steady state Ca^{2+} level.

This reduction in lysosomal Ca^{2+} levels leads to an insufficient release of Ca^{2+} to facilitate lysosomal fusion and/or trafficking in the endocytic pathway, both of which are Ca^{2+} dependent processes (13). This trafficking defect traps the glycosphingolipids (GSLs) and cholesterol esters in the LE/Lys where they accumulate (13). The suggested pathogenic cascade in **Figure 1.4** demonstrates the sequence of events described following NPC1 inactivation (2).

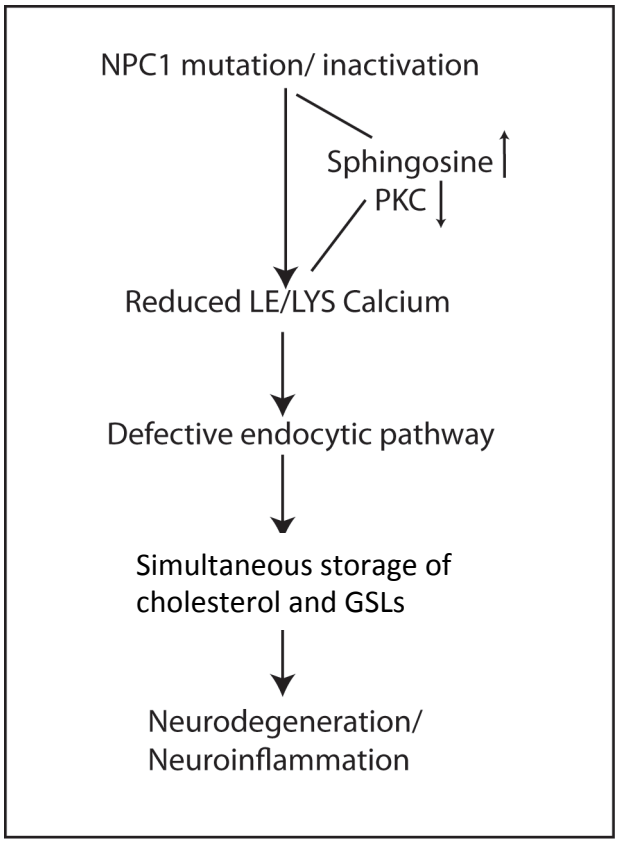

Figure 1.4. Putative pathogenic cascade following NPC1 mutation/inactivation in the cell. With minor modifications from Lloyd-Evans and Platt 2010 (2).

LSDs are generally characterized by the accumulation of substrates in the lysosome, however, many of the cellular pathologies associated with NPC are unique to this disorder. NPC is one of the few disorders to date found to have an accumulation of sphingosine, although an accumulation of sphingoid bases in livers to a similar extent as seen in NPC has also been observed in GM2 gangliosidosis variant 0 [Sandhoff disease], GM1 gangliosidosis, Gaucher disease, and Mucopolysccharidosis type VII (47). In the case of NPC, the accumulation of sphingosine has been found specifically to occur in the LE/Lys, and has been shown that this lysosomal sphingosine accumulation contributes to the reduced acidic store Ca^{2+} release observed in this disease (46). NPC is the only lysosomal storage disorder to date

with a reduced level of acidic store Ca^{2+}, however, further examination of other disorders particularly the sphingolipidoses is still required.

While NPC is the only LSD to have altered acidic store Ca^{2+} thus far, altered intracellular calcium homeostasis has emerged as a common pathway amongst these disorders (48). Despite this emerging common pathway, the mechanisms leading to altered Ca^{2+} homeostasis varies between individual diseases as the primary storage lipids, or pathways involved, differ amongst the disorders. For instance, in Gaucher disease an increased Ca^{2+} release from the endoplasmic reticulum (ER) is found (49), whereas in Sandhoff and NPA an increase in cytosolic calcium is observed (50, 51). Both the neuronal models of GM1 and in Mucolipidosis type IV had altered mitochondrial Ca^{2+} levels (52, 53), although for different reasons, and in the mouse model of the juvenile form of neuronal ceroid lipofuscinosis impaired plasma membrane voltage-gated Ca^{2+} channels was observed (54).

It is intriguing to speculate whether some of these features that are apparently unique to NPC/LSDs occur in other human diseases. In particular various neurodegenerative, as well as other non-degenerative disorders, have been implicated as converging with the NPC pathogenic cascade (55-57).

1.2.5 Shared NPC1 Pathogenic Cascade

The link between rare and common disorders is continually being explored. Particularly with the emerging role lysosomal dysfunction may have in neurodegenerative diseases, including Alzheimer's and Parkinson's disease (58, 59). Specifically, mutations in glucocerebrosidase (*GBA)*, the gene involved in the LSD Gaucher disease, has been identified as the greatest genetic risk factor for Parkinson's (60). In the case of NPC, it has been suggested that heterozygous carriers of *NPC1/2* mutations also have a higher risk of Alzheimer's disease (AD) (57), although there has been mixed findings for Parkinson's (61-63).

Characterization of these disorders, in particular for AD, in terms of "NPC-like" features is underway. Loss of functionality of presenilin 1 has been found to lead to reduced acidic store Ca^{2+} levels, and the subsequent trafficking defect and secondary storage of lipids (64) seen in NPC disease (**Figure 1.5**). As NPC phenotypes have been observed in AD, phenotypes associated with AD, such as neurofibrillary tangles, have likewise been observed in NPC patients (65), although not in the NPC mouse model (66).

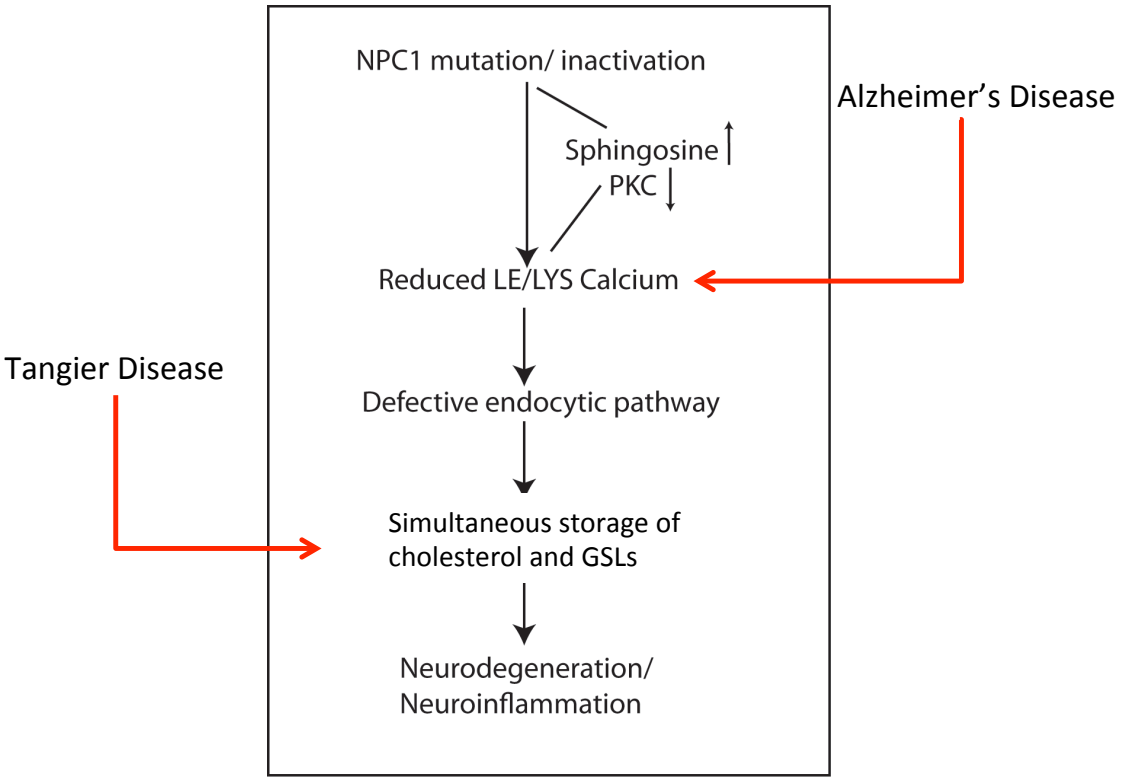

Figure 1.5. Putative pathogenic cascade following NPC1 mutation/inactivation and where pathway converges with Alzheimer's and Tangier disease. With minor modifications from Lloyd-Evans and Platt 2010 (2).

In addition to neurodegenerative diseases convergent with the NPC1 pathogenic cascade, other diseases have also been suggested to have links with NPC. Specifically, the familial alpha-lipoprotein deficiency disease, Tangier disease, has been shown to have a relationship with NPC disease (**Figure 1.5**).

1.2.5.1 Tangier Disease

Tangier disease is caused by a mutation in the ATP-binding cassette A1 transporter (*ABCA1)*, a gene involved in cholesterol and phospholipid cellular efflux. Patients with Tangier disease have been found to have dysregulated cholesterol homeostasis,

and NPC patient cells have been found to have impaired regulation and activity of ABCA1. This results, for NPC patients, in decreased phospholipid and cholesterol efflux and reduced high density lipoprotein (HDL) plasma levels (67).

In Tangier patients it has been found that up-regulation of the NPC1 protein can promote intracellular cholesterol transport and increased efflux to apolipoprotein A-I (apoA1) and HDL formation (56). The relationship between these two proteins has been explored in terms of therapies, as pharmacological treatment of NPC1 disease fibroblasts with the ABCA1 regulator Liver-X-receptor (LXR) can correct ABCA1 expression and reduce cholesterol accumulation (67). Interestingly, increasing ABCA1 activity proved beneficial in NPC1 deficient cells, but did not have the same effect in NPC2 deficient cells (68).

This sheds light on the relationship of the NPC1/NPC2 protein in the lysosome as it suggests that NPC2 delivers cholesterol to the membrane where either NPC1 or ABCA1 can efflux it out of the lysosome (**Figure 1.6**) (68). However, it has also been suggested that NPC2 may sense LE/Lys cholesterol levels and activate a non-cholesterol transporting activity of the NPC1 protein (69). The cholesterol would then be transported in an alternative method, such as through contact sites between the LE/Lys and the ER (i.e. VAP-A and MLN64) (70).

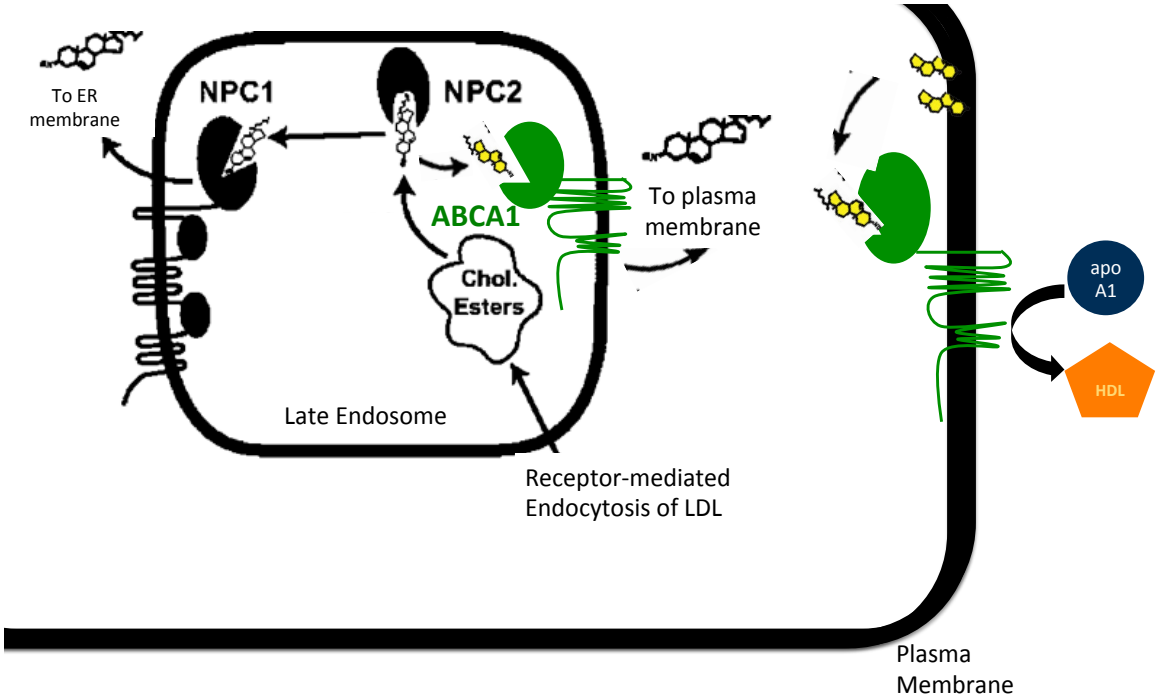

Figure 1. 6. Suggested interactions between NPC1 and NPC2 in the cell with ABCA1. ABCA1 has been shown to be localized to both the LE/Lys and the plasma membrane. Modified from Infante RE et al 2008 (9).

1.2.5.2 NPC and Tangier disease: Therapeutic Link

The relationship between NPC and Tangier disease was further highlighted following a misdiagnosis of a Tangier patient with NPC. The patient was treated with the European-Union approved drug, miglustat, and reported significant clinical improvement (71). Genetic analysis later revealed that the patient did not have mutations in either *NPC1* or *NPC2*, but had an atypical mutation in *ABCA1* and was then correctly diagnosed with Tangier disease (71).

This suggests shared therapies could be useful for "NPC-like" diseases including, but not limited to, Tangier and Alzheimer's disease. However, why miglustat may be effective as a treatment for an ABCA1 deficient patient is of particular interest, and is examine further in **Chapter 3**.

1.2.6 NPC1 Mouse Models

Research efforts on NPC has yielded multiple and varied animal models that are used to better characterize the disease and test the effectiveness of experimental therapies. In addition to the yeast NPC model, as described in **Section 1.2.2.1**, various mouse models are being used to further our understanding of this disease.

To date four mouse models can be used to effectively model NPC disease. Briefly these include: 1) A spontaneous mutant, *Npc1*^{m1N}, available from the Jax laboratory, that is completely null for the NPC1 protein and correlates well with the more severe forms of this disease. 2) The *Npc1*$^{flox/-}$ is a Purkinje neuron cell specific conditional null mutant model used to study neurodegeneration (72). 3) The model *Npc1*^{nmf164} was generated used ethyl-nitrosaurea (ENU) mutagenesis to generate a D1005G mutation in the NPC1 protein and has been shown to be a good representative model for the late-onset version of this disease (73). 4) The most recently characterized NPC1 mouse model, *NPC1*$^{tm(I1061T)Dso}$ is a knock-in for the most commonly found patient mutation I1061T.

The spontaneous *Npc1*^{m1N} mouse model is null for the NPC1 protein due to a 121 base pair insertion resulting in a frame-shift and premature truncation of the NPC1 protein deleting 11 of the 13 trans-membrane domains (74). This mouse develops a tremor and ataxia around 7 weeks (75), suffers from weight loss at 7 to 8 weeks (76), and eventual, premature death at approximately 11 weeks of age (75). This model's disease progression is illustrated in **Figure 1.7**, and is the mouse model used for the *in vivo* studies in **Chapter 4** and **Chapter 5.**

Npc1$^{-/-}$ mouse model disease progression (weeks)

1 2	3 4	5 6	7 8	9 10 11 12+
Npc1$^{-/-}$ mice tend to be born with lower body weight and gain weight slower than wild types. Otherwise no clear phenotypes	Any weight differences between wild type and *Npc1*$^{-/-}$ have been evened out. Coat condition looks similar and no behavioral symptoms visible First evidence of micorglial activation and purkinje neuron degeneration	Behavoiral defecits, such as tremor and ataxic gate begin Coat condition begins to decline Can be differentiated by eye from wild type counterparts	*Npc1*$^{-/-}$ mice reach peak weight and begin to lose weight Motor control issues become more prominent Staggered gait and tremor	Large scale behavoiral issues -Tremor -Loss of motor controls Drop in body weight Coat condition poor Approaching humane end-point (loss of 1g/ 24hr)

Figure 1.7. Symptoms of disease progression in the *Npc1*$^{-/-}$ moue model. With modifications from Platt et al 2016 (5).

The mouse model *Npc1*$^{flox/-}$ is a Purkinje neuron cell specific null model. Using this disease model it was determined that loss of specifically Purkinje neurons contributed to impaired motor functions in NPC (72). These mice did not, however, suffer from the weight loss or premature death that is observed in the null *Npc1*^{m1N} model, suggesting that Purkinje cell loss does not contribute to those phenotypes (72).

The D1005G point mutation in *Npc1* creates the mouse model *Npc1*^{nmf164}, which has a slower developing phenotype then that observed in the *Npc1*^{m1N} null model (73). This model has all the hallmarks of NPC including: lipid accumulation, microglial activation and Purkinje neuronal loss, but present themselves in a milder form (73). This model may better reflect the phenotype found in patients, as one third of human mutations fall in the cysteine-rich domain that the D1005G mutation occurs in (73). Additionally, as unlike in *Npc1*^{m1N} or the *Npc1*$^{flox/-}$, the *Npc1*^{nmf164} mouse model produces the NPC1 protein so could be used to evaluate chaperon mediated therapies.

Also in the cysteine-rich domain is the most commonly found patient mutation, I1061T, which was knocked into the murine NPC1 locus to generate the *Npc1*$^{tm(I1061T)Dso}$ model, commonly referred to as *Npc1*^{I1061T} (77).This mouse also has the conditional deletion of exons 14-20 providing the option for a *Npc1* knockout mouse (77). These mice have an average lifespan of nearly 18 weeks, onset of tremor at 8 weeks of age, weight loss from 10 weeks, and loss of motor coordination from 12 weeks (77). These mice also exhibit both progressive neurodegeneration as well as systemic lipid accumulation (77), and like the *Npc1*^{nmf164}, the NPC1 protein is made in the *Npc1*^{I1061T} mouse model, so would also serve as a good model to evaluate chaperon mediated therapies.

While mouse models can very closely model the human disease phenotype, other organisms such as *S. cerevisiae, C. elegans* and *Danio rerio* have proven to be very

useful for modelling the disease in terms of elucidating protein function or as a method to screen therapeutic compounds.

1.2.7 Therapies

Currently, all LSDs have treatment options that to different extents manage the symptoms of each disorder. However, what is needed is specific disease modifying therapies that target the unique steps in the pathogenic cascade, and in the case of NPC, most likely a combination of therapies will prove to be most effective to tackle the various systemic and neurological manifestations.

1.2.7.1 Current EMA - Approved Disease Modifying Therapy

The compound miglustat [*N*-butyl-deoxynojirimycin (*N*B-DNJ), Zavesca™, **Figure 1.8A**] is the current EU approved treatment for NPC. It reversibly inhibits the enzyme ceramide glucosyl-transferase (GlcCerT) [IC_{50} 20-40μM], which catalyses the first step of GSL biosynthesis (78, 79). Miglustat also differentially inhibits both the non-lysosomal β-glucosidase 2 (GBA2) [IC_{50} 0.31μM] and glucocerebrosidase (GBA) [IC_{50} 520μM] (79, 80). Miglustat acts as a substrate reduction therapy (SRT) by reducing the influx of GSLs into the lysosome, so less are stored, reducing the storage burden.

Miglustat has already been used for the treatment of type 1 Gaucher disease since its approval in 2002 and 2003 for use in Europe and the US respectively (81, 82). It was

then later given orphan drug designation for NPC in 2006 and approved by the EMA for the treatment of NPC in 2009 (81). Miglustat has a generally good safety profile, however in mice it has been shown to induce weight loss due to central appetite suppression (83) and in patients the major side effect is osmotic diarrhoea (usually self-resolves) due to intestinal disaccharidase inhibition (84, 85).

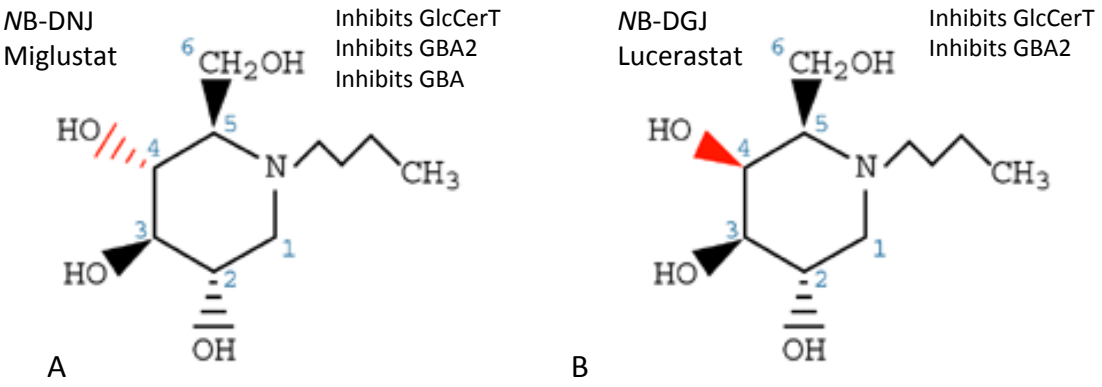

Figure 1. 8. Structures of EMA approved A) miglustat (*N*B-DNJ, Zavesca™) for the treatment of Niemann-Pick disease type C and B) the galactose analogue lucerastat, *N*B-DGJ. Modified from Platt FM and Butters TD, 2000 (6).

Miglustat's galactose analogue, lucerastat [*N*-butyl-deoxygalactonojirimycin (*N*B-DGJ), **Figure 1.8B**], is also a ceramide glucosyl-transferase inhibitor. Lucerastat also inhibits GBA2 activity, but does not inhibit GBA, nor disaccharides in the GI tract (80). Lucerastat is more selective than miglustat, but has been shown to have equivalent distribution and degree of GSL depletion in the liver of *Npc1*$^{-/-}$ mutant mice (86). Comparative studies of the two drugs have shown that while lucerastat is better tolerated than miglustat and does not induce weight loss (87), miglustat shows greater functional improvement in mice as it may have additional anti-inflammatory properties (88, 89). However, in mice there is no survival benefit with

miglustat treatment compared to that observed with lucerastat treatment, although as lucerastat has reduced side effects dose escalation is possible to achieve higher concentrations of drug in the central nervous system (CNS) (88).

While miglustat is the only approved drug for the treatment of NPC in Europe, other drugs are currently being prescribed either off-licence or as compassionate use in both Europe and the USA. Cyclodextrin, specifically hydroxyl-propyl-β-cyclodextrin (HPβCD), is one of these therapeutic compounds and is being taken under compassionate use protocols mainly in the USA, but also in Brazil, Japan and the rest of the world. Three clinical trials (HPβCD, arimoclomol, and vorinostat) are now underway to assess these new treatments and determine the most effective therapy for NPC.

1.2.7.2 Ongoing Clinical Trials in NPC

1.2.7.2.1 Hydroxyl-propyl-β-cyclodextrin (HPβCD)

Since its first use in 2009 by the Hempel twins in the USA, patients have followed the FDA-approved protocol for off-label cyclodextrin (Trappsol®Cyclo™ [CTD Holdings]) intravenous (IV) infusions with mixed results. For the vast majority of patients receiving HPβCD there is only anecdotal, uncontrolled data to evaluate, however, three case studies have been published thus far. A case study from two Japanese patients reported that HPβCD (IV administration) treatment did not

improve the patient's neurological deficits due to the drugs inability to cross the blood-brain barrier (BBB) (90), but it was, however, partially effective in ameliorating their hepatospenomegaly (91).

In accordance with the patient's limited recovery following IV HPβCD treatment, it was determined in the mouse model that HPβCD did not cross the BBB either when injected IP or following brain *in situ* perfusion (92). As a result of these mouse studies and the two patients partial recovery receiving cyclodextrin (CD) via IV infusions, treatment now focuses on intrathecal and/or intracerebroventricular (ICV) injection to deliver HPβCD directly to the CNS.

Another case study reported a patient who initially received two years of IV HPβCD, the second year for which she was also taking miglustat, and then began intrathecal HPβCD therapy for 2 months eventually to receive an Ommaya reservoir implant (93). This patient had no adverse side effects despite the auditory toxicity observed in the cat model receiving HPβCD delivered directly to CNS (90), and maintained residual function and a stable clinical state for the two years receiving cyclodextrin ICV (93). However, it is difficult to know what additional effect the miglustat may have contributed to the patient's clinical stability.

In another recent case study involving two adult patients, neither patient observed any improvement or slowing of disease progression and in fact both had either adverse reactions or worsening of neurological symptoms to the intrathecal HPβCD

(94). These findings for these two adult patients contradicted previous reports of clinical improvements or stabilization in paediatric patients, which may suggest that HPβCD is a therapy that would only be applicable to juvenile/infantile patients.

Over 20 patients are currently receiving HPβCD worldwide, yet only 3 case studies have been published to date (95). With many of these case reports or anecdotal stories the patient is often on both miglustat as well as receiving HPβCD through a combination of different routes. Disassociating the effects of the miglustat alone and when combined with HPβCD either IV or ICV in a controlled study is necessary, as will direct the best way of therapeutic intervention.

The commercially produced HPβCD , VTS-270 [Vtesse, Inc], has been granted Orphan Drug status by both the FDA and EMA and is in Phase 2b/3 clinical trials for the treatment of juvenile NPC, which it is now currently recruiting patients (96). Additionally, despite the limited effectiveness published in the case reports (91), IV administration of Trappsol®Cyclo™ [CTD Holdings] is also moving towards a Phase I/II clinical trial in Europe and a Phase I clinical trial in the United States, as a application to the MHRA [Medicines and Healthcare products Regulatory Agency] and FDA were submitted in August 2016 (95).

In addition to the cyclodextrin compounds VTS-270 and Trappsol®Cyclo™, two other therapies are currently in clinical trials for the treatment of NPC – the small

molecule heat shock protein 70 (HSP70) inducer, arimoclomol, and the histone deacetylase (HDAC) inhibitor, vorinostat.

1.2.7.2.2 Arimoclomol

Arimoclomol [Orphazyme, ApS], is a small molecule co-inducer of HSP70 that has most recently been designated Fast Track status by the FDA and is in Phase 2b/3 clinical trials (96). The clinical trial for arimoclomol has currently recruited 33 patients for the observational stage of the study, with the intervention study to follow (97). Arimoclomol has been shown to have good systemic drug distribution and cross the BBB via receptor-mediated transport through the low density lipoprotein receptor-related protein 1 [LRP1] and enter neurons (98). Arimoclomol acts as a co-inducer of heat shock proteins, which stabilises the interaction of Heat Shock Factor 1 [HSF1] with heat shock elements (98). It is thought that through this chaperone-mediated action the misfolded NPC1 protein may gain some functionality. HSP70-based treatments have been suggested to be an effective treatment for a range of neurodegenerative diseases, and arimoclomol is also in an investigator led clinical trial for the neurodegenerative disease Amyloid Lateral Sclerosis (ALS) (98).

In the mouse model of NPC1 arimoclomol was found to reduce ataxia and extend the lifespan of the treated mice demonstrating the drug's neuroprotective capacity (98). No significant side effects had been observed in the NPC mouse model or in the ALS clinical studies, however, no studies have been performed on feline models, nor has

the drug been prescribed off license to NPC patients, due to it not being licensed for any other conditions.

1.2.7.2.3 Vorinostat

The third compound currently in clinical trials is the HDAC inhibitor vorinostat, an FDA-approved drug prescribed acutely for the treatment of cutaneous T-cell lymphoma (99). It is thought, like in the case of arimoclomol, that up-regulation of chaperones to overcome misfolded mutant NPC1 or NPC2 proteins may serve to restore the proteins normal function (100). Through altering chromatin structure, HDAC inhibitors, such as vorinostat, can change the expression of a large number of proteins and increase the production of protein chaperones (100). Vorinostat was found to reduce lysosomal cholesterol levels as well as reduce sphingolipid cellular accumulation in NPC (100). However, when vorinostat was tested in the $Npc1^{nmf164}$ mouse model no increased life span was observed, despite promising cellular findings (101).

As vorinostat is poorly soluble and does not permeate the BBB, when coupled with HPβCD and polyethylene glycol (PEG), it was found that the HDAC inhibitor could be delivered both systemically and to the CNS (101). While highly encouraging as the vorinostat/HPβCD/PEG triple combination therapy improved cerebral and systemic aspects of this disease, the HPβCD/PEG combination treatment was not, however, examined as a double combination treatment control (101). Further studies are critical for determining if the triple combination treatment is in fact more effective

than any of the double combinations, especially as vorinostat is currently in an exploratory phase 1 clinical trial for adult NPC patients with 6 patients currently recruited (101, 102).

In addition to the on-going clinical trials, numerous drugs are currently under development and examination for the treatment of NPC. From bile acid replacement (103) to novel gene therapy approaches, various treatments are being further examined to better treat Niemann-Pick disease type C and combination therapies will likely be the most effective method of disease management in the future.

1.3 Aims of the Following Chapters

As the function of the NPC1 protein remains unknown, in **Chapter 2**, we

- Perform an unbiased yeast screen to better understand the conserved function of the NPC1 protein and the pathways it is involved in

In **Chapter 3**, we

- Explore the potential convergent pathogenic cascades and mechanistic relationships between NPC and Tangier disease
- The effectiveness of NPC therapies in Tangier disease is also evaluated

In **Chapter 4**, we

- Take advantage of the convergent pathways that exist between NPC and other disorders as a way to explore novel therapies that target the ABCA1 protein

Finally, in **Chapter 5**, we

- Investigate the therapeutic potential of a re-formulated β-cyclodextrin compound, Crysmeb
- Explore new drug delivery routes to minimize the invasiveness and costs currently associated with cyclodextrin intrathecal/ICV administrations

Chapter 2: Unbiased Screens as Tools for Understanding and Validating the Consequences of NPC1 Dysfunction

2 Unbiased Screens as Tools for Understanding and Validating the Consequences of NPC1 Dysfunction

2.1 Introduction

The first application of high throughput screening techniques was phage display in 1985, and since then has been applied to a variety of scientific areas of research, most notably in terms of drug discovery (104). The probability of success in each screen depends on the number and quality of targets, the quality of data generated, and in drug discovery, the number and diversity of compounds available (105).

2.1.1. Yeast as a Model for NPC

The NPC1 protein is highly conserved throughout evolution, and is found in species from yeast (Ncr1p, Niemann-Pick related protein 1) to man. Yeast cells lacking

Ncr1p are viable and serve as a model for studying human NPC disease as they exhibit sphingolipid mistrafficking, a hallmark of human NPC deficient cells.

Steve Sturley and his group first generated and studied the yeast *Ncr1* mutant (Δncr1) in 2004, where they proposed that the primordial role of the NPC1 protein was that of sphingolipid recycling, rather than cholesterol transport (10). Following this seminal work, groups have since suggested that in yeast Ncr1p may not have a direct role in endocytic membrane transport, as Δncr1 mutants had no changes in sterol homeostasis or defects in endocytosis (14). A phenotype in Δncr1 colonies was also later demonstrated, edelfosine (immune modulator that induces apoptosis) resistance– and this phenotype could be exploited when examining the functional impact of different patient mutants in yeast (12). As many human mutations of the NPC1 protein result in a misfolded protein that is incompletely trafficked to the endocytic system, previous studies identified the adaptor protein complex-3 as facilitating the Ncr1p protein localization to the vacuole and has been identified as a targets for treatment (15).

Further examination of the Δncr1 colonies revealed additional therapeutic targets, including a target that is currently in clinical trials – HDAC inhibitors. These studies took advantage of the ability to perform synthetic lethal screens (**Figure 2.5**), where genes and pathways that exacerbate the lethality of the *NCR1* yeast were identified (106). It was suggested that in NPC there may be an imbalance in histone acetylation levels, and they found that treating patient fibroblasts with HDAC

inhibitors reduced cholesterol storage in NPC1 fibroblasts (106). Chronology of studies using yeast as a model for NPC in **Figure 2.1**.

2004	2005	2007	2011	2014
NCR1 is the yeast orthologue of mammalian *NPC1* Δncr1 has no sterol-related phenotype and defect in endocytosis	Phenotype in Δncr1 yeast found - endelfosine resistance	In yeast, the adaptor protein 3 (AP-3) facilitates the localization of Ncr1p and Npc2p to the vacuole	Synthetic lethal screen in conditions requiring yeast to utilize exogenous sterols Identified importance NuA4 histone acetyltransferase complex Suggested that histone acetylates are key to cholesterol homeostasis in NPC disease	Δncr1 mutants have shortened chronological lifespans, increase of oxidative stress markers and mitochondrial dysfunction Mitochondrial function regulated in Δncr1 mutants by the TORC1 activated Pkh1p-Sch9p sphingolipid signaling complex

Figure 2.1. Chronology of NPC studies using the *S. cerevisiae* model system. Characterization in 2004 by Malathi K and Zhang S (10); 2005 by Berger AC (12); 2007 by Berger AC (15); 2011 by Munkacsi ;and 2014 by Vilaca R (16).

Using yeast as a model to study NPC, mitochondrial dysfunction was also identified (16, 106). It was found that Δncr1 yeast exhibit oxidative stress sensitivity, shortened chronological life spans, and aberrant signalling in pathways regulated by the mammalian target of rapamycin complex 1 (mTORC1) (16). Additionally, an accumulation of long-chain sphingoid bases was observed (16).

From Steve Sturley's initial findings and the subsequent studies of the yeast *Ncr1* mutant, the yeast as a model system for studying NPC1 disease has been validated. We therefore aim to take advantage of this model system to better understand the function of the NPC1 protein and determine compensatory pathways and processes that may be involved in the cellular pathogenesis of this disease.

2.1.2. Protein Based Screens to Validate Yeast Findings

Proteins implicated to play a role in NPC pathogenesis identified in the yeast can be validated in various ways. Often the yeast system itself can be further probed to validate the "hits" identified, where as the other approach is to move straight into mammalian systems. This second approach is the one followed in this study, and proteomic and phosphoproteomic based screens in the mouse model were used to validate our findings from the yeast.

Previously, comprehensive proteomic screens have been performed on both the *Npc1*$^{-/-}$ mouse cerebellum as well as on patient fibroblasts expressing the most common human mutation, I1061T (107, 108). In the mouse cerebellum study an enrichment of proteins involved in pyruvate metabolism, glycolysis, and the citric acid cycle suggested a defect in glucose metabolism and mitochondrial function (107). In addition, enzymes associated with oxidative stress, proteins related to Alzheimer's disease and fatty acid binding proteins were also identified (107).

In the proteomics screen looking at patient fibroblasts with the I1061T mutation, 281 proteins were found to be differentially expressed (108). These proteins identified had functions involved in energy metabolism, lipid metabolism, ROS metabolism, and apoptosis (108). Interestingly, in this study an enrichment of

mitochondrial proteins was also observed, and accumulation of glycogen was observed in the NPC1 patient cells (108).

However, no phosphoproteomic screens have been performed to date in NPC. Previous studies have shown that identification of post-translational modifications of proteins can contribute to the understanding of neurodegenerative pathobiology (109, 110). For example, networks of differentially phosphorylated kinases were identified in Alzheimer's disease and are thought to contribute to the dysregulation of the heat shock and protein quality control pathways in this disease (111).

Additionally, *Npc1*$^{+/-}$ heterozygous mice have been shown to be largely non-symptomatic and have not been studied at the proteomics level extensively. It has been suggested, however, that *Npc1*$^{+/-}$ mice do show cellular pathologies from 2yrs of age onward, as cholesterol accumulation was observed in the brain as well as signs of Purkinje cell loss (112). However, recent studies have shown that at as early as 9 weeks partial motor dysfunction and increased anxiety-like behaviour could be observed in the heterozygous mutant *Npc1*$^{+/-}$ mice, and this phenotype was generally more severe in male mice (113). Any indications of phosphoproteomic changes at early stages of life (~5wks) in the *Npc1*$^{+/-}$ mouse, before behavioural or CNS dysfunction is apparent, may serve as a means of identifying key changes associated with the earliest stages of NPC pathogenesis.

In this chapter we perform complementary high throughput screen that take advantage of two different model systems – *Saccharomyces cerevisiae* and an authentic Npc1 mouse model (*Npc1*^{m1n}). Taken together, these screens provide a robust data set that can provide insights into both the function of the NPC1 protein, as well as elucidate new therapeutic targets.

The specific aims presented in this chapter are:

- Identify proteins that physically interact with the yeast NPC1 orthologue, Ncr1p, on the vacuolar membrane, and proteins that may contribute to NPC cellular dysfunction
- Identify potential compensatory pathways that may be involved in NPC
- Taking advantage of mouse cerebellar proteomic and phosphoproteomic screens to validate novel signalling pathways as therapeutic targets

2.2 Materials and Methods

2.2.1 Yeast Strains and Libraries

All yeast strains in this study are based on the BY4741 laboratory strain (114). Gene deletion was performed using the pFA6 plasmid series (115). Green fluorescent protein (GFP) tagged strains were picked from the GFP library (116), deletion strains were picked from the yeast deletion library (117).

2.2.2 Robotic Library Manipulations

All genetic manipulations on entire libraries were performed using Synthetic Genetic Array techniques (118, 119). To manipulate libraries in 1536-colony high-density format, a RoToR bench top colony arrayer (Singer Instruments, UK) was used.

2.2.3 Systematic Screens

2.2.3.1 GFP Screen

Haploid strain containing the *Ncr1* deletion with Nourseothricin resistance (+Nat) were mated with GFP tagged library without Histidine (-His) of opposing mating type on yeast extract peptone dextrose (YPD) rich media plates. Diploid selection was performed twice on plates containing all selection markers found on both

parent haploid strains (+ Nat, -HIS). Sporulation (5-7days) was induced by transferring colonies to plates containing 10mM Uracil, 10mM Tryptone and normal agar. Haploid cells containing all desired mutations were selected by transferring cells to plates containing selection markers (+Nat, -HIS) alongside the toxic amino acid derivatives arginine and lysine (-ARG, -LYS), canavanine (+CAN) and thialysine (+SAEC) [Sigma-Aldrich]. Double mutants were then selected for using all selection markers, moved to liquid medium, and used for microscopic screening.

2.2.3.2 Synthetic Lethal Screen

Haploid strains containing the *Ncr1* deletion with Nat resistance (+Nat) were mated with knock-out/decreased Abundance by mRNA perturbation (KO/DAmP) library with Kanamycin resistance (+G418 KanR) on YPD rich media plate. Diploid selection was performed twice on plates containing selection markers found on both parent haploid strains (+Nat, +G418). Sporulation (5-7 days) was induced by transferring colonies to nitrogen starvation plates. Haploid cells containing all desired mutations were selected for by transferring cells to plates containing the selection markers (-Leu, -Lys, -Arg, +Can, +Saec). Double mutant selection was performed by plating cells on plates containing selection markers (-Leu, -Lys, -Arg, +Can, +Saec, +Nat, +G418). Plates were then scanned and analysed using Baloney software.

2.2.4 High-Throughput microscopy

Microscopic screening was performed using an automated microscopy system (ScanR system, Olympus) as previously described and performed by Silvia Chuartzman of the Weizmann Institute (118). Briefly, images were acquired for GFP (excitation 490/20nm; emission 535/50nm) and bright field channels. After acquisition, images were manually reviewed in MatLab vs.2012a 7.17 using compare2picturesV5 script. As there were no colocalization markers, we assigned only those localizations that could be easily discriminated by eye.

2.2.5 Protein Complementation Assay Screen using the DHFR Library

Haploid strain "A" is Nat resistant (+Nat), whereas haploid strain "α" is hygromycin B (+Hygror) resistant. Pmc1 haploid strain "A" and "α" were used; however, due to no Ncr1 haploid strain "A", only Ncr1-α was used. Haploid strains of either pmc1 or ncr1 were mated with the vacuolar membrane protein library on YPD rich media plates. Diploid selection was done twice on plates containing selection markers (+Nat, +Hygror). Diploids were then moved to mettalux media [0.200g Methotexate + 20mL DMSO +YPD] for 7 days to select for proteins that are physically interacting. Plates were then scanned and analysed using Baloney software.

2.2.6 Growth Assay

For assaying growth on solid media supplemented with treatments, strains were grown overnight at 30°C in liquid media, back diluted to OD=0.013, allowed to grow until log phase, and serially diluted (10fold) and spotted on pre-conditioned plates. Growth conditions included Myriocin (0.5ng/mL), Fumonosin B (1mg/mL), $CaCl_2$ (5mM), Terbinofin (100µg/mL) and standard SD at 40°C and 16°C.

2.2.7 Proteomics/Phosphoproteomics Screen

Cerebellum samples from *Npc1*$^{+/+}$, *Npc1*$^{+/-}$ and *Npc1*$^{-/-}$ were processed by Nicolas Lebesgue of the University of Utrecht as previously described (120). Briefly, frozen cerebellums were lysed in buffer (8M urea, 50nM ammonium bicarbonate, protease inhibitors [complete mini EDTA-free mixture, Roche Applied Science] and phosphatase inhibitor mixture [PhosSTOP, Roche Applied Science]), and centrifuged (20000g, 10min 4°C). The supernatant was then digested for 4hr at 37°C with Lys-C (1:100), followed by a second overnight digestion at 37°C with trypsin (1:100) in 2M urea. Peptides were chemically labeled using stable isotope dimethyl labeling as previously described (121). Wild type (*Npc1*$^{+/+}$) tissues were labeled 'light', heterozygous (*Npc1*$^{+/-}$) tissues were labeled 'intermediate', and homozygous (*Npc1*$^{-/-}$) tissues were labeled 'heavy'. Samples were mixed 1:1:1, reconstituted in 10% formic acid, and fractionated using strong cation exchange as previously described (120). The Zorbax BioSCX-Series II column fractions were dried under a vacuum and resuspended in 10% formic acid. The peptides then underwent

phosphopeptide enrichment as previously described (122). Briefly, peptides were dried and resuspended in 80% MeCN, 6% trifluoracetic acid and loaded ontol Ti^{4+}-IMAC columns. Column was washed with 50% MeCN, 0.5% trifluoracetic acid, 200nM NaCl followed by 50% MeCN, 0.1% trifluoracetic acid, and samples were eluted with 10% ammonia followed by 80% MeCN, 2% formic acid and elutant was dried under vacuum centnrifuge. Dried peptides were resuspended in 10% formic acid, 5% dimethyl sulfoxide and analyzed on nano flow reverse phase liquid chromatography on Agilent 1200 Infinity nanoLC system (Agilent) coupled to a Q-Exactive mass spectrometer (Thermo, San Jose, USA). The mass spectometry proteomics data has been deposited at the ProteomeXchange Consortium via PRIDE partner repository (123) with dataset identifier PXD003742.

2.2.8 Cells

Human NPC1-mutant and control fibroblasts were obtained from the NIH (Dr Forbes Porter). The NPC1 patient fibroblast line used (NPC5; severity score 14) has two point mutations (compound heterozygous), I1061T and R1186G. The fibroblasts were maintained in DMEM with 10% FCS, 1% penicillin/streptomycin and 1% $_{L}$-glutamine. All cells were cultured at 37°C with 5% CO_2.

2.2.8.1 Cell Drug Treatments

Treatments with CaMKII inhibitors KN-62 (2hrs; 10,30μM) and KN-93 (2hrs; 1,8μM); PKCδβα inhbitors K-252b (2hrs; 20nM, 50nM) and Bisindolymaleimide I

(2hrs; 100nM, 1μM); HSP90 inhibitors 17-DMAG (12hrs; 100nM, 1μM) and Geldanamycin (2hrs; 180nM, 360nM).

2.2.9 Mitochondrial Defect Characterization

2.2.9.1 Oxygen Consumption

Chinese hamster ovary (CHO) cells (control and NPC1$^{-/-}$) were grown and plated in DMEM-F12 growth media at a density of 50,000/well. Cells were moved into 150μL varying glucose DMEM-F12 conditions (25mM, 5mM, 1mM, 0mM) for 24 hours before measuring their oxygen consumption using the MitoXpress-Xtra assay (Luxcel). MitoXpress probe stock solution (10μL, 1μM) was added to each well, followed by a layer of 100μL mineral oil. The plate was then read at 1.5min intervals for 13 hours using 380nm excitation and 650nm emission. Cell respiration reduces the concentration of dissolved oxygen in the sample resulting in an increase in MitoXpress probe signal. An identical plate was stained using 10μM propidium iodide (PI) to obtain cell numbers and standardised accordingly.

2.2.9.2 Mitochondrial Morphology Quantification

Using the high content IN Cell 1000 (GE healthcare Life sciences, 500 cells acquired per well) analyser, we quantitatively measured fluorescent mitochondria labelling in control and NPC1 fibroblasts. Cells were fixed with 4% (w/v) paraformaldehyde

for 15 minutes and immunostained at 20°C for mitochondrial outer membrane translocase complex, subunit TOM20 (TOM20; 1:200) and microtubule-associated protein 1 light chain 3 aplpa (LC3;1:500) for 90 minutes. Dyelight 488 goat anti-rabbit (1:2000) and Dyelight 594 goat anti-mouse (1:2000) secondary antibodies were applied for 1 hour, 20°C. After Hoetsch staining (1:10,000, 5min) the cells were imaged using the IN Cell 1000 analyser. Raw images were processed by Alan Diot, and parameters were obtained using a customized protocol in the IN Cell developer toolbox (GE Healthcare Life Sciences) (124).

2.2.9.3 Mitochondrial DNA (mtDNA) Analysis

Total DNA was extracted using the DNeasy blood and tissue kit (Qiagen) from 10wk old mouse cerebellum. The DNA was diluted to 5ng/µL and performed in triplicates. Real time quantitative PCR was performed on the DNA samples using a multiplexed Taqman assay in a Corbett quantitative PCR machine. Primer and probe sequences are:

Primer Nuclear F (APP-137F):
TTTTTGTGTGCTCTCCCAGGTCT

Primer Nuclear R (APP-210R):
TGGTCACTGGTTGGTTGGC

Primer Mitochondrial F (MitHu-330F):
AGGACAAGAGAAATAAGGCC

Primer Mitochondrial R (MitHu-330R):
TAAGAAGAGGAATTGAACCTCTGACTGTAA

Genomic probe (FAM):
CCCTGAACTGCAGATCACCAATGTGGTAG

Mitochondrial probe (Yellow Yakima):
TTCACAAAGCGCCTTCCCCCGTAAATGA

Nuclear primers were used at a concentration of 300nM, mtDNA primers at 100nM and the two probes at 200nM. DNA was amplified using the Taqman universal PCR mastermix no AmpErase UNG (Life Technologies, 4364341) and the following PCR cycle [94°C 10mins, (94°C 30s, 60°C 1min) x 40; gain optimized at 60 degrees]. Fluorescence was measured in yellow and green wavelengths, for Yakima Yellow (ex530/em549) and 6-Fam (ex495/em520) respectively. The mtDNA copy number was normalised to the single copy nuclear DNA gene amyloid beta and the results are expressed as a ratio of mtDNA/nDNA.

2.2.9.4 Mitochondria Isolation

Mice (P21) were killed by terminal anesthesia, and transcardially perfused with 40ml of ice-cold PBS. Livers were dissected and rinsed in a sucrose solution (0.25M sucrose, 5mM Tris-HCl, 2mM EGTA, pH 7.4). Liver tissue was finely chopped in fresh sucrose solution, homogenized in in glass grinder in 3mL sucrose solution, and centrifuged 500*g,* 10min. The supernatant was retained and pellet homogenized again in glass grinder with 3mL sucrose solution followed by centrifugation 500*g*, 10min. The supernatants were pooled and centrifuged at 10000*g*, 10min, 4°C. The supernatant was then discarded and pellet air dried before being resuspended

gently in 3mL sucrose solution and centrifuged again 10 000*g*, 10min, 4°C. The supernatant was finally aliquoted, centrifuged 1000*g*, 2min and pellets stored at -80°C until use. Protein concentration was quantified using a bicinchoninic acid (BCA) assay kit (Sigma, BCA-1).

2.2.9.5 Western-Blot Analysis

For western blots 20µg of protein was heated for 5mins at 95°C in Laemmli sample buffer (4% SDS, 20% glycerol, 10% 2-mercaptoethanol, 0.004% bromphenol blue, 0.125M TrisHCl, pH 6.8) before loading onto a 4-12% bisacrylamide gradient gel (NuPAGE Novex). The gel was run at 3A, 140V, 300W before being transferred onto PVDF membrane (BioRad Trans-Blot® Turbo™ transfer system). Blotted membranes were blocked for 2hrs in PBS containing 0.1% Tween-20 (PBS-Tw) and 5% milk powder before washing in PBS-Tw. Blocked blots were incubated with primary antibodies (goat anti-LARS2, 1:1000 PBS-Tw, sc-102650, Santa Cruz Biotechnology) overnight, 4°C. Blots were washed three times before incubating with secondary antibody (donkey anti-goat IgG HRP conjugated, 1:12,500 PBS-Tw, sc-2020 Santa Cruz Biotechnology) for 1.5hrs, RT followed by three washes. β-actin was quantified using mouse anti-beta actin HRP conjugated antibody, 1:25,000 (A3854, Sigma), incubated for 2hrs, RT followed by three washes. Washed blots were incubated in ECL reagent (RPN2106, Amersham) for 5 minute, before imaging using the BioRad ChemiDoc XRS+. Images were quantified using the ImageLab software (V3.0, BioRad Laboratories). Bands for LARS2 were normalized for β-actin.

2.2.10 Microtubule Defect Characterization

2.2.10.1 Acetylated α-tubulin

Cells were fixed with 4% (w/v) paraformaldehyde for 15mis and immunostained for mouse anti- acetylated α-tubulin (6-11B-1, Santa Cruz Biotechnology) at 1:250, with 10% goat serum and 0.2% TritonX-100 overnight, 4°C. Cells incubated in Dyelight 488 horse anti-mouse (1:2000) secondary antibody for 1 hour, 20°C and Hoetsch stained(1:10,000, 5min). Cells then imaged on a Zeiss Axiovert fluorescent microscope.

2.2.10.2 Quantification of Staining by Florescent-Activated Cell Sorting (FACS)

Relative lysosomal volumes and acetylated α-tubulin were measured from patient derived fibroblasts following NAD (50μM, 100μM, 250μM; N0632 Sigma) and AGK2 (0.1μM, 1μM, 10μM; 304896-28-4 Cayman Chemical) treatments. Live cells were washed twice with PBS and stained in triplicate using LysoTracker green (200nM PBS) for 10min, RT. Cells were resuspended in FACs buffer (100μL 10% BSA, 100μL 2M NaN3 per 10mL PBS) and PI stained (1μg/mL) immediately prior to FACS analysis. For acetylated α-tubulin quantification, cells were fixed in 4% paraformaldehyde 10min, RT and permeabilized with 0.1% PBS-Tw for 20min RT. Cells were thenstained for mouse anti- acetylated α-tubulin (1:1000, 6-11B-1, Santa Cruz Biotechnology) in PBS with 10% goat serum and 0.3M glycine for 30min, RT. Cells were then washed and incubated with Dyelight 488 horse anti-mouse (1:500)

secondary antibody for 30min, RT. Cells were then washed and resuspended in FACs buffer for FACS analysis. FACS analysis was performed on a BD FACSCantoII flow cytometer with BD Bioscience FACSDiva software, with 10.000 cell events recorded. The molecules of equivalent fluorescence (MEFL) was calculated using 8-peak Rainbow calibration beads (559123, BD), using the fluorescein equivalent values provided.

2.3 Results

2.3.1 Identification of Proteins and Pathways Implicated in NPC

In 2004 Steve Sturley's lab first published the first characterization of the yeast *Ncr1* mutant (10). Since then phenotypes have been observed in the yeast and further validated in mouse and human cell models strengthening its utility as a cellular model of NPC. As the technology to exploit yeast genetics has advanced since this initial publication, we performed a variety of screens and assays to identify some of the key processes and proteins in the yeast model system that may be involved in mammalian NPC1 pathology.

2.3.1.1 Identfication of Proteins Ncr1p Interacts with on the Vacuolar Membrane

One of the many questions surrounding the NPC1 protein is the nature of the proteins it interacts with on the lysosomal membrane. NPC1 is though to interact with NPC2 via its N-terminal cholesterol binding loop on the lysosomal luminal side to transfer cholesterol (9), however other interacting proteins remain unknown. We therefore performed a protein complementation assay (**Figure 2.2A**) to identify any proteins that physically interacted with Ncr1p on the vacuolar membrane. We looked only at the 48 proteins that were also located on the yeast vacuole membrane, and identified Pmc1p, Apc11p, and Fth1p as having a strong interaction with Ncr1p (**Figure 2.2B**). Protein interaction strength was based as a function of colony size divided by vacuolar abundance (Pmc1p = 0.566; Apc11p = 0.275; Fth1p = 0.238).

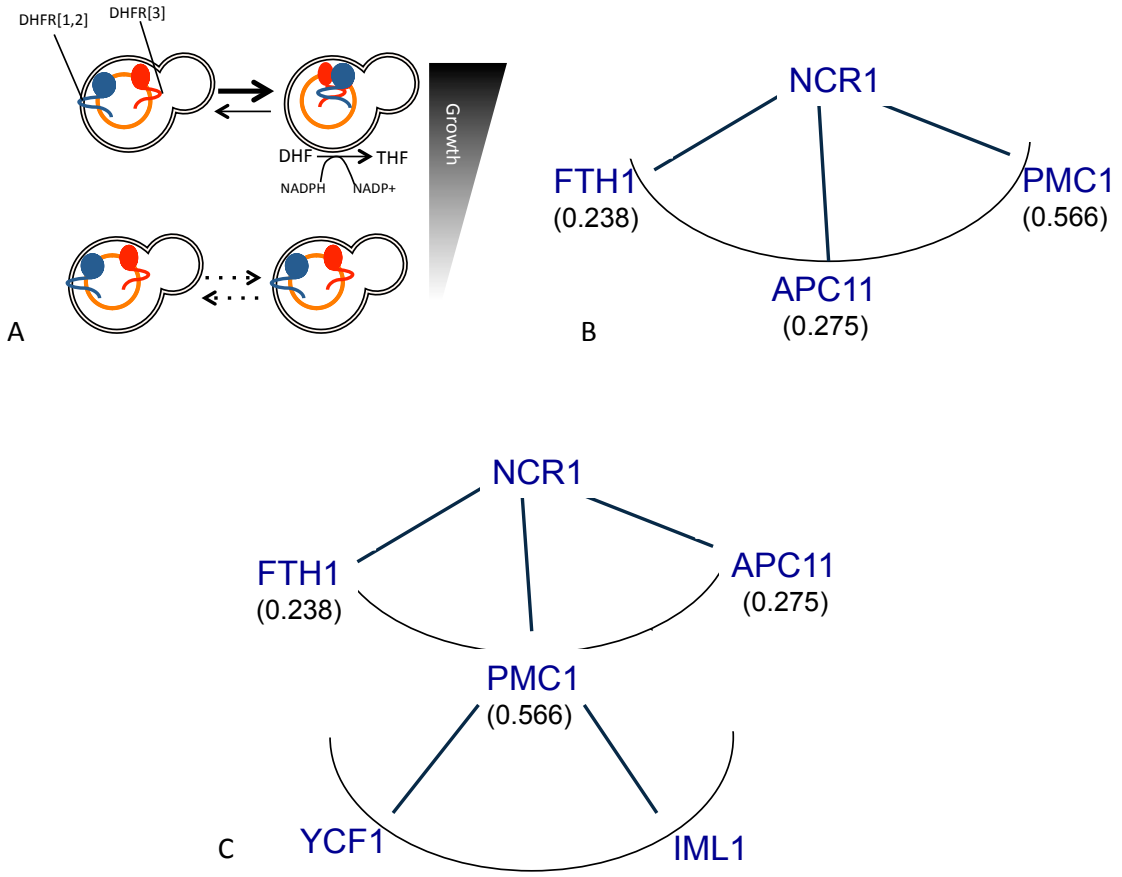

Figure 2.2. *Protein complementation assay to identify physically interacting proteins.* **A)** Assay methods as adapted from Freschi et al. 2013 (4). **B)** The yeast Ncr1 protein physically interacts with 3 vacuolar membrane proteins, these include: Fth1p, Pmc1p, and Apc11p, with interaction strength (colonly size/relative abundance) as indicated. **C)** The interacting partner Pmc1p interacts additionally with Ycf1p and Iml1p on vacuolar membrane.

Pmc1p is a calcium ATPase, Apc11p is anaphase-promoting complex involved in cell cycle regulation, and Fth1p is an iron transport protein. Interestingly, it has been previously shown that in NPC disease there is both an acidic store calcium defect and impaired iron homeostasis (13, 125). Additionally, we also examined the proteins that Pmc1p interacted with on the vacuolar membrane and identified three proteins, one being Ncr1p, and the others Ycf1p and Iml1 (**Figure 2.2C**). Ycf1p is an ABC transporter and Iml1p has a role in autophagy regulation. In NPC a defect in the

autophagic flux has already been characterized (126), suggesting that a mutation in Ncr1p may impact the functionality of proteins that it physically interacts with on the vacuolar membrane, as well as the proteins that interact with Npc1p's binding partners.

2.3.1.2 Modulating Ca^{2+} and Sphingolipid Levels does not Elicit a Growth Phenotype

Once we identified the proteins Ncr1p was physically interacting with on the vacuolar membrane, we next wanted to determine if we could induce a growth phenotype for either *NCR1* knockout (Δncr1) and *NPC2* knockout (Δnpc2) colonies. Despite having a dramatic phenotype in patient fibroblasts, knocking out the *NCR1* gene in yeast shows no observable phenotype when grown in normal conditions nor different temperatures (10). However, if an additional stress such a different growth media or drug treatment is introduced, a phenotype can then be induced in the Δncr1 and Δnpc2 mutant colonies. One aspect we were particularly interested in was the mutant colonies ability to grow in conditions with different Ca^{2+} or lipid levels – to see if this exacerbates the disease phenotype. Both control, Δncr1 and Δnpc2 colonies were plated on media in heat (40°C) and cold (16°C) shock conditions, and on plates containing excess calcium (5mM $CaCl_2$), sphingolipid biosynthesis inhibitor myriocin (0.5ng/mL), sphingosine-sphinganine-transferase and ceramide synthases inhibitor Fumonisin B1 (1mg/mL), and sterol inhibitor Terbinafine (100ug/mL). Here we observed no distinct phenotype in the colonies when grown on these varied conditions (**Figure 2.3**).

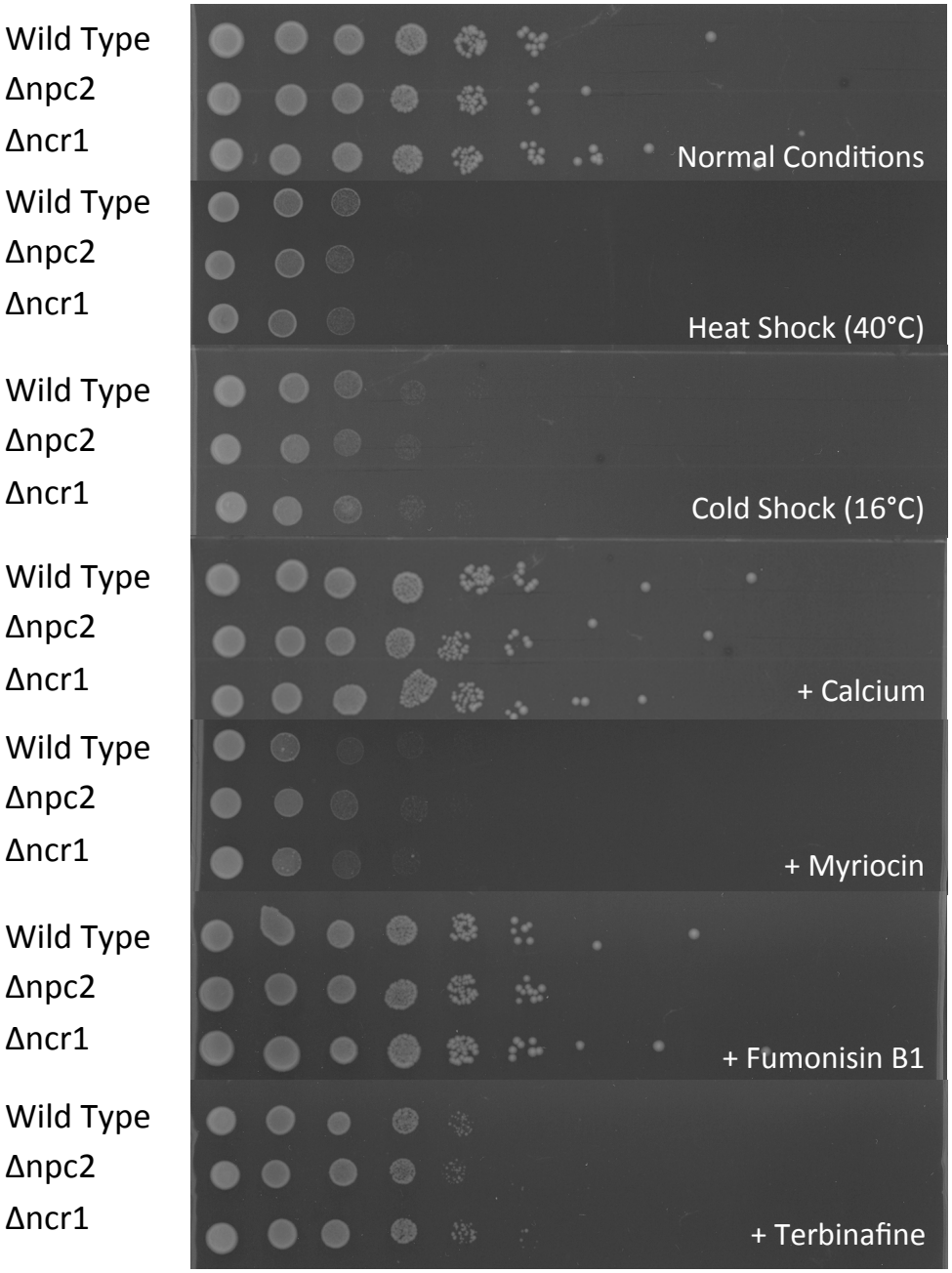

Figure 2.3. No gross phenotype was observed in the Δnpc2 or Δncr1 knockout colonies. Colonies were plated in heat (40°C) and cold (16°C) conditions, excess calcium (5mM $CaCl_2$), with the sphingolipid biosynthesis inhibitor myriocin (0.5ng/mL), with the sphingosine-sphinanine-transferase and ceramide synthesases inhibitor Fumonisin B1 (1mg/mL), and the sterol inhibitor Terbinafine (100μg/mL).

Since we could not generate a phenotype for either of the knockout lines on any of our chosen treatment conditions, we were interested in determining if there were compensatory pathways/proteins that were working in the yeast to mask any phenotypic differences.

2.3.1.3 Protein Localization in the Δncr1 and Wild-Type Yeast

We hypothesized that the cell must be undergoing reorganization to compensate for the mutation. To test this hypothesis we performed a GFP-localization screen where we compared the localization of proteins when expressed on the Δncr1 background as compared to control wild type colonies (**Figure 2.4**).

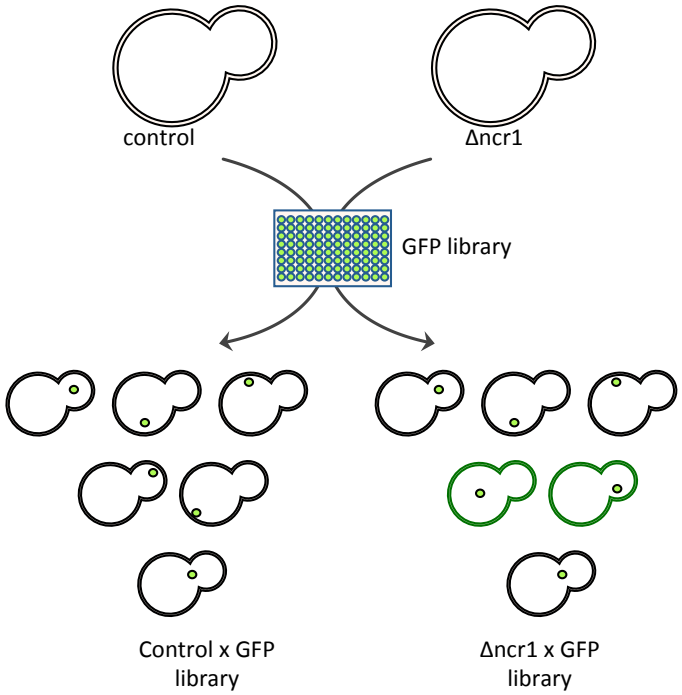

Figure 2.4. *GFP protein localization screen*. The NCR1 knockout mutant (Δncr1) is crossed with the yeast GFP tagged protein library and protein localization in the wild-type colonies is compared microscopically to the Δncr1 colonies.

Over 40 proteins were localized to different organelle in the Δncr1 colonies as compared to their normal localization in wild type colonies (**Appendix table 1**). This suggests that although no growth phenotype was observed in different conditions, the cell is undergoing major changes. These changes in localization may be a compensatory mechanism to maintain normal cellular functionality, or a defect in protein trafficking due to the loss of *NCR1*. Proteins that were found to be mislocalized included those involved in copper transport [Ctr1p], the vacuole protein sorting complex HOPS and ESCRT [Vps41p, Did4p], myosin motor domains [Dim1p], mitochondrial respiratory chain complex [Rsf1p, Rcf1p], sterol transport proteins [Pry1p], peroxisome biogenesis [Pex17p], nutrient sensing [Tco89p] and actin cytoskeleton organization [Prk1p] (**Appendix Table 1**).

3.2.1.4 Pathways that Exacerbate Lethality in the Δncr1 Yeast

We were interested in understanding if there were also parallel or redundant pathways that were involved in maintaining cellular function as Δncr1 had no overt phenotype. To examine this we performed a synthetic lethal screen, this involves comparing the genome wide knock-out library crossed onto the Δncr1 background with that of the knock-out library crossed to the wild type background (**Figure 2.5**). This will identify proteins that may be involved in pathways that are exacerbating lethality when expressed in Δncr1 colonies. Over 50 proteins were identified to possibly provide essential function in redundant or parallel pathways without physically interacting with Δncr1 colonies (**Appendix Table 2**).

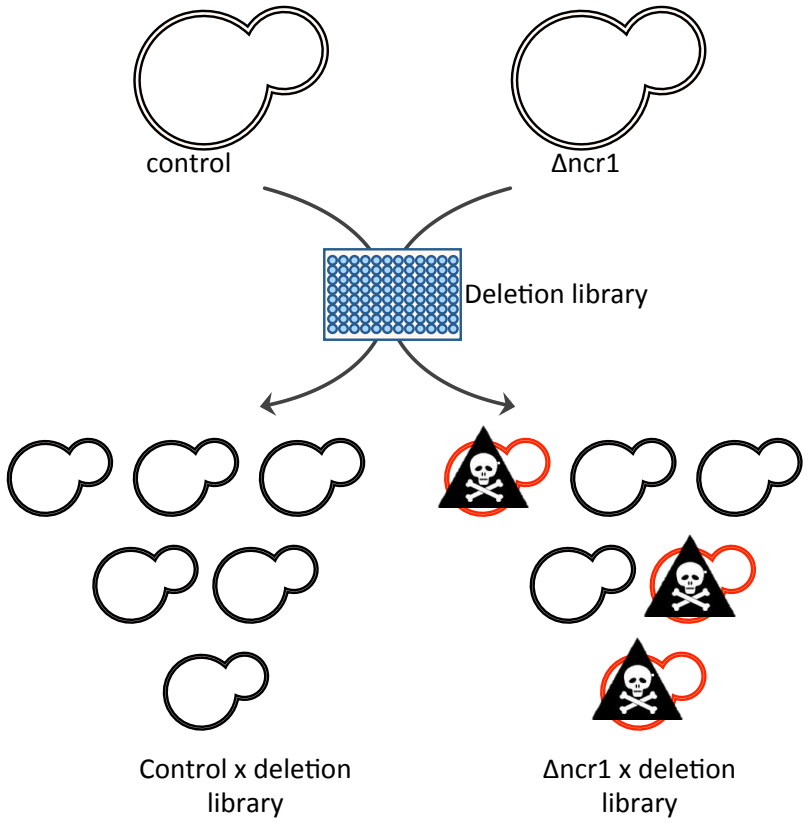

Figure 2.5. *Synthetic Lethal Screen*. The ncr1 knockout mutant (Δncr1) is crossed with the yeast deletion library and growth/survival in the double-knockout colonies is compared to the single-knockout colonies.

This suggests that the cell is compensating for the loss of *NCR1* by relying on other pathways, and that these pathways may be providing some essential function to the cell. Genes that were identified in this screen include those involved in copper transport [*MAC1*], sphingolipid and fatty acid biosynthesis [*FEN1*, *HTD2*], mitochondrial tethering and fusion [*FZO1*], and protein sorting [*MVB12*].

2.3.2 Validating Novel Phenotypes Identified in the Yeast Screen in Mammalian Cells

The screens provided us with processes that may be involved in disease pathogenesis and the complementation assay indicated proteins that Ncr1p may be physically interacting with, however we next wanted to see how this translates in the mammalian system.

As previously described, NPC is characterized by an accumulation of sphingosine, a reduction in acidic store calcium and a defect in the endocytic trafficking [Introduction **Figure 1.4**]. Our findings from this yeast screen support these pathologies, as well as other defects in mitochondrial function and in nutrient sensing pathways that have also been suggested independently across different yeast studies (16, 106).

2.3.2.1 Mitochondrial Dysfunction in NPC

We found in accordance with previous data (127) that CHO cells that were null for *NPC1* had a significantly reduced rate of respiration as compared to control CHO cells when grown in reduced glucose conditions (**Figure 2.6;** $p<0.0001$).

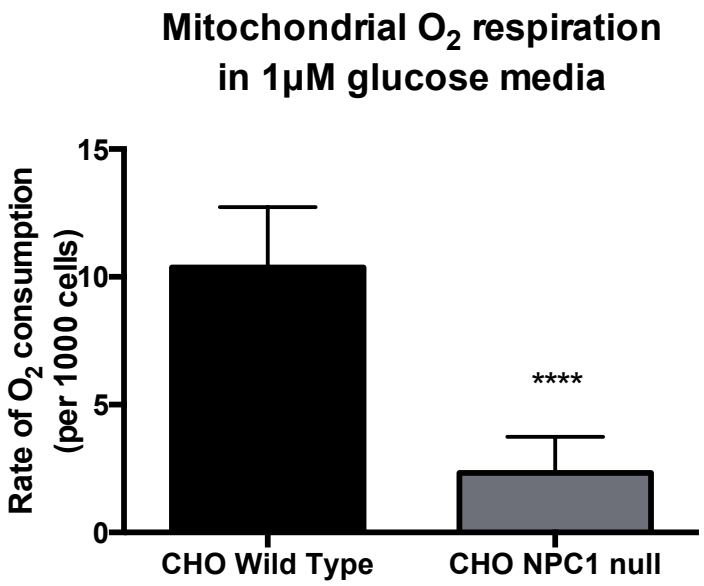

Figure 2.6. *Rate of Oxygen consumption in 1*μ*M reduced glucose media in CHO NPC1 null and wild type cells.* NPC1 null CHO cells exhibited reduced rate of oxygen consumption when grown for 24 hours in reduced glucose conditions (1μM). ****p<0.0001; student t-

In addition to functional readouts, we also examined some of the morphological and structural changes in NPC and control patient fibroblasts. When we quantified mtDNA levels in NPC1 patient cells we observed a significant reduction as compared to healthy controls (**Figure 2.7A**; p=0.0004). Interestingly, one of the genes implicated in mtDNA maintenance, *ILM1*, was identified in the synthetic lethal screen. Mutations in mtDNA have been associated with a range of clinical abnormalities and over 50% of mtDNA mutations are located in one of the mitochondrial tRNA genes (128). One of these mitochondrial tRNA genes is *LARS2*, and was found to be mislocalized in the Δncr1 yeast. However, when we examined the protein expression levels in mitochondria isolated from *Npc1*$^{+/+}$ and *Npc1*$^{-/-}$ livers we found no difference in LARS2 expression (**Figure 2.7B**). Additionally, when we examined the mtDNA levels in the cerebellum of the *Npc1*$^{-/-}$

mouse we observed a significant increase in levels as compared to the wild type control (**Figure 2.7C**; p=0.0003). This may be due to the reduction in nuclear DNA as the *Npc1*$^{-/-}$ mouse has undergone a significant level of neurodegeneration by 10 weeks of age.

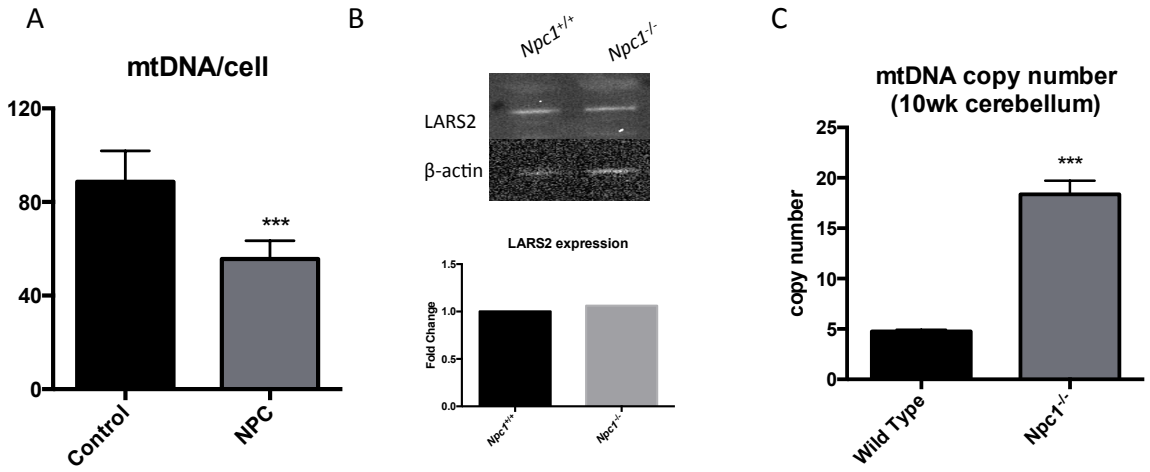

Figure 2.7. *Quantification of mitochondrial DNA in NPC patient fibroblasts and Npc1*$^{-/-}$ *cerebellum, and protein expression of mitochondrial tRNA protein LARS2.* **A)** NPC1 patient fibroblasts have reduced levels of mtDNA as quantified using picogreen staining. **B)** No difference in LARS2 expression was observed in the *Npc1*$^{-/-}$ mouse liver mitochondrial prep. **C)** A significant increase in mtDNA levels in the cerebellum were observed in the *Npc1*$^{-/-}$ untreated mouse as compared to the wild type mouse. ***p<0.001; student t-test

In addition to alterations in mtDNA levels, we also observed a significant increase in mean mitochondrial length (**Figure 2.8A**; p=0.0011). The gene that mediates mitochondrial fusion, *FZO1*, was identified in the synthetic lethal screen. The balance between fission and fusion determines mitochondrial length, and increased fusion can help overcome low levels of stress (129). This increase in mitochondrial length may be a mechanism to increase the calcium buffering of the organelle, as a hyperpolarization of the mitochondrial membrane potential was observed in the NPC1 patient fibroblasts as compared to control cells (**Figure 2.8B**; p<0.0001).

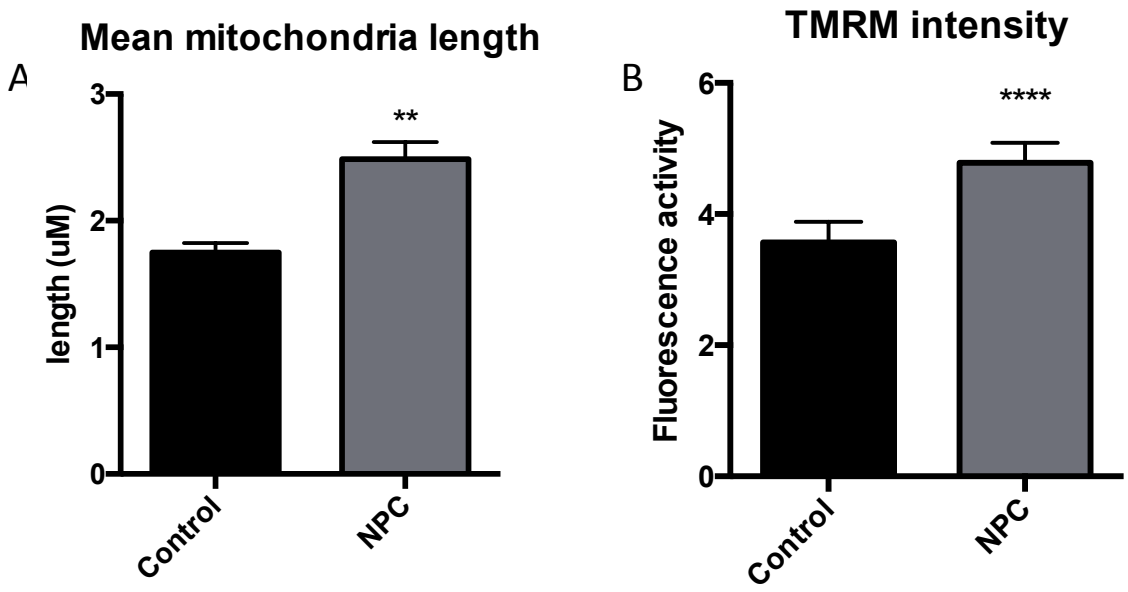

Figure 2.8. *Increased mean mitochondrial length and tetramethylrhodamine (TMRM) staining as a readout for mitochondrial membrane potential in control and NPC1 patient fibroblasts.* **A)** A significant increase in mitochondrial length was observed in NPC patient fibroblasts as compared to healthy controls. **B)** NPC1 patient fibroblasts exhibit significantly increased levels of TMRM staining intensity as compared to control cells. ***p*<0.01; *****p*<0.0001; student t-test

Additionally, there was a significant increase in perinuclear-localized mitochondria in the NPC1 patient cells as compared to the healthy controls (**Figure 2.9**; *p*=0.0062).

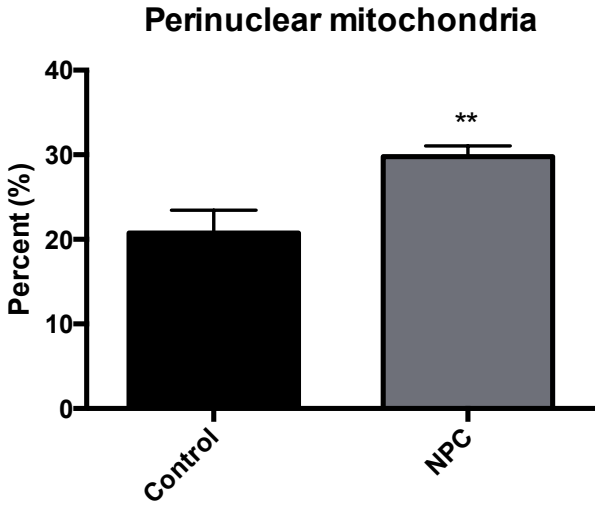

Figure 2.9. *Percentage of perinuclear mitochondria in NPC1 and control patient fibroblasts.* NPC1 patient fibroblasts have significantly higher percentage of perinuclear mitochondria than control cells do. ***p*<0.01; student t-test

2.3.2.2 Cytoskeletal Defects in NPC

In yeast colonies, it has been suggested that actin filaments are used as scaffolds for the attachment and movement of mitochondria and that several actin mutants have impaired mitochondrial morphology (130). Additionally, It has been suggested that an increase in perinuclear mitochondria (**Figure 2.9**) can be caused by reduced mitochondrial motility induced by a static actin cytoskeleton (131).

Interestingly, in yeast microtubules do not seem to have a direct role in mitochondrial motility or distribution (130). This may be due to the fact that yeast do not have an extensive microtubule network (132). However, in multicellular eukaryotic cells microtubules play a much more central role in organelle distribution (132). Microtubules in the cell transport organelles and cargo throughout the cell body and are important for maintaining transport (133). Microtubule dynamics, specifically α-tubulin, can be regulated by acetylation (134). It had been suggested that in NPC there may be an imbalance in histone acetylation (106), and in the NPC1 patient fibroblasts we observed a significant increase in acetylated α-tubulin as compared to healthy controls (**Figure 2.10;** p=0.0193).

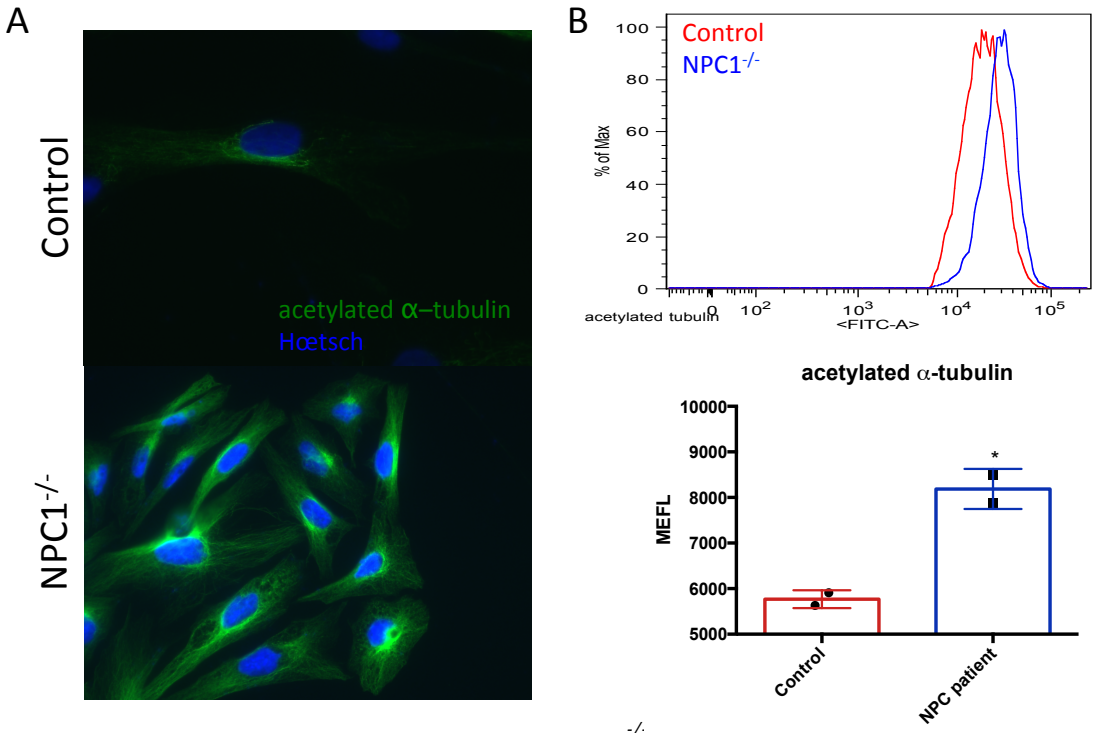

Figure 2.10. *Acetylated α-tubulin in control and NPC1$^{-/-}$ patient fibroblasts. A)* NPC1 patient fibroblasts stained for acetylated α-tubulin have increased levels as compared to control cells. B) Representative FITC trace for the quantification of acetylated α-tubulin, where NPC1 patient cells were found to have significantly increased levels of acetylation as compared to controls. *p<0.05; student t-test

Additionally, the current EMA-approved treatment miglustat and the SERCA antagonist curcumin reduced levels of α-tubulin acetylation in the NCP1 patient fibroblasts (**Figure 2.11**).

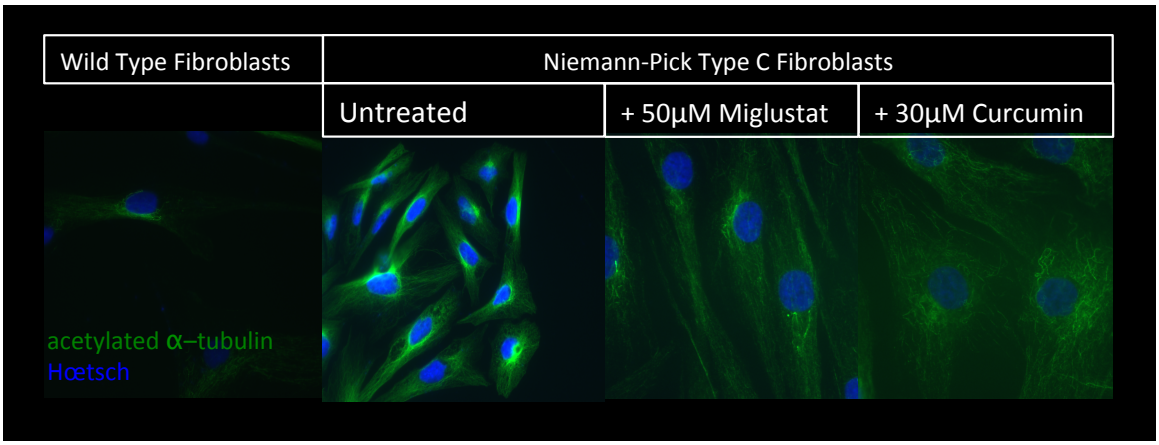

Figure 2.11. *Acetylated α-tubulin in control and NPC1$^{-/-}$ patient fibroblasts following different treatments. A)* NPC1 patient fibroblasts stained for acetylated α-tubulin have increased levels as compared to control cells and treatment with miglustat (50μM, 72hrs) and curcumin (30μM, 24hrs) reduced the intensity of staining in the patient cells.

The major regulators of acetylation of α–tubulin at the lysine-40 residue is the histone deacetylase 6 (HDAC6) and sirtuin 2 (SIRT2), and knockout of either leads to tubulin hyperacetylation, similar to what we observed in the NPC1 patient cells (135) (**Figure 2.12**).

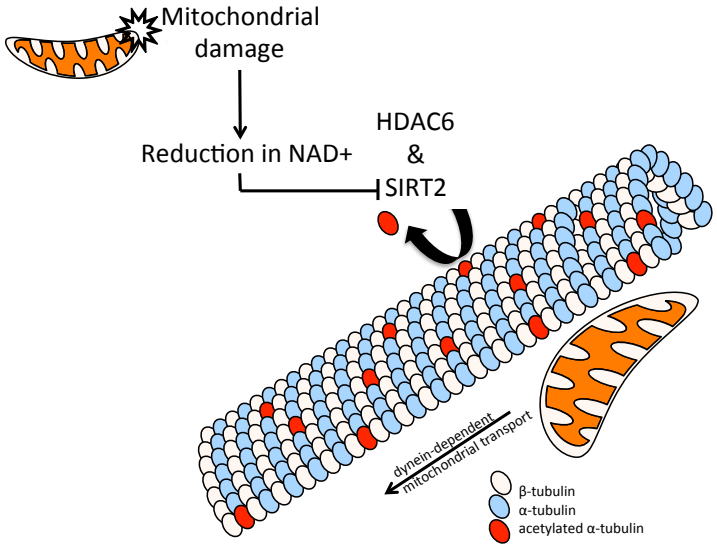

Figure 2.12. The major regulators of acetylation of α –tubulin at the lysine-40 residue is HDAC6 and SIRT2. SIRT2 activity is NAD+ dependent.

Using the SIRT2 inhibitor AGK2 we treated control cells for 24 and 48 hours and quantified the lysosomal volume of these cells. We hypothesized that following the hyperacetylation of these cells we would observe downstream lysosomal dysfunction as a result of a more static microtubule network. After 24hrs of treatment we observed a significant increase in lysosomal volume in the 10μM AGK2 treated cells (**Figure 2.13A**; p=0.0004), and no difference in the 0.1μM or 1μM treatment groups (control vs control + 0.1μM AGK2 p=0.1076; control vs control + 1μM AGK2 p=0.6040). This increase was no longer evident at 48hrs (**Figure 2.13C**; control vs control + 0.1μM AGK2 p=0.7883; control vs control + 1μM AGK2 p=0.9853; control vs control + 10μM AGK2 p=0.1118).

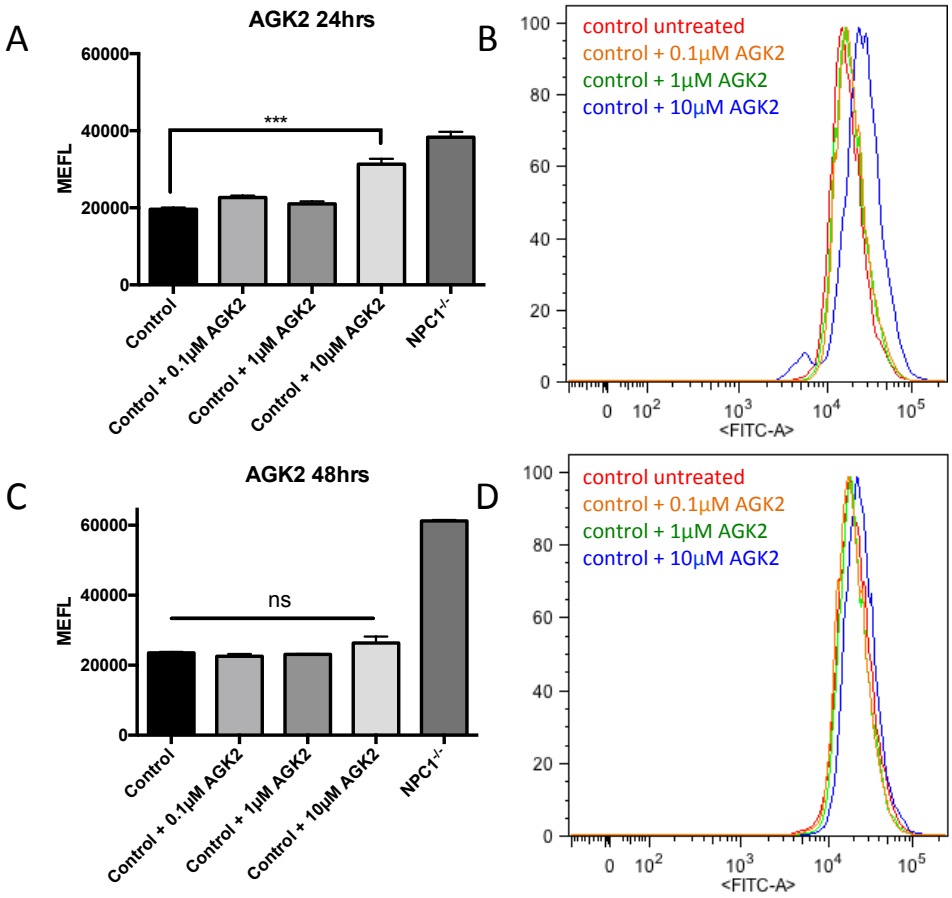

Figure 2.13. *Relative lysosomal volume quantified using LysoTracker staining.* ***A)*** After 24hrs of AGK2 treatment we see a significant increase in relative lysosomal volume in the 10μM AGK2 control cells. **B)** Representative LysoTracker FITC trace after 24hr AGK2 treatment. **C)** After 48hrs of AGK2 treatment no significant differences were observed between the treatment groups. **D)** Representative LysoTracker FITC trace after 48hr AGK2 treatment. ****p*<0.001, two-way ANOVA.

We quantified the extent of acetylation at 24hrs and saw no significant increase in the 10μM AGK2 treatment group despite seeing lysosomal volume changes at this time point (**Figure 2.14;** p=0.9965). We hypothesize that the levels of acetylation will change before seeing lysosomal volume changes, and that we may have missed the time point (~12-16hrs) where an increase of acetylation would have been most likely observed.

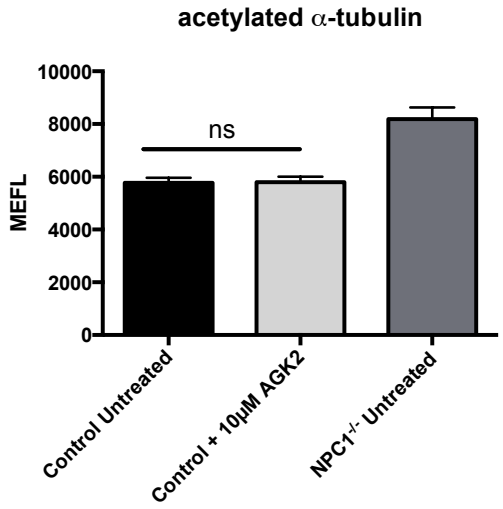

Figure 2.14. *Acetylated α-tubulin in NPC1$^{-/-}$ patient fibroblasts and controls treated with 10μM AGK2 for 24hours.* Using FACs the level of α-tubulin acetylation was quantified and no significant difference was observed following 24hr treatment of the SIRT2 inhibitor, AGK2; one-way ANOVA.

As SIRT2 activity is nicotinamide adenine dinucleotide (NAD^+)-dependent (135), we hypothesized that treating NPC1 patient fibroblasts with NAD could enhance SIRT2 deacetylase activity and rescue some of the NPC pathologies. Following exogenous addition of NAD, acetylated α–tubulin levels in the NPC patient cells were no longer

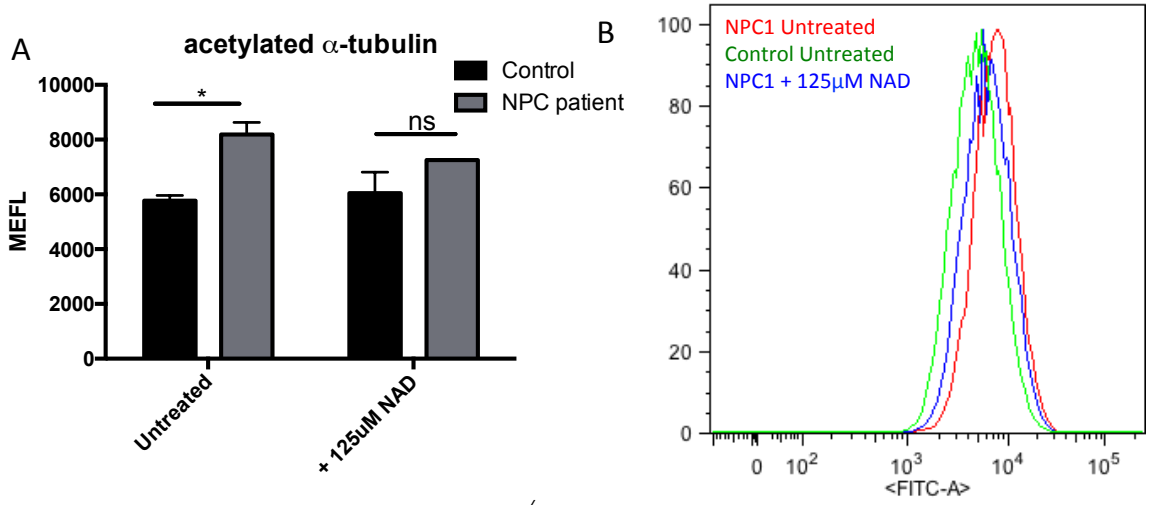

Figure 2.15. *Acetylated α-tubulin in NPC1$^{-/-}$ patient fibroblasts and controls treated with 125μM NAD for 24hours.* **A)** Using FACs the level of α-tubulin acetylation was quantified and after treatment there was no significant difference between the control and the NAD-treated NPC1 patient fibroblasts. **B)** Representative acetylated α-tubulin FITC trace following 24hrs 125μM NAD treatment. *p<0.05; one-way ANOVA.

significantly different from the healthy control cells (**Figure 2.15**; Control + 125μM NAD vs NPC1$^{-/-}$ + 125μM NAD p= 0.1090).

However, when we examined the relative lysosomal volume following NAD addition we observed no reduction after 24hrs (**Figure 2.16**; NPC1$^{-/-}$ vs NPC1$^{-/-}$ + 75μM NAD p=0.0849; NPC1$^{-/-}$ vs NPC1$^{-/-}$ + 125μM NAD p=0.1162; NPC1$^{-/-}$ vs NPC1$^{-/-}$ + 250μM NAD p=0.6465), and a non-significant trend towards reduced lysosomal volume after 48hrs (NPC1$^{-/-}$ vs NPC1$^{-/-}$ + 75μM NAD p=0.2082; NPC1$^{-/-}$ vs NPC1$^{-/-}$ + 125μM NAD p=0.0931; NPC1$^{-/-}$ vs NPC1$^{-/-}$ + 205μM NAD p=0.9824).

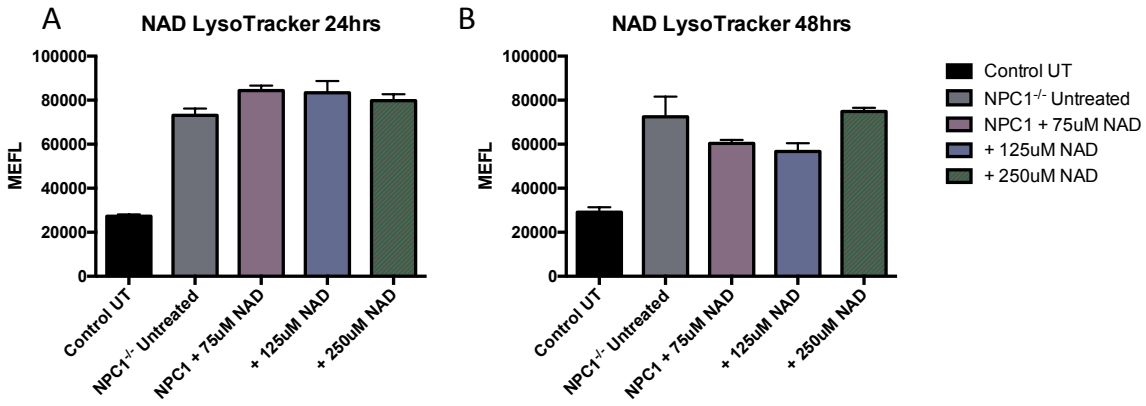

Figure 2.16. *Relative lysosomal volume quantified using LysoTracker staining.* **A)** After 24hrs of NAD treatment we see no significant changes in relative lysosomal volume in any of the NAD treated NPC1 cells. **B)** After 48hrs of NAD treatment we still see no significant changes in relative lysosomal volume in any of the NAD treated NPC1 cells, however there is a trend towards reduced levels; one-way ANOVA

As the effects of modulating α–tubulin acetylation did not immediately affect the lysosomes, we were interested in determining where α–tubulin hyperacetylation fits into the pathogenic cascade following NPC1 inactivation. We treated control fibroblasts with 2μM sphingosine for 30mins, 2hrs, 8hrs, and 24hrs and stained for acetylated α–tubulin. We observed an increase in staining 24hrs after sphingosine addition in the control fibroblasts (**Figure 2.17**).

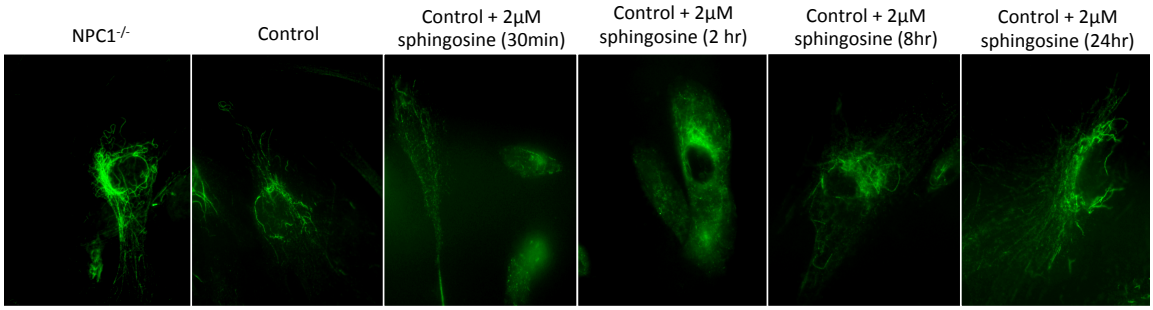

Figure 2.17. *Control fibroblasts were treated with 2μM sphingosine and stained for acetylated α-tubulin.* Time points include 30min, 2hrs, 8hrs, and 24hrs. These time points correspond to the kinetics previously determined of the NPC1 pathogenic cascade, where 30min was when calcium defect was observed, 2hrs sphingolipid trafficking defect could be observed, and by 8hrs cholesterol, sphinogmyelin and GSLs were being stored in the lysosome when NPC1 was pharmacologically inactivated (13, 14).

2.3.3 Phosphoproteomic Analysis of the *Npc1* Mouse Cerebellum

In a parallel study, protein and phosphorylation site changes were quantified in the cerebellum of *Npc1*$^{-/-}$, *Npc1*$^{+/-}$, and *Npc1*$^{+/+}$ pre-symptomatic 5 week old mice. The samples were processed as indicated (**Figure 2.18**), and each group contained 5 biological replicates that were used for both proteome and phosphoproteomic quantification.

Previously two independent proteomic screens have been performed on the *Npc1*$^{-/-}$ brain – one which focused primarily on lysosomal proteins (136) and another that took a more broader view of protein expression levels (107). Our study is unique in that we additionally examine the protein expression levels in the *Npc1* heterozygous mouse, and also changes of phosphorylation levels of the proteins that do not have altered expression levels.

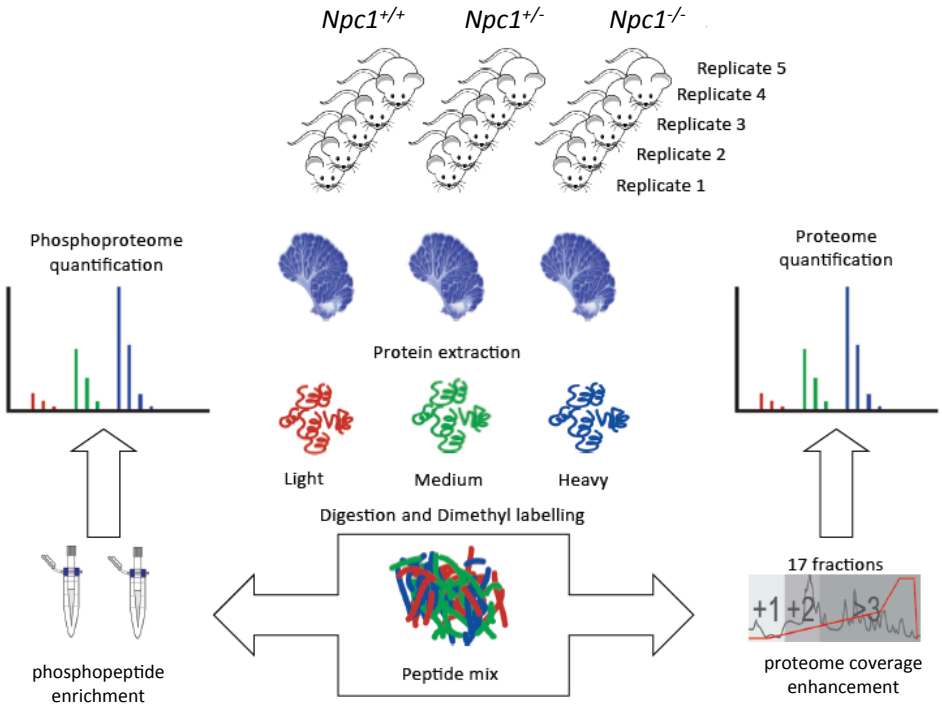

Figure 2.18. *Phosphoproteomics workflow.* Cerebellum from *w*ild type (*Npc1*$^{+/+}$), heterozygous (*Npc1*$^{+/-}$) and homozygous (*Npc1*$^{-/-}$) mice were digested labeled with light, intermediate and heavy reagents and mixed in a 1:1:1 ratio. Peptides to be used for proteome quantificatin underwent strong cation exchange to enhance proteome coverage, and peptides for phosphoproteomic quantification underwent phosphopeptide enrichment. All the (phospho)peptide mixtures were analyzed via ultra-high-performance LC-MS/MS. After protein and phosphopeptide quantitation, the data were subjected to statistical analysis. Performed by Nicolas Lebesgue, modified from Lebesgue 2016 (11).

We found protein expression changes to be most apparent in the *Npc1*$^{-/-}$ group, and the *Npc1*$^{+/-}$ and *Npc1*$^{+/+}$ mice to have similar expression profiles. In accordance with

previous findings, a large proportion (20%) of proteins found to have altered expression levels were lysosomal proteins (indicated in blue; **Appendix Table 3**)(136). Using GOrilla functional analysis, there was also an enrichment of proteins in the myelin sheath (indicated in red) (137). In addition, there was an enrichment of proteins belonging to the mTOR nutrient-sensing pathway (indicated in green). The proteins that had altered expression levels in the *Npc1*$^{-/-}$ mice were largely unaffected in the *Npc1*$^{+/-}$ mice.

However, when we examined the phosphoproteomic data we observed significant alterations to both the *Npc1*$^{-/-}$ and the *Npc1*$^{+/-}$ protein phosphorylation sites (**Appendix Table 4**). *Npc1*$^{+/-}$ mice do not exhibit overt symptoms, and still, even at 5 weeks of age before the *Npc1*$^{-/-}$ mice are symptomatic, we detected changes in the phosphoproteome in both sets of mice as compared to the healthy *Npc1*$^{+/+}$ controls. Approximately 61% of the 70 phosphosites deregulated in the *Npc1*$^{+/-}$ mouse were also deregulated in the *Npc1*$^{-/-}$ mouse, suggesting these pathways could point towards risk markers for neurodegeneration that may occur in an aged *Npc1*$^{+/-}$ mouse.

Some trends in the phosphoproteomic data included deregulation of sites implemented in cytoskeletal transport (Nefm, Nefh, Kcl2, Map1a, Fam21; indicated in blue), calcium transporters (Atp2b1, Atp2b2; indicated in red), transport proteins (Arrb1, Canxx, Cacna1a, Ap3b1, Fam21; indicated in green), and cell cycle regulation proteins (Bclaf1, Thrap3; indicated in orange). Additionally, kinases (CamKIIb-

pT287, Prkcδβα-pT514, Hsp90ab1-pS255) were also found to deregulated (**Figure 2.19**)

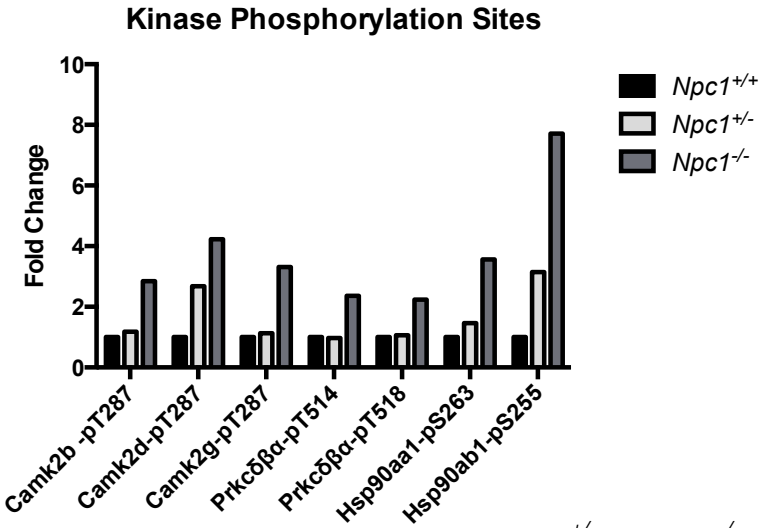

Figure 2.19. *Kinase phosphorylation site profiling in the $Npc1^{+/-}$ and $Npc1^{-/-}$ mice as compared to $Npc1^{+/+}$ site regulation.* Upregulation of Camk2d-pT287, and Hsp90ab1-pS255 was observed in both the $Npc1^{-/-}$ and $Npc1^{+/-}$ mice, although to a lesser extent in the heterozygous mutants.

2.3.4 Identification of Novel Therapeutic Targets

We focused on the modulation of the deregulated phosphorylation sites of the kinases identified in the phosphoproteomic screen as targets for NPC disease as phosphorylation of kinases has been associated with other neurodegenerative diseases (109, 138). We examined the effects of inhibiting Ca^{2+}/calmodulin-dependent protein kinase II (CaMkII), PKCδβα, and heat shock protein 90 (HSP90) signalling cascades in NPC1 patient fibroblasts. As a therapeutic readout, we visualized free cholesterol using filipin staining. We observed significant reduction in filipin staining following KN-62 CaMkII inhibition, K252b PKCδβα inhibition, and

17-DMAG [17-Dimethylaminoethylamino-17-demethoxygeldanamycin] HSP90 inhibitor treatments ($NPC1^{-/-}$ vs $NPC1^{-/-}$ + 30 μM KN-62 $p<0.0001$; $NPC1^{-/-}$ vs $NPC1^{-/-}$ + 50nM K252b $p=0.007$; $NPC1^{-/-}$ vs $NPC1^{-/-}$ + 100nM 17-DMAG $p<0.0001$; **Figure 2.20**). As this proved to be effective at reducing filipin staining, further analysis of which targets and drugs would be clinically relevant is important for understanding how to best target kinase phosphorylation signally cascades.

Figure 2.20. [Page 71] *Modulating kinase activity in NPC1 patient fibroblasts reduce filipin staining although not to the extent observe in control cells.* Using the CAMKII inhibitor KN-62 we significantly reduced filipin staining in the NPC1 patient cells in the high dose treatment, however the CAMKII inhibitor KN-93 did not have an effect to the same extent. Using PKCδβα inhibitors K252b and Sotrastaurin we significantly reduced filipin staining with the high dose K252b treatment, however so no effect with Sotrastaurin treatment. Similarly using the HSP90 inhibitors 17-DMAG and Geldanamycin we only saw a significant reduction in the low dose 17-DMAG treatments. ****p*<0.001, *****p*<0.0001; one-way ANOVA

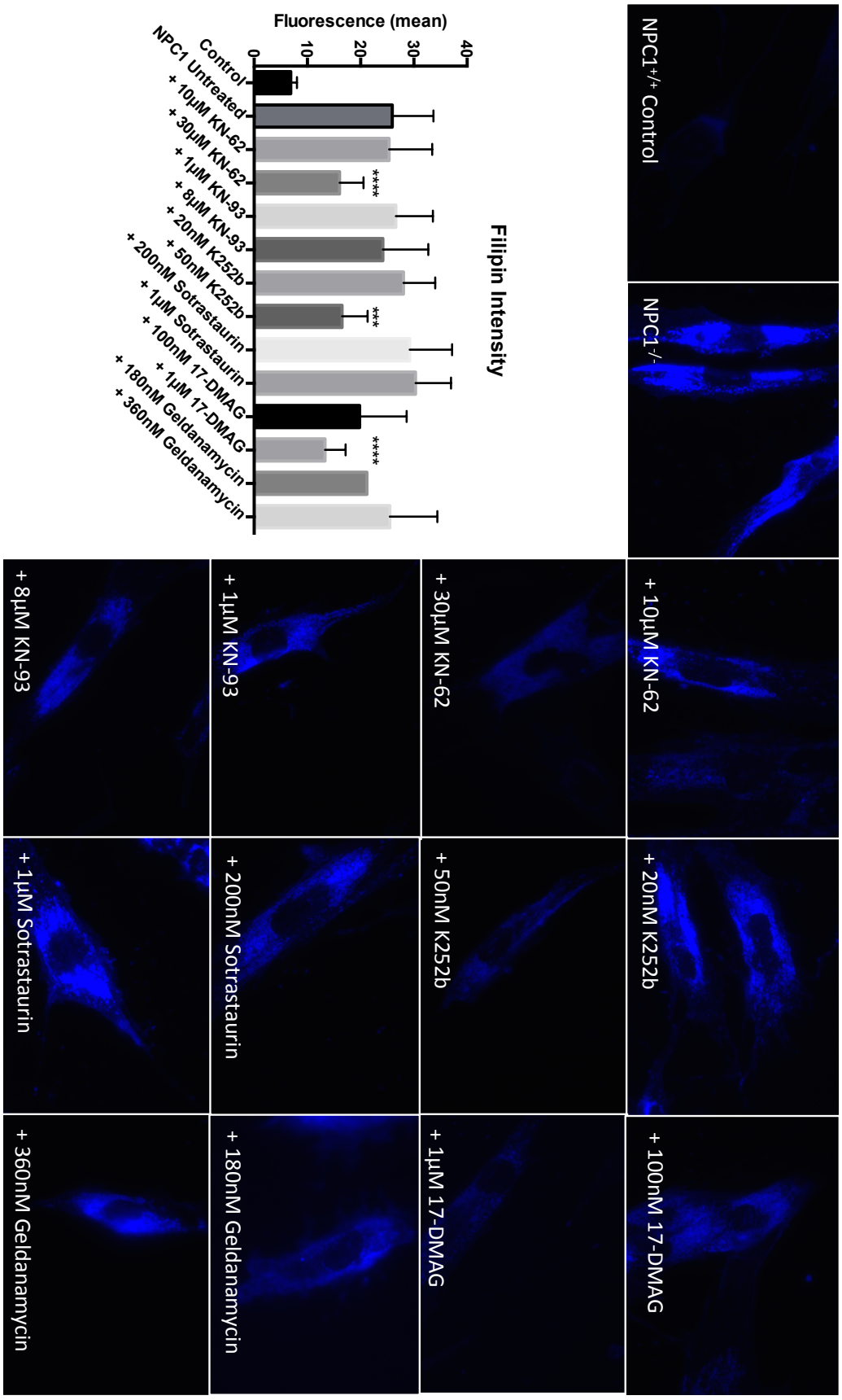
NPC1+/+ Control
NPC1-/-
Filipin Intensity
Fluorescence (mean)
0
10
20
30
40
Control
NPC1 Untreated
+ 10μM KN-62
+ 30μM KN-62
+ 1μM KN-93
+ 8μM KN-93
+ 20nM K252b
+ 50nM K252b
+ 200nM Sotrastaurin
+ 1μM Sotrastaurin
+ 100nM 17-DMAG
+ 1μM 17-DMAG
+ 180nM Geldanamycin
+ 360nM Geldanamycin
****
***
****
CAMK II inhibitor [Representative Images]
PKC δβα Inhibitor [Representative Images]
HSP90 inhibitor [Representative Images]
+ 10μM KN-62
+ 20nM K252b
+ 100nM 17-DMAG
+ 30μM KN-62
+ 50nM K252b
+ 1μM 17-DMAG
+ 1μM KN-93
+ 200nM Sotrastaurin
+ 180nM Geldanamycin
+ 8μM KN-93
+ 1μM Sotrastaurin
+ 360nM Geldanamycin

2.4 Discussion

Taken together, the yeast and mammalian screens performed offer a unique perspective on the underlying dysfunction and identify potential new therapeutic targets for NPC.

The genes and proteins implicated from the yeast screen can be can be organized into seven main categories. Several have been well defined as characteristics of NPC (points 1-3), while others are more novel (points 5-7).

1. Calcium Regulation
2. Metal Ion Regulation
3. Trafficking Defects
4. Interactions with ABC transporters
5. Mitochondrial Dysfunction
6. Actin/Cytoskeletal
7. Nutrient Sensing (mTorc1)

With regards to the pathogenic cascade following NPC1 inactivation, we propose cytoskeletal defects to be downstream to sphingosine storage (**Figure 2.21**). Cytoskeletal defects may either be contributing to, or are exacerbated by, the mitochondrial dysfunction, however, we have not identified which is the initial player in the case of NPC.

Interestingly, modulation of α-tubulin acetylation through inhibiting the deacetylase protein SIRT2 did lead to increase in relative lysosomal volume after 24hrs, yet was not sustained at 48hrs (**Figure 2.13**). As α-tubulin is regulated by both the deacetylases SIRT2 and HDAC6, we hypothesize that by 48hrs we are observing compensation by HDAC6 following the inhibition of SIRT2. In a previous study, it was found that in 2 of the 3 NPC patient fibroblasts examined there was an upregulation of HDAC6 expression and that HDAC inhibitor treatment could reduce expression back to control levels (106). This upregulation of HDAC6 may be compensating for an increase in acetylation observed in NPC and inhibiting levels could actually contribute to some aspects of pathology.

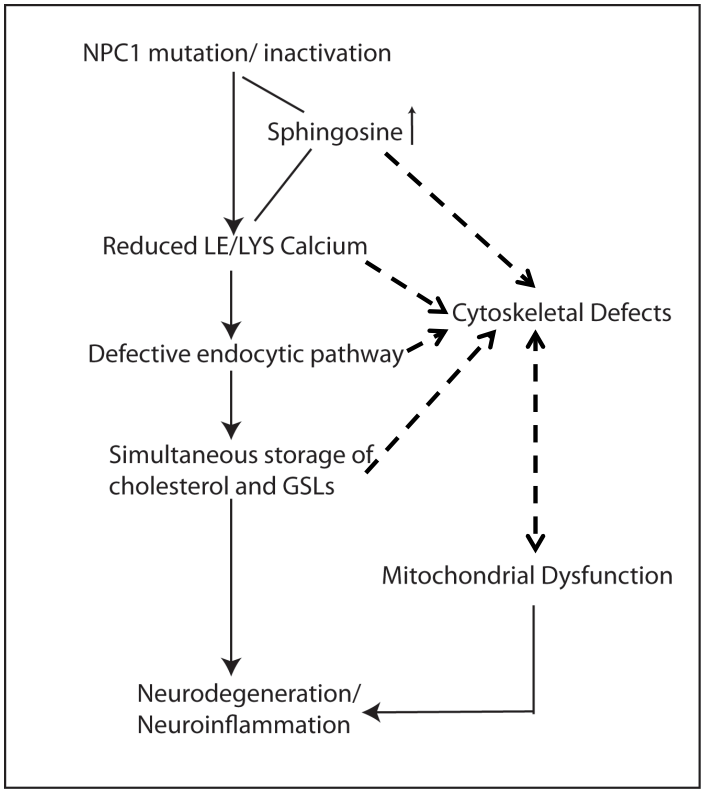

Figure 2.21. Hypothetical pathogenic cascade following NPC1 inactivation including cytoskeletal and mitochondrial defects. Modified from Lloyd-Evans and Platt, 2010 (2).

This is particularly interesting with regards to the drug vorinostat, an HDAC inhibitor that is currently in clinical trials for the treatment of NPC (**Introduction 1.2.7.2.3**). Vorinostat does not, however, have an inhibitory effects on SIRT2 so would not effect the deacetylase activity of this protein, although would reduce

HDAC6 expression (139). The relationship between microtubule acetylation and organelle (mitochondrial and lysosomal) dysfunction needs further examination to best determine how to intervene therapeutically as it is likely that HDAC inhibitors could potentially also aggravate this cellular disease phenotype in the long term.

The yeast findings were validated as they were also observed in the *Npc1* mouse cerebellum proteomic and phosphoproteomic screen. In both the proteomics and phosphoproteomic screen an enrichment of proteins involved in Ca^{2+} regulation, protein trafficking, and associated with mitochondria, the cytoskeleton and mTOR nutrient sensing complex were observed. These findings are particularly exciting as mitochondrial, cytoskeleton, and nutrient sensing proteins have been less well characterized in NPC.

Additionally, the phosphoproteomic screen identified proteins that did not have changes in their protein expression levels, but did have changes to their phosphorylation status (**Appendix Table 4**). The proteins with altered phosphorylation sites are interesting as there was a high overlap between the changes in the *Npc1*$^{-/-}$ and *Npc1*$^{+/-}$ mice suggesting that phosphorylation changes could be early indicators of the pathogenic process, especially as many of these proteins found are involved in cytoskeleton and Ca^{2+} transporters, cell cycle regulation or are kinases. With the exception of kinases, proteins involved in the cytoskeleton, Ca^{2+} and cell cycle were identified in both the yeast and proteomics

screen, suggesting that even in the heterozygous *Npc1*$^{+/-}$ mutant mice we can identify potential underlying cellular dysfunction.

These early changes to the phosphorylation sites can be used to identify novel therapeutic targets, as they are present before we observe proteomic changes. Targeting the kinases, particularly CaMkII, PKC, and HSP90 proved to have some therapeutic efficacy (**Figure 2.20**). However, drugs that targeted the same kinase did not all have similar levels of efficacy in reducing filipin staining. This may due to both the selectivity of the targets of each inhibitor – KN-93 is a also selective inhibitor of Fyn, Haspin, Hck, Lck, MLCK, Tec and TrkA in addition to CAMKII (140), as well as the drugs half-life or bioavailability, which may be why we observed differential effects with drugs with the same target. Despite the variation in staining there were significant reductions in filipin staining in the high dose KN-62, K252b, and 17-DMAG treatment groups. Targeting kinases may serve as acute modulating drugs as changes were observed after 2-12 hours treatment in the patient fibroblasts and sporadic treatment rather than maintaining steady state levels may be an option with these therapies. This could also reduce any toxicity or adverse side effects that may arise with a chronic treatment.

In summary:

- In yeast we implicated Ca^{2+}, copper and iron regulation, trafficking defects, the involvement of ABC transporters, mitochondrial and cytoskeletal defects, and the nutrient sensing complex in NPC cellular pathogenesis
- We validated mitochondrial and microtubule defects in NPC1 patient fibroblasts
- Modulation of α–tubulin acetylation may prove to have therapeutic potential
- Phosphoproteomic screening identified altered phosphorylation status of proteins in both the *Npc1*$^{-/-}$ and *Npc1*$^{+/-}$ mouse suggesting these may play a role in disease progression
- Modulation of kinases and their signalling pathways may have therapeutic potential

Chapter 3: Mechanistic Convergence of NPC and Tangier disease

3 Mechanistic Convergence of NPC and Tangier disease

3.1 Introduction

The ATP-binding cassette (ABC) transporter family of proteins are membrane bound proteins involved in the transport of molecules across cell surfaces and organelle membranes (141). Structurally ABC transporters have a nucleotide binding domain, trans-membrane domains containing hydrophobic helices, and together these domains bind and hydrolyze ATP and move substrates across membranes (141). In humans, the 49 ABC family members of proteins can be divided into 7 subfamilies [A-G], which are ordered based on evolutionary divergence (141).

The ABCA family comprises 12 genes, many which are involved in lipid trafficking, and includes *ABCA1*, the gene which when mutated causes Tangier disease (142). ABCA1 regulates cellular cholesterol and phospholipid homeostasis by effluxing lipids across the plasma membrane to extracellular receptors (143). In particular, ABCA1 transfers cholesterol to apolipoproteins, specifically apolipoprotein A-I (apoA-1), to form HDL particles, which carry these lipids through the bloodstream to the liver where they can be redistributed throughout the body or converted into bile acids for removal or reabsorption (**Figure 3.1)**(144).

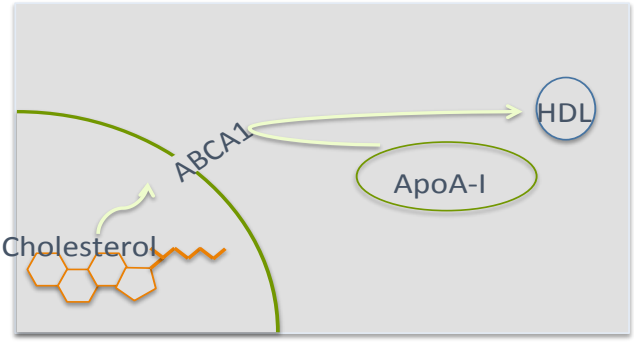

Figure 3.1. ABCA1 transports cholesterol and phospholipids out of the cell to apoA-1 to form HDL.

Mutations in ABCA1 result in the ultra-rare Tangier disease (also known as familial alpha-lipoprotein deficiency), with only about 100 cases having been described worldwide. This disease was first described in 1961 by Dr Fedrickson when he examined two siblings from Tangier Island, Virginia, USA (145). Tangier disease typically manifests itself as enlarged, orange-coloured tonsils in children, yet in adults, symptoms do not include the characteristically orange tonsils but instead severe peripheral neuropathy (142, 145). While generally exhibiting no overt symptoms, Tangier disease patients have decreased levels of HDL and cholesterol, mild hypertriglyceridemia of the blood, and a higher rate of premature coronary artery disease development (142, 146). However, due to the small number of

patients described to date the full spectrum of clinical manifestations in this disease remains incompletely defined, especially as there is considerable variation amongst paediatric and adult patients.

As mentioned in **Introduction 1.2.5.1**, a recent clinical case report has suggested that there may be a convergent mechanistic link between cellular pathogenesis in NPC and Tangier disease. An adult female patient (age 64) presenting with thrombocytopenia, splenomegaly, and neurological symptoms (neuropathy, dysphagia and ataxia) was misdiagnosed with NPC and put on the current European Union–approved treatment for NPC, miglustat (147). After four months of treatment, the patient's neurological and dermatological symptoms improved (147). The patient subsequently underwent molecular testing, no mutations in either *NPC1* or *NPC2* were found, and was correctly diagnosed with Tangier disease (147).

We are interested in determining if the proposed convergence between the NPC cellular pathway and ABCA1 reflects both proteins being involved in some aspects of cellular cholesterol homeostasis, or if there is another stronger mechanistic connection underlying the Tangier disease patient's positive response to miglustat. Here we investigated whether a mutation in ABCA1, which has previously been shown to be down regulated in NPC, could converge with the NPC cellular pathway (148). If this were the case, we would predict that all the cellular hallmarks of NPC would be present in Tangier disease patient cells, including the acidic store Ca^{2+} defect, endocytic mistrafficking of sphingolipids, and the accumulation of lysosomal

sphingosine, cholesterol and GSLs; in addition to the primary Tangier disease defect in ABCA1.

The specific aims presented in this chapter are therefor to:

- Characterize Tangier disease patient's cellular and their biochemical phenotypes and identify shared traits with Niemann-Pick disease type C cells
- Evaluate to what extent miglustat, or other substrate reduction therapies (SRT), may function as an effective treatment for Tangier disease

3.2 Materials and Methods

3.2.1 Cells

We obtained human ABCA1-mutant fibroblasts from the University Hospital-Udine and Addenbrooke's Hospital, Cambridge. The Tangier patient fibroblast line 'MF' has a mutation c.4464-486_4698+382 Del (Ex32-Ex34Del), line 'FL' has a mutation c4367delT resulting in a truncated protein, line 'T15/0067 BREAM' has a mutation c.4550_4551 del Exon 32, and line 'T16/0005 BREAM' also had mutation c.4550_4551 del Exon 32. Patient T15/0067 BREAM and T16/0005 BREAM are siblings. The fibroblasts were maintained in DMEM with 10%FCS, 1% penicillin/streptomycin and 1% $_{L}$-glutamine. All cells were cultured at 37°C with 5% CO_2. Cell treatment with miglustat (*N*B-DNJ) and the galactose analogue lucerastat (*N*B-DGJ) were used at a concentrations of 15μM and 50μM for 72 hours.

3.2.2 Microscopy

3.2.2.1 LysoTracker Staining

Control, NPC and Tangier patient cells were incubated with 200nM LysoTracker in complete DMEM media for 10mins. Cells were then immediately imaged on a Zeiss Axiovert fluorescent microscope.

3.2.2.2 BODIPY-Lactosylceramide and Cholera Toxin Subunit B Transport

BODIPY-lactosylceramide (BODIPY-LacCer, Molecular Probes) transport was determined as previously described (149) with minor modifications. BODIPY-LacCer was used at a concentration of 5μM with an initial incubation for 30 minutes at 20°C followed by a 2 hour chase at 37°C and washed 3x medium containing 10% FCS and 1% BSA. Cholera Toxin subunit B (CTxB, binds GM1 ganglioside) transport was performed as previously described (150) with minor modifications. Cells were incubated with 1μg/mL CtxB for 30min at RT, washed, and incubated for 90min with fresh media, 1% BSA at 37°C. After incubation cells were washed 3x fresh media, fixed with 4% paraformaldehyde and visualized.

3.2.2.3 Filipin Staining

Free cellular cholesterol was visualized with Filipin complex from *Streptomyces filipinensis* (Sigma) as previously described (149). Briefly, cells fixed with 4% paraformaldehyde were washed 3xPBS and incubated with 1.5mg/mL glycine for 10min to quench autofluorescence. Cells were then incubated with filipin (0.05mg/mL in PBS/10% FBS/0.2% Triton x100) for 2 hours, washed 3xPBS and visualised.

3.2.4 Quantification of LysoTracker Staining by FACS

Relative lysosomal volumes was measured from patient derived fibroblasts and performed by Ecem Kaya as detailed in section 2.2.9.2.

3.2.5 Sphingomyelin Visualization

Cells were fixed with 4% paraformaldehyde and sphingomyelin was visualized with lysenin. Cells were incubated for 8 hours in blocking buffer [1%BSA, 0.1% Saponin, PBS], and then incubated with lysenin (0.1 μg/mL) in blocking buffer solution overnight at 4°C. Cells were washed 3xPBS for 5 minutes and incubated with a lysenin antiserum primary antibody (Peptides International; 1:1000) for 1 hour in the blocking buffer. Coverslips were washed 3xPBS for 5 minutes, incubated in DyeLight Red anti-rabbit (1:500 blocking buffer) for 30 minutes in the blocking buffer, washed 3xPBS for 5 minutes and visualized on a Zeiss Axiovert fluorescent microscope.

3.2.6 Glycosphingolipid Analysis

GSLs were extracted from cell homogenates (1mg protein, BCA protein assay) in 4 parts volume chloroform/methanol (C:M) (1:2 v/v) overnight at 4°C. The mixture was centrifuged (1500*g*/10min) and 2 parts chloroform and 2 parts PBS were added to the supernatant and centrifuged (1500*g*/10min). The lower phase was

dried under N_2, resuspended in 50uL C:M 1:3 and recombined with the upper phase. GSLs were recovered using C_{18} Isolute columns (100mg, Biotage) pre-equilibrated with 4x1mL MeOH and 2x1mL H_2O. Following the addition of the sample, columns were washed 3x1mL H_2O and eluted with1mL C:M 98:2, 2x1mL C:M 1:3, 1mL MeOH. Column elutant was dried under N_2, re-suspended in 100uL C:M 2:1, dried under N_2 and resuspended in ceramide glycanase (CGase) buffer (50mM sodium acetate pH 5.5, 1mg/mL sodium taurodeoxycholate). CGase (50mU, Orphazyme, APS) was added, and samples incubated at 37°C overnight. Released oligosaccharides were anthranilic acid (2-AA) labelled and purified by mixing with 3mL MeCN:H_2O 97:3 and added to Discovery DPA-6S columns (SUPELCO) pre-equilibrated with 1mL MeCN, 2x1mL H_2O, and 2x1mL MeCN. Columns were washed with 2x1mL MeCN:H_2O 95:5, and eluted in 0.6mL H_2O. Samples were loaded 60:140 H_2O:MeCN (v/v) for normal phase high-performance liquid chromatography (HPLC). Solvent A was MeCN, solvent B was mQ H_2O, and solvent C was 100mM NH_4OH (pH 3.85) in mQ H_2O. Separation was carried out at 30°C using Waters Alliance 2695 separation module, excitation 360, emission 425 using Waters 2475 Fluorescence detector.

3.2.7 Sphingosine Analysis by HPLC

Sphingoid bases were extracted from homogenized cells (10mg w/w) in 100uL H_2O and spiked with an internal standard [C20, 3uL 0.1mM]. To the homogenate, 500µL C:M 1:2 was added and sonicated for 10min, RT. To the samples 500uL 1N NaCl, 500µL chloroform, and 100uL 3M NaOH were added and incubated for 15min, RT

and vortexed every 5 minutes. Samples were then centrifuged (13000*g*/10min) and the lower phase purified on SPE NH2 columns [Biotage] pre-equilibriated with 2x1mL chloroform and eluted with 3x300µL acetone. The column elutant was then dried down under N_2, and resuspended in 50µL pre-warmed HPLC grade EtOH. Sphingoid bases were labelled with 50µL OPA labelling solution (o-Phtalaldyhyde dissolved in 20x EtOH, 1x 2-mercaptoethanol and diluted in 2000x 3% Boric acid pH 10.5) and incubated at 20°C for 20min, vortexing at 10min intervals. Samples were buffered in 100µL MeOH:5mM Tris pH7 9:1, centrifuged (5000*g*/2min), and the supernatant was loaded for normal phase HPLC. Solvent A was MeOH, solvent B was H_2O, solvent C was MeCN, and solvent D was MeCN:H_2O 1:4. Separation was carried out using Hitachi L-2485 FL Detector , excitation 340, and emission 455.

3.2.8 Sphingosine Visualization

Cells were seeded onto 11mm coverslips placed in wells of a 24-well plate and labeled with 4µM TFS in imaging buffer for 5 min. Cells were washed, overlaid with 1mL imaging buffer and UV-irradiated on ice for 2.5min at wavelength > 400nm. After this uncaging step, cells were put back to 37 °C for the duration of the chase (10min - 1hr) and further irradiated for 2.5min at wavelengths of > 345nm. Cells were immediately fixed with MeOH -20°C, 20 min. Lipids that were not crosslinked were washed away with 3x 1mL of $CHCl_3$/MeOH/AcOH 10:55:0.75 (v/v) at RT. Cells were the incubated with 50µl of click mixture (1mM ascorbic acid, 100µM TBTA, 1mM $CuSO_4$ and 2µM Alexa 488 azide in PBS) for 1hr, RT in the dark. Cells were then

washed with PBS and incubated with 50µl of primary antibody (rabbit α-LAMP1, Cell Signaling, 1:100 in PBS supplemented with 4 % BSA and 0.02 % Triton) overnight at 4°C. Coverslips were again washed in PBS and incubated with secondary antibody (α-rabbit conjugated to AlexaFluor555, Cell Signaling, 1:800) for 1hr, washed and mounted in DAPI-containing mounting medium (Vectashield, Vector Laboratories). Microscopy images were captured at room temperature using a confocal laser-scanning microscope (Zeiss LSM780) with a 63x oil objective. Settings were as follows: DAPI-channel (405nm excitation (ex), 409 - 475nm emmission (em); green channel: 488nm ex, 489 - 550nm em; red channel: 561nm ex, 569 - 655nm em). Images were further processed using Fiji software (http://fiji.sc/Fiji). Experiment performed by Doris Höglinger

3.2.9 Acidic Store Calcium Measurements

Single cell lysosomal Ca^{2+} measurements were performed as previously described (151) with minor modifications by Lianne Davis. Briefly, cells were loaded with 5µM Fura2-AM and 0.03% pluronic acid in calcium imaging buffer for 45 minutes at 20 °C followed by a 15 minutes de-esterification period, washed, and visualized on a Zeiss LSM 510 confocal microscope. Concentrations of 200µM GPN, 2µM Ionomycin, and 4mM $MnCl_2$ were used, and all agents were added in DMSO. Analysis was performed with Magipix and Magigraph software (developed and distributed by R. Jacob).

3.2.10 NPC1 and NPC2 Protein Levels

Protein levels were assessed using western blots performed by Elias Adriaenssens on 30µg of protein. NPC2 primary antibody (SantaCruz) was used at 1:200 dilution, and NPC1 primary antibody was used 1:1000 dilution.

3.2.11 siABCA1 Time Course

Control fibroblasts were transfected with siABCA1 pools (siTools) to silence ABCA1 gene expression, and results validated by Danielle te Vruchte. Reverse transfection was performed in 6-well plates and the siABCA1 pools and scramble control were diluted to both 1nM and 5nM in serum free media and added to empty wells. This was followed by addition of 5µL of Lipofectamine RNAiMax (ThermoFisher Scientific) and incubated for 20 minutes at 20°C. Cells were diluted in 2.5mL complete DMEM without antibiotics and added to each well to make a total volume of 3mL/well. Cells were the incubated for 24, 48, 72, and 96 hours before analysis. Real time polymerase chain reaction (RT-PCR) was performed by siTools. siABCA1 transfected cell pellets were then processed for cholesterol and glycosphingolipid quantification.

3.2.12 Cholesterol Measurement

Cholesterol quantification was performed by Folch extraction followed by quantification using the Amplex Red cholesterol assay kit (Molecular Probes). Briefly, samples were diluted to 0.1mL in H_2O to a final concentration of 5mg/mL and homogenized in 2mL C:M 2:1. Samples were rotated (2hrs, spiramix) at 20°C. To the sample, 0.4mL MeOH was added and centrifuged (13000g/10min) at 20°C. The supernatant was collected and 0.8mL CH_3Cl and 0.73mL H_2O were added, vortexed for 10sec and centrifuged (13000g/10min). The lower phase was washed with 3x C:M: H_2O 3:48:47, and dried under stream of N_2. Extracted cholesterol was then quantified using Amplex Red Molecular Probes kit according to the manufacturer's instructions.

3.3 Results

3.3.1 Tangier Disease Patients Share Cellular and Biochemical Phenotypes with NPC Cells

As previously described (**Introduction 1.2.4, Figure 1.4**) the pathogenic cascade following NPC1 mutation has been well characterized and we examined the cellular and biochemical phenotypes of four Tangier disease patient cell lines in comparison with these phenotypes.

The four patient-derived fibroblast lines were examined to see if the lysosomal compartment was enlarged in these cells, as is observed in NPC and has been implicated as a biomarker for lysosomal storage diseases (152). We observed an increase in relative lysosomal volume (approximately 3-fold increase; control vs Tangier patient 1 $p<0.0001$, control vs Tangier patient 2 $p<0.0001$, control vs Tangier patient 3 $p<0.0001$, control vs Tangier patient 4 $p<0.0001$) similar to that observed in NPC disease cells (approximately 5-fold increase; control vs NPC patient 1 $p<0.0001$; control vs NPC patient 2 $p<0.0001$; control vs NPC patient 3 $p<0.0001$; **Figure 3.2**).

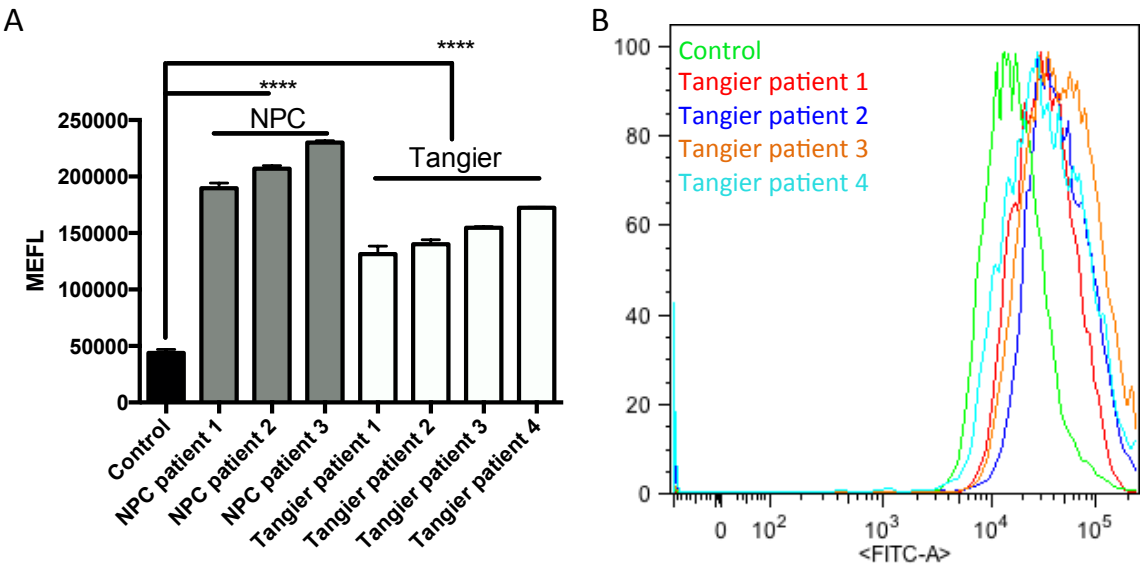

Figure 3.2. *LysoTracker (MEFL) values of patient-derived fibroblasts for NPC1 and Tangier patients and controls.* **A)** The four Tangier patients exhibited significantly elevated LysoTracker values similar to that seen in NPC disease. **B)** Representative FACs trace of the mean FITC level for the live single cells analyzed. LysoTracker mean values are standardized to molecules of equivalent of fluorescein (MEFL) using Rainbow Calibration Beads; one-way ANOVA. Performed by Ecem Kaya.

This increase in relative lysosomal volume was confirmed microscopically (**Figure 3.3A)**. We also then examined the endocytic trafficking pathway in these fibroblasts using a BODIPY-LacCer trafficking assay and observed an endocytic trafficking defect in Tangier cells similar to NPC (**Figure 3.3B**). Additionally, filipin and lysenin staining indicated both increased cholesterol (**Figure 3.3C**) and sphingomyelin (**Figure 3.3D**) accumulation in the Tangier patient fibroblasts similar to that observed in NPC.

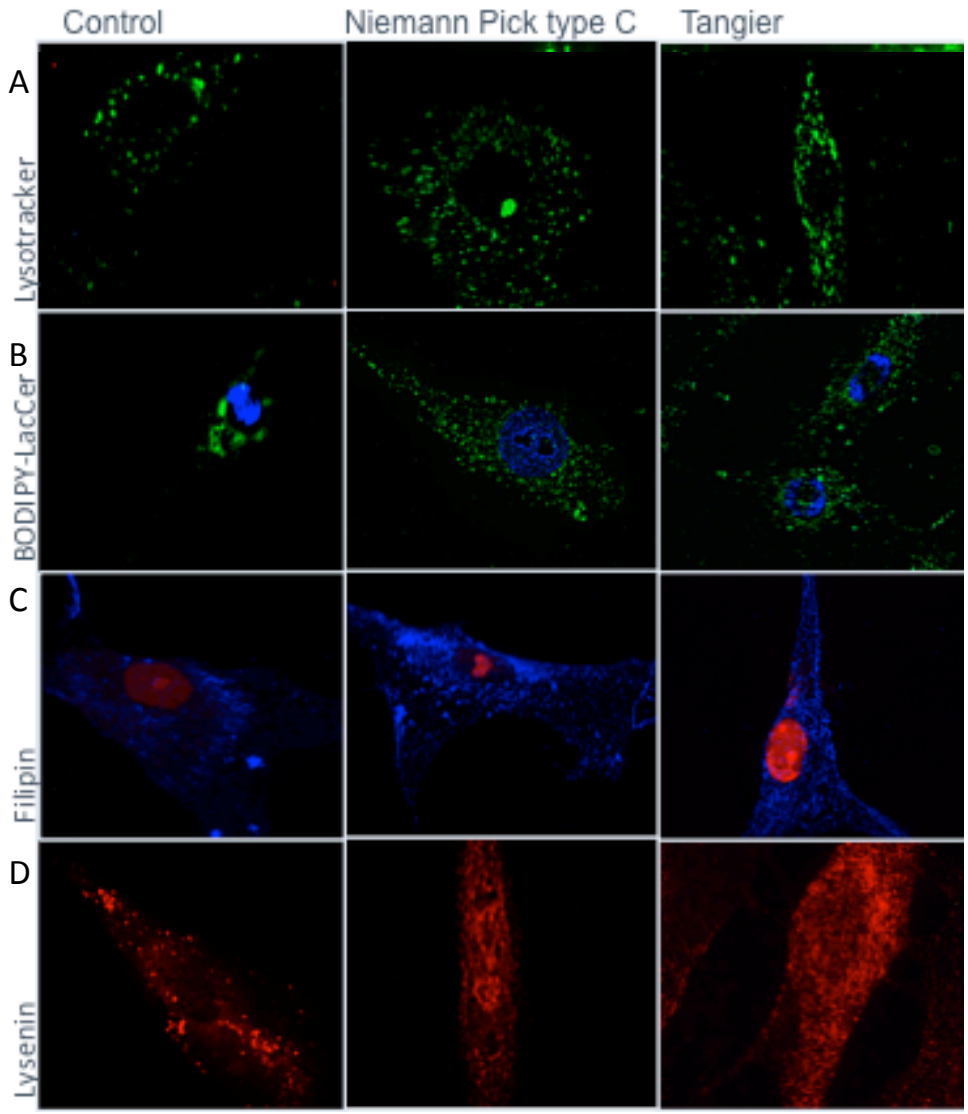

Figure 3.3. *Fluorescent imaging of control, Tangier and NPC1 patient fibroblasts*. **A)** LysoTracker was used to examine the relative acidic compartment volume. **B)** BODIPY-LacCer was used to study glycosphingolipid trafficking. **C)** Filipin was used to stain cholesterol. **D)** Lysenin was used to stain cellular sphingomyelin. Increased acidic compartment, cholesterol and sphingomyelin accumulation in Tangier disease fibroblasts were similar to levels observed in NPC1 fibroblasts. Additionally, punctate BODIPY-LacCer staining suggests glycosphingolipid mistrafficking in Tangier disease, as seen in NPC1 patient fibroblasts.

Quantification of storage material was performed, and an accumulation of GSLs, fatty acids and cholesterol in the Tangier disease patient lines was observed. Total GSLs were elevated (nearly 4-fold in Tangier and nearly 5-fold in NPC) and the

species globotriaosylceramide (Gb3), which is the most prevalent GSL species in fibroblasts, was significantly increased similar to that observed in NPC disease (**Figure 3.4;** Total GSLs: control vs Tangier patients p=0.0019, control vs NPC patients p=0.0001; Gb3: control vs Tangier patients p=0.0214, control vs NPC patients p=0.0408).

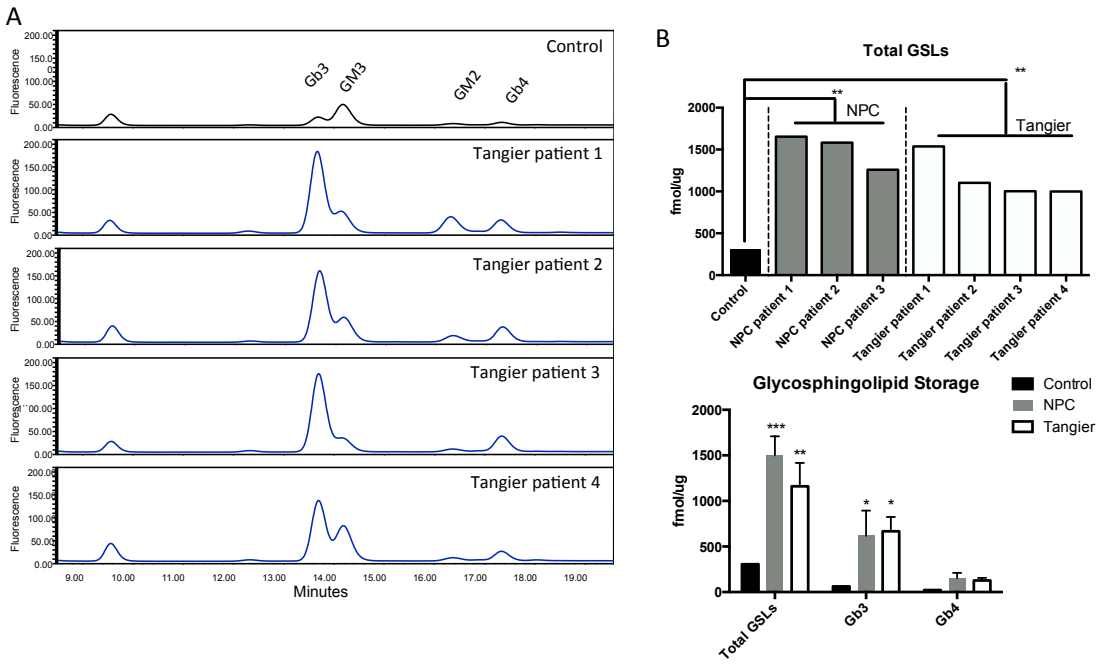

Figure 3.4. *Glycosphingolipid (GSL) levels in NPC1 and Tangier patient fibroblasts and controls*. **A)** Representative traces of control and Tangier fibroblasts. Peaks are identified by determining their glucose units using a 2-AA labeled glucose oligomer ladder standard. **B)** Total glycosphingolipids (excluding Lac-Ceramide) were measured from 0.5mg of protein isolated from NPC1, Tangier and control fibroblasts. Total GSL levels were significantly elevated in the Tangier fibroblast cell lines to a similar extent as that observed in NPC as compared to control cells. There was also significant accumulation of gb3, the most abundant GSL species in fibroblasts. *p<0.05, **p<0.01, ***p<0.001; two-way ANOVA

Similarly, a significant increase in cholesterol (over 1.5 fold change in both NPC and Tangier patients) and free fatty acids (2-3 fold increase observed in both NPC and Tangier patients) was observed in the patient cells analyzed (**Figure 3.5**; Free cholesterol: control vs Tangier patient 1 p<0.0001, control vs NPC patient 1

p<0.0001, control vs NPC patient 2 p<0.0001; Free fatty acids: control vs Tangier patient 1 p<0.0001, control vs Tangier patient 2 p<0.0001, control vs NPC patient 1 p<0.0001).

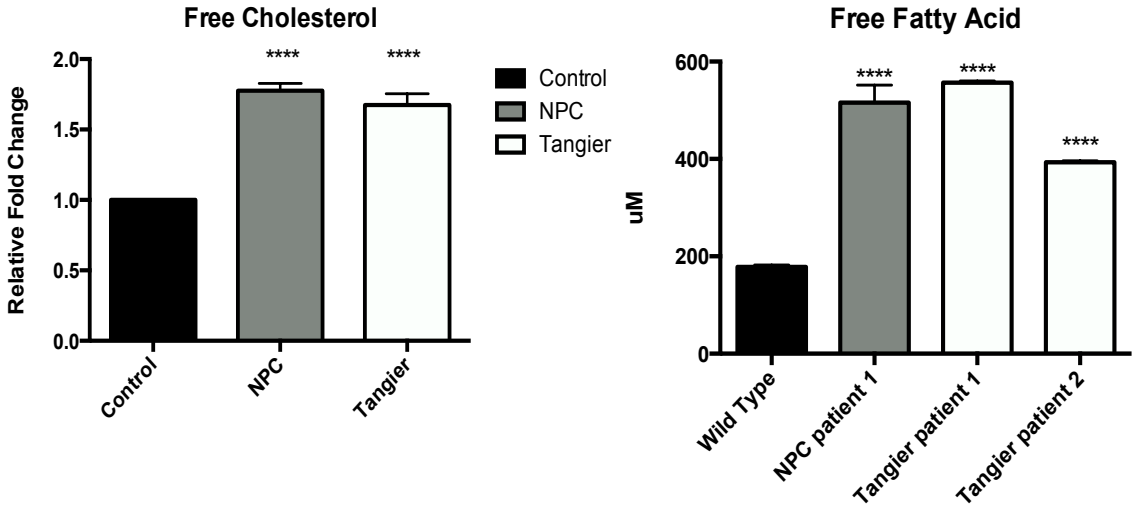

Figure 3.5. F*ree cholesterol and free fatty acid quantification in NPC1 and Tangier patient fibroblasts and controls*. **A)** Cholesterol was quantified using amplex red cholesterol kit following Folch extraction and was assayed from 0.1mg/ml of protein. **B)** Unesterified free fatty acid was quantified from 0.5mg/ml of protein and showed significant accumulation of free fatty acids in both Tangier and NPC1 patient fibroblasts as compared to controls. ****p<0.0001; one-way ANOVA

As the Tangier cell lines seemed to share many of the downstream defects and lipid storage seen in NPC, we next examined if Tangier disease also had an acidic store Ca^{2+} defect. Of the two patient cell lines examined, both patients exhibited significantly reduced acidic store Ca^{2+} release as compared to control cells (**Figure 3.6**; control vs Tangier disease patients p<0.0001, control vs NPC patients p<0.0001). The acidic store Ca^{2+} defect is a characteristic that has been attributed uniquely amongst the lysosomal storage disorders to NPC. In the case of NPC, this reduction in acidic store Ca^{2+} has been attributed to the accumulation of lysosomal sphingosine (13).

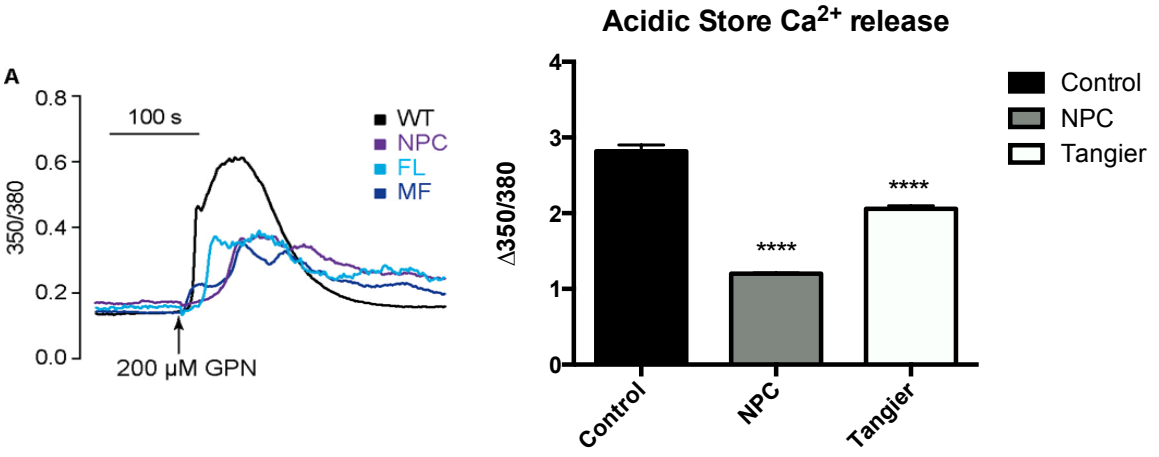

***Figure 3.6**. Defective lysosomal Ca^{2+} homeostasis in NPC1 and Tangier fibroblasts.* **A)** Representative traces showing intracellular [Ca^{2+}] changes monitored in single fura-2-loaded fibroblasts. Lysosomal Ca^{2+} content was assessed upon addition of 200µM GPN, which lyses Cathepsin-containing acidic intracellular Ca^{2+} stores. **B)** Maximal peak fluorescence changes were determined as the difference between basal and the maximum fluorescence, upon addition of 200 µM GPN. Experiment performed by Lianne Davis. *** $p<$ 0.001; one-way ANOVA test.

However, no accumulation of sphingosine was observed in the Tangier fibroblasts. HPLC quantification found no increase in sphingosine levels, and quite conversely, a trend toward reduced levels as compared to wild type, although not significantly (**Figure 3.7A;** not enough replicates for statistics). Additionally, to confirm this, using a fluorescently labelled endogenous sphingosine we were able to monitor the lipids localization and it was found in Tangier cells sphingosine did not accumulate in vesicles as was found to occur in the NPC cell lines (**Figure 3.7B)**.

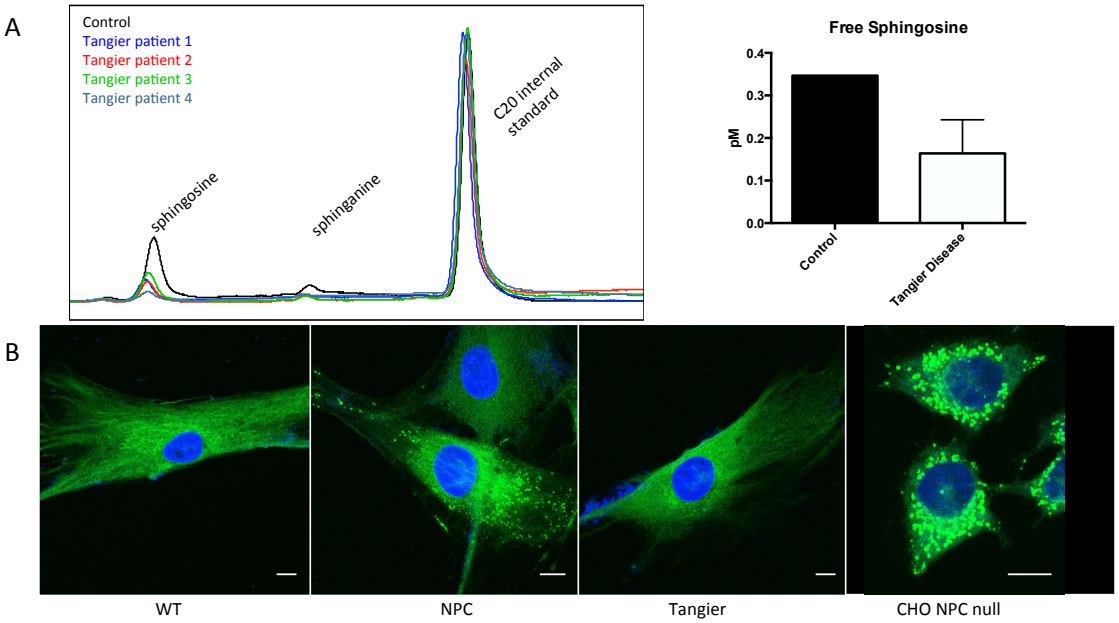

Figure 3.7. *No accumulation of sphingosine is observed in tangier patient fibroblasts.* **A)** Quantification of sphingosine levels using HPLC observed no elevated levels of sphingosine in the Tangier patient fibroblasts. **B)** These findings were confirmed using a sphingosine probe to observe the molecules intracellular localization following a pulse/chase, performed by Doris Höglinger. No accumulation of the fluorescent sphingosine probe was observed in the Tangier fibroblasts as was observed in the both the NPC fibroblasts and *NPC1*$^{-/-}$ CHO cells.

Furthermore, we also observed no increase in α-tubulin acetylation in the Tangier patient fibroblasts (**Figure 3.8**). Despite these two differences - α-tubulin acetylation and sphingosine accumulation, all of the other hallmarks of NPC disease were observed in the Tangier patient fibroblasts (summarized in **Table 3.1**).

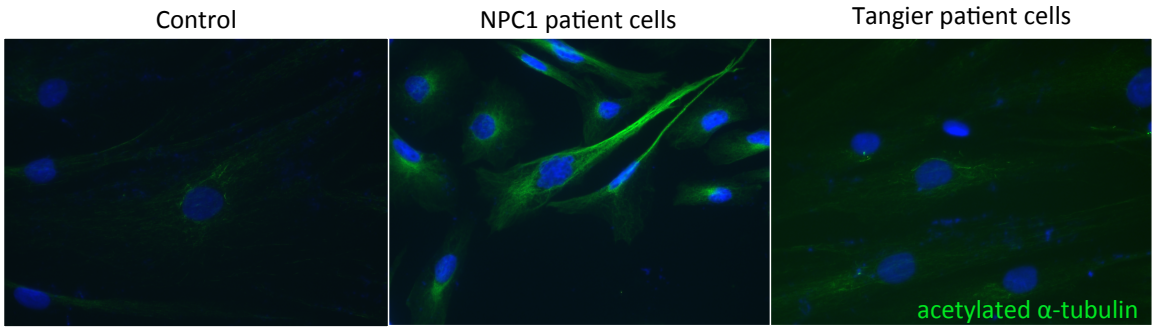

Figure 3.8. *Levels of α-tubulin acetylation in Tangier patient fibroblasts.* An increase in α-tubulin acetylation was not observed in the Tangier patient fibroblasts to the extent observed in NPC patient cells.

Phenotype	NPC	Tangier
Sphingolipid mistrafficking	+	+
GSL storage	+	+
Cholesterol storage	+	+
Sphingosine storage	+	X
Sphingomyelin storage	+	+
Acidic store calcium defect	+	+
Fatty acid storage	+	+
Cytoskeletal defects	+	X

Table 3.1. *Cellular phenotypes observed in Niemann-Pick Type C Disease and Tangier Disease*. It has been observed that NPC patient fibroblasts have sphingolipid mistrafficking from the endocytic vesicles to the Golgi, an accumulation of glycosphingolipids, cholesterol, sphingosine, and sphingomyelin in the lysosomes, reduced acidic store calcium levels, an increase in fatty acid storage, and cytoskeletal defects. These characteristics are also observed in Tangier disease, with the notable exception of sphingosine and cytoskeletal defects.

When we examined protein expression of NPC1 and NPC2 we found there to be a significant up-regulation of NPC1 and no significant difference in NPC2 expression in Tangier cells (**Figure 3.9;** NPC1: control vs Tangier patients p=0.0107; NPC2: control vs Tangier patients p=0.1018).

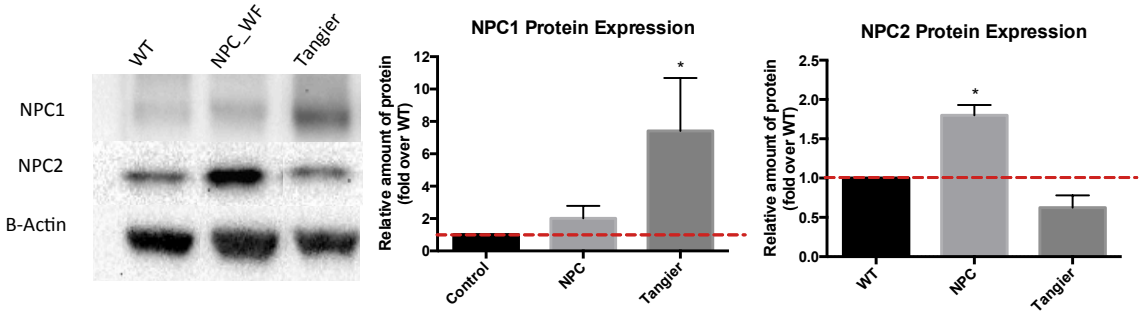

Figure 3.9. *NPC1 and NPC2 protein expression levels in Tangier patient fibroblasts.* Significant increase in NPC1, but not NPC2, protein levels in Tangier patient fibroblasts. Performed by Elias Adriaenssens. *p<0.05; one-way ANOVA

As we had some key differences, lack of sphingosine accumulation and no hyperacetylation of α-tubulin, in Tangier cells as compared to NPC, we wanted to elucidate the sequence of events that occurred following ABCA1 inactivation to better understand what was going on at the cellular level. We silenced ABCA1 in control fibroblasts and observed cholesterol and GSL levels at 24, 48, 72 hours post transfection. Despite 80-90% knockdown of ABCA1 mRNA levels we were unable to observe any biochemical changes following knockdown (**Figure 3.10**).

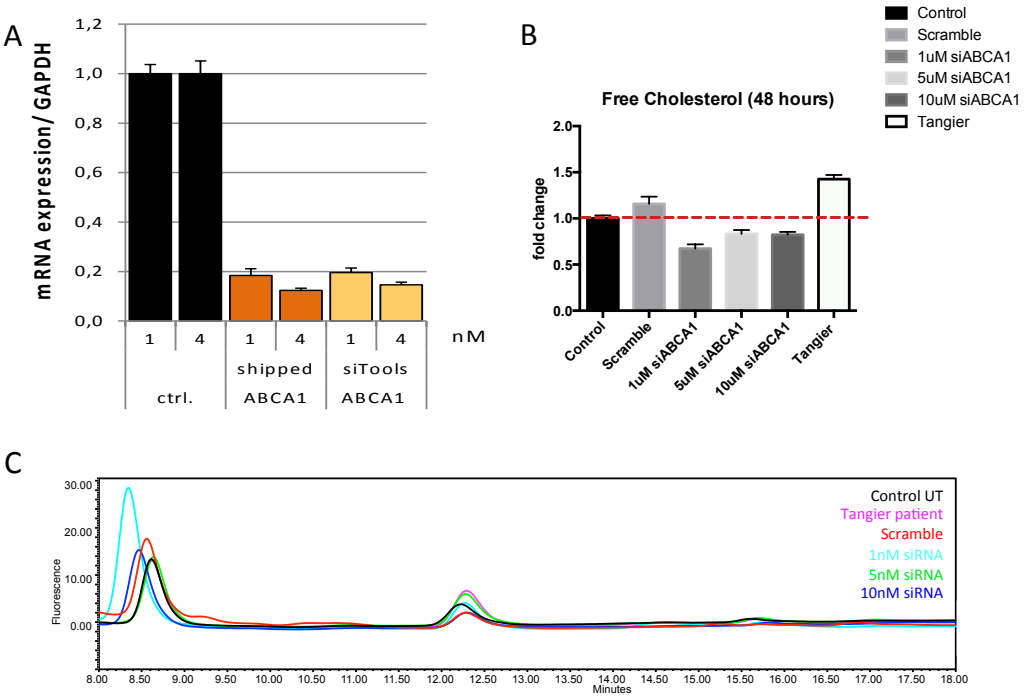

Figure 3.10 *mRNA expression levels of ABCA1 and cholesterol and GSL quantification following ABCA1 silencing.* **A)** mRNA levels of ABCA1 were quantified using RT-PCR and found to achieve knockdown of over 80%; performed by Michaela Beitzinger, siTools™ **B)** Quantification of free cholesterol levels 48hours post ABCA1 silencing resulted in no significant increase in cholesterol levels. **C)** GSL levels did increase to a small extent, but not significantly.

3.3.2 Miglustat as a Therapy for Tangier Disease

As the initially misdiagnosed Tangier patient improved clinically following miglustat treatment (147), we then studied the effects of miglustat at the cellular and biochemical level in Tangier disease cells.

Following 50μM miglustat treatment for 72 hours we observed a significant reduction in relative lysosomal volume as measured by LysoTracker staining. (**Figure 3.11;** Tangier patient 1 UT vs Tangier patient 1 + 50μM miglustat p=0.0015 ; Tangier patient 2 UT vs Tangier patient 2 + 50μM miglustat p<0.0001 ; Tangier patient 3 UT vs Tangier patient 3 + 50μM miglustat p<0.0001; Tangier patient 4 UT vs Tangier patient 4 + 50μM miglustat p<0.0001). As LysoTracker staining has been validated as a biomarker for evaluating the therapeutic response in NPC, this suggests that miglustat treatment is having a therapeutic effect on the Tangier patient fibroblasts (152).

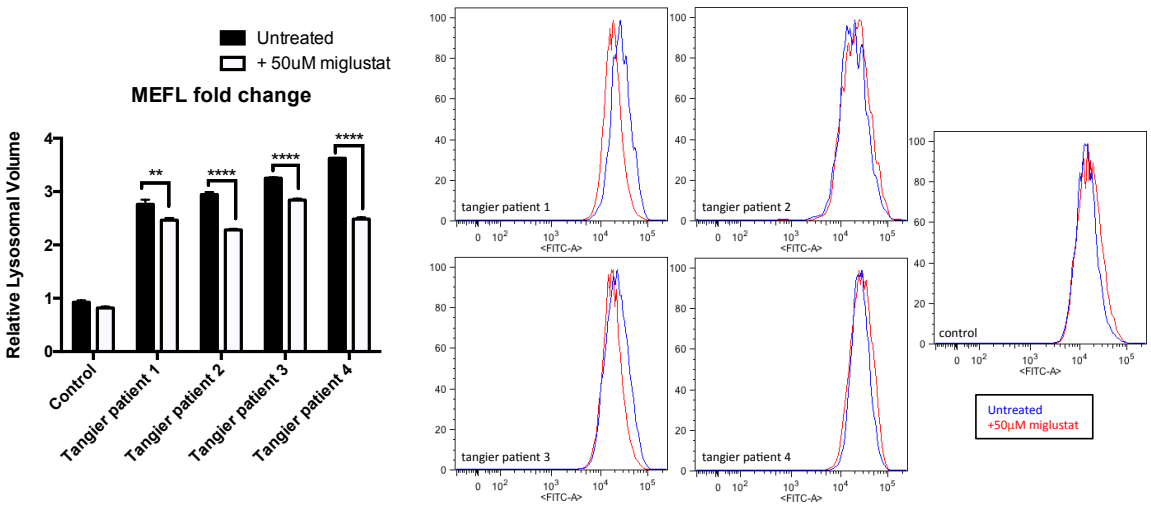

Figure 3.11 *LysoTracker (MEFL) values of patient-derived fibroblasts for NPC1 and Tangier patients and controls following 50*μM miglustat treatment. A) The four Tangier patients exhibited significantly reduced LysoTracker values following miglustat treatment. B) Representative FACs trace of the mean FITC level for the live single cells analyzed. LysoTracker mean values are standardized to MEFL using Rainbow Calibration Beads. Performed by Ecem Kaya. **p<0.01, ****p<0.0001; two-way ANOVA

Following miglustat treatment all Tangier patient total GSL levels returned to levels not significantly different to that observed in control, as did Gb3 (**Figure 3.12**; Total GSLs: control +50μM miglustat vs. Tangier patients +50μM miglustat p=0.4336; Gb3: control + 50μM miglustat vs. Tangier patients + 50μM miglustat p=0.9891).

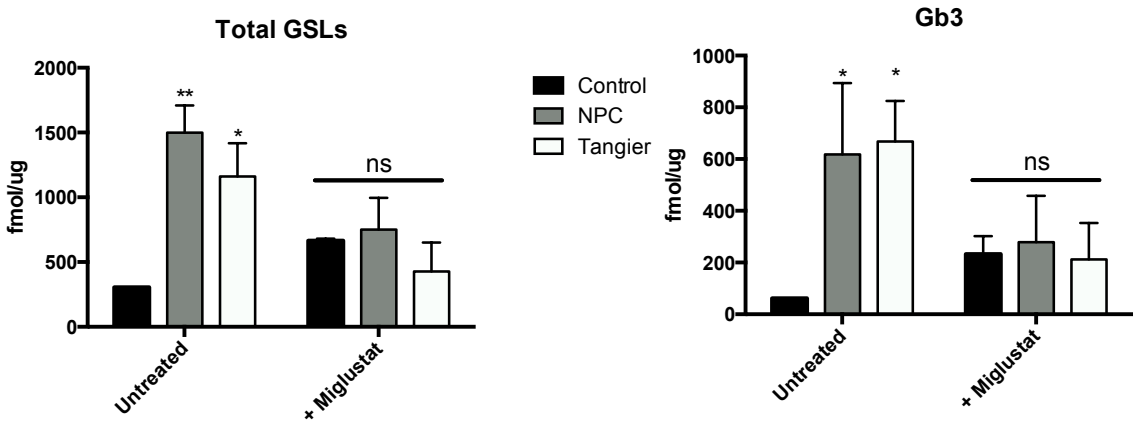

Figure 3.12. *Total GSLs and gb3 levels in 50μM miglustat treated Tangier disease fibroblasts.* **A)** Total glycosphingolipids (excluding Lac-Ceramide) were measured from 0.5mg of protein isolated from NPC1, Tangier and control fibroblasts treated with 50μM miglustat for 72 hours. **B)** Specific GSL species gb3 was restored to normal levels in the treated Tangier fibroblasts. Peaks are identified by determining their glucose units using a 2-AA labeled glucose oligomer ladder standard. *p<0.05; **p<0.01; two-way ANOVA

We also observed an increase in the acidic store Ca^{2+} levels to control levels (**Figure 3.13**; control vs Tangier + 50μM miglustat p=0.1269).

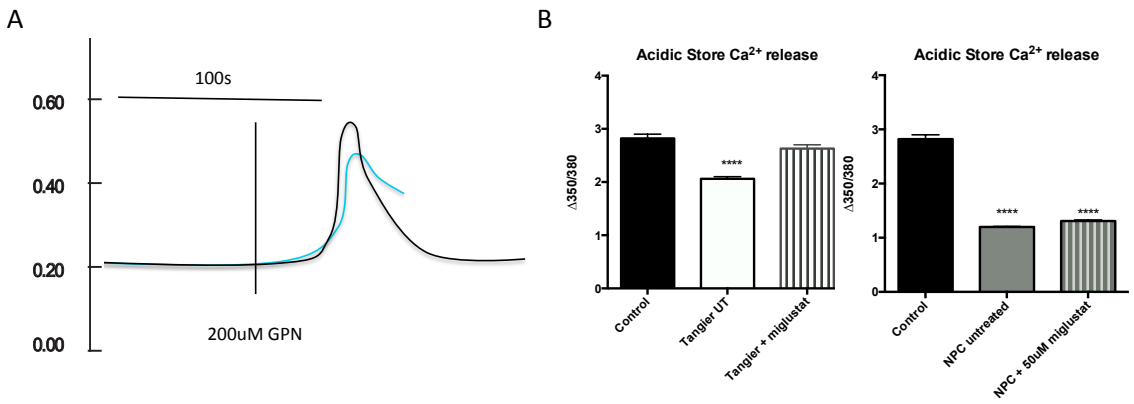

Figure 3.13. *Restoration of lysosomal Ca^{2+} homeostasis in Tangier fibroblasts following 50μM miglustat treatment*. **A)** Representative traces showing intracellular [Ca^{2+}] changes monitored in single fura-2-loaded fibroblasts. Lysosomal Ca^{2+} content was assessed upon addition of 200μM GPN which lyses Cathepsin-containing acidic intracellular Ca^{2+} stores. **B)** Maximal peak fluorescence changes were determined as the difference between basal and the maximum fluorescence, upon addition of 200μM GPN. Experiment performed by Lianne Davis. **** $p < 0.0001$; one-way ANOVA

As miglustat does not correct the acidic store calcium release in NPC patient cells (**Figure 3.13B**; control vs. NPC + 50μM miglustat $p<0.0001$), this was remarkable. We also observed an improvement of the sphingolipid trafficking defect, as noted through an increase in Golgi localized CtxB staining and a reduction in cholesterol as visualized through filipin staining (**Figure 3.14**).

Figure 3.14*. [Page 102] Fluorescent imaging of control, NPC, and Tangier patient fibroblasts following miglustat treatment*. Cholera Toxin was used to study glycosphingolipid trafficking. Punctate cholera toxin (green) staining suggests glycosphingolipid mistrafficking. Filipin (blue) was used to stain free cholesterol.

Miglustat has severed known enzyme targets (GlcCerT, GBA2, GBA) that it differentially targets at different concentration (**Table 3.2**) (79). At the 50μM concentration, which used here, all three targets are differentially inhibited (GBA2>GlcCerT>GBA). A reduced dose of 15μM miglustat only inhibits GBA2 and not GLcCerT nor GBA. Additionally we used the galactose analogue, lucerastat (*N*B-DGJ), as it inhibits only GBA2 and GlcCerT (**Table 3.2**).

Compound		GlcCerT inhibitor	GBA inhibitor	GBA2 inhibitor	Effective in NPC		Effective in Tangier	
					cholesterol	Endocytic trafficking	cholesterol	Endocytic trafficking
Miglustat	50μM	+	-	++	NO	YES	YES	YES
Miglustat	15μM	X	-	++	NO	partially	YES	YES
Lucerastat	50μM	+	-	++	YES	YES	YES	YES

Table 3.2. *Differential activities of the imino sugar analogues miglustat and lucerastat and their effects of cholesterol storage and endocytic trafficking in NPC and Tangier disease.*

We examined the efficacy of a reduced, 15μM, miglustat dose (**Figure 3.15**) and 50μM lucerastat (**Figure 3.16**).

Figure 3.15. [Page 104] *Fluorescent imaging of control, NPC, and Tangier patient fibroblasts following 15μM miglustat treatment*. Cholera Toxin was used to study glycosphingolipid trafficking. Punctate cholera toxin staining suggests glycosphingolipid mistrafficking. Filipin was used to stain free cholesterol.

Figure 3.16. [Page 105] *Fluorescent imaging of control, NPC, and Tangier patient fibroblasts following 50μM lucerastat treatment*. Cholera Toxin was used to study glycosphingolipid trafficking. Punctate cholera toxin staining suggests GSL mistrafficking. Filipin was used to stain free cholesterol.

We found that treatment with the reduced 15μM miglustat dose (**Figure 3.15**) still resulted in improvement of the trafficking defect and a reduction of cholesterol in the Tangier patient cells, but not in the NPC patient cells. Following 50μM lucerastat treatment (**Figure 3.16**), we also observed similar improvement in both the Tangier and NPC patients.

Miglustat treatment was examined due the unexpected clinical improvement in the misdiagnosed Tangier patient. We also were interested to see if other experimental NPC therapies would have similar therapeutic effectiveness in Tangier disease as that may provide insight on the underlying pathogenic mechanisms. We examined the effects of the Angiotensin II receptor blocker losartan (discussed further as a therapy for NPC disease in **Chapter 4**) and the cyclodextrin compound HPβCD (new formulations and mode of delivery of this compound are examined in **Chapter 5**), which is currently in clinical trials as a new therapy for NPC.

We hypothesize that the ARB losartan increases ABCA1 activity, and we expect to see therapeutic efficacy as a treatment for Tangier disease, as these patients have impaired ABCA1 activity. Consistent with this hypothesis, we observed significant reduction (~30%) in relative lysosomal volume as measured by LysoTracker staining (**Figure 3.17;** Tangier patient 1 UT vs Tangier patient 1 + 100μM losartan

p=0.0009; Tangier patient 2 UT vs Tangier patient 2 + 100μM losartan *p*<0.0001 ; Tangier patient 3 UT vs Tangier patient 3 + 100μM losartan *p*<0.0001; Tangier patient 4 UT vs Tangier patient 4 + 100μM losartan *p*<0.0014)

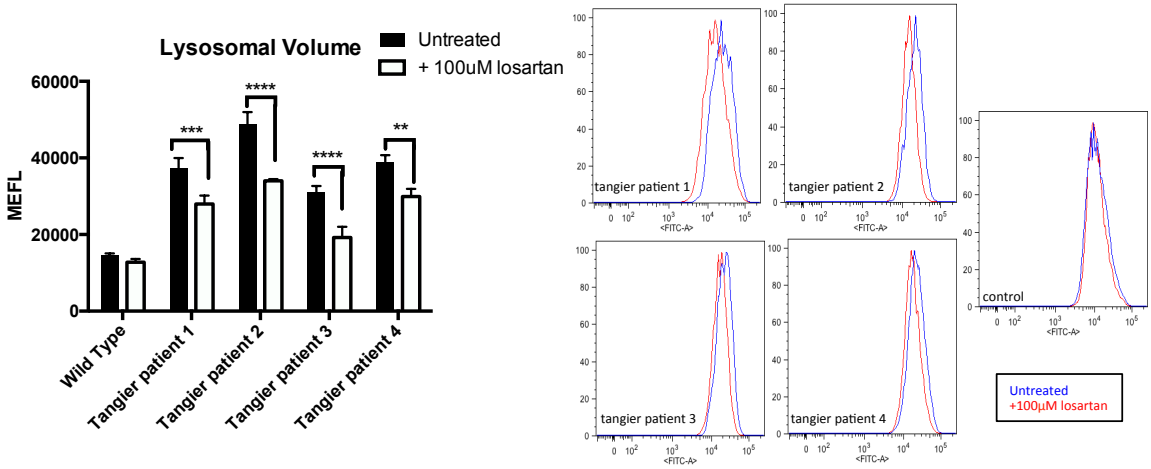

Figure 3.17 *LysoTracker (MEFL) values of patient-derived fibroblasts for NPC1 and Tangier patients and controls following 100*μM losartan treatment. **A)** The four Tangier patient cells exhibited significantly reduced LysoTracker values following losartan treatment. **B)** Representative FACs traces of the mean FITC level for the live single cells analyzed. LysoTracker mean values are standardized to MEFL using Rainbow Calibration Beads. Performed by Ecem Kaya. ***p*<0.01, ****p*<0.001, *****p*<0.0001; two-way ANOVA

The effects of HPβCD is less well understood, however it is thought that through enhancing exocytosis these cyclodextrin compounds have therapeutic effects in NPC (153). We observed no changes in acidic store lysosomal volume as measured by LysoTracker staining following HPβCD treatment (**Figure 3.18;** Tangier patient 1 UT vs Tangier patient 1 + 250μM HPβCD *p*>0.9999; Tangier patient 2 UT vs Tangier patient 2 + 250μM HPβCD *p*=0.9652; Tangier patient 3 UT vs Tangier patient 3 + 250μM HPβCD *p*=0.9776; Tangier patient 4 UT vs Tangier patient 4 + 250μM HPβCD *p*=0.9998).

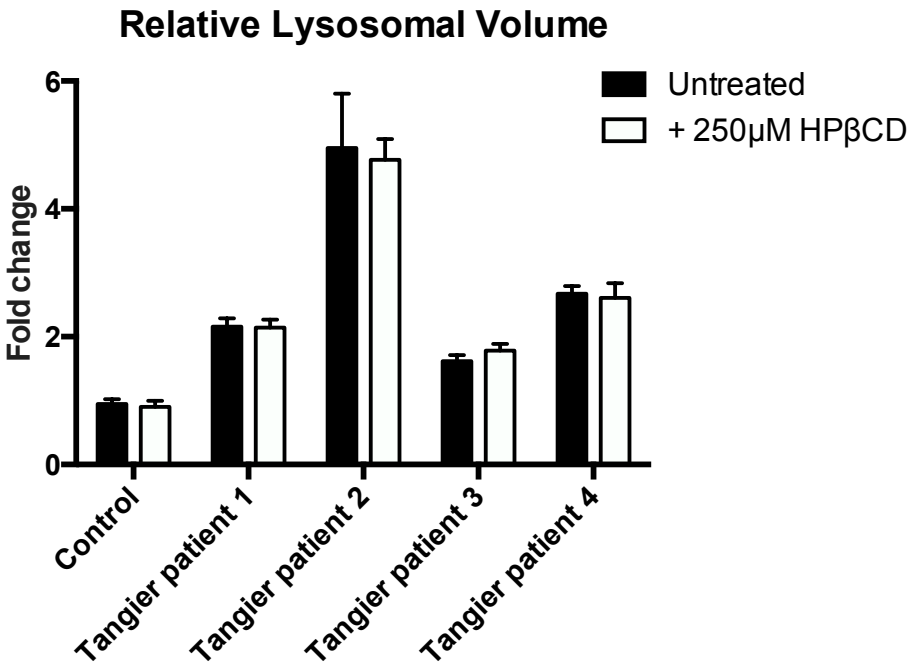

Figure 3.18 *Fold changes of relative lysosomal volume MEFL values of patient-derived fibroblasts for NPC1 and Tangier patients and controls following* 250μM HPβCD treatment. The four Tangier patients exhibited no reduction of LysoTracker values following HPβCD treatment. Performed by Ecem Kaya; two-way ANOVA

3.4 Discussion

Following the misdiagnosis of a patient with NPC who was subsequently correctly diagnosed with Tangier disease and their clinically improvements following miglustat substrate reduction therapy (147), we were interested to see if Tangier disease shared some of the cellular and biochemical disease phenotypes with NPC to explain why the treatment was so effective.

Previous research has already identified many shared characteristics between Tangier disease and other lysosomal storage disorders – including abnormal lysosomal compartment and endocytic trafficking defects (154). Additionally, there have also been investigation on the link between Niemann-Pick disease type C and Tangier disease, specifically the interplay between the NPC1 and ABCA1 proteins (155).

Extending these findings, we have found many characteristics linking Tangier disease specifically with NPC. These traits include enlarged lysosomes, endocytic mistrafficking, cholesterol, glycosphingolipid, sphingomyelin and other lipid storage in the cell – it also uniquely has the acidic store defect. As NPC is the only storage disorder, to date, that has been found to have a lysosomal Ca^{2+} defect this strongly suggests that there is mechanistic convergence between NPC and Tangier disease (13).

However, it is important to highlight that while Tangier fibroblasts shared nearly all cellular and biochemical pathologies associated with NPC, we observed no storage of sphingosine. Sphingosine triggers the pathogenic cascade in NPC (13)(**Figure 1.4**), and has been implicated in regulating Ca^{2+} release from the acidic stores (46). Additionally, we propose that the cytoskeletal defects observed in NPC are due to sphinogosine storage, as it was not observed in Tangier disease patient cells (**Figure 3.19**) and all the cellular pathologies downstream of the Ca^{2+} defect are.

Additionally, we observed complete rescue of all phenotypes observed in Tangier disease following 50μM miglustat treatment, including the acidic store Ca^{2+} defect, which in NPC is not rescued. The additional therapeutic potency of miglustat in the Tangier fibroblasts may be due to the acidic store calcium defect being caused by something other than sphingosine (**Figure 3.19**). Conversely, as we observed a reduction in sphingosine levels (**Figure 3.7**) this pathogenic cascade could also perhaps be

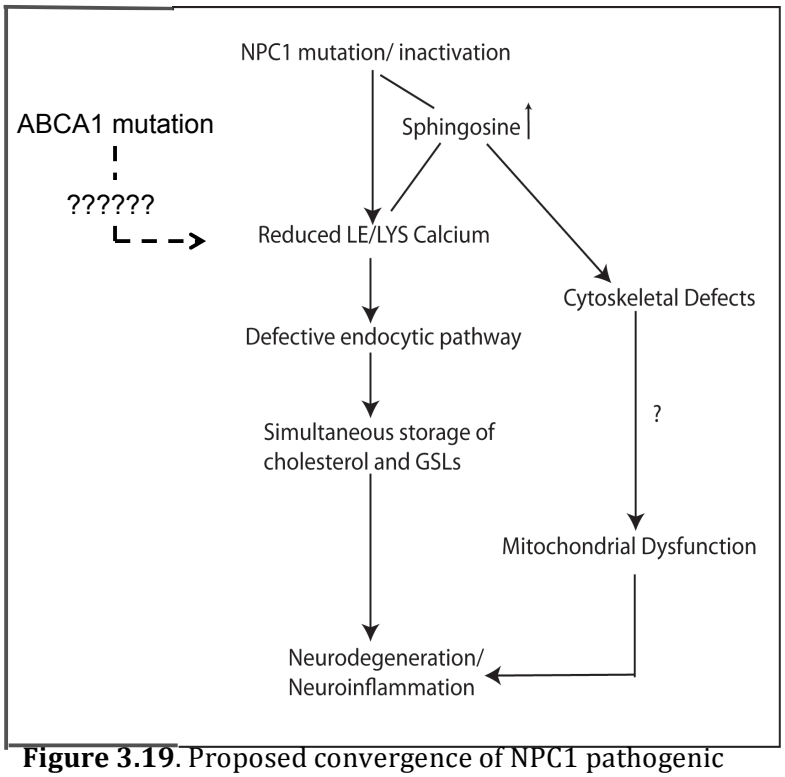

Figure 3.19. Proposed convergence of NPC1 pathogenic cascade following ABCA1 mutation in Tangier disease.

caused by a dysregulation of sphingosine levels. In other words, increased or decreased sphingosine levels perturb acidic store Ca^{2+} homeostasis.

By characterizing the sequence of events following the silencing of ABCA1 we aimed to determine what may cause the initial acidic store Ca^{2+} defect in Tangier disease, however, due to technical difficulties, what that may be remains elusive. As we could only achieve knockdown of 80-90%, the 10-20% residual ABCA1 activity may be enough to mask any phenotype. Patients heterozygous for an ABCA1 mutation (*ABCA1*$^{+/-}$) have reduced cholesterol efflux, some individuals with levels as low as 35% (156, 157). This residual activity in our ABCA1 silencing experiment most likely prevented us from observing a phenotype in these cells, and more extensive knock-out techniques such as CRISPR-Cas may be needed to determine the sequence of events.

To better understand why miglustat was having a more significant benefit in the Tangier patient cells as we observe in NPC patient cells, we examined the therapeutic efficacy of a reduced miglustat dose and the galactose anologue of miglustat, lucerastat.

As previously discussed (**Introduction 1.2.7.1**), both miglustat and lucerastat are GlcCerT inhibitors. Comparative studies of the two drugs in NPC disease have shown that while lucerastat is better tolerated than miglustat, miglustat shows greater functional improvement in mice as miglustat may have additional anti-inflammatory

effects (158). When lucerastat was used as a treatment for Tangier disease the cells had significant cellular improvement (**Figure 3.16**), suggesting that the better-tolerated lucerastat may be a more suitable therapeutic option for this disease.

Likewise, when we reduced the dose of miglustat from 50μM to 15μM, we again saw therapeutic efficacy in the Tangier cells similar to that observed with the 50μM miglustat cellular treatment. Treatment with a reduced miglustat dose of that range will have still inhibit GBA2, but will not inhibit GlcCerT at this lower dose (**Table 3.2**) (80, 159). Research has suggested that the anti-inflammatory benefits of miglustat treatment are due to the inhibitory effects of GBA2 (159), so at this reduced dose miglustat would still have its anti-inflammatory properties. As this dose is effective in Tangier disease, while only partially effective in NPC, low-dose miglustat treatment could also be a potential treatment for Tangier disease as would also reduce the side effects of the drug (**Figure 3.15**).

As both lucerastat and the reduced miglustat dose (15μM) were effective in Tangier disease, it suggests that the therapeutic benefits of these compounds are due to the inhibition of GBA2, rather than GlcCerT. Further analysis of these two compounds are required to better understand their therapeutic potential for Tangier disease – and if the other cellular pathologies, particularly acidic store Ca^{2+} defect, would also be ameliorated.

Additionally, the therapeutic benefits of FDA-approved, easily available ARB losartan is interesting. It has been suggested that by inhibition the angiotensin II-mediated suppression of ABCA1 with losartan treatment we would see an increase in ABCA1 expression and enhance cellular cholesterol efflux. While we were unable to quantify ABCA1 expression levels, we expect the therapeutic effects observed with losartan treatment is due to the rescue of the impaired ABCA1 efflux in these patients. However, functional efflux assays would be required to confirm this.

Additionally, the ineffectiveness of HPβCD treatment is interesting as it suggests again at the underlying differences that must exist between Tangier and NPC diseases, as HPβCD is very effective in the treatment of NPC (160). Previous studies had also found that cholesterol storage could not be depleted in Tangier cells following cyclodextrin treatments (161), in line with our findings of no reduction in relative lysosomal volume (**Figure 3.18**).

The serendipitous discovery that Tangier patients may benefit from miglustat therapy has led to further examination of the Tangier disease phenotypes and found that this disease shares many of the cellular and biochemical characteristics observed in NPC. While differences exist, most notably the lack of sphingosine accumulation in Tangier disease, the benefits following miglustat treatment were substantial. Miglustat seemed to be even more effective in Tangier disease fibroblasts than it was in NPC cells. Further analysis of the effects of a lower dose miglustat treatment and other substrate reduction therapies, as well as drugs

targeting ABCA1 expression may lead to effective long-term treatment for the currently un-treatable Tangier disease.

It is important to note that based upon the cellular correction studies, Dr Patrick Deegan (Addenbrooke's Hospital, Cambridge) has obtained miglustat under compassionate use to trial in the patient whose fibroblasts I have studied and showed clear correction in.

In summary:

- Tangier disease mechanistically converges with the NPC pathogenic cascade at the level of the acidic store calcium defect
- All cellular/biochemical phenotypes were ameliorated following miglustat treatment suggesting miglustat may be the first treatment described for Tangier patients

Chapter 4: Losartan as a Novel Therapy for NPC

4 Losartan as a Novel Therapy for NPC

4.1 Introduction

The unexpected convergence of the cellular pathology of Tangier disease and Niemann-Pick disease type C (**Chapter 3**) led us to examine if a drug upregulating ABCA1, the product of the gene mutated in Tangier disease, could serve as a disease modifying therapy for NPC.

One of the mechanisms that modulates ABCA1 expression is through the activation of liver-X-receptors (LXR) and retinoid-X-receptors (RXR) **(Figure 4.1)**, which leads to oxysterols binding to the DR4 site of the *ABCA1* promoter (162). It has been proposed that LXR may act as a sterol sensor and activate the transcription of cholesterol transporting genes (i.e. *ABCA1*) when cholesterol levels are high (163). Targeting *ABCA1* expression through activation of LXR has previously been shown to reduce cholesterol accumulation in NPC1 patient fibroblasts, furthering support as a therapeutic target for NPC (164).

It has also been demonstrated that Angiotensin II (Ang II) can inhibit the rate of ABCA1-mediated cholesterol efflux through the Angiotensin II type 1 (AT-1) receptor (165). Some of the downstream effects of Ang II-mediated ABCA1 repression via the AT-1 receptor are foam cell formation and atherosclerosis (166). Previous studies have linked using Angiotensin II receptor blockers (ARBs) such as losartan and valsartan with a reduction in Ang II/AT-1 receptor mediated inhibition of ABCA1 expression (**Figure 4.1**), and an increase in cellular cholesterol efflux (162, 165).

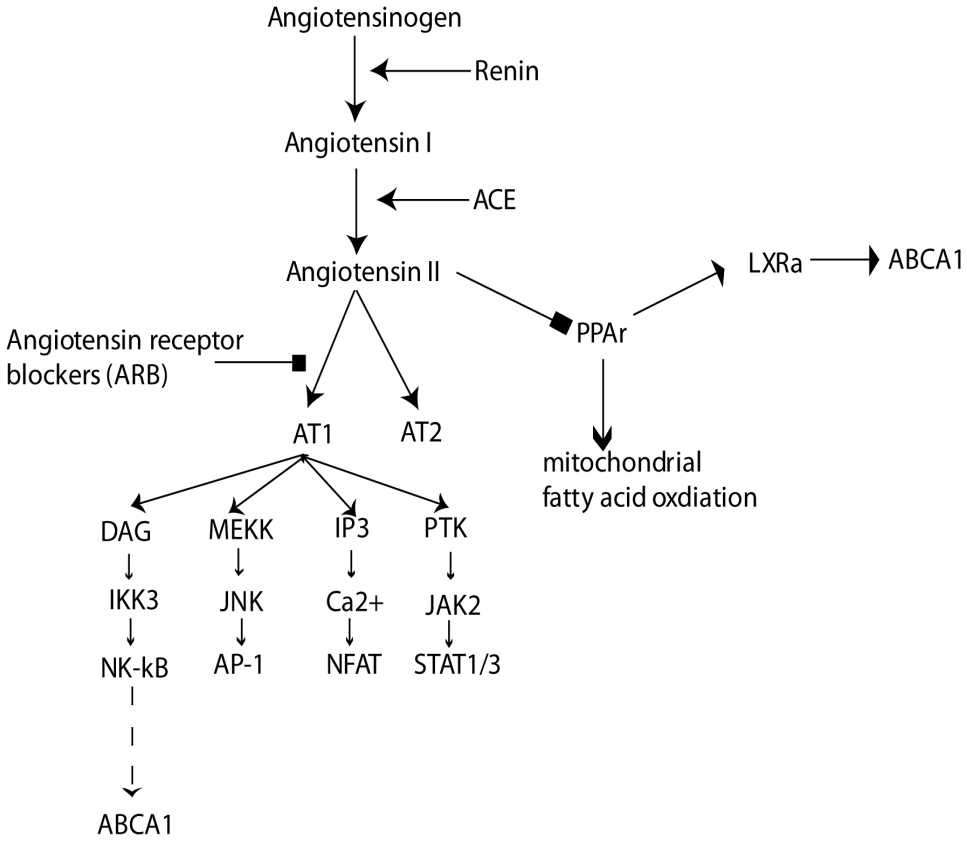

Figure 4.1. *Angiotensin signaling cascade.*

Both losartan (Cozaar™) and valsartan (Diovan™) are FDA-approved selective AT-1 antagonists that modulate the renin-angiotensin system and historically have been prescribed for hypertension. Losartan is metabolized by cytochrome p450 to the active

metabolite, EXP-3174, which has a half-life of 6 to 9 hours and has no known adverse effects (167, 168). Valsartan, which is not cytochrome p450 metabolized, also has a half-life of 6 to 9 hours and no known adverse effects (168). The two ARB's have a bioavailability of 33% (losartan) and 25% (valsartan), and if administered with food the area under the plasma concentration curve of losartan is reduced by approximately 10%, and for valsartan 50% (167).

Losartan and its active metabolite can cross the BBB as well as act as a partial peroxisome proliferator-activating receptor gamma (PPARγ) activator (**Figure 4.1**) (169, 170). In addition, losartan has also been suggested to have neuroprotective effects in reducing Ang II induced CNS inflammation, as ARB treatment can reduce cerebral inflammation via the brain's AT-1 receptors (171, 172). It has also been found that ARBs can reduce levels of activated microglial, which is observed in high levels across the cerebellum of the *Npc1*$^{-/-}$ mouse (173, 174). Angiotensin II and its role in the inflammatory signal pathway summarized in **Figure 4.2**.

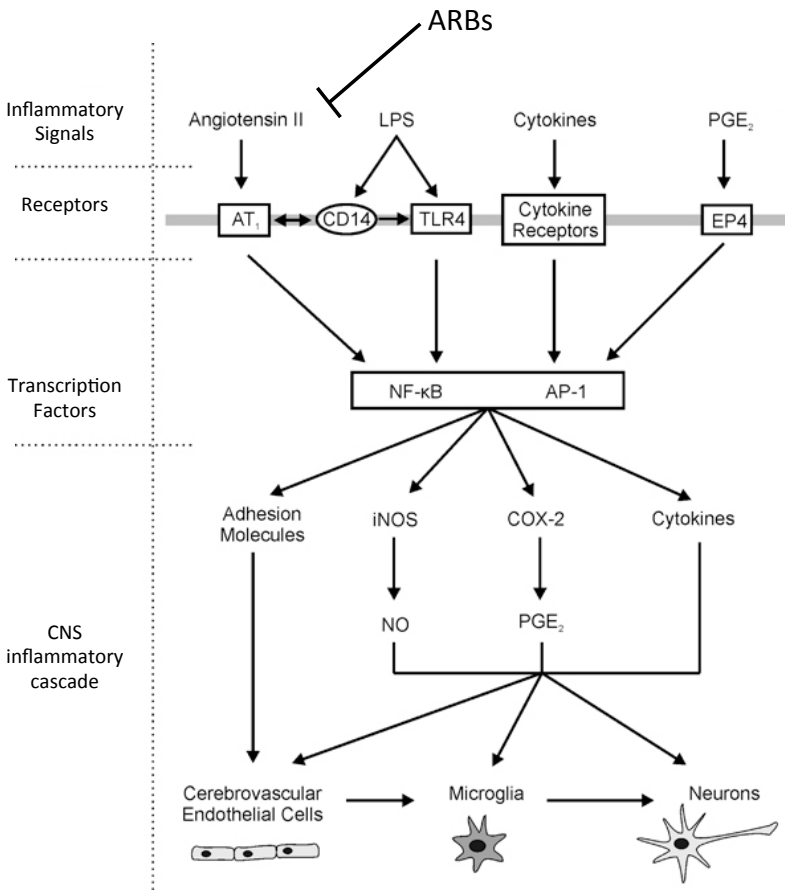

Figure 4.2. *Angiotensin II and inflammatory signal pathways in the brain.*

In light of the potential therapeutic benefits of losartan in NPC, both as an ARB and as a partial PPARγ activator, the effects of this drug were further examined in the cellular and then mouse model of NPC1 disease.

The specific aims presented in this chapter are:

- Determine efficacy of losartan as a potential disease modifying therapy for NPC disease alone and in combination with the current approved NPC treatment, miglustat

4.2 Materials and Methods

4.2.1 Cells

Human NPC1-mutant and control fibroblasts were obtained from the NIH (Dr. Forbes Porter). The NPC1 patient fibroblast line used (NPC17; severity 7) has a 10bp deletion in exon 19 at codon 962, I1061T. Fibroblasts were maintained in DMEM supplemented with 10% FCS, 1% penicillin-streptomycin and 1% $_{L}$-glutamine.

4.2.3 Cellular Drug Treatments

Miglustat (*N*B-DNJ, Actelion) was used at a concentration of 50μM and losartan (Sigma) at 2, 20, 100μM.

4.2.4 Quantification of LysoTracker Staining via FACS

As detailed in section 2.2.9.2.

4.2.5 Mice

BALBc/NPC^{m1n} mice were bred as heterozygotes to generate *Npc1*$^{-/-}$ mice and control genotypes. Mice were bred and housed under non-sterile condition, with food and water available *ad lib*. All experiments were conducted using protocols approved by the UK Home Office Animal Scientific Procedures Act, 1986.

4.2.6 Mouse Drug Treatments

Miglustat (1200mg/kg)(n=7) was supplemented as a dry mixture in powdered chow from 3 weeks of age. Losartan potassium (Sigma) (n=7) was supplemented in the powdered chow (2mg/kg) from 3 weeks of age. Untreated mice were fed on powdered chow (n=5). Treatment groups were made up of approximately equal number of males and females.

4.2.7 Mouse Behavioural Analysis

4.2.7.1 Determination of Humane End-Point

Weight was recorded weekly for each mouse until they reached the humane end-point (loss of 10% body weight within 24hrs).

4.2.7.2 Measuring Activity

Spontaneous activity of each mouse was determined in an open-field (Cambridge Eurotech, UK) according to the manufacturer's instructions, with each mouse analyzed for 5 min. Rearing was manually recorded for 5min (the number of times the mouse reared on its hind legs with our without support of the cage wall).

4.2.7.3 Measuring Tremor

Tremor was monitored as previously described (13). Briefly, a commercial tremor monitor (San Diego Instruments) was used according to the manufacturer's instructions and was housed on an anti-vibration table. Each mouse was monitored for 256 sec, after a 30 sec acclimatization period. The tremor monitor was connected to a computer via a National Instrument PCI card and the output (amplitude/time) was analysed using LabView software to give a measurement of power for each frequency (0-64 Hz).

4.2.7.4 Gait Analysis

Gait analysis was performed using a CatWalk 10.5 system (Noldus) according to the manufacturer's instructions and five runs were recorded per animal at each time point. The camera was set to 40cm below the walkway, the walkway was approximately 4cm wide, and detection settings were set to camera gain 14.05 and green intensity 0.12.

4.2.8 Glycosphingolipid Measurement

GSLs were extracted from cellular homogenate (1mg protein) as previously described in section 3.2.8. GSLs extracted from mouse tissue were analysed as described in section 3.2.8 with a slight modification – tissues were homogenized in water to make a 5mg/mL solution.

4.2.9 Tissue Immunohistochemistry

Mice were perfusion fixed under terminal anaesthesia in 4% paraformaldehyde in phosphate buffer, pH7.4. Liver and brain were dissected out and moved into a 30% sucrose solution after 24 hours 4°C in 4% paraformaldehyde (w/v). Tissues were mounted on cutting blocks and cut 30μM thick at -19°C and placed in PBS+0.1% TritonX-100 solution. To stain cerebellar Purkinje neurons, tissue sections were incubated overnight at 4°C in 1:3000 monoclonal mouse anti-calbindin antibody (CB-300, Swant) with PBS-TritonX, and 2% horse serum solution and washed 3 x 5mins PBS. The secondary anti-mouse DyeLight 594was used at 1:2000 in PBS-TritonX-100, 2% horse serum for 2hr, RT. It was washed 3x PBS, blocked for 2hr, RT with 1% BSA in PBS-TritonX-100 then washed 3x PBS. They were then incubated in rat anti-CD68 (MCA1957, Bio-Rad) 1:500 PBS-TritonX-100 2% goat serum overnight at 4°C. Sections were washed 3x PBS and labelled with donkey anti-rat DyeLight 488at 1:2000 PBS-TritonX-100 with 2% goat serum for 2hr, RT and washed 3x PBS. The sections were then incubated for 30min, RT in 1:400 filipin

solution in 0.25% PBS-TritonX, washed 3x PBS and visualized on a Zeiss Axiovert fluorescent microscope.

4.2.10 Purkinje Cell Counts.

For each treatment 3 mice with an average of five 30μM cerebellum sections were counted. The number of Purkinje cells visible were counted down the Zeiss Axiovert fluorescent microscope for each lobule across the cerebellum.

4.2.11 Microglial Counts

For each treatment 3 mice with an average of five 30μM cerebellum sections were counted. The activated microglial were counted from lobule 7 for each treatment group.

4.2.12 Cholesterol Quantification

As detailed in section 3.2.13.

4.2.13 Sphingoid Base Quantification

As detailed in section 3.2.9.

4.2.14 Acidic Store Calcium Measurements

As detailed in section 3.2.10.

4.3 Results

4.3.1 Losartan, Alone and in Combination with Miglustat, Effectively Targets NPC Cellular Pathologies

Using the FDA-approved angiotensin-II receptor agonist losartan, we can inhibit angiotensin-II modulated ABCA1 repression in the cell, elevating ABCA1 levels. In light of the mechanistic convergence between NPC and Tangier disease (**Chapter 3**) we therefore tested the effectiveness of losartan alone, as well as in combination with miglustat in NPC patient fibroblasts.

We first investigated losartan's effect on cholesterol storage and determined that 100μM losartan was the most effective dose at reducing filipin staining, although both 2μM and 20μM had some effectiveness (**Figure 4.3**).

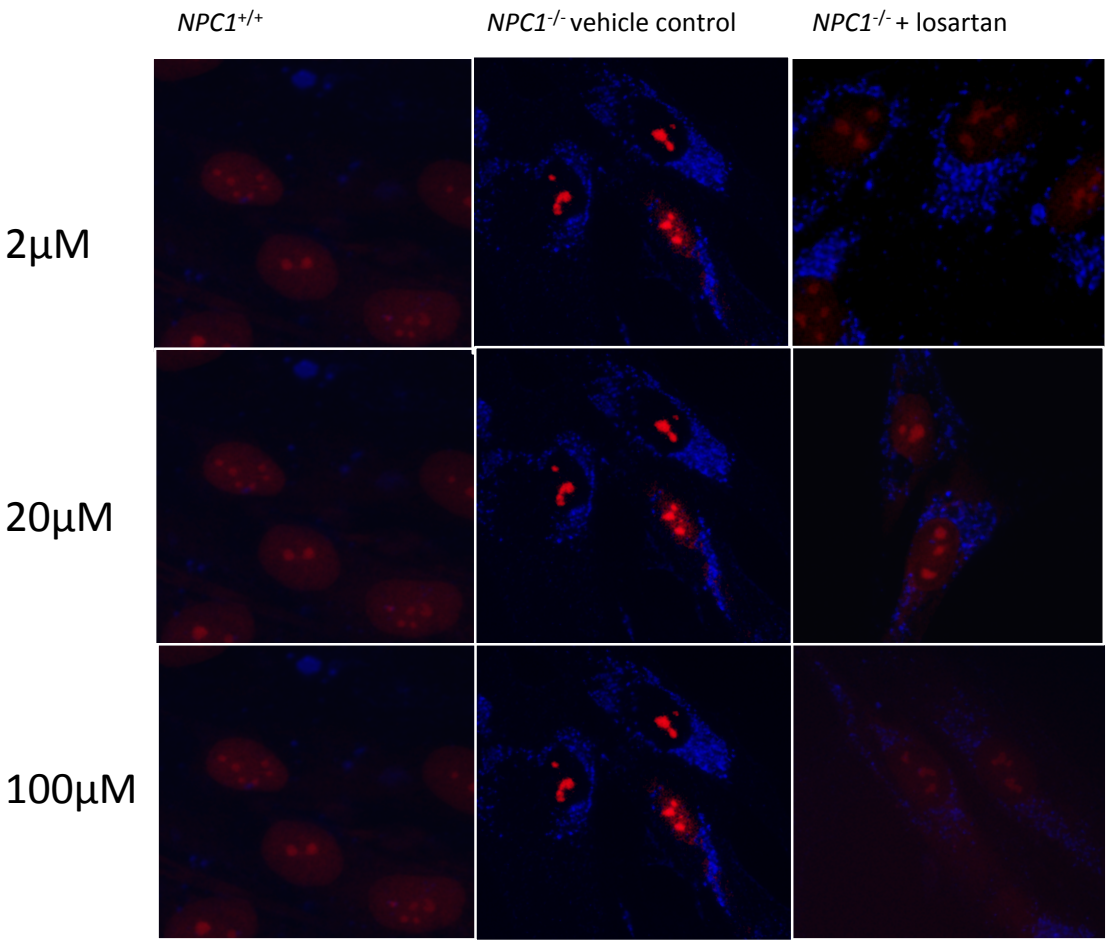

Figure 4.3. *Cholesterol levels observed with filipin staining*. *NPC1*$^{-/-}$ patient fibroblasts were treated with 2, 20, and 100μM losartan for 72 hours. Free cholesterol was visualized with filipin staining, and a reduction was observed following 100μM losartan treatment.

We subsequently studied the effects of 100μM losartan on acidic store Ca^{2+} levels, alone or in combination with miglustat. There was a significant increase in acidic store Ca^{2+} levels following 72 hours of treatment with both losartan treatment alone (p<0.0001) and the combination of losartan/miglustat (p=0.0007) (**Figure 4.4**). Losartan treatment alone was not significantly different from the combination of the losartan/miglustat (p=0.2886).

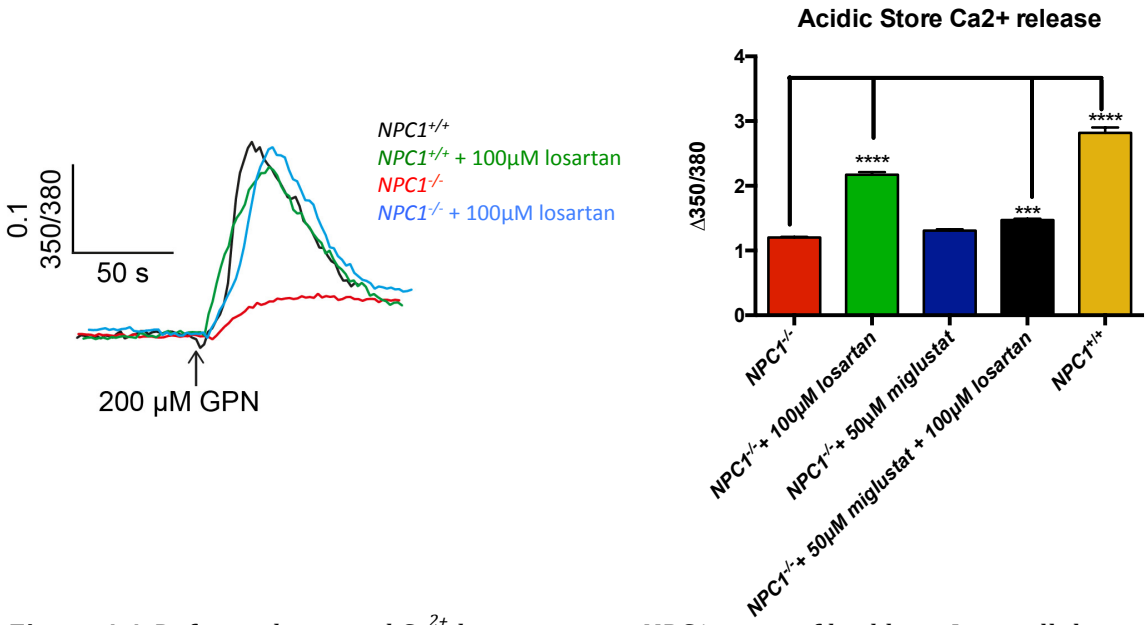

***Figure 4.4**. Defective lysosomal Ca^{2+} homeostasis in NPC1 patient fibroblasts*. Intracellular Ca^{2+} changes were monitored in single fura-2-loaded fibroblasts. Lysosomal Ca^{2+} content was assessed upon addition of 200μM GPN, which lyses cathepsin-containing acidic intracellular Ca^{2+} stores. Maximal peak fluorescence changes were determined as the difference between basal and the maximal fluorescence upon addition of 200μM GPN. ****p<0.0001, **p<0.01; one-way ANOVA.

Based on these promising findings, we continued exploring the effect of losartan alone, and in combination with miglustat, on the cellular and biochemical phenotypes of NPC. The combination treatment of losartan and miglustat restored the endocytic trafficking defect observed with CtxB staining, as did both individual treatments albeit to a lesser extent (**Figure 4.5**).

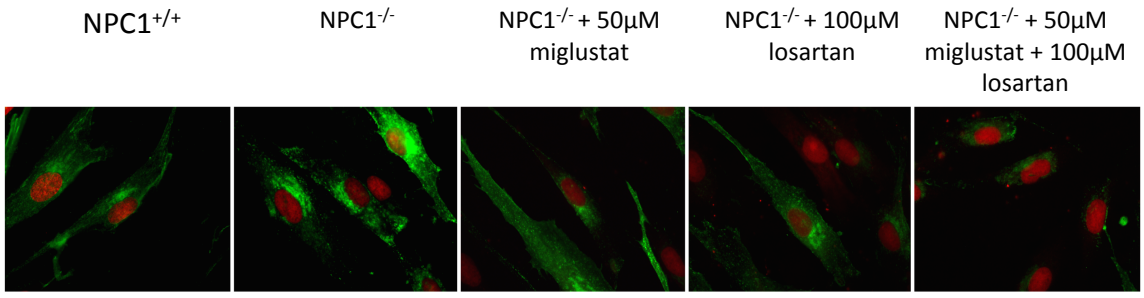

Figure 4.5. *Defective GM1 trafficking to the Golgi recycling pathway from LE/Lys in $NPC1^{-/-}$ patient fibroblasts.*. In $NPC1^{+/+}$ cells Golgi staining is observed, but in $NPC1^{-/-}$ patient fibroblasts punctate staining of GM1 in the LE/Lys the cell is observed.

In terms of GSL storage, losartan alone did not reduce total levels relative to untreated *NPC1*$^{-/-}$ fibroblasts (p=0.3127), and remained significantly elevated relative to control cells (p=0.0310) (**Figure 4.6**). As expected, treatment with miglustat, and inhibitor of GSL biosynthesis, significantly reduced total GSL levels to control levels (**Figure 4.6**; *NPC1*$^{-/-}$ + 50μM miglustat vs. *NPC1*$^{+/+}$ p=0.9981), as did the combination treatment (*NPC1*$^{-/-}$ + 50μM miglustat + 100μM losartan vs. *NPC1*$^{+/+}$ p=0.6397). No significance difference was observed between the miglustat treatment alone and the combination treatment (p=0.8428).

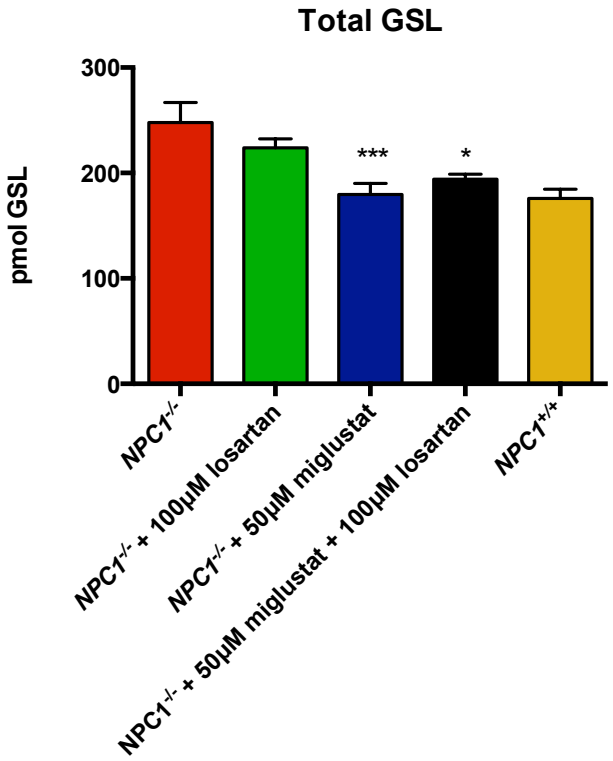

Figure 4.6. *GSL levels in NPC1*$^{-/-}$ *patient fibroblasts* . Total GSL levels (excluding Lac-Ceramide) were measured from 0.5mg of protein isolated from *NPC1*$^{+/+}$, *NPC1*$^{-/-}$ untreated and treated fibroblasts. *NPC1*$^{-/-}$ patients have significant GSLs accumulation in the cells, and following treatment of 50μM miglustat alone and the combination treatment there was no significant differences from *NPC1*$^{+/+}$ cells. ***p<0.001, *p<0.05; one-way ANOVA test.

Despite losartan having no effect on GSL storage, losartan and the combination of the losartan/miglustat reduced the level of filipin staining in *NPC1*$^{-/-}$ fibroblasts (**Figure 4.7A**). However, no reduction in free fatty acid levels in the *NPC1*$^{-/-}$ fibroblasts was observed in any of the treatment groups (**Figure 4.7B**; *NPC1*$^{-/-}$ vs. *NPC1*$^{-/-}$ + 50μM miglustat p=0.1404, *NPC1*$^{-/-}$ vs. *NPC1*$^{-/-}$ + 100μM losartan p=0.8218, *NPC1*$^{-/-}$ vs. *NPC1*$^{-/-}$ + 100μM losartan + 50μM miglustat p=0.9333).

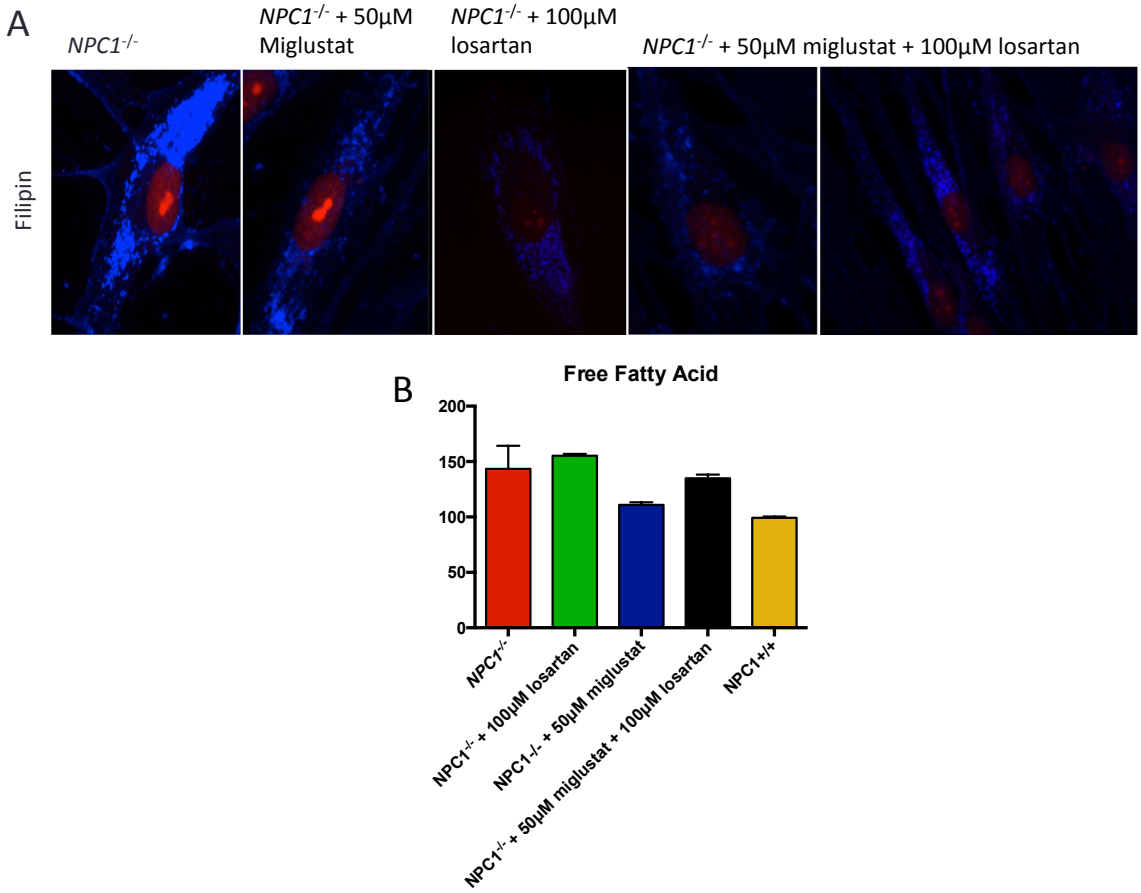

Figure 4.7. *Cholesterol and fatty acid levels in NPC1*$^{-/-}$ *patient fibroblasts*. **A)** Free cholesterol was visualized with filipin staining, and a reduction was most apparent in both the losartan treatment alone and the losartan/miglustat combination treatment. **B)** There were, however, no significant reductions in fatty acid accumulation in any of the treatment groups; one-way ANOVA

Additionally, as cytoskeletal defects were identified in the *S. cerevisiae* screen detailed in **Chapter 2,** we examined the effects of losartan and miglustat on this cellular pathology. Both losartan and miglustat reduced the intensity of the acetylated α-tubulin staining, indicative of more dynamic microtubules (**Figure 4.8**).

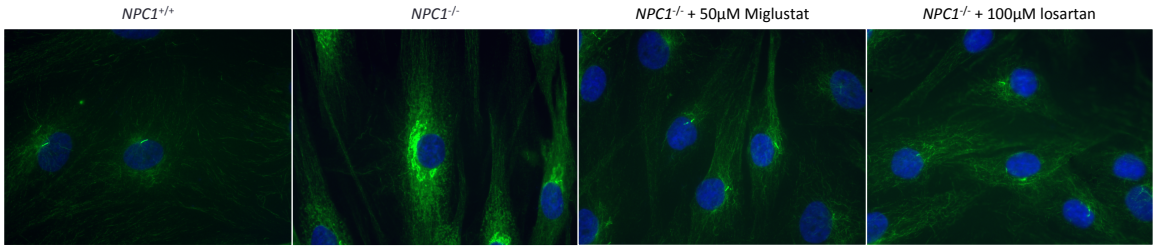

Figure 4.8. *Acetylated α-tubulin staining in NPC1$^{-/-}$ patient fibroblasts treated with miglustat and losartan.* Acetylated α-tubulin is found on stable microtubules, and is observed at higher intensity in NPC disease patient cells as compared to *Npc1$^{+/+}$* fibroblasts.

As the losartan and miglustat treatments seemed partially effective in the patient fibroblasts, the drugs were further evaluated in the *Npc1$^{-/-}$* mouse model.

4.3.2 Losartan as a Disease Modifying Drug in the *Npc1$^{-/-}$* Mouse Model

Untreated *Npc1$^{-/-}$* mice survive to approximately 12 weeks of age and have progressive neurodegenerative with onset of clinical signs at approximately 6-7 weeks of age (75). Initially, miglustat (1200mg/kg) treatment was started at 3 weeks and losartan (10mg/kg) at 6 weeks of age. The mice were dosed with losartan dissolved in the drinking water, but due to the cytochrome p450 enzyme deficiency in NPC disease (103), this dose proved to be toxic and was later reduced to 2mg/kg. Additionally, we had concerns that when dissolved in the drinking water

losartan could be precipitating out of solution and that the mice were not receiving consistent dosing of the drug. To examine this, mice were also trialled on a powdered diet containing losartan to determine if this was a more effective method to deliver the drug to the mice.

The reduced losartan dose (2mg/kg) delivered either via the drinking water or the diet from 6 weeks of age was found to have no effect on survival relative to the untreated *Npc1*$^{-/-}$ mice (**Figure 4.8A**) or weight loss (**Figure 4.8B**).

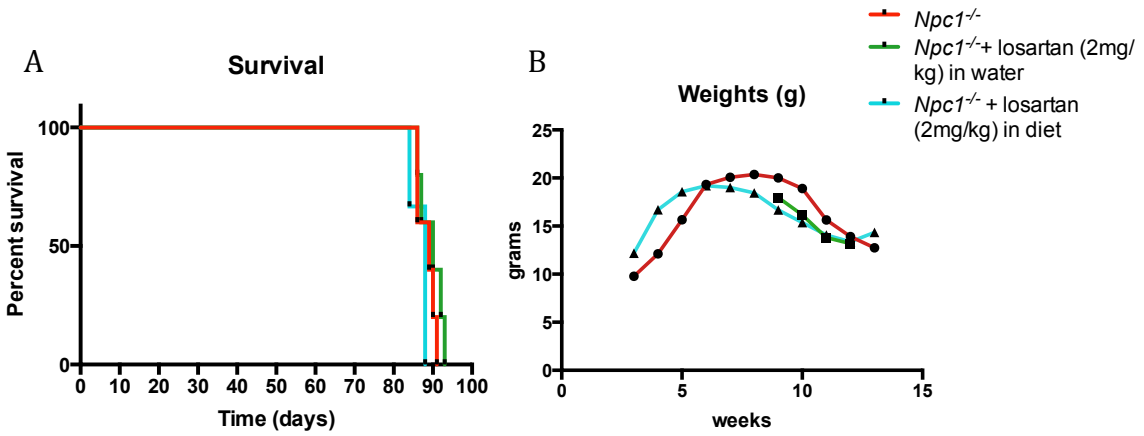

Figure 4.8. *Kaplan-Meier survival curves and average weight curves for losartan (2mg/kg) drinking water and losartan (2mg/kg) diet treated Npc1*$^{-/-}$ mice. **A)** Losartan water and diet treated mice did not live significantly longer than untreated *Npc1*$^{-/-}$ mice. Average survival for *Npc1*$^{-/-}$: 89 days, *Npc1*$^{-/-}$ + losartan diet: 90 days, *Npc1*$^{-/-}$ + losartan water: 88 days. **B)** No significant differences in weight between the treatment groups suggesting that the reduced dose (2mg/kg) was well tolerated in the mice.

No reduction in tremor at 9 or 12 weeks of age was observed (**Figure 4.9A**) and we observed a mixture of improvements and worsening in different aspects of the losartan diet treated animals gait (**Figure 4.9B**; Losartan diet vs. untreated *Npc1*$^{-/-}$ front stand mean p=0.0244, hind stand mean p=0.0116, front step cycle p=0.0298, hind duty cycle p=0.0051, step sequence AB p=0.0005; parameters detailed in

Appendix Table 5 (175)). Additionally, a small improvement in activity of the diet treated mice (**Figure 4.9C**; p=0.0005 as compared to untreated *Npc1*$^{-/-}$) and no change in rearing was observed (**Figure 4.9D**).

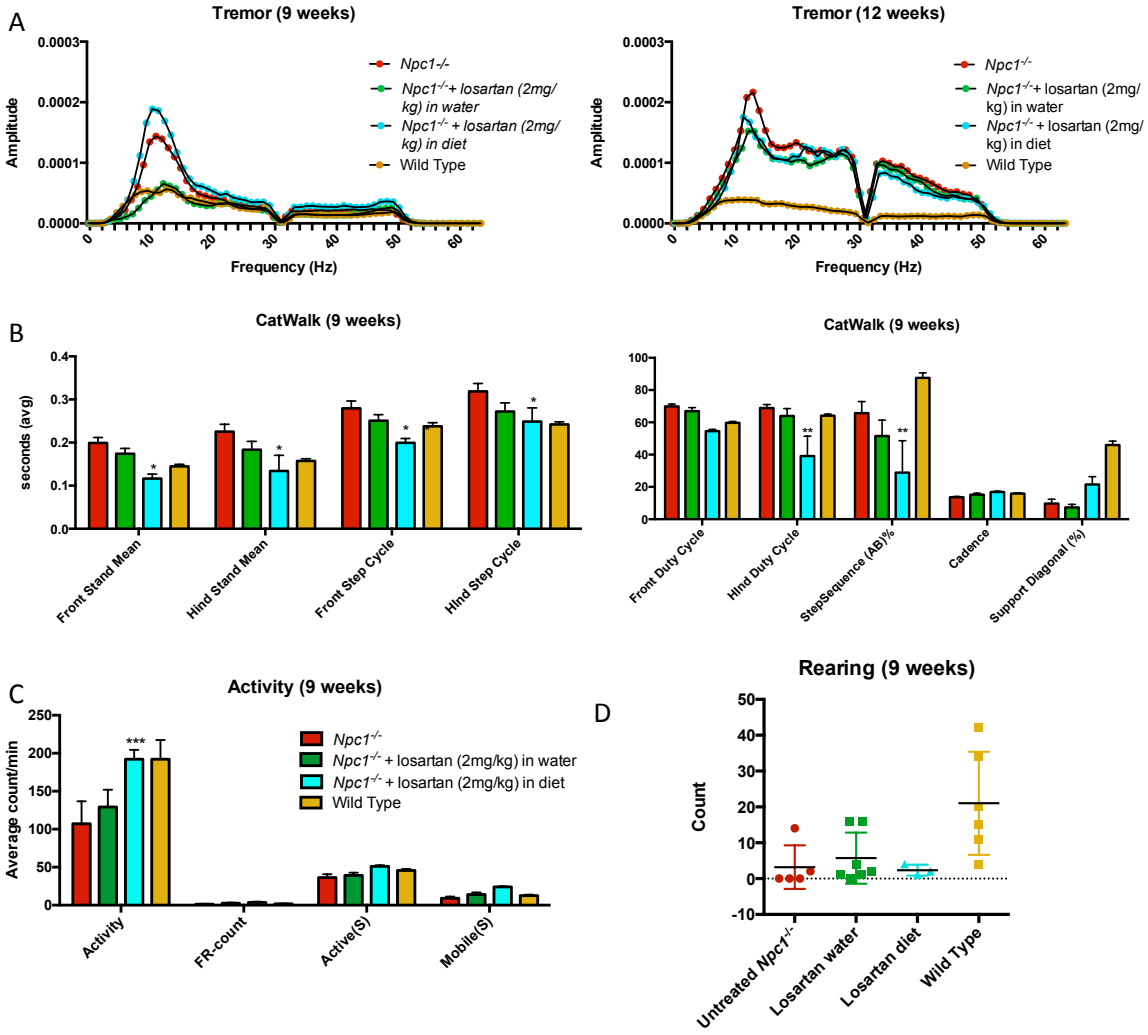

Figure 4.9. *The effect of losartan (2mg/kg) in drinking water or diet on tremor, gait, activity, and rearing.* **A)** No significant reduction of tremor was observed in either treatment groups at 9 or 12 weeks of age. **B)** A significant reduction in the front and hind stand mean and the front step cycle and hind duty cycle are indicative of an improved gait in the losartan diet treated mice. However, a reduced percentage of time spent in step sequence AB was seen as a worsening of the phenotype. **C)** At 9 weeks of age, a significant increase in activity was observed in the mice treated with losartan in the diet. **D)** No significant differences were observed in the rearing abilities of the losartan treated mice. Wild type control mice included for comparison. *p<0.05, **p<0.01***p<0.001, one-way ANOVA

Summary of losartan in water *vs.* diet data in **Table 4.1**.

Parameter compared to *Npc1*$^{-/-}$	losartan (drinking water)	losartan (in diet)
Survival	=	=
High frequency tremor	=	=
Mobility / Activity	=	+
Gait / Motor Coordination	=	+

Table 4.1. *Comparative table of losartan drug delivery comparison as compared to untreated Npc1*$^{-/-}$ *mice in terms of the different behavioral parameters measured.* Losartan (2mg/kg) treatment from 6 weeks of age in drinking water provided no survival or behavioral benefits. Losartan delivered in the diet did have improved activity as well as gait/coordination as compared to the untreated mouse, although no survival benefits.

Following these findings we started a new group of mice that began treatment in the diet at 3 weeks of age, to determine if an earlier point of intervention could result in further improvements. Additionally, we included a combination treatment (losartan/miglustat) as the two drugs have different mechanism's of action so may complement each other.

When losartan treatment was started at 3 weeks of age we saw a small but significant improvement in lifespan as compared to the untreated mice (p=0.0345), and a significant improvement in both the miglustat (p<0.0001) and the losartan/miglustat combination treatment (p<0.0001) groups (**Figure 4.10**). There was however no difference in lifespan between those mice receiving miglustat alone and those receiving the combination treatment (p=0.3006).

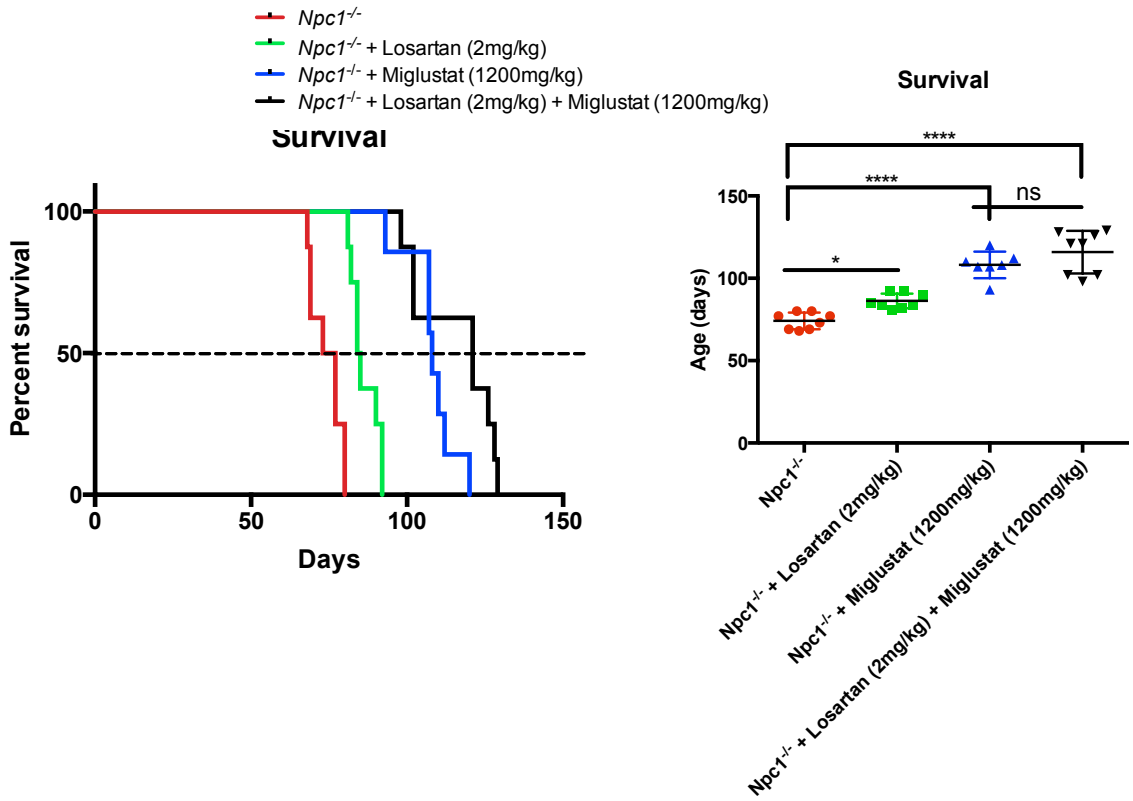

Figure 4.10. *Kaplan-Meier survival curve for losartan (2mg/kg) diet, miglustat (1200mg/kg) and combination losartan/miglustat treated mice, all treatments starting at 3 weeks of age.* Losartan treated mice lived significantly longer than untreated *Npc1*$^{-/-}$ mice, as did both miglustat treated mice and the combination treated mice. No difference in survival in the miglustat and combination treatment mice. Average survival for *Npc1*$^{-/-}$: 75 days, *Npc1*$^{-/-}$ + losartan: 84.5 days, *Npc1*$^{-/-}$ + miglustat: 108 days, *Npc1*$^{-/-}$ + losartan + miglustat: 121. *p<0.05; ***p<0.001; ****p<0.0001; one-way ANOVA

Extensive behavioural analysis was performed to measure motor function (rearing activity), tremor amplitude and activity. An increased ability to rear demonstrates enhanced hind leg strength and balance. A significant increase in rearing activity was observed in the miglustat and losartan/miglustat treated mice at both 7 and 10 weeks of age as compared to the untreated *Npc1*$^{-/-}$ mice. (**Figure 4.11**; 7wk *Npc1*$^{-/-}$ vs. 7wk *Npc1*$^{-/-}$ + miglustat p=0.0017, 7wk *Npc1*$^{-/-}$ vs. 7wk *Npc1*$^{-/-}$ + losartan p=0.847, 7wk *Npc1*$^{-/-}$ vs. 7wk *Npc1*$^{-/-}$ + losartan + miglustat p=0.0010, 7wk *Npc1*$^{-/-}$ + miglustat vs. 7wk *Npc1*$^{-/-}$ + losartan + miglustat p=0.9729, 10wk *Npc1*$^{-/-}$ vs. 10wk *Npc1*$^{-/-}$ + miglustat p<0.0001, 10wk *Npc1*$^{-/-}$ vs. 10wk *Npc1*$^{-/-}$ + losartan p=0.9972, 10wk *Npc1*$^{-/-}$ vs. 10wk *Npc1*$^{-/-}$ + losartan + miglustat p<0.0001; 10wk *Npc1*$^{-/-}$ + miglustat vs. 10wk *Npc1*$^{-/-}$ + losartan + miglustat p=0.1687).

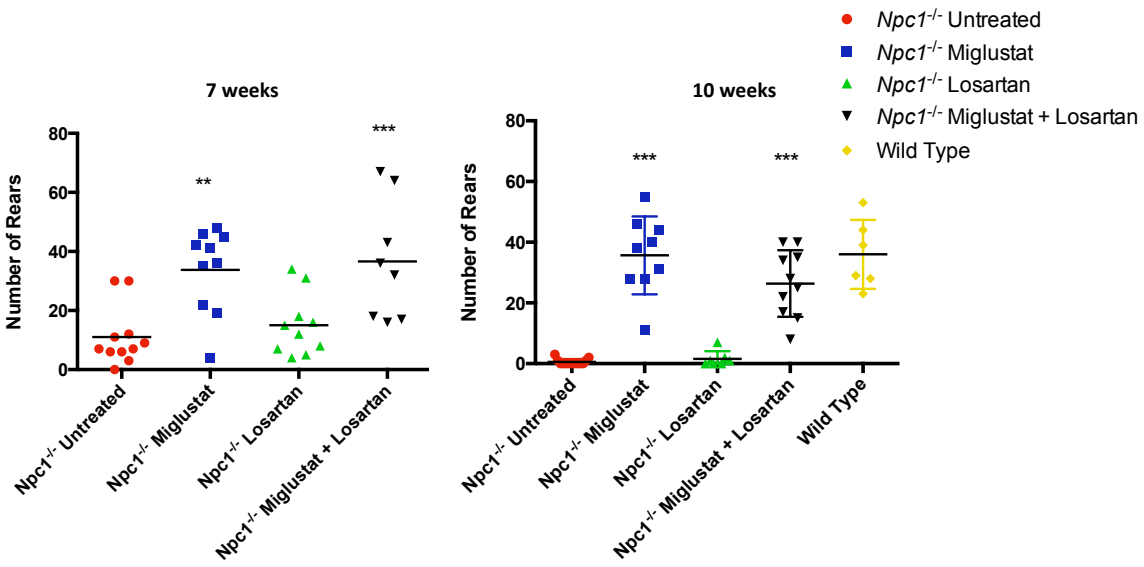

Figure 4.11. *Rearing data for Npc1*$^{-/-}$*, losartan (2mg/kg), and NB-DGJ (1200mg/kg) treated Npc1*$^{-/-}$ *and WT mice*. **A)** At 7 weeks there was a significant increase in rearing ability in the miglustat and the losartan/miglustat combination treated mice as compared to untreated *Npc1*$^{-/-}$. **B)** At 10 weeks there continued to be a significant increase in the miglustat and the losartan/miglustat combination treated mice as compared to untreated *Npc1*$^{-/-}$. Wild type 10week data included for comparison. ****p<0.0001, **p<0.01; one-way ANOVA

At 10 weeks of age there was a significant high frequency tremor reduction in all the treatment groups (**Figure 4.12A**; *Npc1*$^{-/-}$ vs. *Npc1*$^{-/-}$ + miglustat $p<0.0001$, *Npc1*$^{-/-}$ vs. *Npc1*$^{-/-}$ + losartan $p<0.0001$, *Npc1*$^{-/-}$ vs. *Npc1*$^{-/-}$ + losartan + miglustat $p<0.0001$, *Npc1*$^{-/-}$ + miglustat vs. *Npc1*$^{-/-}$ + losartan + miglustat $p>0.9999$). This trend continued, and at 12 weeks of age all treated mice continued to have significantly reduced high frequency tremors as compared to the untreated 10 week *Npc1*$^{-/-}$ mice (**Figure 4.12B;** *Npc1*$^{-/-}$ vs. *Npc1*$^{-/-}$ + miglustat $p<0.0001$, *Npc1*$^{-/-}$ vs. *Npc1*$^{-/-}$ + losartan $p=0.0034$, *Npc1*$^{-/-}$ vs. *Npc1*$^{-/-}$ + losartan + miglustat $p<0.0001$). There was no significant difference between any of the treatment groups suggesting superiority of any one drug (*Npc1*$^{-/-}$ + miglustat vs. *Npc1*$^{-/-}$ + losartan $p=0.8712$, *Npc1*$^{-/-}$ + miglustat vs. *Npc1*$^{-/-}$ + losartan + miglustat $p=0.9142$, *Npc1*$^{-/-}$ + losartan vs. *Npc1*$^{-/-}$ + losartan + miglustat $p=0.1838$). At 16 weeks, all the untreated and losartan treatment alone mice had reached humane end point, however the miglustat and the losartan/miglustat treated mice continued to have a reduced tremor that was not significantly different from a wild type mouse at this age (**Figure 4.12C;** Wild type vs. *Npc1*$^{-/-}$ + miglustat $p=0.9841$, Wild type vs. *Npc1*$^{-/-}$ + losartan + miglustat $p=0.2308$, *Npc1*$^{-/-}$ + miglustat vs. *Npc1*$^{-/-}$ + losartan + miglustat $p>0.9999$).

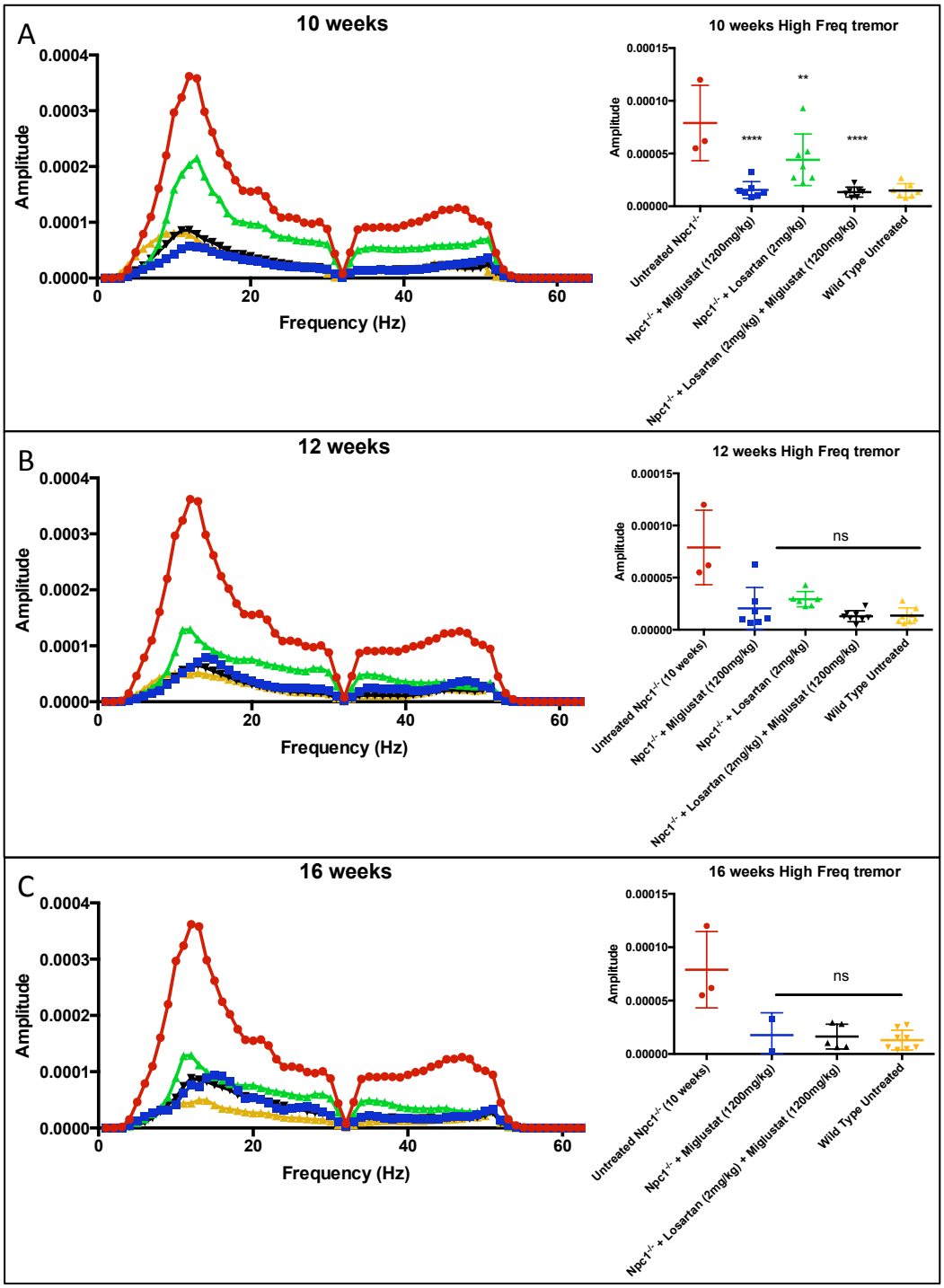

Figure 4.12. *Tremor data for Npc1$^{-/-}$, losartan (2mg/kg), and miglustat (1200mg/kg) treated* Npc1$^{-/-}$ *and wild type mice.* **A)** At 10 weeks there was a significant reduction in high frequency tremor in all the treatment groups as compared to the *Npc1$^{-/-}$* mice. **B)** At 12 weeks there continued to be a significant reduction in high frequency tremor for all the treatment groups, and there was no significant difference between any of the groups and the wild type controls. **C)** At 16 weeks both miglustat and losartan/miglustat treatment groups do not have a significantly different tremor from the wild type controls. Untreated *Npc1$^{-/-}$* 10wk mice included in 12 and 16 week charts for comparison. Average high frequency tremor was calculated by taking the average tremor from 32 to 55 seconds. ****p<0.0001, **p<0.01; one-way ANOVA

Many neurological diseases also present with movement deficits and locomotion problems, and these gait disturbances can be observed and quantified (176) using an automated gait analysis system (CatWalk). The parameters examined were front and hind stand mean, front and hind step and duty cycle, step sequence (AB)%, cadence, and support diagonal (%) as a progressive decline in these parameters in the untreated *Npc1*$^{-/-}$ mouse has been characterized. For full definition of CatWalk gait parameters analysed see **Appendix Table 5** (175).

Gait and coordination analysis showed that at 11 weeks of age significant improvements could be observed amongst the miglustat and losartan/miglustat treated mice, although no improvement was observed with losartan treatment alone. *Npc1*$^{-/-}$ mice treated with miglustat alone and the losartan/miglustat combination had a significantly shorter front step cycle, indicative of a healthy mouse, compared to the untreated mice (**Figure 4.13B**; *Npc1*$^{-/-}$ vs. *Npc1*$^{-/-}$ + miglustat p=0.0239, *Npc1*$^{-/-}$ vs. *Npc1*$^{-/-}$ + losartan p=0.9113, *Npc1*$^{-/-}$ vs. *Npc1*$^{-/-}$ + losartan + miglustat p=0.0187). The losartan/miglustat combination treatment had a significantly longer front duty cycle, indicative of a healthy mouse, compared to the untreated mice (**Figure 4.13F**; *Npc1*$^{-/-}$ vs. *Npc1*$^{-/-}$ + miglustat p=0.1658, untreated *Npc1*$^{-/-}$ vs. *Npc1*$^{-/-}$ + losartan p=0.3736, *Npc1*$^{-/-}$ vs. *Npc1*$^{-/-}$ + losartan + miglustat p=0.0202). Additionally, both miglustat and losartan/miglustat combination treatment groups spent a significantly larger percentage of time walking in AB step sequence as compared to the untreated mice (**Figure 4.13D**; *Npc1*$^{-/-}$ vs. *Npc1*$^{-/-}$ + miglustat p=0.0100, *Npc1*$^{-/-}$ vs. *Npc1*$^{-/-}$ + losartan p=0.5292, *Npc1*$^{-/-}$ vs. *Npc1*$^{-/-}$ + losartan +

miglustat p=0.0308). However, these were the only gait parameters where we observed any significant improvements.

At this age both the miglustat and losartan/miglustat treatment groups have a relatively healthy gait as demonstrated by the inclusion of a healthy wild type mouse for comparison (**Figure 4.13**).

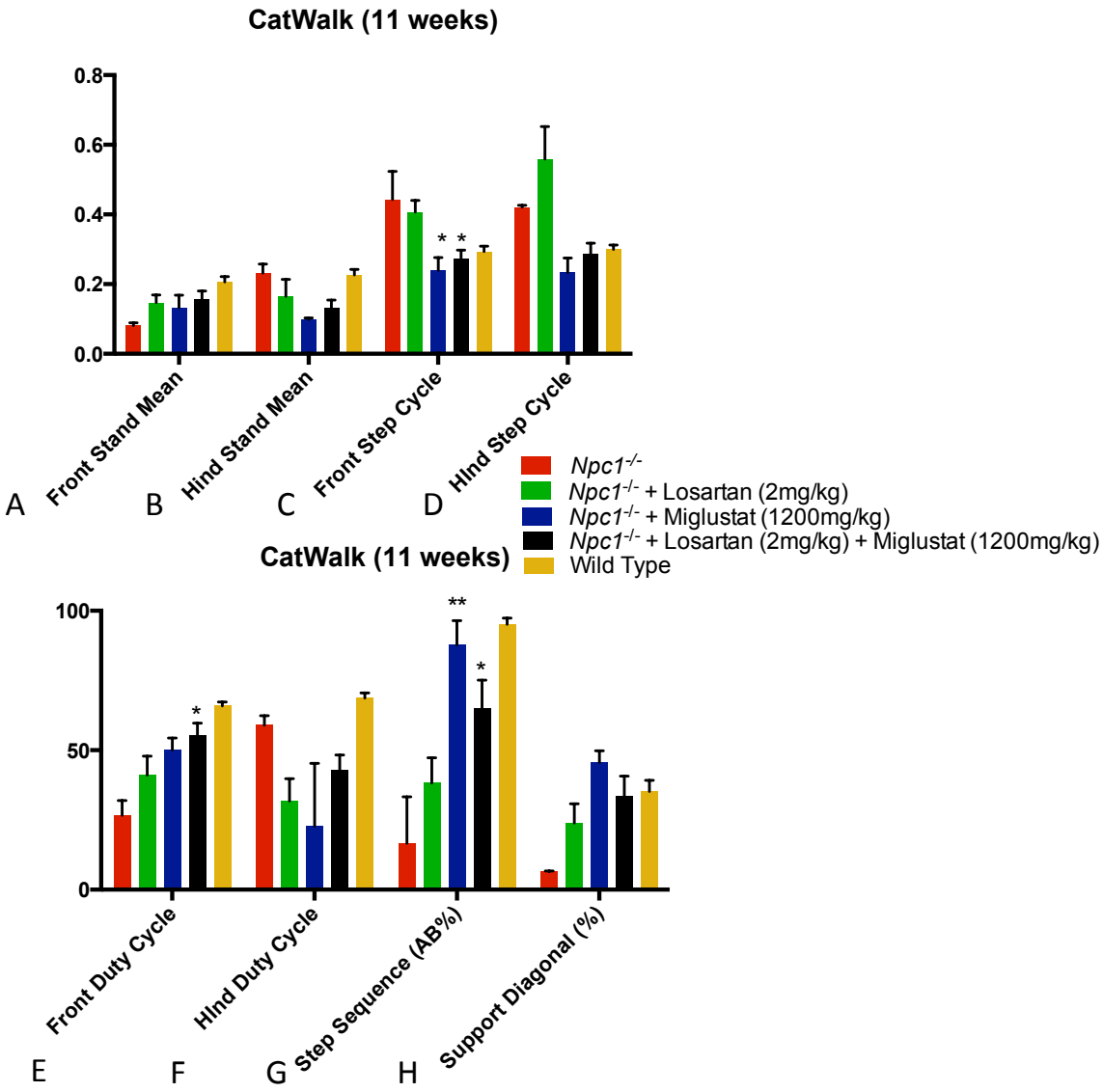

Figure 4.13. *Gait analysis (CatWalk) for Npc1$^{-/-}$, losartan (2mg/kg), and miglustat (1200mg/kg) treated Npc1$^{-/-}$ and WT mice at 11 weeks.* **A)** No significant difference was observed in any of the treatment groups for front stand or **B)** for hind stand mean times. **C)** There was significantly reduced length of time (s) in each front step walking cycle in the miglustat and the losartan/miglustat treated mice as compared to the untreated *Npc1*$^{-/-}$. **D)** There was no significant differences in any of the hind step cycle times for any of the treated groups. **E)** The losartan/miglustat combination treatment were the only treatment group that had significantly longer front duty cycle compared to the untreated *Npc1*$^{-/-}$. **F)** No significant differences were observed in the hind duty cycles. **G)** There was a significant increase in miglustat and losartan/miglustat treated mice walking in AB step sequence similar to that observed in wild type, healthy mice. **H)** At 11 weeks of age, there was no significant difference in percentage of time walking support diagonal between the treatment groups although there may have been a trend towards a higher percentage. Wild type mice are included for comparison. *p<0.05, **p<0.01 as compared to untreated *Npc1*$^{-/-}$ calculated by a one-way ANOVA

An additional cohort of losartan, miglustat, and losartan/miglustat treated mice were sacrificed at 10 weeks for biochemical analysis of tissues. Miglustat and losartan/miglustat treatment was associated with significantly reduced (60-70%) total GSL levels in the liver, and there was no significant difference in the losartan treated livers (**Figure 4.14A**; *Npc1*$^{-/-}$ vs. *Npc1*$^{-/-}$ + miglustat p=0.0004, *Npc1*$^{-/-}$ vs. *Npc1*$^{-/-}$ + losartan p=0.342, *Npc1*$^{-/-}$ vs. *Npc1*$^{-/-}$ + losartan + miglustat p=0.0006). There where no significant differences in the total level of GSLs between the miglustat treatment alone and the losartan/miglustat combination (p=0.9916). For the most abundant liver GSL species, GM2-Gc and GA2, there was no difference between the miglustat and the losartan/miglustat treatments, and both were significantly reduced (50-70%) as compared to the untreated *Npc1*$^{-/-}$ liver. (**Figure 4.14B,C**; *Npc1*$^{-/-}$ + miglustat GM2-Gc vs. *Npc1*$^{-/-}$ + losartan + miglustat GM2-Gc p=0.6600*; Npc1*$^{-/-}$ + miglustat GA2 vs. *Npc1*$^{-/-}$ + losartan + miglustat GA2 p>0.9999).

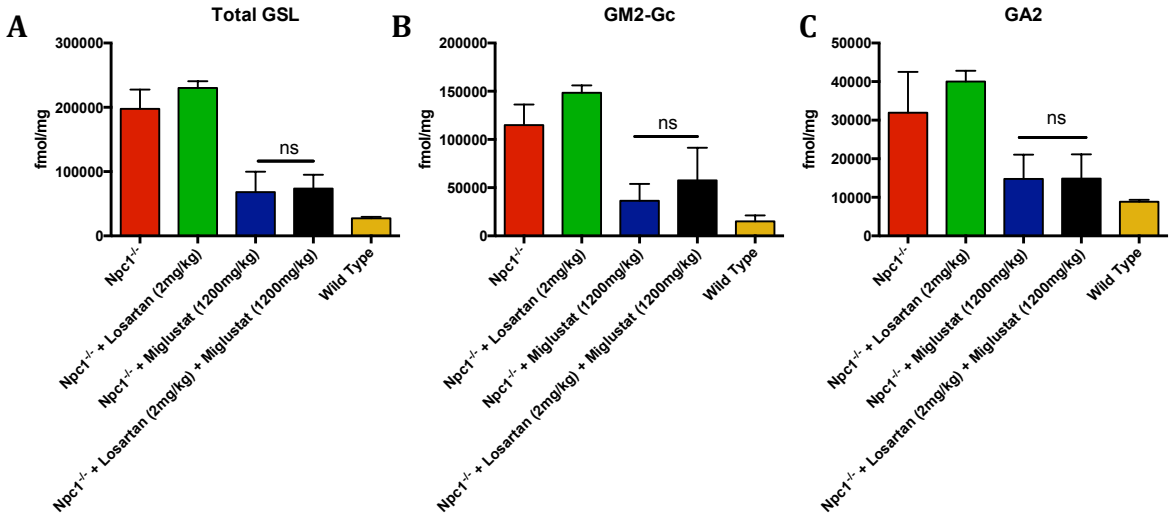

Figure 4.14. *GSL levels in untreated, losartan, miglustat, and losartan/miglustat treated Npc1$^{-/-}$ and wild type livers.* **A)** Total GSLs (excluding Lac-Ceramide) were measured and there was no significant difference in liver GSL levels in the losartan and miglustat treated as compared to the wild-type mice. Both the miglustat and the losartan/miglustat treated *Npc1*$^{-/-}$ mice had significantly reduced total levels at 10 weeks compared to UT; however, there was no difference between these two treatments. **B)** The two most abundant liver GSL species are GM2-Gc and **C)** GA2. There was no significant difference in the levels of Gm2-Gc between the miglustat treatment group and the losartan/miglustat combination group. There was also no significant difference in GA2 levels between those two treatment groups. Peaks were identified by determining their glucose units using a 2-AA labeled glucose oligomer ladder standard; one-way ANOVA

Additionally, neither losartan nor miglustat treatment had any effect on the levels of free cholesterol in the liver of the *Npc1*$^{-/-}$ mice (**Figure 4.15;** *Npc1*$^{-/-}$ vs. *Npc1*$^{-/-}$ + miglustat p=0.6721, *Npc1*$^{-/-}$ vs. *Npc1*$^{-/-}$ + losartan p=0.2868, *Npc1*$^{-/-}$ vs. *Npc1*$^{-/-}$ + losartan + miglustat p=0.6280)

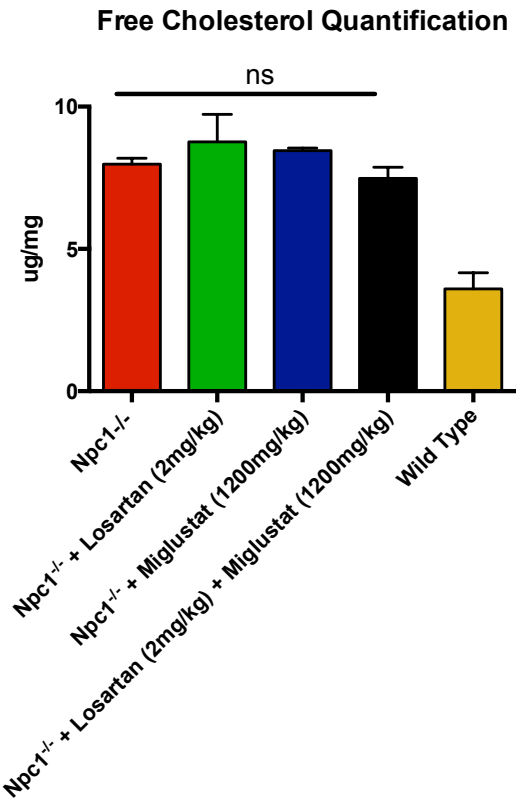

Figure 4.15. *Free cholesterol levels in untreated, losartan, miglustat, and losartan/miglustat treated Npc1*$^{-/-}$ *and wild type livers*. No significant differences were observed between any of the treatment groups and the untreated *Npc1*$^{-/-}$ livers; one-way ANOVA

By 10 weeks the *Npc1*$^{-/-}$ mouse has undergone significant neurodegeneration, and we examined the cerebellum of the losartan and miglustat treated mice to see if these drugs offered any level of neuroprotection. Miglustat has been previously been demonstrated to have a neuroprotective effect (177), and significantly protected the early degenerating lobules 1-4 (p<0.0001). This protection was also observed in the early degenerating lobules of the losartan/miglustat combination treatment mice (p=0.065), but not to the extent observed in the miglustat treatment (**Figure 4.16A**; *Npc1*$^{-/-}$ + miglustat vs *Npc1*$^{-/-}$ + losartan/miglustat p<0.0001). No

significant increase in Purkinje cell survival was observed in the losartan treatment alone mice (p=0.9988).

Level of microglial infiltration is also high in the untreated *Npc1*$^{-/-}$ mouse at 10 weeks of age and we examined the level of microgliosis in lobule 7 as a readout for the overall inflammatory response (**Figure 4.16B**). As had also been previously demonstrated (177), levels of microglial infiltrations were significantly reduced with miglustat treatment (p<0.0001). There was no significant reduction in the losartan treatment groups level of microgliosis in lobule 7 (p=0.5227), however, there did appear to be an overall total reduction that my have not been reflected in our lobule 7 counts. Despite this, there was a significant reduction in the losartan/miglustat combination treatment mice as compared to miglustat treatment alone (p=0.0131). This suggests that the combination treatment may offer additional anti-inflammatory protection as compared to miglustat treatment alone. Representative cerebellum images for losartan, miglustat and the losartan/miglustat treatment in **Figure 4.17**.

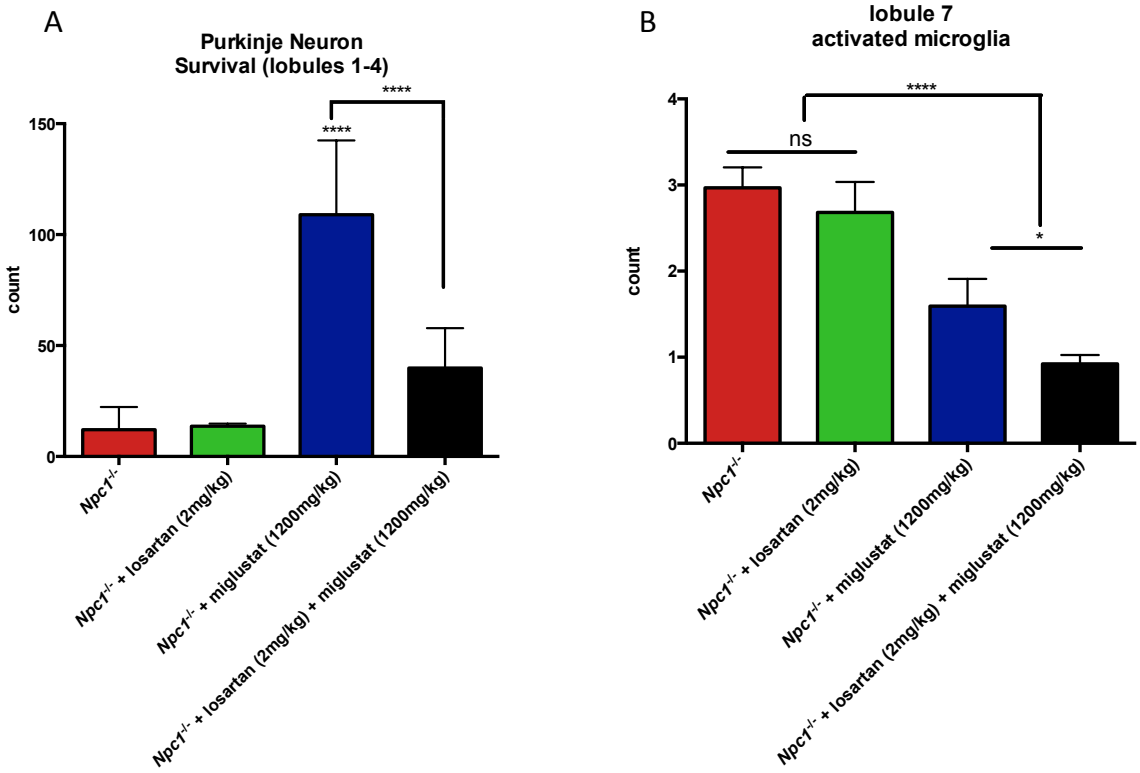

Figure 4.16. *Purkinje cell and microglial infiltration counts in the Npc1$^{-/-}$ treated cerebellum.* A) Purkinje neuron counts were performed on lobules 1-4, which are early degenerating lobules. B) Microglial counts were taken of lobule 7. **p*<0.05, ***p*<0.01, *****p*<0.0001; one-way ANOVA.

Figure 4.17. *Representative cerebellum images for Npc1$^{-/-}$, Npc1$^{-/-}$ + losartan, Npc1$^{-/-}$ + miglustat and Npc1$^{-/-}$ + losartan + miglustat treated mice.* Sections stained for calbindin (Purkinje cells, red) and CD68 (microglia, green). Lobules 1-10 indicated on the untreated *Npc1$^{-/-}$* , and arrows as to indicate lobule 7 from which microlglial counts were performed.

Summary of miglustat and losartan treatments in **Table 4.2**.

Parameter compared to *Npc1*$^{-/-}$	losartan	miglustat	Losartan + miglustat
Survival	+	+	+
High frequency tremor	=	+	+
Mobility / Activity	=	+	+
Gait / Motor Coordination	=	+	+
GSL storage	=	+	+
Cholesterol storage	=	+	+
Purkinje neuron counts (Early degenerating lobules)	=	+	=
Reduction in activated microglia	=	+	++

Table 4.2. *Comparative table of treatment groups compared to untreated Npc1*$^{-/-}$ *mice in terms of the different behavioral and biochemical parameters measured.* Losartan (2mg/kg) treatment starting at 3 weeks of age provided no survival or behavioral benefits. Miglustat diet (1200mg/kg) starting at 3 weeks of age resulted in a significant increase in survival, reduction of high frequency tremor, and improved gait and coordination. Combination treatment of losartan (2mg/kg) and miglustat (1200mg/kg) resulted in increased mean survival compared to miglustat treatment alone (121 days vs. 108) although not significantly. Combination treated mice also had significantly reduced high frequency tremor, increased activity, and increased gait and coordination. Both miglustat and losartan/miglustat treatments significantly reduced GSL and cholesterol storage.

4.4 Discussion

The relationship between the ABCA1 and NPC1 protein was recently brought to our attention through the misdiagnosis of a Tangier patient who was erroneously diagnosed initially with NPC (147), and made a very significant recovery following miglustat treatment as was discussed in **Chapter 3**. While much research is currently on going in identifying the direct/indirect mechanism for interaction between ABCA1 and NPC1, we also looked at these two proteins in terms of their potential as points of therapeutic intervention in NPC. Using the drug losartan to enhance ABCA1 expression, we treated NPC patient fibroblasts with losartan alone and in combination with the current EU-approved NPC treatment, miglustat. We have not, however, quantified the increase ABCA1 expression following losartan treatment and functional assays would be required to confirm this.

Interestingly, the two drugs did not appear to work synergistically in the NPC patient fibroblasts, despite being involved in different processes. As there were no additional benefits seen with the combination treatments in any of the cellular or biochemical parameters compared to the individual treatments alone. However, as neither treatment alone ameliorated all phenotypes we moved the individual drugs, as well as the combination treatment, to be trialled in the *Npc1*$^{-/-}$ mouse to see if we could observe more synergistic effects in the intact organism.

In the mouse model we found some tolerability issues due to losartan being metabolized in the liver by the cytochrome P450 system, but a reduced dose and a change of administration from the water to the diet helped these initial problems.

While losartan had significant benefits at the cellular level, it was not as effective in the mouse model alone as compared to the current treatment miglustat. This is most likely due to the plasma level in the mice being much lower than the 100μM losartan cellular treatment we did *in vitro*. Characterizing lower dose losartan treatments may be a more accurate reflection of the *in vivo* results we observed. The combination of the two drugs did suggest an increase in lifespan (losartan/miglustat 121 vs. miglustat 108 days, p=0.3006; **Figure 4.10**), however no dramatic functional improvement was observed in the combination treatment (**Table 4.2**).

We hypothesized that reduction in activated microglial infiltration in the losartan/miglustat treated *Npc1*$^{-/-}$ mice may be due not to the enhancement of cholesterol efflux via ABCA1, but rather through its repression of Ang II induced inflammatory signal cascade (**Figure 4.16**) (178). Also, as both cytoskeletal defects and mitochondrial dysfunction were identified in NPC disease through the *S. cerevisiae* screen (**Chapter 2)**, it is possible that losartan may be influencing these through its action as an Ang II receptor blocker as well.

Ang II can modulate the cytoskeletal composition and organization by inducing integrin and focal adhesion changes (178). As we observed partial rescue to the

cytoskeletal defects in the losartan treated NPC1$^{-/-}$ fibroblasts (**Figure 4.7**), it suggests that losartan may be working in this way as well. Additionally, Ang II is a stimulant of mitochondrial oxidant production, and Ang II activity can lead to an increase in reactive oxygen species (ROS) in the cell. Previous work has already implicated increases in ROS in NPC (127), suggesting that a stimulation of Ang II production may be responsible. Furthermore, previous work found that losartan treatment improved both general mitochondrial function, as well as reduced mitochondrial H_2O_2 through its action on AT-1 (179). Mitochondrial dysfunction has been well characterized as one of the causative factors in neurodegenerative diseases and neuronal mitochondrial death is most likely caused by mitochondrion-mediated apoptosis triggered by elevated ROS (180).

Taken together this suggests that losartan may be modifying NPC both through enhancing cholesterol efflux via ABCA1, and also by repressing Ang II induced cytoskeletal and mitochondrial changes. Additionally, as losartan is a weak PPARγ activator, it may also be through this function that it can modulate mitochondrial function, thereby potentially enhancing a neuoroprotective effects in the *Npc1*$^{-/-}$ mouse model. However, further studies are required to understand the effect to which losartan is having in these different pathways.

Moreover, a multi-center clinical trial investigating the effects of losartan as a treatment for Alzheimer's disease is currently underway (181). This trial, called RADAR (Reducing pathology in Alzheimer's disease through Angiotensin targeting),

is recruiting patients across the UK and is measuring whether losartan reduces the rate of brain shrinkage, a symptom of AD (181). This is particularly interesting as AD has a well characterized mitochondrial defect and it has been suggested that this mitochondrial dysfunction acts as a trigger for it's disease pathogenesis (182).

While losartan has proved to be a promising compound for the treatment of NPC disease, and is currently being investigated for Alzheimer's, it does raise the question why favor losartan over the other ARBs on the market. Telmisartan, for instance, is one of the later developed ARBs with a well characterized safety profile (183) and of all the commercial ARBs has the longest half-life of about 24 hours and largest volume of distribution of 500L (184). In addition, Telmisartan is not P450 metabolized so there should be a reduced risk of toxicity in the case of NPC due to the reduced cyp enzyme activity (103). Telmisartan is, like losartan, also a PPARγ activator so should exhibit all the neuroprotective and mitochondrial modulation activity we expect with losartan treatments. It would be worth following up on these findings by examining the response of other ARBs, particularly telmisartan, as an NPC therapy as it may allow for a reduced dose and may be more effective in the clinic.

In summary:

- Losartan, an angiotensin receptor A-1 blocker, could serve as a novel disease modifier for NPC disease in combination with the current treatment, miglustat and merits further examination
- Losartan may be an effective therapy both through increasing ABCA1 expression and enhancing cholesterol efflux, but also possibly through its modulation of some of the mitochondrial and cytoskeletal defects observed in NPC. However further experimentation is required to fully understand how this class of drugs impact NPC

Chapter 5: Evaluation of the Cylclodextrin Analogue Crysmeb

5 Evaluation of the cyclodextrin analogue Crysmeb

5.1 Introduction

Cyclodextrins (CD) are a class of carbohydrate molecules with a hydrophilic exterior ring and a hydrophobic interior cavity mainly used as solubilizers for poorly water-soluble chemicals and drugs (185). The cyclic oligosaccharides are joined via α-1,4 glucosidic linkages and designated as α,β,γ-cyclodextrins according to the number of glucose units (186). β-cyclodextrins (βCD) are the most commonly employed of the cyclodextrin structures, but have a relatively low solubility due to their structure. However, substitution of multiple βCD hydroxyls on the rims of the moiety results in

an improved aqueous solubility – making HPβCD (2-hydroxypropyl-β-cyclodextrin) a more conducive formulation for cellular delivery (185).

While cyclodextrins were discovered over 120 years ago, and have been used since the 1980s in the pharmaceutical, household and food industries (187), it was recently found to be an effective treatment for the lysosomal storage disorder Niemann-Pick disease type C (188) (**Table 5.1**).

Cyclodextrin Application
Stabilization of light or oxygen sensitive compounds
Modification of the chemical reactivity of guest molecules
Fixation of volatile substances
Improve substance's solubility
Modify liquids to powders
Protect substances from degradation
Mask ill smell/tastes of substances
Mask pigment/color of substance
Remove cholesterol/free fatty acids from animal products
In clinical trials as a therapy for NPC disease
Potential therapy for atherosclerosis

Table 5.1. Applications for cyclodextrin compounds.

In 2001 it was demonstrated that in the mouse model HPβCD (500mg/kg) treatment from 3-weeks of age delayed the onset of neurological symptoms by 20% and that intrathecal delivery via minipump did not have any additional benefits to systemic delivery (188). They concluded that HPβCD was unlikely to be helpful in patients, however as it had some effects on somatic cholesterol further studies should be taken (188). In 2004, however, HPβCD was used again in the NPC1 mouse model, this time as a vehicle for the delivery of the neurosteroid allopregnanolone and it was found that

allopregnanolone/CD-vehicle therapy was a highly effective treatment for NPC (189). It was not until the allopregnanalone/CD-vehicle therapy was further examined that it was determined that the HPβCD vehicle alone was effective in extending the lifespans and delaying disease onset (160). Cyclodextrin therefore began to be further studied again in its own right as a potential therapy for NPC (160).

HPβCD is one of the many modified forms of β-cyclodextrins. β-CDs can be modified in different ways to functionalize the molecule, such as increasing the rate and selectivity of reactions, adding metal-binding groups, etc (190). A new β-CD derivative, Crysmeb [Roquette], is a second-generation product that is being marketed as a solubilizing aid for pharmaceutical formulations on the basis of having several advantages over HPβCD (191). Crysmeb is a more highly purified mixture of methyl β-cyclodextrins containing on average 4 methyl groups per native β-CD molecule with a higher aqueous solubility (**Figure 5.1**)(191).

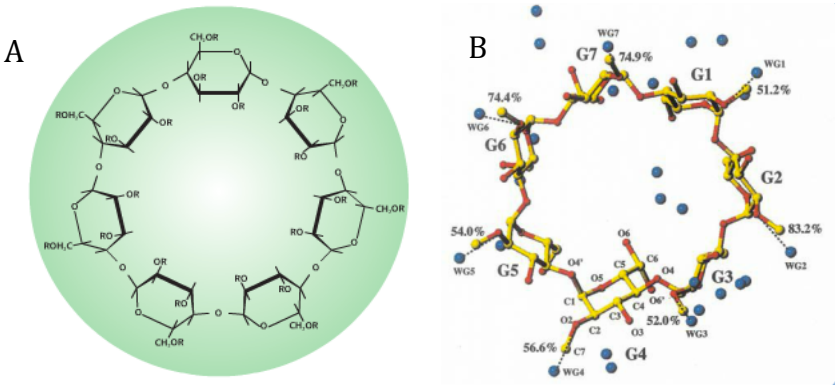

Figure 5.1 Structural view of (A) HPβCD and (B) Crysmeb cyclodextrin compounds from Roquette.

Crysmeb has already been implicated as therapy for advanced stages of atherosclerosis, as it was found that treatment reduced the inflammatory response as well as reduced the atherosclerotic plaque size in the mouse model (192), but has not previously been examined for the treatment of NPC.

Previous *in vitro* studies had suggested that low levels of HPβCD were able to cross the BBB and enter the CNS (193). However, subsequent studies have shown that the amount that crosses the BBB from plasma in mature mice is very small (92), leading to studies determining the efficacy of injecting HPβCD directly into the brain (90). As intrathecal or intracerebral administration requires lengthy hospital visits and a high potential for complications when performed in patients, here we have investigated alternative routes of drug delivery to the brain. Additionally, negative side effects including macrophage infiltration of the lungs and an irreversible hearing loss suggesting that potential toxic side effects needs to be addressed, especially in context of the clinical trials currently underway (**Introduction 1.2.7.2.1**)(160, 194, 195).

Intranasal (IN) delivery is a non-invasive and rapid mode of drug delivery that bypasses the BBB and directly targets the CNS (196). This mode of delivery may also reduce systematic exposure and side effects of the drug as levels of the drug delivered are lower (197). It is thought that IN administration of compounds bypasses the BBB through the olfactory and trigeminal neural pathways (**Figure 5.2**)(196). Both these neural pathways innervate the nasal cavity, and it is suggested

that it is through bulk flow and diffusion that these compounds enter the brain (196). Cyclodextrin can be used to enhance the absorption of compounds across the nasal mucus layer, so we hypothesized that Crysmeb may diffuse well through the nasal cavity and reach the CNS (198).

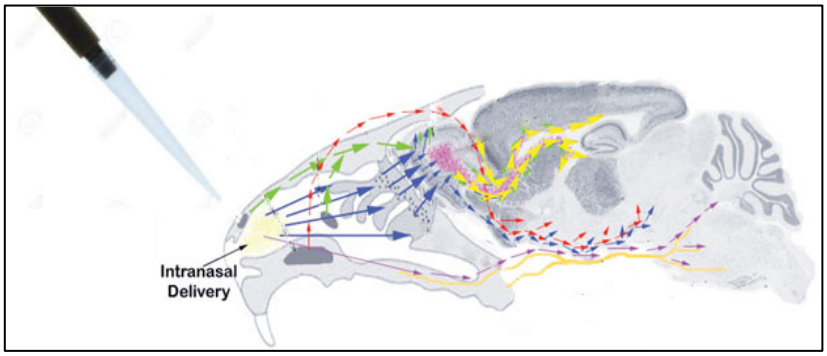

Figure 5.2. Major routes of drug entry following intranasal delivery in mice. Modified from Xiao et al (8).

The specific aims presented in this chapter are:

- To investigate whether Crysmeb acts as a more effective β-cyclodextrin compound for the treatment of Niemann-Pick disease type C as compared to HPβCD
- Investigate whether Crysmeb can be effectively delivered in a non-invasive way directly to the CNS through intranasal administration

5.2 Materials and Methods

5.2.1 Mice

As detailed in section 4.2.5.

5.2.2 Drug treatments

HPβCD (Roquette) and Crysmeb (Roquette) cyclodextrin compounds were kindly provided by Christoph Poincilit (NPSuisse, Switzerland). HPβCD (4000mg/kg), Crysmeb (4000mg/kg), and PBS (vehicle control) were administered weekly intraperitoneal (IP) from post natal day 7 (p7). To examine route of drug delivery, Crysmeb (100mg/kg; 200mg/kg) and PBS (vehicle control) were administered weekly intranasal (IN) from p7 as compared to Crysmeb (4000mg/kg; 100mg/kg; 200mg/kg) administered IP from p7 weekly.

5.2.2.1 Mode of Delivery

IP injection volumes were 20mL/kg and intranasal doses were 0.33mL/kg. For mice under 6 weeks of age, IN administration was done following isofluorane anaesthesia at minimum alveolar concentration of 2.5% and oxygen at 4 L/min. Following administration, mice were placed on heat pad until fully recovered. Once mice reached 6 weeks of age, intranasal administration was performed without

anaesthetic. Typical IN volume for a 6 week old mice was 6μL, typical IP volume for a 6 week old mice was 360μL.

5.2.3 Mouse behavioural analysis

5.2.3.1 Determination of humane end-point

As detailed in section 4.2.7.1

5.2.3.2 Measuring activity

As detailed in section 4.2.7.2

5.2.3.3 Measuring tremor

As detailed in section 4.2.7.3

5.2.3.4 Gait analysis

As detailed in section 4.2.7.4

5.2.4 Glycosphingolipid measurement

As detailed for cellular homogenates in section 3.2.8, and for tissues in section 4.2.8

5.2.5 Cholesterol measurement

As detailed in section 3.2.13

5.2.6 Sphingoid base quantification

As detailed in section 3.2.9

5.3 Results

5.3.1 Crysmeb as a Novel Cyclodextrin for Treatments of NPC

Cyclodextrin compounds as NPC therapeutics are most commonly administered to animal models (feline and murine) IP at a dose of 4000mg/kg (20% cyclodextrin). Crysmeb and HPβCD were both administered at this dose weekly from p7. Crysmeb significantly extended the life span of the *Npc1*$^{-/-}$ mouse as compared to HPβCD treatment (p<0.0001) (**Figure 5.3**).

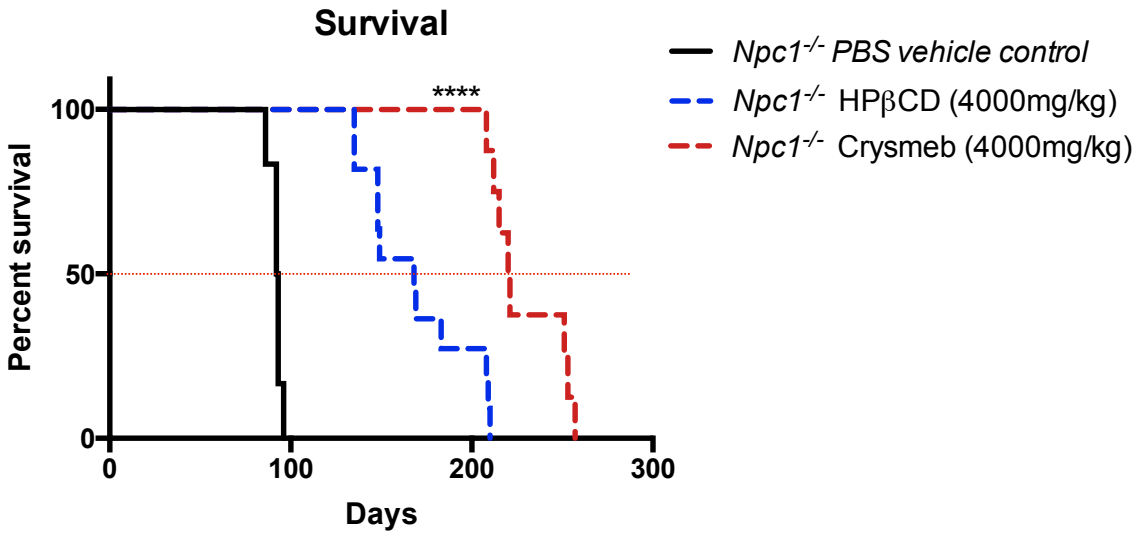

Figure 5.3. *Kaplan-Meier survival curve for HPβCD (4000mg/kg) and Crysmeb (4000mg/kg) IP treated mice.* Both treatments significantly improved survival compared to PBS vehicle control *Npc1*$^{-/-}$ mice. Additionally, Crysmeb treated mice lived significantly longer than HPβCD treated mice. Average survival (days) for PBS vehicle control: 92.5, HPβCD: 168, Crysmeb: 220.5. ****p<0.0001; one-way ANOVA.

Additionally, Crysmeb treated mice reached and maintained a consistently higher body weight throughout their life spans as compared to the HPβCD treated mice (**Figure 5.4**).

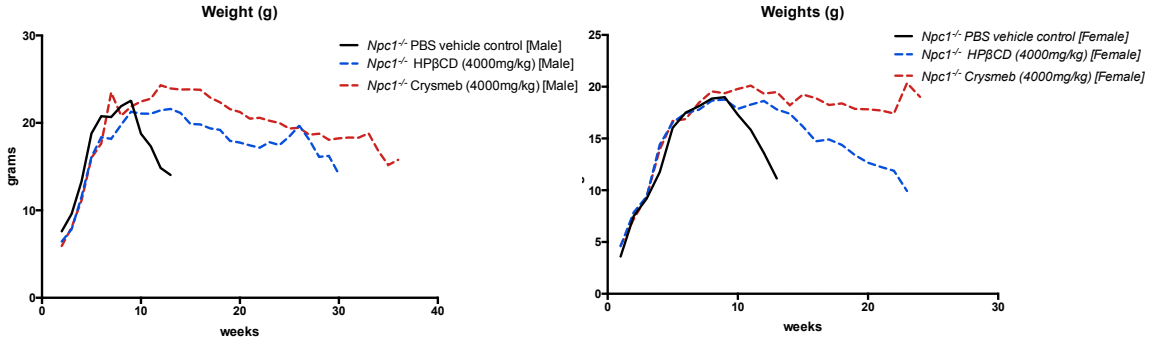

Figure 5.4. *Average weights curve for HPβCD and Crysmeb treated male and female mice.* Mice treated with HPβCD and Crysmeb maintained body weight more similar to that observed in a wild type mouse, and this weight was maintained for longer in the Crysmeb treatment group.

Extensive behavioural analysis was performed to measure motor function through rearing activity, tremor amplitude and activity logs. An increased ability to rear demonstrates enhanced hind limb strength and balance. No significant differences in rearing activity was initially observed between the HPβCD and Crysmeb treated mice until the mice reached 16 weeks of age, where it was found that Crysmeb treated mice reared significantly more than HPβCD treated mice (p=0.0399) (**Figure 5.5**).

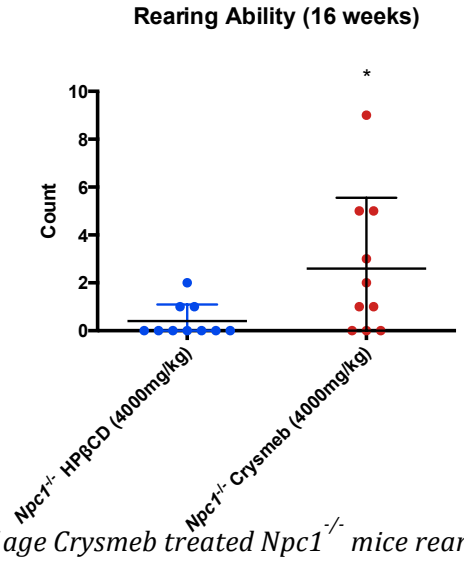

Figure 5.5. *At 16 weeks of age Crysmeb treated Npc1$^{-/-}$ mice reared significantly more than HPβCD treated mice.* This was the earliest time points significant differences in behaviour could be detected between the two treatment groups. *p=0.0399, Mann Whitney test as non-gaussian distribution.

Tremor is a disease phenotype observed in the *Npc1*$^{-/-}$ mouse model from about 7 weeks of age and can function as a read out for disease progression and evaluation of therapies (199). A significant reduction in high frequency tremor amplitude was observed in both HPβCD and Crysmeb treated mice at 12 weeks of age as compared to the untreated *Npc1*$^{-/-}$ mice (**Figure 5.6A**; *Npc1*$^{-/-}$ vs *Npc1*$^{-/-}$ Crysmeb p=0.0053; *Npc1*$^{-/-}$ vs *Npc1*$^{-/-}$ HPβCD p=0.0078) and no significant differences between treatment groups was observed throughout the lifespans of treated mice (**Figure 5.6A-C**; 12 weeks: *Npc1*$^{-/-}$ Crysmeb vs *Npc1*$^{-/-}$ HPβCD p=0.9390; 18weeks: *Npc1*$^{-/-}$ Crysmeb vs *Npc1*$^{-/-}$ HPβCD p=0.7664; 22 weeks: *Npc1*$^{-/-}$ Crysmeb vs *Npc1*$^{-/-}$ HPβCD p=0.9995). However, the data suggests a trend towards a reduced tremor in the Crysmeb treated mice relative to HPβCD at 25 weeks, although this reduction was not significant (**Figure 5.6D**; p=0.067).

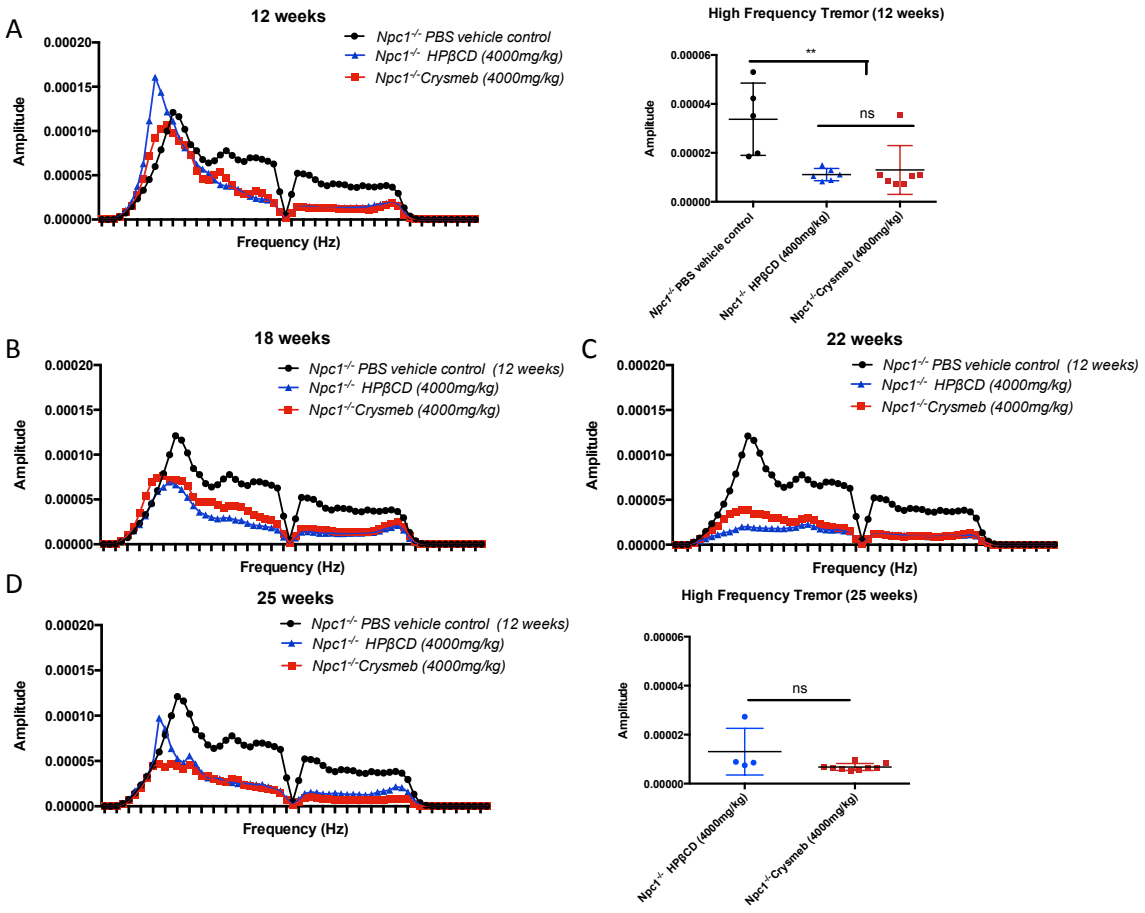

Figure 5.6. *Tremor data for PBS vehicle control Npc1*$^{-/-}$*, HPβCD (4000mg/kg), and Crysmeb (4000mg/kg) treated Npc1*$^{-/-}$ *mice.* **A)** At 12 weeks there was a significant reduction in high frequency tremor in the treated *Npc1*$^{-/-}$ mice compared to the PBS vehicle control treated *Npc1*$^{-/-}$ mice. **B)** From 18 weeks to **C)** 22 weeks there was no significant difference in tremor in the Crysmeb and HP*β*CD treated *Npc1*$^{-/-}$ mice. **D)** At 25 weeks of age, a higher but not significantly elevated tremor is observed in the HP*β*CD treated mice as compared to the Crysmeb treated mice. Average high frequency tremor was calculated by taking the average tremor from 32 to 53. PBS vehicle control *Npc1*$^{-/-}$ mice at 12 weeks included for comparison. ***p<0.001; one-way ANOVA

Additionally, there was no significant difference in the activity of the Crysmeb and HPβCD treated mice as they aged (**Figure 5.7;** 13 weeks: *Npc1*$^{-/-}$ Crysmeb vs *Npc1*$^{-/-}$ HPβCD p=0.2291; 15weeks: *Npc1*$^{-/-}$ Crysmeb vs *Npc1*$^{-/-}$ HPβCD p=0.9998; 18 weeks: *Npc1*$^{-/-}$ Crysmeb vs *Npc1*$^{-/-}$ HPβCD p=0.7356; 22 weeks: *Npc1*$^{-/-}$ Crysmeb vs *Npc1*$^{-/-}$

HPβCD p=0.8146; 26 weeks: *Npc1*$^{-/-}$ Crysmeb vs *Npc1*$^{-/-}$ HPβCD p=0.3632; 29 weeks: *Npc1*$^{-/-}$ Crysmeb vs *Npc1*$^{-/-}$ HPβCD p=0.8200).

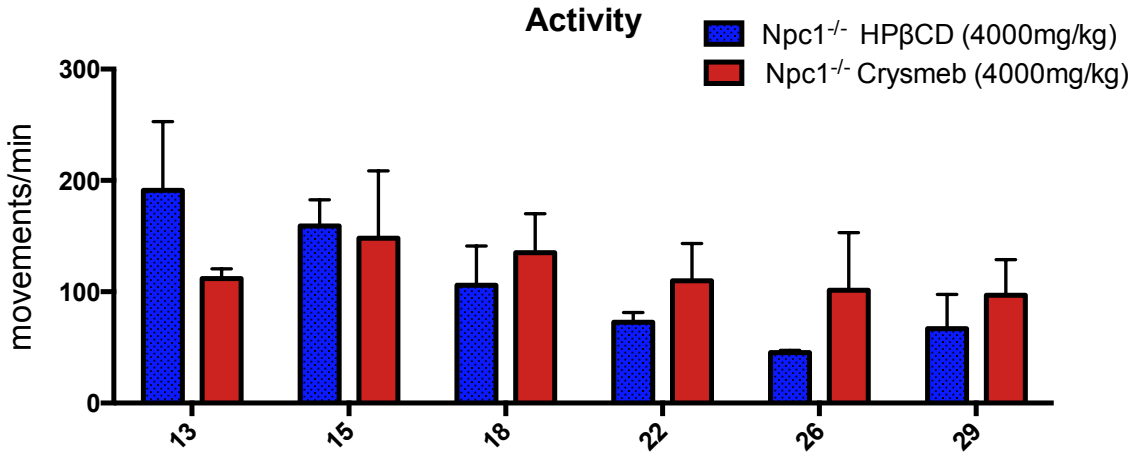

Figure 5.7. *Activity data for PBS vehicle control Npc1*$^{-/-}$*, HPβCD (4000mg/kg), and Crysmeb (4000mg/kg) treated Npc1*$^{-/-}$ *mice.* No significant difference was observed at any time point between the Crysmeb and the HPβCD treated mice; one-way ANOVA.

There were also no significant differences between the gait of HPβCD and Crysmeb treated mice at 16 weeks of age, by which point the untreated mice had all reached humane end point (**Figure 5.8**). Of the gate parameters measured (See **Appendix Table 5** for full description), none were significantly different between the treatment groups. A 12 week *Npc1*$^{-/-}$ mouse is included for comparison (**Figure 5.8**; Front Stand Mean: *Npc1*$^{-/-}$ Crysmeb vs *Npc1*$^{-/-}$ HPβCD p=0.1686; Hind Stand Mean: *Npc1*$^{-/-}$ Crysmeb vs *Npc1*$^{-/-}$ HPβCD p=0.0655; Front Step Cycle: *Npc1*$^{-/-}$ Crysmeb vs *Npc1*$^{-/-}$ HPβCD p=0.1859; *Npc1*$^{-/-}$ Crysmeb vs *Npc1*$^{-/-}$ HPβCD p=0.0448; Front Duty Cycle: *Npc1*$^{-/-}$ Crysmeb vs *Npc1*$^{-/-}$ HPβCD p=0.881; Hind Duty Cycle: *Npc1*$^{-/-}$ Crysmeb vs *Npc1*$^{-/-}$ HPβCD p=0.5292; Step sequence AB *Npc1*$^{-/-}$ Crysmeb vs *Npc1*$^{-/-}$ HPβCD p=0.2633; Support Diagonal *Npc1*$^{-/-}$ Crysmeb vs *Npc1*$^{-/-}$ HPβCD p=0.8524).

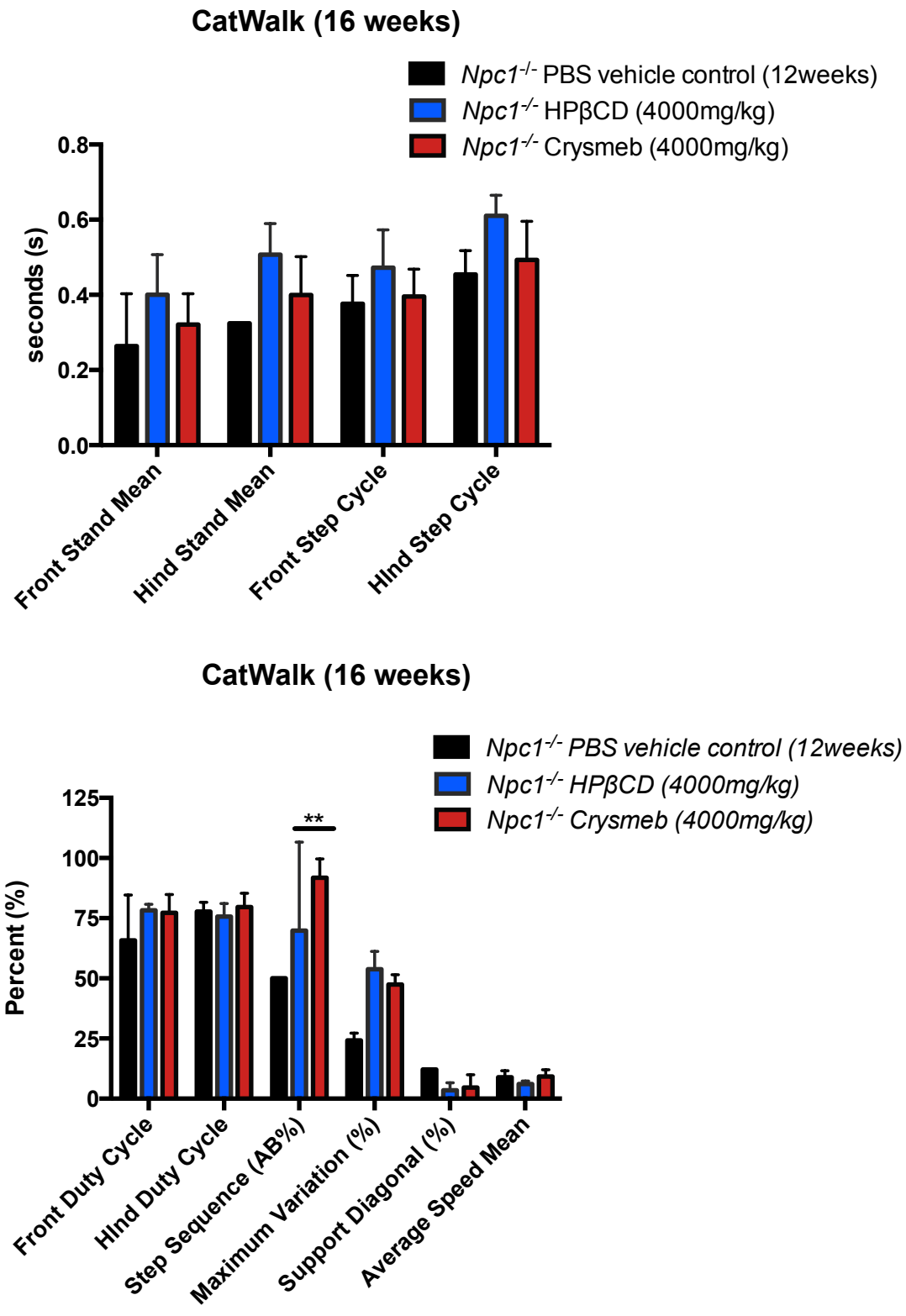

Figure 5.8. *Gait analysis (Catwalk) for representative 12 week Npc1$^{-/-}$ mice, and 16 week Crysmeb (4000mg/kg) and HPβCD (4000mg/kg) treated mice.* At 16 weeks of age there were no significant differences in gait between either the Crysmeb or HPβCD treatment groups. **p<0.01; student t-test.

An additional cohort of Crysmeb and HPβCD treated mice were taken for tissues at 18 weeks and for comparison 10wk vehicle treated *Npc1*$^{-/-}$ and wild type mice were included. Crysmeb and HPβCD treatment significantly reduced cholesterol levels in liver as compared to the 10week vehicle control *Npc1*$^{-/-}$ (*Npc1*$^{-/-}$ vs *Npc1*$^{-/-}$ Crysmeb p=0.0095; *Npc1*$^{-/-}$ vs *Npc1*$^{-/-}$ HPβCD p=0.0118), however, no significant differences between the treatments were observed (p=0.9088; **Figure 5.9**). Furthermore, both Crysmeb and HPβCD treated *Npc1*$^{-/-}$ mice livers had cholesterol levels not significantly different to that found in wild type mice (Wild type vs *Npc1*$^{-/-}$ Crysmeb p=0.8386; Wild type vs *Npc1*$^{-/-}$ HPβCD p=0.7334).

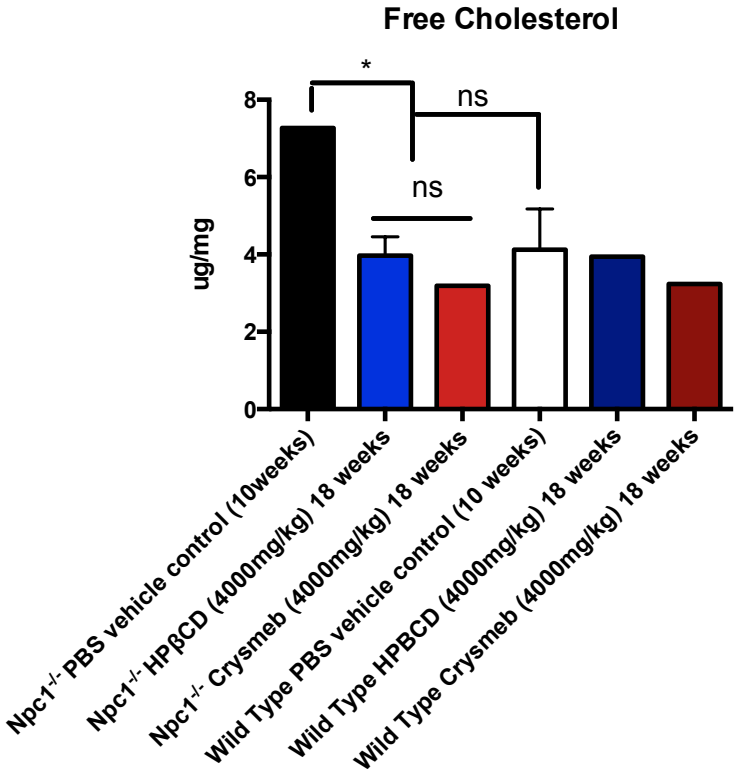

Figure 5.9. *Cholesterol levels in PBS vehicle (n=3), Crysmeb (n=7) and HPβCD (n=7) treated Npc1*$^{-/-}$ *and wild type livers.* There was no significant difference in liver cholesterol levels in the Crysmeb and HPβCD treated *Npc1*$^{-/-}$ mice. Both had significantly reduced levels at 18 weeks compared to a 10 week untreated liver but there was no difference between treatments. *p<0.05; one-way ANOVA.

Similarly, no significant difference was observed between the total GSL levels in the Crysmeb and the HPβCD treated *Npc1*$^{-/-}$ mouse livers (p=0.1108; **Figure 5.10A**). Total GSL levels were significantly reduced in both treatment groups as compared to the untreated 10 wk *Npc1*$^{-/-}$ mouse livers, and not significantly different from their treated wild type counterparts (*Npc1*$^{-/-}$ vs *Npc1*$^{-/-}$ Crysmeb p<0.0001; *Npc1*$^{-/-}$ vs *Npc1*$^{-/-}$ HPβCD p=0.0002; Wild type + Crysmeb vs *Npc1*$^{-/-}$ Crysmeb p=0.2354; Wild type + HPβCD vs *Npc1*$^{-/-}$ HPβCD p=0.3175). Additionally, the major liver GSL species GM2-Gc was also significantly reduced in both the Crysmeb and HPβCD treatment groups as compared to the 10 week *Npc1*$^{-/-}$ and not significantly different from wild type controls (**Figure 5.10B**). Again, the two treatment groups were not significantly different from each other in the extent of reducing GM2-Gc storage in the liver (p=0.9547).

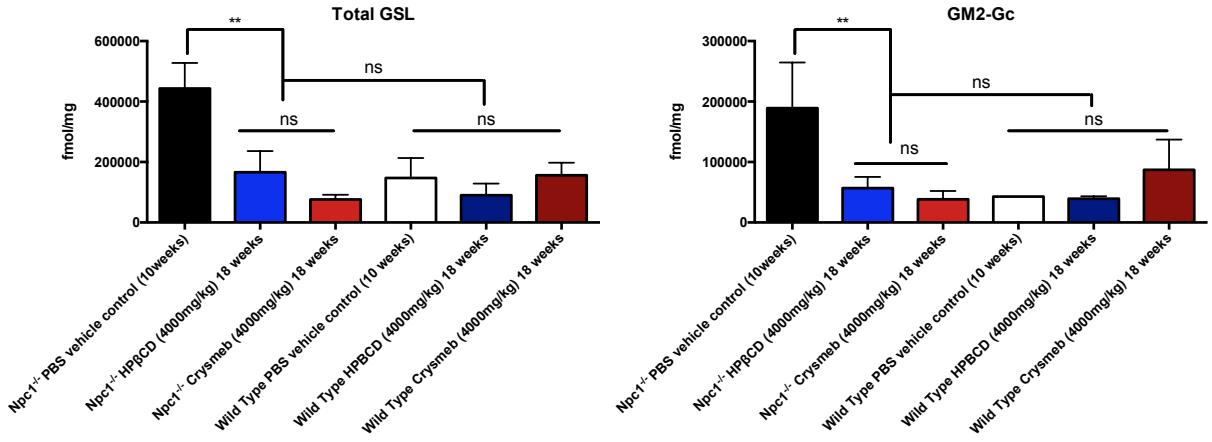

Figure 5.10. *GSL levels in PBS vehicle, Crysmeb and HPβCD treated Npc1*$^{-/-}$ *and wild type livers*. GSLs (excluding Lac-Ceramide) were measured from 5mg w/w livers. A) Both treatment groups had significantly reduced total GSL levels compared to untreated 10wk livers, but there was no significant difference between the treatment groups. B) The most abundant liver GSL species is GM2-Gc. There was no significant differences in the level of GM2-Gc between the treatment groups, and both were significantly reduced as compared to the 10wk *Npc1*$^{-/-}$ mouse GM2-Gc levels. Peaks are identified by determining their glucose units using a 2-AA labeled glucose oligomer ladder standard. *p<0.05; one-way ANOVA

Summary of Crysmeb and HPβCD treatments in **Table 5.2**.

Parameter compared to *Npc1*$^{-/-}$	HPβCD (4000mg/kg)	Crysmeb (4000mg/kg)
Survival	+	++
High frequency tremor	+	+
Mobility / Activity	+	+
Gait / Motor Coordination	+	+
GSL storage	+	+
Cholesterol storage	+	+

Table 5.2. *Comparative table of treatment groups compared to untreated Npc1*$^{-/-}$ *mice in terms of the different behavioral and biochemical parameters measured.* HPβCD (4000mg/kg) treatment starting at post natal day 7 provided significant survival and behavioral benefits. Crysmeb (4000mg/kg) treatment starting at p7 also provided significant survival and behavioral benefits. Crysmeb treated mice lived significantly longer than HPBCD treated mice (220.5 vs 168 days).

5.3.2 Effective Cyclodextrin Drug Delivery via Nasal Cavity

We then explored the effectiveness of delivering the cyclodextrin analogue Crysmeb directly to the CNS through the nasal cavity. Intranasal (IN) Crysmeb delivery of 100mg/kg and 200mg/kg doses was administered weekly, and was compared to the efficacy of the classical 4000mg/kg IP injection as well as reduced IP doses of 100mg/kg and 200mg/kg. Both IP and IN doses were delivered weekly from p7.

Intranasal Crysmeb delivery of 100mg/kg did significantly improve the lifespan of *Npc1*$^{-/-}$ mice compared with vehicle treated *Npc1*$^{-/-}$ mice (p=0.0186). Increasing the dose to 200mg/kg was not significantly different from the 100mg/kg dose (p=0.9793) (**Figure 5.11**).

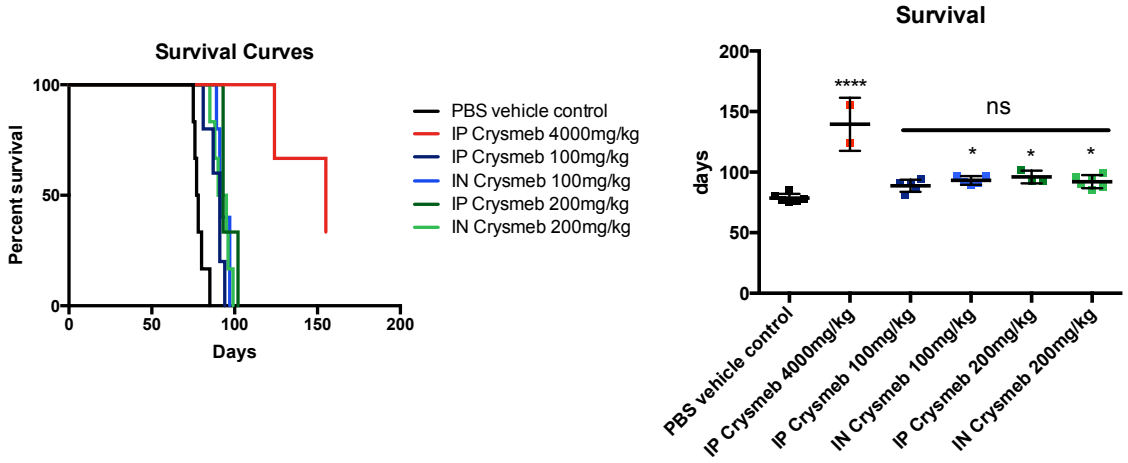

Figure 5.11. *Kaplan-Meier survival curves for Crysmeb IP and IN treated Npc1*$^{-/-}$ *mice and PBS vehicle control.* The IP 4000mg/kg, IP 200mg/kg, IN 100mg/kg and IN 200mg/kg all lived significantly longer than the vehicle control *Npc1*$^{-/-}$ mice. Additionally, there were no significant differences between any of the reduced dose treatments. *p<0.05, ****p<0.000; one-way ANOVA.

However, IN delivery of either 100mg/kg or 200mg/kg had no effect on lifespan as compared to the 100mg/kg and 200mg/kg IP injected mice (IP Crysmeb 200mg/kg vs. IN Crysmeb 200mg/kg p=0.9585; IP Crysmeb 100mg/kg vs. IN Crysmeb 100mg/kg p=0.8897). The 100mg/kg and 200mg/kg IP and IN mice had reduced lifespans as compared to the IP Crysmeb 4000mg/kg dose (IP Crysmeb 4000mg/kg vs IP Crysmeb 200mg/kg p<0.0001; IP Crysmeb 4000mg/kg vs IP Crysmeb 100mg/kg p<0.0001; IP Crysmeb 4000mg/kg vs IN Crysmeb 200mg/kg p<0.0001; IP Crysmeb 4000mg/kg vs IN Crysmeb 100mg/kg p<0.0001). Additionally, the IP and IN reduced doses had no effects

on body weight in the treated animals, and had weight curves similar to that observed in the untreated *Npc1*$^{-/-}$ mice (**Figure 5.12**).

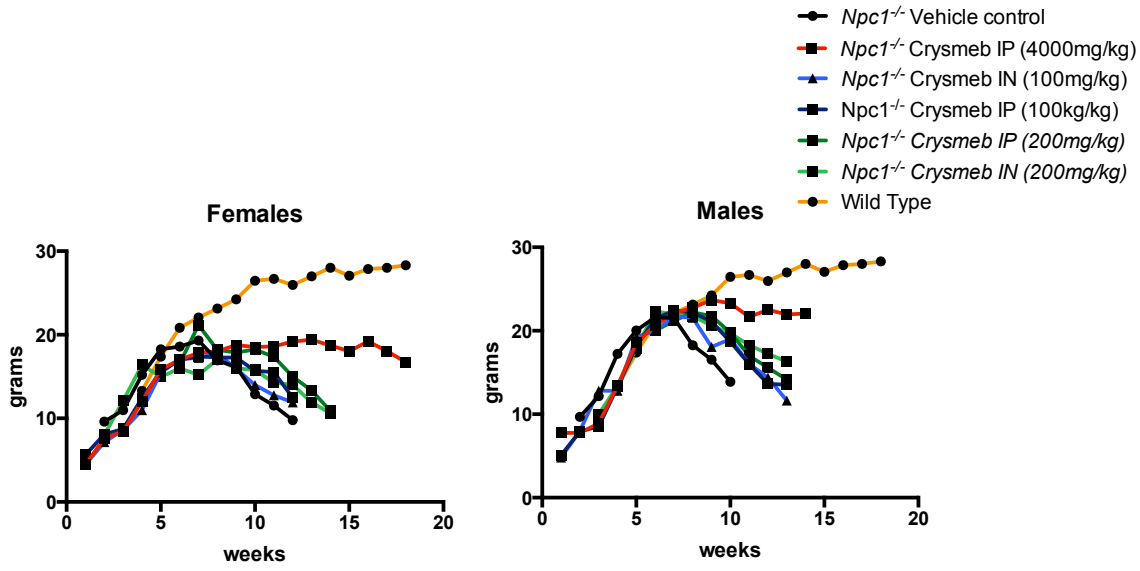

Figure 5.12. *Average weights curve for Crysmeb IP and IN male and female treated Npc1*$^{-/-}$ *mice.* No substantial weight differences were observed in any of the treatment groups. *Npc1*$^{-/-}$ Crysmeb IP (4000mg/kg) mice maintained body weight better than other treatment groups.

We then investigated whether IN delivery had significant improvements on the motor functions of the *Npc1*$^{-/-}$ mouse. At 6 weeks of age no differences were observed between any of the treatment groups and the vehicle control *Npc1*$^{-/-}$ mice (**Figure 5.13A**, *Npc1*$^{-/-}$ vs IP Crysmeb 4000mg/kg p=0.8164; *Npc1*$^{-/-}$ vs IP Crysmeb 200mg/kg p=0.9967; *Npc1*$^{-/-}$ vs IP Crysmeb 100mg/kg p=0.8885; *Npc1*$^{-/-}$ vs IN Crysmeb 100mg/kg p>0.9999). However, at 9 weeks significant improvements in rearing ability in the IP 4000mg/kg Crysmeb treated mice was evident (p=0.0133), although no changes were observed in any of the other treatment groups (**Figure 5.13B,** *Npc1*$^{-/-}$ vs IP Crysmeb 200mg/kg p>0.9999;

Npc1$^{-/-}$ vs IP Crysmeb 100mg/kg p>0.9999; *Npc1*$^{-/-}$ vs IN Crysmeb 200mg/kg p=0.7544; *Npc1*$^{-/-}$ vs IN Crysmeb 100mg/kg p=0.9990).

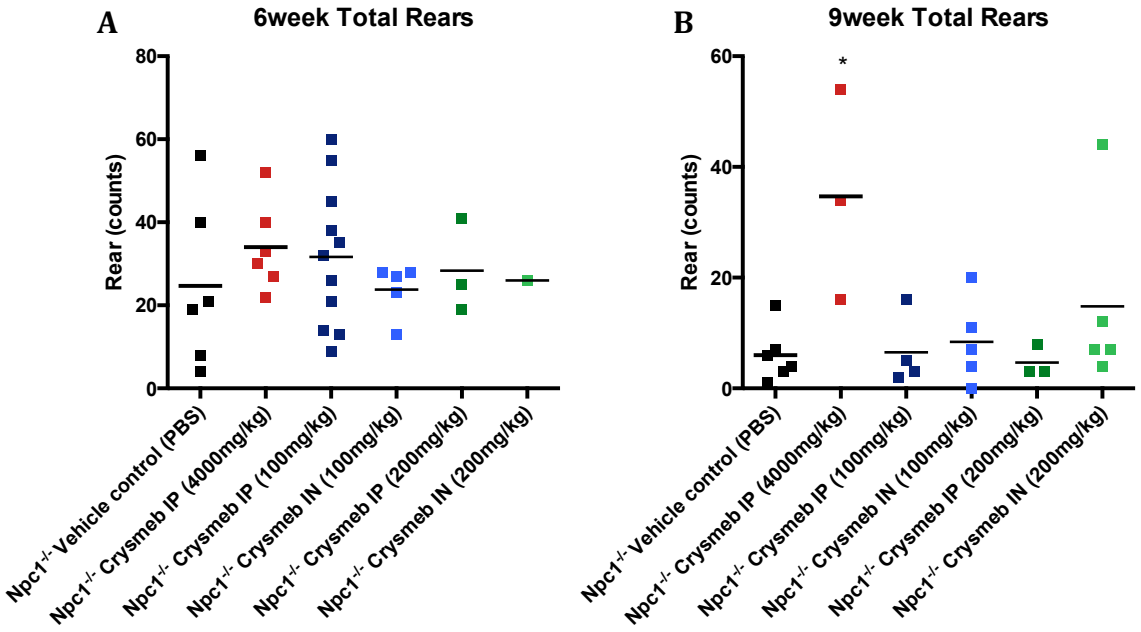

Figure 5.13. *Rearing data for the IP and IN treated mice at 6 and 9 weeks of age.* **A)** At 6 weeks of age no significant differences were observed between any of the treatment groups. **B)** At 9 weeks, the only group that had significantly maintained rearing ability was the Crysmeb IP 4000mg/kg treated group. All the reduced dose IN and IP treatment groups were not significantly different from the PBS vehicle control *Npc1*$^{-/-}$ mice. *p<0.05; one-way ANOVA.

There was not, however, a significant reduction in high frequency tremor in any of the IN and IP reduced Crysmeb dose mice at 6, 9, or 12 weeks of age (**Figure 5.14**; *6 weeks*: *Npc1*$^{-/-}$ vs IP Crysmeb 4000mg/kg p=0.2000; *Npc1*$^{-/-}$ vs IP Crysmeb 200mg/kg p=0.4835; *Npc1*$^{-/-}$ vs IP Crysmeb 100mg/kg p=0.9999; *Npc1*$^{-/-}$ vs IN Crysmeb 200mg/kg p=0.3775; *Npc1*$^{-/-}$ vs IN Crysmeb 100mg/kg p=0.4725; *9 weeks*: *Npc1*$^{-/-}$ vs IP Crysmeb 4000mg/kg p=0.2162; *Npc1*$^{-/-}$ vs IP Crysmeb 200mg/kg p=0.6642; *Npc1*$^{-/-}$ vs IP Crysmeb 100mg/kg p=0.7835; *Npc1*$^{-/-}$ vs IN Crysmeb 200mg/kg p=0.1717; *Npc1*$^{-/-}$ vs IN Crysmeb 100mg/kg p=0.4039; *12 weeks*: 9 week *Npc1*$^{-/-}$ vs IP Crysmeb 4000mg/kg p=0.8176; 9 week *Npc1*$^{-/-}$

vs IP Crysmeb 200mg/kg p=0.9924; 9 week *Npc1*$^{-/-}$ vs IP Crysmeb 100mg/kg p=0.5813; 9 week *Npc1*$^{-/-}$ vs IN Crysmeb 200mg/kg p=0.1518; 9 week *Npc1*$^{-/-}$ vs IN Crysmeb 100mg/kg p=0.7093.). This is despite a significant reduction in high frequency tremor that had been observed in our original study, where IP Crysmeb 4000mg/kg reduced the tremor as compared to *Npc1*$^{-/-}$ vehicle control (**Figure 5.6**, p=0.0053).

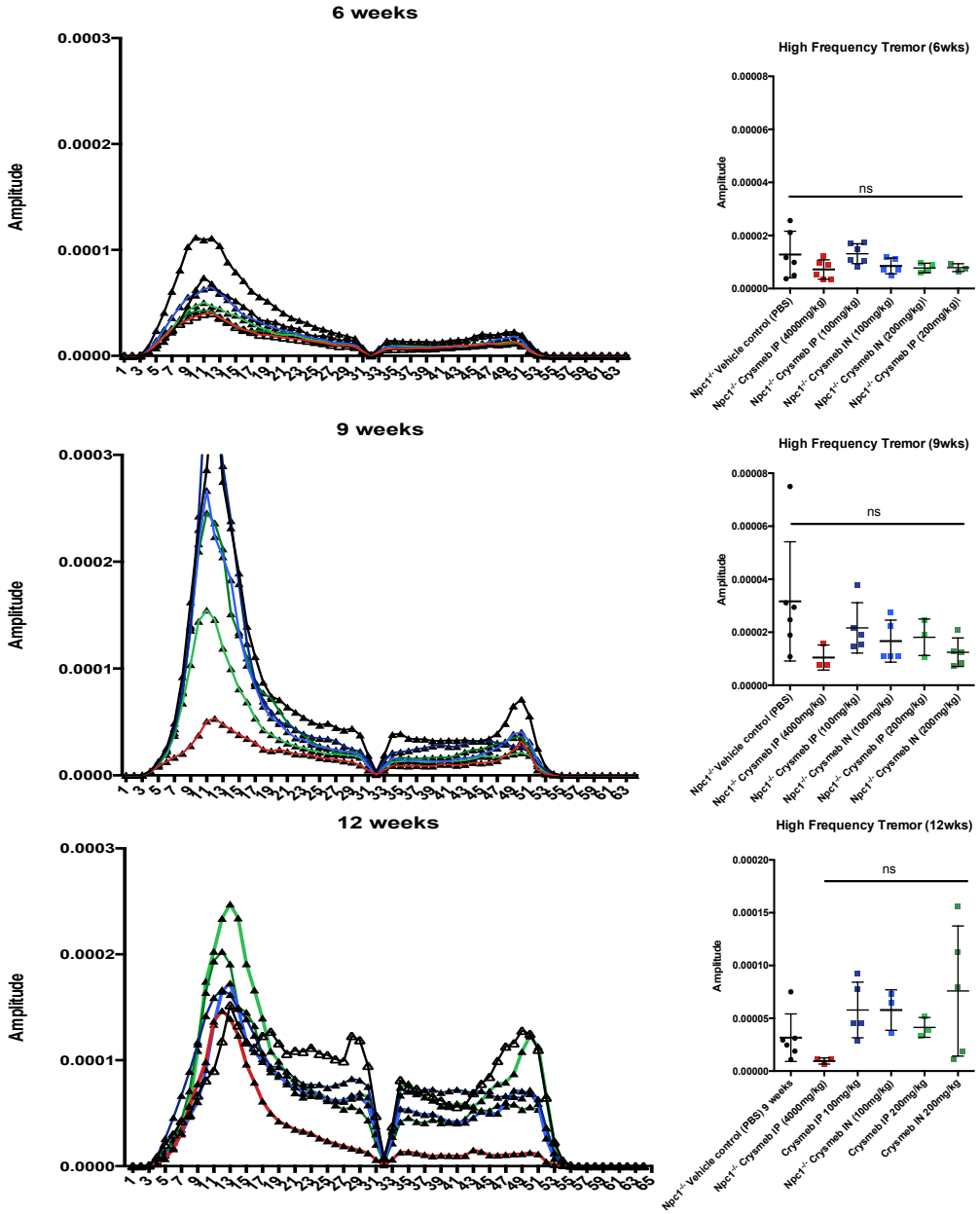

Figure 5.14. *Tremor data for Crysmeb IP and IN treated Npc1*$^{-/-}$ *mice.* At 6,9, and 12 weeks there was no significant differences between any of the treatment groups and the vehicle treated control *Npc1*$^{-/-}$ mouse. Average high frequency tremor was calculated by taking the average tremor from 32 to 53 seconds; one-way ANOVA

When we examined the activity of the mice, at 6 and 9 weeks we observed no significant differences in any of the treatment groups (**Figure 5.15,** *6 weeks*: *Npc1*$^{-/-}$ vs IP Crysmeb 4000mg/kg $p>0.9999$; *Npc1*$^{-/-}$ vs IP Crysmeb 200mg/kg $p=0.9485$; *Npc1*$^{-/-}$ vs IP Crysmeb 100mg/kg $p=0.9950$; *Npc1*$^{-/-}$ vs IN Crysmeb 200mg/kg $p=0.4829$; *Npc1*$^{-/-}$ vs IN Crysmeb 100mg/kg $p=0.9999$; *9 weeks*: *Npc1*$^{-/-}$ vs IP Crysmeb 4000mg/kg $p=0.8774$; *Npc1*$^{-/-}$ vs IP Crysmeb 200mg/kg $p>0.9999$; *Npc1*$^{-/-}$ vs IP Crysmeb 100mg/kg $p=0.8204$; *Npc1*$^{-/-}$ vs IN Crysmeb 200mg/kg $p=0.9984$; *Npc1*$^{-/-}$ vs IN Crysmeb 100mg/kg $p>0.9999$).

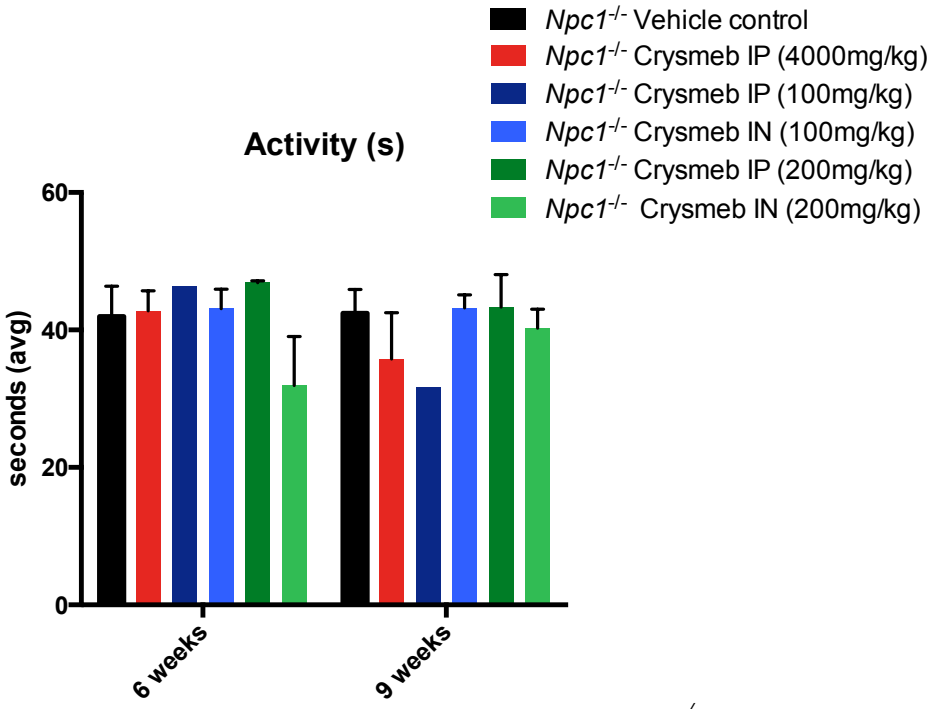

Figure 5.15. *Activity data for Crysmeb IP and IN treated Npc1*$^{-/-}$ *mice.* At both 6 and 9 weeks of age no significant differences were observed the time spent active in any of the IP or IN Crysmeb treatment groups; two-way ANOVA.

Gait analysis (parameters described in **Appendix Table 5**) of the different treatment groups revealed there to be no significant differences at 6 weeks of age between any of the treatment groups for the different parameters examined (**Figure 5.16A**). However, by 9 weeks of age we observed significant gait improvements in the percentage of time

walking in AB step pattern parameter. In all treatment groups, except the Crysmeb 200mg/kg IP group, which had a trend (p=0.0597), there was a significant improvement to this parameter (**Figure 5.16B**; *Npc1*$^{-/-}$ vs IP Crysmeb 4000mg/kg $p<0.0001$; *Npc1*$^{-/-}$ vs IP Crysmeb 100mg/kg $p<0.0001$; *Npc1*$^{-/-}$ vs IN Crysmeb 200mg/kg $p=0.0028$; *Npc1*$^{-/-}$ vs IN Crysmeb 100mg/kg $p=0.0079$). Suggesting that both low doses of IP and IN Crysmeb resulted in a significantly improved gait.

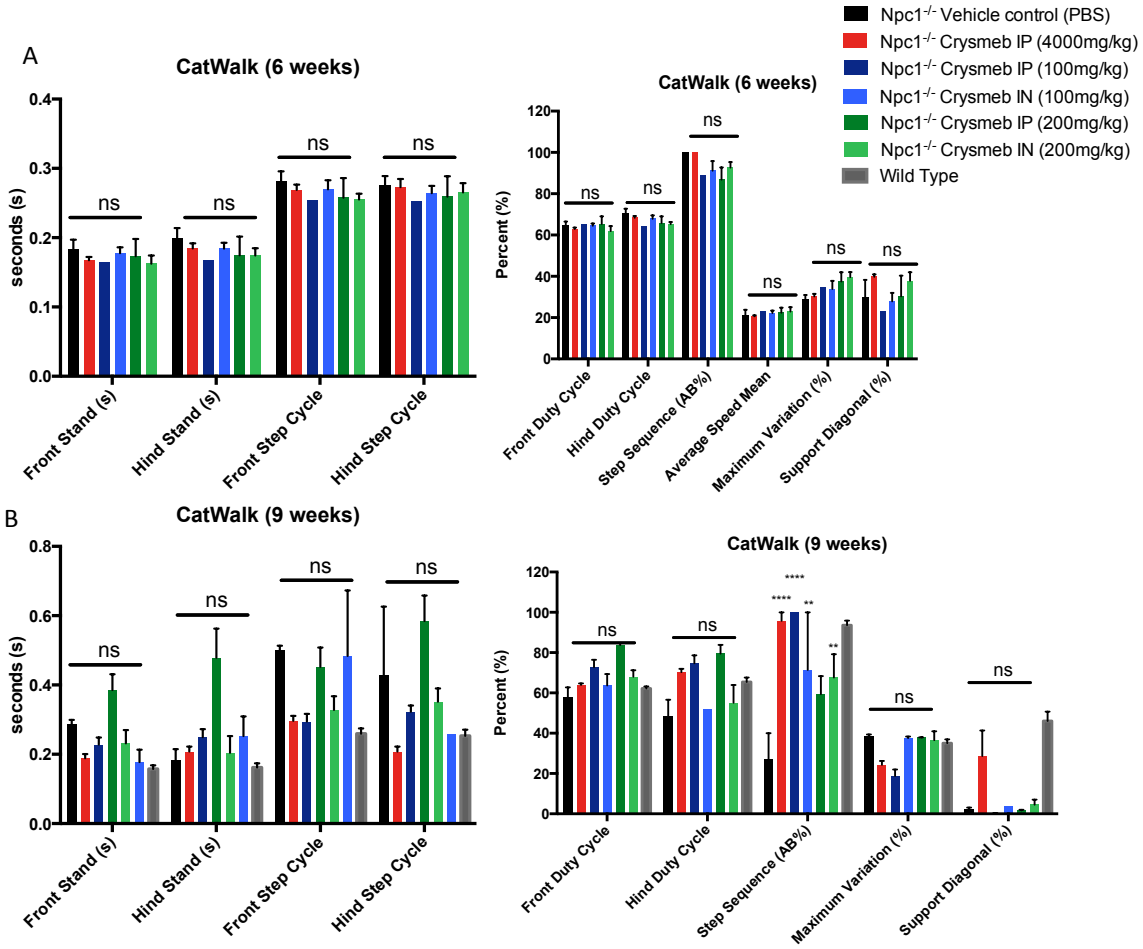

Figure 5.16. *Gait analysis (Catwalk) for 6 and 9 week IN and IP treated Npc1*$^{-/-}$ *mice.* At 6 weeks of age there were no observable gait differences between any of the IN and IP Crysmeb treated mice and the PBS vehicle control *Npc1*$^{-/-}$ mouse. Wild type mouse included for comparison.**$p<0.01$; ****$p<0.0001$; two-way ANOVA

We also examined to what extent Crysmeb may be reaching the systemic system when delivered IN by examining GSL storage in the liver of the 100mg/kg IN treated mice. We did not observe a significant reduction in total GSLs in the IN Crysmeb 100mg/kg treated mice (**Figure 5.17A**; p=0.2778). We did, as expected, observed a significant reduction in the IP Crysmeb 4000mg/kg treated mice (p=0.0007), and these levels were not significantly different from a wild type control (p=0.9719). This was similarly observed in the levels of GM2-Gc storage, the most abundant liver GSL (**Figure 5.17b**; *Npc1*$^{-/-}$ vs IN Crysmeb 100mg/kg p= 0.0960; *Npc1*$^{-/-}$- vs IP Crysmeb 4000mg/kg p=0.0001).

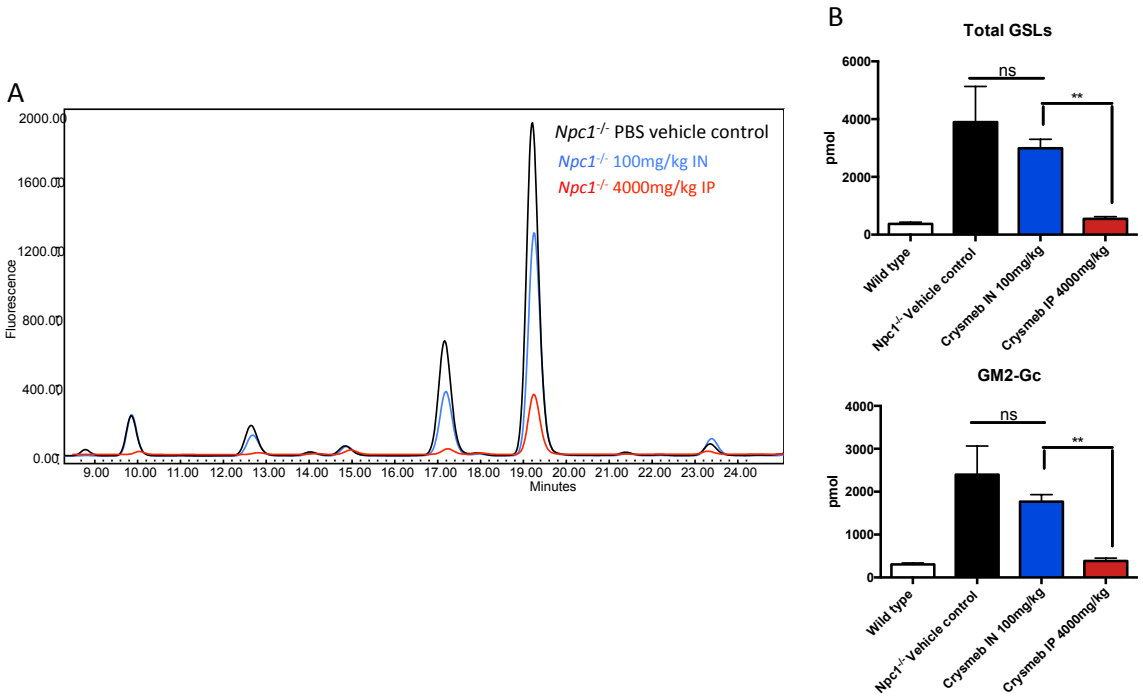

Figure 5.17. *GSL levels in PBS vehicle, Crysmeb IN 100mg/kg and Crysmeb IP 4000mg/kg treated 10 week Npc1*$^{-/-}$ *and wild type livers.* GSLs (excluding Lac-Ceramide) were measured from 5mg w/w livers. A) Representative trace of the vehicle control, 100mg/kg IN, and 4000mg/kg IN GSL liver profiles. B)The IP 4000mg/kg group had significant reduced total and GM2-Gc liver GSL levels as compared to the Crysmeb IN 100mg/kg mouse liver. The 100mg/kg IN mouse did not have any significant reduction in GSL or GM2-Gc levels. Peaks are identified by determining their glucose units using a 2-AA labeled glucose oligomer ladder standard. **p<0.01; one-way ANOVA

Summary of IN and IP cyclodextrin date in **Table 5.3**.

Parameter compared to *Npc1*$^{-/-}$	Crysmeb (4000mg/kg) IP	Crysmeb (100mg/kg) IP	Crysmeb (200mg/kg) IP	Crysmeb (100mg/kg) IN	Crysmeb (200mg/kg) IN
Survival	++	=	+	+	+
High frequency tremor	+	=	=	=	=
Mobility / Activity (9weeks)	=	=	=	=	=
Gait / Motor Coordination	+	+	=	+	+
GSL storage	+	not determined	not determined	=	not determined

Table 5.3. *Comparative table of treatment groups compared to untreated Npc1*$^{-/-}$ *mice in terms of the different behavioral and biochemical parameters measured.* Average lifespan for the treatment groups were Crysmeb (4000mg/kg) IP: 155 days, Crysmeb (100mg/kg) IP: 87 days, Crysmeb (200mg/kg) IP: 93 days, Crysmeb (100mg/kg) IN: 92 days, Crysmeb (200mg/kg): 92.5 days. Only the mice receiving 4000mg/kg IP dose had a significant reduction in tremor, and all treatment groups excluding the Crysmeb (200mg/kg) IP had significant improvement in gait as determined by percentage of time walking in step pattern AB.

5.4 Discussion

Cyclodextrin compounds have been studied extensively over the past 7 years and have shown to be very beneficial for the treatment of NPC; extending the life span in both the mouse and cat models and slowing the rates of neurodegeneration. In this chapter we explored the therapeutic effects of the experimental compound Crysmeb, and have found additional benefits using this HPβCD analogue in the *Npc1*$^{-/-}$ mouse model.

The additional benefits observed in the Crysmeb treated mice include an increase in lifespan (**Figure 5.3**), an increase in rearing ability (**Figure 5.5**), and improved gait (**Figure 5.8**). Additionally, we observed a heavy, more laboured breathing in the HPβCD treated mice as compared to the Crysmeb treated mice.

While it still remains unclear through which mechanism Crysmeb has increased efficacy in the treatment of NPC, the action of the traditional HPβCD still also remains controversial. It has been suggested that HPβCD is effective through its ability to extract cholesterol from the cell membrane and shuttle it between membranes (200, 201). It is also contended that through an unknown mechanisms HPβCD enhances cholesterol release in an NPC1/NPC2 independent manner from the LE/Lys into the cytosol, where the cholesterol is then metabolized and any excess converted to bile acids and excreted (202). Interestingly, HPβCD as a treatment for other LSD's where cholesterol and GSL storage occurs, such as GM1

gangliosidosis, has been shown to be ineffective, suggesting that it may have a more indirect role in cholesterol mobilization (160). Additionally, other studies have suggested that HPβCD can stimulate lysosomal exocytosis and in this way reduce cholesterol storage in NPC disease (153, 203). Further studies would need to be performed to determine if Crysmeb has either enhanced cholesterol mobilization or lysosomal exocytosis, or if it is through a different mechanism entirely that Crysmeb has increased efficacy in the treatment of the *Npc1*$^{-/-}$ mouse model.

Interestingly, the enhanced therapeutic potential of Crysmeb was not reflected in any of the biochemical readouts. There were no differences in the levels of cholesterol or GSLs in the livers of the treated mice (**Figure 5.9, 5.10**). The tissue analysis was performed at 18 weeks of age, which may have been too early in disease progression to compare the effects of these drugs, although, by this time behavioural differences could be readily observed.

As both HPβCD and methylated-β-CD (Crysmeb) have been found to not cross the BBB it is surprising that there is still considerable neurological improvements following treatment (92). It was observed that in *in vitro* models Crysmeb, despite not crossing the BBB, increased the trans-endothelial permeability of lipophilic drugs across the BBB and this effect was not observed following HPβCD treatments (204). While this does not account for the reduction in neurological symptoms following either HPβCD or Crysmeb, it does suggest the potential for other drugs to be combined with Crysmeb for enhanced crossing of the BBB.

As one of the biggest barriers of treating neurodegenerative diseases is getting around the BBB, the increased drug permeability inferred by Crysmeb treatment may offer a new potential for CNS drug delivery. It may also allow for a reduced dose, mitigating against the potential side effects (hearing loss, macrophage lung infiltration, etc). Additionally, even in the 200mg/kg Crysmeb IP treated mice we observed mild survival and behavioural benefits (**Table 5.3**), suggesting that a low dose treatment combined with a more effective CNS targeting compound may have merit.

This potential for combination treatments is particularly interesting in terms of the IN delivery route. Intranasal delivery of Crysmeb did not offer additional lifespan or behavioural benefits as compared to the IP dose equivalent treated mice (**Figure 5.11**, **Figure 5.13**). This suggests that the improvements we observe in the IN mice may not be specific to Crysmeb reaching the CNS, but rather the general effects of low dose cyclodextrin treatment. The ineffectiveness of Crysmeb when delivered IN could be due to the lack of precision in the technique, or because it is no more effective when delivered to the CNS than when delivered systemically. Had we radiolabelled Crysmeb and traced the IN delivery it would have enabled us to determine the level of Crysmeb that reached the CNS, however, we were unable to examine this.

The lipid analysis of the liver does, however, suggest that Crysmeb delivered IN remained in the CNS and did not enter the blood stream at levels sufficient to impact

liver GSLs, as no significant reduction in total GSLs was observed when compared to the untreated *Npc1*$^{-/-}$ mouse liver (**Figure 5.17**). These data suggest that if IN delivery is no more effective than IP, then intrathecal/ICV delivery to get higher levels of cyclodextrin in the CNS may not be the most effective method of treatment. But rather, a combination of compounds and low dose systemic Crysmeb to enhance other lipohphilic drugs cross the BBB may be a safer, less invasive method of treatment.

In summary

- Crysmeb is a new cyclodextrin analogue that has increased efficacy in the treatment of NPC
- Non-invasive CNS drug delivery *via* the nasal cavity did not prove as effective as the traditional 4000mg/kg IP dose; however, even at dose as low as 100mg/kg we observed a mild increase in survival

Chapter 6: Concluding Remarks

6 Concluding Remarks

6.1 Conclusions

Despite the remarkable progress achieved to date developing NPC therapies – one approved drug and 4 clinical trials evaluating three very different treatment options – the function of the NPC1 protein itself still remains poorly understood and controversial. The two causative genes were identified over a decade ago, but how and why these gene products interact and the function of the pathway they regulate remains unknown.

As NPC1 is a highly conserved protein, with orthologous proteins in yeast and strong structural homology with bacterial multi-drug effluxers (RND permeases), we can take advantage of different model organisms to better understand the conserved function of the human NPC1 protein. In this thesis I used yeast as a model system, where the yeast orthologue of NPC1, Ncr1p, is functionally equivalent to the

human protein. We therefore investigated Ncr1p binding partners and the pathways Ncr1p influences. We identified three direct interacting partners, the calcium ATPase Pmc1p, the iron transporter Fth1p, and the cell cycle regulation protein Apc11p. It has been previously identified that in NPC disease there is an acidic store Ca^{2+} defect and in patients and the NPC1 mouse model anaemia due to impaired iron homeostasis, suggesting that mutations in the NPC1 protein may influence the functionality of the proteins it interacts with. This notion of a protein complex that involves NPC1 is interesting, as the protein it interacted with the strongest (Pmc1p), interacted strongly with an ABC transporter Ycf1p, an orthologue to human ABCC1 and ABCC7. The potential involvement of the cell cycle gene is interesting as this is the first association between NCP1 and cell cycle regulation and merits further study.

A parallel proteomic/phosphoproteomic screen in the *Npc1* homozygous and heterozygous mouse cerebellum confirmed many of the findings resulting from the yeast screen, particularly the mitochondrial and cytoskeletal defects that were observed in the *Npc1*$^{-/-}$ mouse. In addition to validating the yeast screen hits, it also highlighted the therapeutic potential of kinases, and the effects of modulating their signalling pathways in the cell.

As additional cellular pathologies are identified in NPC, such as those identified in the yeast and mouse screens, determining their place in the pathogenic source, or initiating steps in the pathogenic cascade becomes more important. However, as we

uncover more about this disease the non-linear nature of these pathogenic processes becomes more apparent (**Figure 6.1**). Taking advantage of the convergence between NPC and other disorders may allow us to better understand how these secondary defects (i.e. mitochondrial or cytoskeletal) arise.

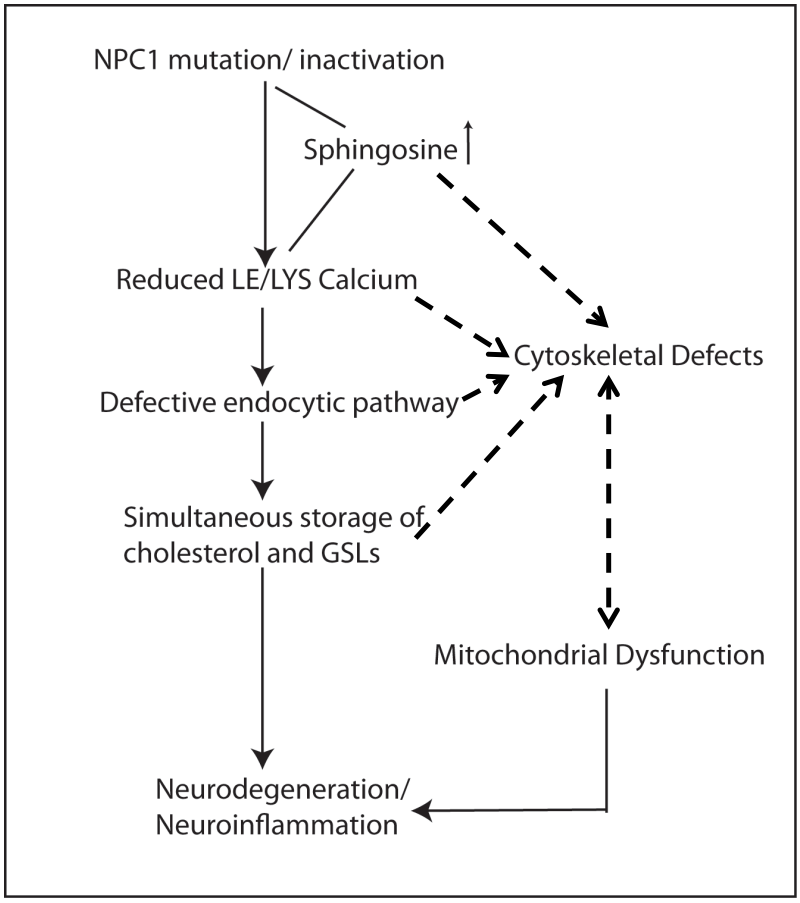

Figure 6.1. Proposed pathogenic cascade following NPC1 inactivation including pathologies identified from yeast screen.

For instance, in Tangier disease we observed many of the shared cellular and biochemical pathogenic hallmarks of NPC, however, these defects in Tangier patient cells were not the result of sphingosine storage. Furthermore, Tangier fibroblasts also did not have a hyperacetylation of α-tubulin suggesting that the acidic store Ca^{2+} defect, sphingolipid mistrafficking, and storage of cholesterol and GSLs do not directly lead to cytoskeletal defects (**Figure 6.2**). Furthermore, a therapy that targets only cholesterol storage and has no effect on sphingosine may not ameliorate the

microtubule defect, which is why determining the highest converging point of the pathogenic cascade is important.

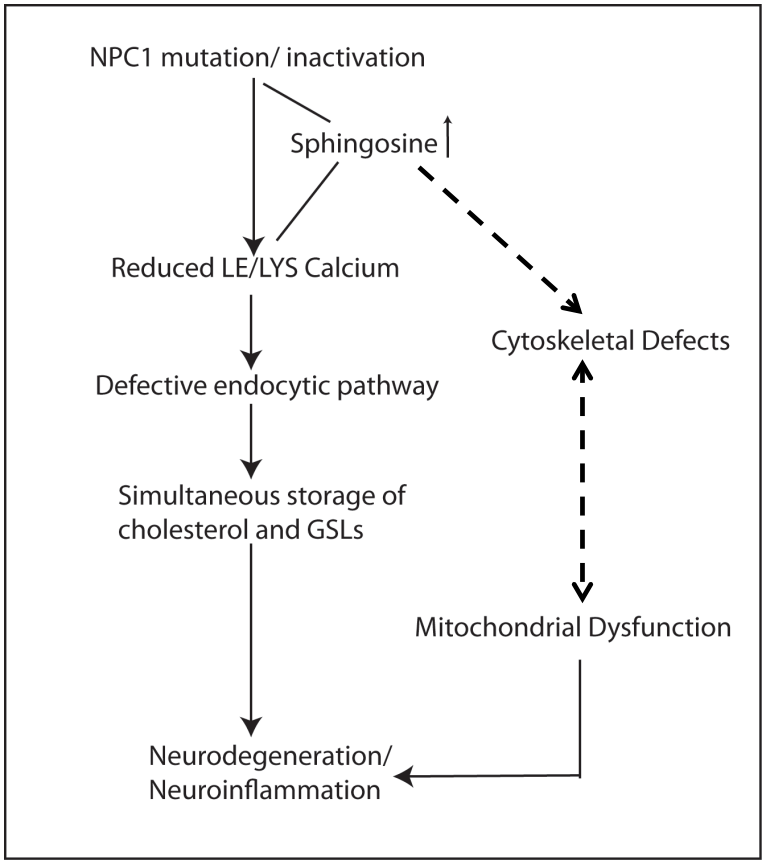

Figure 6.2. Simplified pathogenic cascade following NPC1 inactivation suggesting cytoskeletal defects runs parallel to acidic store calcium defect.

Likewise, understanding the converging nature of seemingly unrelated diseases will also enable us to examine other therapeutic treatments for these disorders – for instance the highly effective nature of miglustat treatment on Tangier disease. This was suggested following the misdiagnosis of a Tangier disease patient with NPC and their subsequent improvement following miglustat treatment. Characterizing the effects that miglustat has, at the cellular level on these patient cells, allowed us to better understand points of convergence but also led directly to other Tangier patients receiving miglustat treatment.

Equally, targeting the gene involved in Tangier disease as a therapy for NPC has proved to be effective both at the cellular level and in the NPC1 mouse model. The

ARB losartan is thought to inhibit Ang II-mediated ABCA1 repression, and thus enhance ABCA1 cellular expression. At the cellular level, losartan ameliorates the acidic store Ca^{2+} defect and all downstream cellular pathologies, as well as partially restores α-tubulin acetylation levels – however the effect that this drug has on sphingosine levels has not yet been determined. Surprisingly, in the mouse model we also observed a reduction in neuroinflammation with a significant reduction of infiltrating microglial was observed in the losartan/miglustat combination treatment mice. Losartan has been shown to have multiple targets in addition to enhancing ABCA1 expression, and has been implicated as having an effect on the immune system, which may account for the significant improvement in inflammation in the brain.

Additionally, the cyclodextrin analogue Crysmeb was also found to be highly effective in the NPC1 mouse model, significantly extending lifespan as compared to HPβCD, the cyclodextrin compound currently in clinical trials. Furthermore when we examined the intranasal route of delivery to bypass the BBB and deliver Crysmeb directly to the CNS we observed minor survival and behavioural benefits which is promising and merits further optimization (higher dose, more frequent delivery). These improvements were no greater than that observed with equivalent low dose systemic treatments, however it was remarkable that a 40x reduction in dose could still have some therapeutic effect with such a non-invasive mode of delivery.

However, as cyclodextrin did not have any therapeutic effect on Tangier disease cells it brings into question by what mechanism these drugs may be working, as there is considerable cholesterol storage in Tangier disease. Additionally, as cyclodextrin may be working by a different mechanism than either miglustat or losartan then it may serve as a good combination treatment as it may target different cellular aspects of NPC disease.

Determining the key points of therapeutic intervention in NPC will become clearer as we better understand the function of the NPC1 protein and its role in cellular pathways. Using the yeast to identify novel binding partners we now have insights about what pathways it may affect and these will now be a major focus to follow up studies. As these pathways are better understood, both the current (miglustat, arimoclomol, vorinostat, HPβCD) and therapies we have found to be effective here (losartan, Crysmeb, kinases inhibitors) can be combined to target different aspects of this disease, as well as related disease, and work towards developing more effective treatment options for these rare diseases.

6.2 Future Studies

If time had allowed, I would have liked to pursue further these interacting partners identified in the yeast screen– particularly Pmc1p.

Pmc1p is the yeast vacuolar Ca^{2+} ATPase that is similar to the PMCA1a (ATP2B1) protein in humans. The family of PMCA proteins (1-4) have all been localized to the plasma membrane, and none have been found on LE/Lys - but it is not inconceivable that they are endocytosed and traffic to the late endocytic system. In NPC we observe what is most likely an acidic store Ca^{2+} filling defect or change in steady state levels of calcium due to an imbalance between filling and leak rates, however, the identification of a protein responsible for transporting Ca^{2+} into the LE/Ly has not yet been determined. PMCA1a is therefore a potential candidate and merits further exploration in yeast and mammalian cells.

In addition to the binding partners identified in the screen, I would also be interested in following up on the α-tubulin hyperacetylation phenotype observed in NPC patient cells. Determining if there is a defect in the activity of the histone deacetylases HDAC6 and SIRT2 enzymes themselves, and the role hyperacetylation has on lysosomal and mitochondrial function will be important. Additionally, I was only able to begin to examine the effects of modulating the levels of acetylation on the NPC phenotype and am interested in examining this further as a therapeutic target.

In terms of the therapies examined in this thesis, I would have liked to have looked further into both the mechanism of action of losartan and Crysmeb and further understand the effects these drugs have on the cellular system. In the case of losartan it has been proposed to have targets in addition to Angiotensin II, and would have liked to explore its effects as a PPARγ activator and its effect on mitochondria, especially as mitochondrial dysfunction is becoming better characterized in NPC disease. With respect to Crysmeb, understanding its mechanism of action may be possible by understanding why cyclodextrin is beneficial at the cellular level in NPC, but not in Tangier disease. I think that this may be an avenue for understanding how cyclodextrin works in the cell as we have two cholesterol storage disorders that respond differentially to treatment.

While I have been unable to fully explore the yeast screen data to the extent I would have liked, this screen serves as a basis for future studies to determine what NPC1 does and how it might work in a larger protein complex as well as how it triggers the pathogenic cascade. Additionally, the therapeutic compounds that have been tested can be further investigated and particularly with the intranasal delivery of cyclodextrin there is still much room for optimizing the concentration of drug delivered. Furthermore, understanding the convergence of other diseases with the NPC pathogenic cascade will allow for these “NPC-like” diseases to be examined in term of therapies but also will enable better understanding of the pathogenesis of the NPC1 protein itself and the mechanisms leading to convergence. Together, this

will provide fundamental insights into basic cellular homeostasis and disease pathogenesis.

1. Vanier M. Niemann-Pick disease type C. Ophanet - Journal of Rare Diseases 2010;5:16.
2. Lloyd-Evans E, Platt F. Lipids on trial: the search for the offending metabolite in Niemann-Pick type C disease. Traffic 2010;11(4):419-428.
3. Davies J, Chen F, Ioannou Y. Transmembrane molecular pump activity of Niemann-Pick C1 protein. Science 2000;290(5500):2295-2298.
4. Freschi L, Torres-Quiroz F, Dube A, Landry C. qPCA: a scalable assay to measure the perturbation of protein–protein interactions in living cells. Molecular BioSystems 2013;9:36-43.
5. Platt N, Speak A, Colaco A, Gray J, Smith D, Williams I, Wallom K, Platt F. Immune dysfunction in Niemann‐Pick disease type C. Journal of Neurochemistry 2016;136(Suppl Suppl 1):74-80.
6. Platt F, Butters T. Substrate deprivation: a new therapeutic approach for the glycosphingolipid lysosomal storage diseases. Expert Reviews in Molecular Medicine 2000;2(1):1-17.
7. Eisenkolb M, Zenzmaier C, Leitner E, Schneiter R. A specific structural requirement for ergosterol in long-chain fatty acid synthesis mutants important for maintaining raft domains in yeast. Molecular Biology of the Cell 2002;13(12):4414-4428.
8. Xiao C, Davis F, Chauhan B, Viola K, Lacor P, Velasco P, Klein W, Chauhan N. Brain transit and ameliorative effects of intranasally delivered anti-amyloid-β oligomer antibody in 5XFAD mice. Journal of Alzheimer Disease 2013;35(4):777-788.
9. Infante R, Wang M, Radhakrishnan A, Kwon H, Brown M, Goldstein J. NPC2 facilitates bidirectional transfer of cholesterol between NPC1 and lipid bilayers, a step in cholesterol egress from lysosomes. PNAS 2008;105(40):15287-15292.
10. Malathi K, Higaki K, Tinkelenberg A, Balderes D, Almanzar-Paramio D, Wilcox L, Erdeniz N, Redican F, Padamsee M, Liu Y, Khan S, Alcantara F, Carstea E, Morris J, Sturley S. Mutagenesis of the putative sterol-sensing domain of yeast Niemann Pick C-related protein reveals a primordial role in subcellular sphingolipid distribution. Journal of Cell Biology 2004;164(4):547-556.
11. Lebesgue N, Colaco A, Wu W, Fitzpatrick M, Gray J, Raaijmakers L, Heck A, Platt F, Lemeer S. Unravelling signaling pathways in Niemann-Pick type C disease by phosphoproteomic analysis of mouse cerebellum. *In Preperation* 2016.
12. Berger A, Hanson P, Nichols J, Corbett A. A yeast model system for functional analysis of the Niemann-Pick type C protein 1 homolog, Ncr1p. Traffic 2005;6(10):907-917.
13. Lloyd-Evans E, Morgan A, He X, Smith D, Elliot-Smith E, Sillence D, Churchill G, Schuchman E, Galione A, Platt F. Niemann-Pick disease type C1 is a sphingosine storage disease that causes deregulation of lysosomal calcium. Nature Medicine 2008;14(11):1247-1255.
14. Zhang S, Ren J, Li H, Zhang Q, Armstrong J, Munn A, Yang H. Ncr1p, the yeast ortholog of mammalian Niemann Pick C1 protein, is despensable for endocytic transport. Traffic 2004;5(12):1017-1030.

15. Berger A, Salazar G, Styers M, Newell-Litwa K, Werner E, Maue R, Corbett A, Faundez V. The subcellular localization of the Niemann-Pick Type C proteins depends on the adaptor complex AP-3. Journal of Cell Science 2007;120:3640-3652.
16. Vilaca R, Silva E, Nadais A, Teixeira V, Matmati N, Gaifem J, Hannun Y, Miranda M, Costa V. Sphingolipid signaling mediates mitochondrial dysfunctions and reduced chronological lifespan in the yeast model of Niemann-Pick type C1. Molecular Microbiology 2014;91(3):438-451.
17. Coutinho M, Alves S. From rare to common and back again: 60 years of lysosomal dysfunction. Molecular Genetics and Metabolism 2016;117(2):53-65.
18. Cox T, Cachon-Gonzalez M. The cellular pathology of lysosomal diseases. The Journal of Pathology 2011;226(2):241-254.
19. Ratko T, Marbella A, Godfrey S, Aronson N. Enzyme-replacement therapies for lysosomal storage diseases. Agency for Healthcare Research and Quality (US) Technical Briefs 2013(12).
20. Bosh M, Kielian T. Neuroinflammatory paradigms in lysosomal storage diseases. Frontiers in Neuroscience 2015;9:417.
21. Fuller M, Meikle P, Hopwood J. Epidemiology of lysosomal storage diseases: an overview. In: Mehta A, Beck M, Sunder-Plassman G, editors. Fabry Disease: Perspectives fom 5 years of FOS. Oxford: Oxford PharmaGenesis; 2006.
22. Meikle P, Hopwood J, Clague A, Carey W. Prevalence of lysosomal storage disorders. JAMA 1999;281:249-254.
23. Wassif C, Cross J, Iben J, Sanchez-Pulido L, Cougnoux A, Platt F, Ory D, Ponting C, Bailey-Wilson J, Biesecker L, Porter F. High incidence of unrecognized visceral/neurological late-onset Niemann-Pick disease, type C1, predicted by analysis of massively parallel sequencing data sets. Genetics in Medicine 2016;18(1):41-48.
24. Patterson M. Niemann-Pick disease type C: Seattle (WA): University of Washington, Seattle; 2000.
25. Greenberg C, Barnes J, Kogan S, Seargeant L. A rare case of Niemann-Pick disease type C without neurological involvement in a s 66-year old patient. Molecular Genetics and Metabolism Reports 2015;3:18-20.
26. Scott C, Ioannou Y. The NPC1 protein: structure implied function. Biochimica et Biophysica Acta (BBA) - Molecular and Cell Biology of Lipids 2004;16385(1-3):8-13.
27. Vanier M, Millat G. Structure and function of the NPC2 protein. Biochimica et Biophysica Acta (BBA) - Molecular and Cell Biology of Lipids 2004;16385(1-3):14-21.
28. Okamura N, Kiuchi S, Tamba M, Kashima T, Hiramoto S, Baba T, Dacheux F, Dacheau J, Sugita Y, Jin Y. A porcine homolog of the major secretory protein of human epididymis, HE1, specifically binds cholesterol. Biochimica et Biophysica Acta (BBA) - Molecular and Cell Biology of Lipids 1999;1438(3):377-387.
29. Babalola J, Wendeler M, Breiden B, Arenz C, Schwarzmann G, Locatelli-Hoops S, Sandhoff K. Development of an assay for the intermembrane transfer of cholesterol by Niemann-Pick C2 protein. Biological Chemistry 2007;388(6):617-626.
30. Friedland N, Liou H, Lobel P, Stock A. Structure of a cholesterol-binding protein deficient in Niemann-Pick type C2 disease. PNAS 2003;100(5):2512-2517.

31. Kolter T, Sandhoff K. Lysosomal degradation of membrane lipids. FEBS Letters 2010;584(9):1700-1712.
32. Abdul-Hammed M, Breiden B, Adebayo M, Babalola J, Schwarzmann G, Sandhoff K. Role of endosomal membrane lipids and NPC2 in cholesterol transfer and membrane fusion. Journal of Lipid Research 2010;51(7):1747-1760.
33. Li X, Wang J, Coutavas E, Shi H, Hao Q, Blobel G. Structure of human Niemann-Pick C1 protein. PNAS 2016;113(29):8212-8217.
34. Ioannou Y. The structure and function of the Niemann-Pick C1 protein. Molecular Genetics and Metabolism 2000;71:175-181.
35. Sturley S. Conservation of eukaryotic sterol homeostasis: new insights from studies in budding yeast. Biochimica et Biophysica Acta (BBA) - Molecular and Cell Biology of Lipids 2000;1529(1-3):155-163.
36. Guan X, Souza C, Pichler H, Dewhurst G, Schaad O, Kajiwara K, Wakabayashi H, Ivanova T, Castillon G, Piccolis M, Abe F, Loewith R, Funato K, Wenk M, Riezman H. Functional interactions between sphingolipids and sterols in biological membranes regulating cell physiology. Molecular Biology of the Cell 2009;20(7):2083-2095.
37. Baudry K, Swain E, Rahier A, Germann M, Batta A, Rondet S, Mandala S, Henry K, Tint G, Edlind T, Kurtz M, Nickels JJ. The effect of the *erg*26-1 mutation on the regulation of lipid metabolism in *Saccharomyces cerevisiae*. The Journal of Biological Chemistry 2001;276:12702-12711.
38. Pagano R, Puri V, Dominguez M, Marks D. Membrane traffic in sphingolipid storage diseases. Traffic 2000;1(11):807-815.
39. Chen C, Patterson M, O'Brien J, Pagano R, Wheatley C. Broad screening test for sphingolipid-storage diseases. The Lancet 1999;354(9182):901-905.
40. Puri V, Watanabe R, Dominguez M, Sun X, Wheatley C, Marks D, Pagano R. Cholesterol modulates membrane traffic along the endocytic pathway in sphingolipid-storage diseases. Nature Cell Biology 1999;1:386-388.
41. Gulati S, Liu Y, Munkacsi A, Wilcox L, Sturley S. Sterols and sphingolipids: dynamic duo or partners in crime? Progressive Lipid Research 2010;49(4):353-365.
42. Horton J, Goldstein J, Brown M. SREBPs: activators of the complete program of cholesterol and fatty acid synthesis in the liver. The Journal of Clinical Investigations 2002;109(9):1125-1131.
43. Wang X, Sato R, Brown M, Hua X, Goldstein J. SREBP-1, a membrane-bound transcription factor released by sterol-regulated proteolysis. Cell 1994;77(1):53-62.
44. Garver W, Jelinek D, Francis G, Murphy B. The Niemann-Pick C1 gene is downregulated by feedback inhibition of the SREBP pathway in human fibroblast. Journal of Lipid Research 2008;49(5):1090-1102.
45. Chen H, Yang J, Low P, Cheng J. Cholesterol level regulates endosome motility via Rab proteins. Biophysical Journal 2008;94(4):1508-1520.
46. Hoglinger D, Haberkant P, Aguilera-Romero A, Riezman H, Porter F, Platt F, Galione A, Schultz C. Intracellular sphingosine releases calcium from lysosomes. eLife 2015;4:e10616.
47. Rodriguez-Lafrasse C, Rousson R, Pemtchev P, Louisot P, Vanier M. Free spingoid bases in tissues from patients with type C Niemann-Pick disease and other lysosomal storage disorders. Biochimica et Biophysica Acta (BBA) 1994;1226:138-144.

48. Vitner E, Platt F, Futerman A. Common and uncommon pathogenic cascades in lysosomal storage diseases. The Journal of Biological Chemistry 2010;285(20423-20427).
49. Korkotian E, Schwarz A, Pelled D, Schwarzmann G, Segal M, Futerman A. Elevation of intracellular glucosylceramide levels results in an increase in endoplasmic reticulum density and in functional calcium stores in cultured neurons. The Journal of Biological Chemistry 1999;274(21673-21678).
50. Pelled D, Lloyd-Evans E, Riebeling C, Jeyakumar M, Platt F, Futerman A. Inhibition of calcium uptake via the sarco/endoplasmic reticulum Ca^{2+}-ATPase in a mouse model of Sandhoff disease and prevention by treatment with N-Butyldeoxynojirimycin. The Journal of Biological Chemistry 2003;278:29496-29501.
51. Ginzburg L, Futerman A. Defective calcium homeostasis in the cerebellum in a mouse model of Niemann–Pick A disease. Journal of Neurochemistry 2005;95(6):1619-1628.
52. Sano R, Annanuziata I, Patterson A, Moschiach S, Gomero E, Opferman J, Forte M, d'Azzo A. GM1-ganglioside accumulation at the mitochondria-associated ER membranes links ER stress to Ca^{2+}-dependent mitochondrial apoptosis. Molecular Cell 2009;36(3):500-511.
53. Jennings JJ, Zhu J, Rbaibi Y, Luo X, Chu C, Kiselyov K. Mitochondrial aberrations in Mucolipidosis type IV. The Journal of Biological Chemistry 2006;281:39041-39050.
54. Luiro K, Kopra O, Blom T, Gentile M, Mitchison H, Hovatta I, Tornquist K, Jalanka A. Batten disease (JNCL) is linked to disturbances in mitochondrial, cytoskeletal, and synaptic compartments. Journal of Neuroscience Research 2006;84(5):1124-1138.
55. Platt F, Wassif C, Colaco A, Dardis A, Lloyd-Evans E, Bembi B, Porter F. Disorders of cholesterol metabolism and their unanticipated convergent mechanisms of disease. Annual Review of Genomics and Human Genetics 2014;15:173-194.
56. Yu X, Jiang N, Yao P, Zheng X, Cayabyab F, Tang C. NPC1, intracellular cholesterol trafficking and atherosclerosis. Clinica Chimica Acta 2014;429:69-75.
57. Kresojevic N, Dobricic V, Svetel M, Kostic V. Mutations in Niemann Pick type C gene are risk factor for Alzheimer's disease. Medical Hypotheses 2014;83(5):559-562.
58. Orr M, Oddo S. Autophagic/lysosomal dysfunction in Alzheimer's disease. Alzheimer's Research & Therapy 2013;5(5):53.
59. Dehay B, Martinez-Vicente M, Caldwell G, Caldwell K, Yue Z, Cookson M, Klein C, Vila M, Bezard E. Lysosomal impairment in Parkinson's disease. Movement Disorders 2013;28(6):725-732.
60. Goker-Alpan O, Schiffman R, LaMarca M, Nussbaum R, McInerney-Leo A, Sidransky E. Parkinsonism among Gaucher disease carriers. Journal of Medical Genetics 2004;41(12):937-940.
61. Zech M, Nubling G, Castrop F, Jochim A, Schulte E, Mollenhauer B, Lichtner P, Peters A, Gieger C, Marquardt T, Vanier M, Latour P, Kluenemann H, Trenkwalder C, Diehl-Schmid J, *et al.* Niemann-Pick C disease gene mutations and age-related neurodegenerative disorders. PLoS One 2013;8(12):e82879.

62. Josephs K, Matsumoto J, Lindor N. Heterozygous Niemann-Pick disease type C presenting with tremor. Neurology 2004;63(11):2189-2190.
63. Kluenemann H, Nutt J, Davis M, Bird T. Parkinsonism syndrome in heterozygotes for Niemann-Pick C1. Journal of Neurological Sciences 2013;335(1-2):219-220.
64. McBrayer M, Nixon R. Lysosome and calcium dysregulation in Alzheimer's disease - partners in crime. Biochemical Society Transactions 2013;41(6):1495-1502.
65. Suzuki K, Parker C, Pentchev P, Katz D, Ghetti B, D'Agostino A, Carstea E. Neurofibrillary tangles in Niemann-Pick disease type C. Acta Neuropathology 1995;89(3):227-238.
66. German D, Quintero E, Liang C, Ng B, Punia S, Xie C, Dietschy J. Selective neurodegeneration, without neurofibrillary tangles, in a mouse model of Niemann-Pick C disease. The Journal of Comparative Neurology 2001;433(3):415-425.
67. Choi H, Karten B, Chan T, Vance J, Greer W, Heidenreich RA, Garver WS, Francis GA. Impaired ABCA1-dependent Lipid Efflux and Hypoalphalipoproteinemia in Human Niemann-Pick type C Disease. The Journal of biological chemistry 2003;278:32569-32577.
68. Boadu E, Nelson R, Francis GA. ABCA1-dependent mobilization of lysosomal cholesterol requires functional Niemann–Pick C2 but not Niemann–Pick C1 protein. Biochim Biophys Acta 2012;1821(3):396-404.
69. Lange Y, ye J, Steck T. Activation mobilizes the cholesterol in the late endosomes-lysosomes of Niemann Pick type C cells. PLos One 2012;7(1):e30051.
70. Wijdeven R, Jongsma M, Neefjes J, Berlin I. ER contact sites direct late endosome transport. Bioessays 2015;37(12):1298-1302.
71. Sechi A, Dardis A, Zampieri S, Rabacchi C, Zanoni P, Calandra S, De Maglio G, Pizzolitto S, Maruotti V, Di Muzio A, Platt F, Bembi B. Effects of miglustat treatment in a patient affected by an atypical form of Tangier Disease. Orphanet Journal of Rare Diseases 2014;9(1):143.
72. Elrick M, Pacheco C, Yu T, Dadgar N, Shakkottai V, Ware C, Paulson H, Lieberman A. Conditional Niemann-Pick C mice demonstrate cell autonomous Purkinje cell neurodegeneration. Human Molecular Genetics 2010;19(5):837-847.
73. Maue R, Burgess R, Wang B, Wooley C, Seburn K, Vanier M, Rogers M, Chang C, Chang T, Harris B, Graber D, Penatti C, Porter D, Szwergold B, Henderson L, *et al.* A novel mouse model of Niemann-Pick type C disease carrying a D1005G-Npc1 mutation comparable to commonly observed human mutations. Human Molecular Genetics 2012;21(4):730-750.
74. Loftus S, Morris J, Carstea E, Gu J, Cummings C, Brown A, Ellison J, Ohno K, Rosenfeld M, Tagle D, Pentchev P, Pavan W. Murine model of Niemann-Pick C dIsease: mutations in a cholesterol homeostasis gene. Science 1997;277(5323):232-235.
75. Smith D, Wallom K, Williams I, Jeyakumar M, Platt F. Beneficial effects of anti-inflammatory therapy in a mouse model of Niemann-Pick disease type C1. Neurobiology of Disease 2009;36(2):242-251.

76. Xie C, Turley S, Pentchev P, Dietschy J. Cholesterol balance and metabolism in mice with loss of function of Niemann-Pick C protein. American Journal of PHysiology - Endocrinology and Metabolism 1999;276(2):E336-E344.
77. Praggastis M, Tortelli B, Zhang J, Fujiwara J, Sidhu R, Chacko A, Chen Z, Chung C, Lieberman A, Sikora J, Davidson C, Walkley S, Pipalia N, Maxfield F, Schaefer E*, et al.* A murine Niemann-Pick C1 I1061T knock-in model recapitulates the pathological features of the most prevalent human disease allele. The Journal of Neuroscience 2015;35(21):8091-8106.
78. Platt FM, Neises GR, Dwek RA, Butters TD. N-butyldeoxynojirimycin is a novel inhibitor of glycolipid biosynthesis. J Biol Chem 1994;269(11):8362-8365.
79. Agency EM. Miglustat - Scientific Discussion. http://www.ema.europa.eu: EMA; 2003.
80. Ridley C, Thur K, Shanahan J, Thillaiappan N, Shen A, Uhl K, Walden C, Rahim A, Waddington S, Platt F, van der Spoel A. β-Glucosidase 2 (GBA2) activity and imino sugar pharmacology. The Journal of Biological Chemistry 2013;288:26052-26066.
81. (EMA) EMA. Zavesca - product information documents. 09 November 2015 [cited 2016 01 June 2016]; Available from: http://www.eudrapharm.eu/eudrapharm/productDetailsAction.do
82. (FDA) USFaDA. Drug approval package - Zavesca (miglustat) capsules. 2002 [cited 2016 1 June 2016]; Available from: http://www.accessdata.fda.gov/drugsatfda_docs/nda/2003/21-348_Zavesca.cfm
83. Priestman D, van der Spoel A, Butters T, Dwek R, Platt F. N-butyldeoxynojirimycin causes weight loss as a result of appetite suppression in lean and obese mice. Diabetes, Obesity and Metabolism 2008;10(2):159-166.
84. Amiri M, Naim H. Long term differential consequences of miglustat therapy on intestinal disaccharidases. Journal of Inherited Metabolic Disease 2014;37(6):929-937.
85. Ficicioglu C. Review of miglustat for clinical management in Gaucher disease type 1. Therapeutics and Clinical Risk Management 2008;4(2):425-431.
86. Andersson U, Butters TD, Dwek R, Platt FM. N-butyldeoxygalactonojirimycin: a more selective inhibitor of glycosphingolipid biosynthesis than N-butyldeoxynojirimycin, in vitro and in vivo. Biochemical Pharmacology 2000;59(7):821-829.
87. Andersson U, Butters T, Dwek R, Platt F. N-butyldeoxygalactonojirimycin: a more selective inhibitor of glycosphingolipid biosynthesis than N-butyldeoxynojirimycin, in vitro and in vivo. Biochemical Pharmacology 2000;59(7):821-829.
88. Elliot-Smith E, Speak AO, Lloyd-Evans E, Smith DA, Spoel AC, Jeyakumar M, Butters TD, Dwek RA, d'Azzo A, Platt FM. Beneficial effects of substrate reduction therapy in a mouse model of GM1 gangliosidosis. Mol Genet Metab 2008.
89. Platt F, Reinkensmeier G, Dwek R, Butters T. Extensive glycosphingolipid depletion in the liver and lymphoid organs of mice treated with N-butyldeoxynojirimycin. The Journal of Biological Chemistry 1997;272(31):19365-19372.
90. Vite C, Bagel J, Swain G, Prociuk M, Sikora T, Stein V, O'Donnell P, Ruane T, Ward S, Crooks A, Li S, Mauldin E, Stellar S, De Meulder M, Kao M*, et al.* Intracisternal

cyclodextrin prevents cerebellar dysfunction and Purkinje cell death in feline Niemann-Pick type C1 disease. Science Translational Medicine 2015;7(276):276ra226.
91. Matsuo M, Togawa M, Hirabaru K, Mochinaga S, Narita A, Adachi M, Egashira M, Irie T, Ohno K. Effects of cyclodextrin in two patients with Niemann-Pick type C disease. Molecular Genetics and Metabolism 2013;108(1):76-81.
92. Pontikis C, Davidson C, Walkley S, Platt F, Begley D. Cyclodextrin alleviates neuronal storage of cholesterol in Niemann-Pick C disease without evidence of detectable blood-brain barrier permeability. Journal of Inherited Metabolic Disease 2013;36(3):491-498.
93. Matsuo M, Shraishi K, Wada K, Ishisuka Y, Doi H, Maeda M, Mizoguchi T, Eto J, Mochinaga S, Arima H, Irie T. Effects of intracerebroventricular administration of 2-hydroxypropyl-β-cyclodextrin in a patient with Niemann-Pick Type C disease. Molecular Genetics and Metabolism Reports 2014;1:391-400.
94. Garcia-Robles A, Company-Albir M, Megias-Vericat J, Fernandez-Megia M, Perez-Miralles F, Lopez-Briz E, Alcala-Vicente C, Galeano I, Casonova B, Poveda J. Use of 2 hydoxypropyl-beta-cyclodextrin therapy in two adult Niemann Pick type C patients. Journal of Neurological Sciences 2016;366:65-67.
95. CTD Holdings I. CTD Listening Circle presentation Aug 11 2016. 2016 [cited; Available from:
96. Vtesse I. Vtesse, Inc announces FDA's granting of breakthrough therapy designation for VTS-270 in Niemann-Pick type C1 disease. [Press Release] 2016 [cited 2016; Available from: http://www.vtessepharma.com/ - !blank/uxqkj
97. (NPD) NN-PDFI. Update #5 on the AiDNPC clinical programme. http://www.nnpdf.org/documents/AIDNPCUpdate5.pdf; 28 April 2016.
98. Kirkegaard T, Gray J, Priestman D, Wallom K, Atkins J, Olsen O, Klein A, Drndarski S, Ingemann L, Bornaes C, Jorgensen S, Williams I, Hinsby A, Arenz C, Begley D*, et al.* Heat Shock Protein-based therapies as clinical candidates for sphingolipidoses. Science Translational Medicine *In Press*.
99. Grant S, Easley C, Kirkpatrick P. Vorinostat. Nature Reviews Drug Discovery 2007;6:21-22.
100. Helquist P, Maxfield F, Wiech N, Weist O. Treatment of Niemann-Pick type C disease by histone deacetylase inhibitors. Neurotherapeutics 2013;10(4):688-697.
101. Alam S, Getz M, Haldar K. Chronic administration of an HDAC inhibitor treated both neurological and systemic Niemann-Pick type C disease in a mouse model. Science Translational Medicine 2016;8(326):326ra323.
102. Health NIo. NIH NPC update 2-27. In: Services DoHaH, editor. nnpdf.org: National Niemann-Pick Disease Foundation Inc (NPD); 2015.
103. Nicoli E, Al Eisa N, Cluzeau C, Wassif C, Gray J, Burkert K, Smith D, Morris L, Cologna S, Peer C, Sissung T, Uscatu C, Figg W, Pavan W, Vite C*, et al.* Defective cytochrome P450-catalysed drug Mmtabolism in Niemann-Pick type C disease. PLoS One 2016;11(3):e0152007.
104. Encyclopedia of canoscience and society: SAGE Publications, Inc; 2010.
105. Major J. Challenges and opportunities in high throughput screening: implications for new technologies. Journal of Biomolecular Screening 1998;3(1):13-17.

106. Munkacsi A, Chen F, Brinkman M, Higaki K, Gutierrez G, Chaudhari J, Layer J, Tong A, Bard M, Boone C, Ioannou Y, Sturley S. An “exacerbate-reverse” strategy in yeast identifies histone deacetylase inhibition as a correction for cholesterol and sphingolipid transport defects in human Niemann-Pick type C disease. Journal of Biological Chemistry 2011;286:23842-23851.
107. Cologna S, Jiang X, Backlund P, Cluzeau C, Dail M, Yanjanin N, Siebel S, Toth C, Jun H, Wassif C, Yergey A, Porter F. Quantitative proteomic analysis of Niemann-Pick disease, type C1 cerebellum identifies protein biomarkers and provides pathological insight. PLoS one 2012;7(10):e47845.
108. Rauniyar N, Subramanian K, Lavallee-Adam M, Martinez-Bartolome S, Balch W, Yates Jr. Quantitative proteomics of human fibroblasts with I1061T mutation in Niemann-Pick C1 (NPC1) protein provides insights into the disease pathogenesis. Molecular & Cellular Proteomics 2015;14(7):1734-1749.
109. Tenreiro S, Eckermann K, Outeiro T. Protein phosphorylation in neurodegeneration: friend or foe? Frontiers in Molecular Neuroscience 2014;7(42).
110. Ren R, Dammer E, Wang G, Seyfried N, Levey A. Proteomics of protein post-translation modifications implicated in neurodegeneration. Translational Neurodegeneration 2014;3(23).
111. Dammer E, Lee A, Duong D, Gearing M, Lah J, Levey A, Seyfried N. Quantitative phosphoproteomics of Alzheimer's disease reveals crosstalk between kinases and small heat shock proteins. Proteomics 2015;15(0):508-519.
112. Yu W, Ko M, Yanagisawa K, Michikawa M. Neurodegeneration in heterozygous Niemann-Pick type C1 (NPC1) mouse - implications of heterozygous NPC1 mutations being a risk for tauopathy. The Journal of Biological Chemistry 2005;280:27296-27302.
113. Huang Y, Walterfang M, Churilov L, Bray L, Jacobson L, Barnham K, Jones N, O'Brien T, Velakoulis D, Bush A. Neurological dysfunction in early maturity of a model for Niemann-Pick C1 carrier status. Neurotherapeutics 2016;13:614-622.
114. Brachmann C, Davies A, Cost G, Caputo E, Li J, Hieter P, Boeke J. Designer deletion strains derived from Saccharomyces cerevisiae S288C: a useful set of strains and plasmids for PCR-mediated gene disruption and other applications. Yeast 1998;14(2):115-132.
115. Longtine M, McKenzie A, Demarini D, Shah N, Wach A, Brachat A, Philippsen P, Pringle J. Additional modules for versatile and economical PCR-based gene deletion and modification in Saccharomyces cerevisiae. Yeast 1998;14(10):953-961.
116. Huh W, Falvo J, Gerke L, Carroll A, Howson R, Weissman J, O'Shea E. Global analysis of protein localization in budding yeast. Nature 2003;425:686-691.
117. Giaever G, Chu A, Ni L, Connelly C, Riles L, Veronneau S, Dow S, Lucau-Danila A, Anderson K, Andre B, Arkin A, Astromoff A, El-Baddoury M, Bangham R, Benito R, *et al.* Functional profiling of the *Saccharomyces cerevisiae* genome. Nature 2002;418(6896):387-391.
118. Cohen Y, Schuldiner M. Advanced methods for high-throughput microscopy screening of genetically modified yeast libraries. Methods in Molecular Biology 2011;781:127-159.
119. Tong A, Boone C. Synthetic genetic array analysis in Saccharomyces cerevisiae. Methods in Molecular Biology 2006;313:171-192.

120. Corradini E, Vallur R, Raaijmakers L, Feil S, Feil R, Heck A, Scholten A. Alterations in the cerebellar (Phospho)proteome of a cyclic guanosine monophosphate (cGMP)-dependent protein kinase knockout mouse. Molecular & Cellular Proteomics 2014;13(8):2004-2016.
121. Boersema P, Raijmakers R, Lemeer S, Mohammed S, Heck A. Multiplex peptide stable isotope dimethyl labeling for quantitative proteomics. Nature Protocols 2009;4(4):484-494.
122. Zhou H, Ye M, Dong J, Corradini E, Cristobal A, Heck A, Zou H, Mohammed S. Robust phosphoproteome enrichment using monodisperse microsphere-based immobilized titanium (IV) ion affinity chromatography. Nature Protocols 2013;8(3):461-480.
123. Vizcaino J, Csordas A, del-Toro N, Dianes J, Griss J, Lavidas I, Mayer G, Perez-Riverol Y, Reisinger F, Ternent T, Zu Q, Wang R, Hermjakob H. 2016 update of the PRIDE database and its related tools. Nucleic Acids Research 2016;44(D1):D447-D456.
124. Diot A, Hinks-Roberts A, Lodge T, Liao C, Dombi E, Morten K, Brady S, Fratter C, Carver J, Muir R, Davis R, Green C, Johnston I, Hilton-Jones D, Sue C*, et al.* A novel quantitative assay of mitophagy: Combining high content fluorescence microscopy and mitochondrial DNA load to quantify mitophagy and identify novel pharmacological tools against pathogenic heteroplasmic mtDNA. Pharmacological Research 2015;100:24-35.
125. Arguello G, Martinez P, Pena J, Chen O, Platt F, Zanlungo S, Gonzalez M. Hepatic metabolic response to restricted copper intake in a Niemann–Pick C murine model. Metallomics 2014;6(8):1527-1539.
126. Sarkar S, Carroll B, Buganim Y, Maetzel D, Ng A, Cassady J, Cohen M, Chakraborty S, Wang H, Spooner E, Ploegh H, Gsponer J, Korolchuk V, Jaenisch R. Impaired autophagy in the lipid storage disorder Niemann–Pick type C1 disease. Cell Reports 2013;5(5):1302-1315.
127. Kennedy B, Madreiter C, Vishnu N, Malli R, Graier W, Karten B. Adaptations of energy metabolism associated with increased levels of mitochondrial hcolesterol in NIemman-Pick type C1-deficient cells. Journal of Biological Chemistry 2014;289:16278-16289.
128. Brandon M, Lott M, Nguyen K, Spolim S, Navathe S, Baldi P, Wallace D. MITOMAP: a human mitochondrial genome database--2004 update. Nucleic Acids Research 2005;1(33):D611-613.
129. van der Bliek A, Shen Q, Kawajiri S. Mechanisms of mitochondrial fission and fusion. Cold Spring Harbor Perspectives in Biology 2013;5(6).
130. Anesti V, Scorrano L. The relationship between mitochondrial shape and function and the cytoskeleton. Biochimica et Biophysica Acta (BBA) - Bioenergetics 2006;1757(5-6):692-699.
131. Geyp M, Ireland C, Pittman S. Increased tubulin acetylation accompanies reversion to stable ploidy in vincristine-resistant CCRF-CEM cells. Cancer Genetics 1996;87(2):116-122.
132. Hermann G, Shaw J. Mitochondrial dynamics in yeast. Annual Review of Cell and Developmental Biology 1998;14:265-303.

133. Cooper G. Microtubule motors and movements. In: Associates S, editor. The Cell: A Molecular Approach 2nd edition. Sunderland, MA: Sinauer Associates; 2000.
134. Zilberman Y, Ballestrem C, Carramusa L, Mazitschek R, Khochbin S, Bershadsky A. Regulation of microtubule dynamics by inhibition of the tubulin deacetylase HDAC6. Journal of Cell Science 2009;122(Pt 19):3531-3541.
135. North B, Marshall B, Borra M, Denu J, Verdin E. The human Sir2 ortholog, SIRT2, is an NAD^+-dependent tubulin deacetylase. Molecular Cell 2003;11(2):437-444.
136. Sleat D, Wiseman J, Sohar I, El-Banna M, Zheng H, Moore D, Lobel P. Proteomic analysis of mouse models of Niemann-Pick C disease reveals alterations in the steady-state levels of lysosomal proteins within the brain. Proteomics 2013;12(0):3499-3509.
137. Eden E, Navon R, Steinfeld I, Lipson D, Zakhini Z. GOrilla: a tool for discovery and visualization of enriched GO terms in ranked gene lists. BMC Bioinformatics 2009;10(1):48.
138. Kamat P, Rai S, Swarnkar S, Shukla R, Nath C. Molecular and cellular mechanism of okadaic acid (OKA)-induced neurotoxicity: a novel tool for Alzheimer's disease therapeutic application. Molecular Neurobiology 2014;50(3):852-865.
139. Kazantsev A, Thompson L. Therapeutic application of histone deacetylase inhibitors for central nervous system disorders. Nature Reviews Drug Discovery 2008;7:854-868.
140. Gao Y, Davies S, Augustin M, Woodward A, Patel U, Kovelman R, Harvey K. A broad activity screen in support of a chemogenomic map for kinase signaling research and drug discovery. Biochemical Journal 2013;451(2):318-328.
141. Vasiliou V, Vasiliou K, Nebert D. Human ATP-binding cassette (ABC) transporter family. Human Genomics 2009;3(3):281-290.
142. Puntoni M, Sbrana F, Bigazzi F, Sampietro T. Tangier disease: epidemiology, pathophysiology, and management. Americal Journal of Cardiovascular Drugs 2012;12(5):303-311.
143. Knight B. ATP-binding cassette transporter A1: regulation of cholesterol efflux. Biochemical Society Transactions 2004;32:124-127.
144. Yuhua L, Chongren T. Regulation of ABCA1 function by signalling pathways. Biochimica et Biophysica Acta (BBA) - Molecular and Cell Biology of Lipids 2012;1821(3):522-529.
145. Frederickson D, Altorcch iP, Avioli L, Goodman D, Goodman H. Tangier disease: combined clinical staff conference at the National Institute of Health. Annals of Internal Medicine 1961;55(6):1016-1031.
146. Assmann G, von Eckardstein A, Brewer H. Familial analphalipoproteinemia: Tangier disease. 8 ed: New York: McGraw-Hill; 2001.
147. Sechi A, Dardis A, Zampieri S, Rabacchi C, Zanoni P, Calandra S, De Maglio G, Pizzolitto S, Maruotti V, Di Muzio A, Platt F, Bembi B. Effects of miglustat treatment in a patient affected by an atypical form of Tangier disease. Orphanet - Journal of Rare Diseases 2014;9:143.
148. Choi H, Karten B, Chan T, Vance J, Greer W, Heidenreich R, Garver W, Francis G. Impaired ABCA1-dependent lipid efflux and hypoalphalipoproteinemia in human

Niemann-Pick type C disease. Journal of Biological Chemistry 2003;278(35):32569-32577.
149. te Vruchte D, Lloyd-Evans E, Veldman R, Neville D, Dwek R, Platt F, van Blitterswijk W, Sillence D. Accumulation of glycosphingolipids in Niemann-Pick C disease disrupts endosomal transport. Journal of Biological Chemistry 2004;279(25):26167-26175.
150. Choudhury A, Dominguez M, Puri V, Sharma D, Narita K, Wheatley C, Marks D, Pagano R. Rab proteins mediate Golgi transport of caveola-internalized glycosphingolipids and correct lipid trafficking in Niemann-Pick C cells. The Journal of Clinical Investigations 2002;109(12):1541-1550.
151. Christensen K, Myers J, Swanson J. pH-dependent regulation of lysosomal calcium in macrophages. Journal of Cell Science 2002;115(Pt 3):599-607.
152. Te Vruchte D, Speak A, Wallom K, Al Eisa N, Smith D, Hendriksz C, Simmons L, Lachmann R, Cousins A, Hartung R, Mengel E, Runz H, Beck M, Amraoui Y, Imrie J*, et al.* Relative acidic comparment volume as a lysosomal sotrage disorder-associated biomarker. The Journal of Clinical Investigations 2014.
153. Chen F, Li C, Ioannou Y. Cyclodextrin induces calcium-dependent lysosomal exocytosis. PLoS One 2010;5(11):e15054.
154. Hobenek H, Schmitz G. Abnormal processing of Golgi elements and lysosomes in Tangier disease. Arteriosclerosis, Thrombosis, and Vascular Biology 1991;11:1007-1020.
155. Boadu E, Francis G. The role of vesicular transport in ABCA1-dependent lipid efflux and its connection with NPC pathways. Journal of Molecular Medicine 2006;84:266-275.
156. Clee S, Kastelein J, van Dam M, Marcil M, Roomp K, Zwarts K, Collins J, Roelants R, Tamasawa N, Stulc T, Suda T, Ceska R, Boucher B, Rondeau C, DeSouich C*, et al.* Age and residual cholesterol efflux affect HDL cholesterol levels and coronary artery disease in ABCA1 heterozygotes. The Journal of Clinical Investigations 2000;106(10):1263-1270.
157. Marcil M, Brooks-Wilson A, Clee S, Roomp K, Zhang H, Yu L, Collins J, van Dam M, Molhuizen H, Loubster O, Ouellette B, Sensen C, Fichter K, Mott S, Denis M*, et al.* Mutations in the ABC1 gene in familial HDL deficiency with defective cholesterol efflux. The Lancet 1999;354(9187):1341-1346.
158. Elliot-Smith E, Speak A, Lloyd-Evans E, Smith D, Spoel A, Jeyakumar M, Butters T, Dwek R, d'Azzo A, Platt F. Beneficial effects of substrate reduction therapy in a mouse model of GM1 gangliosidosis. Molecular Genetics and Metabolism 2008;94(2):204-211.
159. Loberto N, Tebon M, Lampronti I, Marchetti N, Aureli M, Bassi R, Vrazia Giri M, Bezzerri V, Lovato V, Cantu C, Munari S, Cheng S, Cavazzini A, Gambari R, Sonnino S*, et al.* GBA2-encoded β-Glucosidase activity is involved in the inflammatory response to *Pseudomonas aeruginosa*. PLoS One 2014;9(8):e104763.
160. Davidson C, Ali N, Micsenyi M, Stephney G, Renault S, Dobrenis K, Ory D, Vanier M, Walkley S. Chronic cyclodextrin treatment of murine Niemann-Pick C disease ameliorates neuronal cholesterol and glycosphingolipid storage and disease progression. PLoS One 2009;4(9):e6951.

161. Neufeld E, Stonik J, Demosky SJ, Knapper C, Combs C, Cooney A, Comly M, Dwyer N, Blanchette-Mackie J, Remaley A, Santamarina-Fojo S, Brewer HJ. The ABCA1 transporter modulates late endocytic trafficking: insights from the correction of the genetic defect in Tangier disease. Journal of Biological Chemistry 2004;279(15):15571-15578.
162. Costet P, Luo Y, Wang N, Tall A. Sterol-dependent transactivation of the ABC1 promoter by the liver X receptor/retinoid X receptor. Journal of Biological Chemistry 2000;275:28240-28245.
163. Repa J, Turley S, Lobaccaro J, Medina J, Li L, Lustig K, Shan B, Heyman R, Dietschy J, Mangelsdorf D. Regulation of absorption and ABC1-mediated efflux of cholesterol by RXR heterodimers. Science 2000;289(5484):1524-1529.
164. Rigamonti E, Helin L, Lestavel S, Mutka A, Lepore M, Fontaine C, Bouhlel M, Bultel S, Fruchart J, Ikonen E, Clavey V, Staels B, Chinetti-Gbaguidi G. Liver X receptor activation controls intracellular cholesterol trafficking and esterification in human macrophages. Circulation Research 2005;97:682-689.
165. Kaplan M, Aviram M, Knopf C, Keidar S. Angiotensin II reduces macrophage cholesterol efflux: a role for the AT-1 receptor but not for the ABC1 transporter. Biochemical Biophysical Research Communications 2002;290(5):1529-1534.
166. Zuo Y, Yancey P, Castro I, Khan W, Motojima M, Ichikawa I, Fogo A, Linton M, Fazio S, Kon V. Renal dysfunction potentiates foam cell formation by repressing ABCA1. Arteriosclerosis, Thrombosis, and Vascular Biology 2010;29(9):1277-1282.
167. Sica D, Gehr T, Ghosh S. Clinical pharmacokinetics of losartan. Clinical Pharmacokinetics 2005;44(8):797-814.
168. Meredith P. Comparative ARB pharmacology. The British Journal of Cariology 2010;17:s3-s5.
169. Li Z, Bains J, Ferguson A. Functional evidence that the angiotensin antagonist losartan crosses the blood-brain barrier in the rat. Brain Research Bulletin 1993;30(1-2):33-39.
170. Schupp M, Lee L, Frost N, Umbreen S, Schmidt B, Unger T, Kintscher U. Regulation of peroxisome proliferator-activated receptor gamma activity by losartan metabolites. Hypertension 2006;47(3):586-589.
171. Lanz T, Ding Z, Ho P, Luo J, Agrawal A, Srinagesh H, Axtell R, Zhang H, Platten M, Wyss-Coray T, Steinman L. Angiotensin II sustains brain inflammation in mice via TGF-β. The Journal of Clinical Investigations 2010;120(8):2782-2794.
172. Benicky J, Sanchez-Lemus E, Honda M, Pang T, Orecna M, Wang J, Leng Y, Chuang D, Saavedra J. Angiotensin II AT1 receptor blockade ameliorates brain inflammation. Neuropsychopharmacology 2011;36(4):857-870.
173. Pressey S, Smith D, Wong A, Platt F, Cooper J. Early glial activation, synaptic changes and axonal pathology in the thalamocortical system of Niemann–Pick type C1 mice. Neurobiology of Disease 2011;45(3):1086-1100.
174. MIyoshi M, Miyano K, Moriyama N, Taniguchi M, Watanabe T. Angiotensin type 1 receptor antagonist inhibits lipopolysaccharide-induced stimulation of rat microglial cells by suppressing nuclear factor kappaB and activator protein-1 activation. European Journal of Neuroscience 2008;27(2):343-351.

175. Wang X, Lu G, Hu X, Tsang K, Kwong W, Wu F, Meng H, Jiang S, Liu S, Ng H, Poon W. Quantitative assessment of gait and neurochemical correlation in a classical murine model of Parkinson's disease. BMC Neuroscience 2012;13:142.
176. Hamers F, Koopmans GC, Joosten EAJ. CatWalk-Assisted Gait Analysis in the Assessment of Spinal Cord Injury. Journal of Neurotrama 2006;23(3-4):537-548.
177. Williams I, Wallom K, Smith D, Al Eisa N, Smith C, Platt F. Improved neuroprotection using miglustat, curcumin and ibuprofen as a triple combination therapy in Niemann-Pick disease type C1 mice. Neurobiology of Disease 2014;67:9-17.
178. de Cavanagh E, Ferder M, Inserra F, Ferder L. Angiotensin II, mitochondria, cytoskeletal, and extracellular matrix connections: an integrated viewpoint. American Journal of Physiology - Heart and Circulatory Physiology 2009;296(3):H550-H558.
179. Dikalov S, Nazarawicz R. Angiotensin II-induced production of mitochondrial reactive oxygen species: potential mechanism and relevance for cardiovascular disease. Antioxidant and Redox Signalling 2013;19(10):1085-1094.
180. Johri A, Beal M. Mitochondrial dysfunction in neurodegenerative diseases. Journal of Pharmacology and Experimental Therapeutics 2012;342(2):619-630.
181. Bristol Uo. New Alzheimer's disease drug trial opens across Scotland. 2015 [cited 2016 May 23]; Available from: http://www.bristol.ac.uk/news/2015/november/radar-trial.html
182. Swerdlow R, Khan S. A "mitochondrial cascade hypothesis" for sporadic Alzherimer's disease. Medical Hypotheses 2004;63(1):8-20.
183. Schumacher H, Mancia G. The safety profile of telmisartan as monotherapy or combined with hydrochlorothiazide: a retrospective analysis of 50 studies. Blood Pressure Supplement 2008;1:32-40.
184. Burnier M, Maillard M. The comparative pharmacology of angiotensin II receptor antagonists. Blood Pressure Supplement 2001;1(6-11).
185. Kurkov S, Loftsson T. Cyclodextrins. International journal of pharmaceutics 2013;453(1):167-180.
186. Li Z, Wang M, Wang F, Gu Z, Du G, Wu J, Chen J. gamma-Cyclodextrin: a review on enzymatic production and applications. Applied microbiology and biotechnology 2007;77(2):245-255.
187. Crini G. Review: a history of cyclodextrins. Chemical Reviews 2014;114(21):10940-10975.
188. Camargo F, Erickson R, Garver W, Hossain G, Carbone P, Heidenreich R, Blanchard J. Cyclodextrins in the treatment of a mouse model of Niemann-Pick C disease. Life Sciences 2001;70:131-142.
189. Griffin L, Gong W, Verot L, Mellon S. Niemann–Pick type C disease involves disrupted neurosteroidogenesis and responds to allopregnanolone. Nature Medicine 2004;10:704-711.
190. Bricout H, Hapiot F, Ponchel A, Tilloy S, Monflier E. Chemically modified cyclodextrins: an attractive class of supramolecular hosts for the development of aqueous biphasic catalytic processes. Sustainability 2009;1(4):924-945.

191. Roquette. CRYSMEB methylated beta-cyclodextrin- documentation. [cited 2016 30/7]; Available from: http://www.roquette-pharma.com/crysmeb-beta-cyclodextrin-pharmaceutical-excipient-injectable-dosage-forms/)
192. Montecucco F, Lenglet S, Carbone F, Boero S, Pelli G, Burger F, Roth A, Bertolotto M, Nencioni A, Cea M, Dallegri F, Fraga-Silva R, Fougere L, Elfakir C, Gassner A*, et al.* Treatment with KLEPTOSE® CRYSMEB reduces mouse atherogenesis by impacting on lipid profile and Th1 lymphocyte response. Vascular Pharmacology 2015;72:197-208.
193. Monnaert V, Tilloy S, Bricout H, Fenart L, Cecchelli R, Monflier E. Behavior of α-, β-, and γ-cyclodextrins and their derivatives on an in vitro model of blood-brain barrier. The Journal of Pharmacology and Experimental Therapeutics 2004;310(2):745-751.
194. Ward S, O'Donnell P, Fernandez S, Vite C. 2-hydroxypropyl-β-cyclodextrin raises hearing threshold in normal cats and in cats with Niemann-Pick type C disease. Pediatric Research 2010;68:52-56.
195. Zimmer S, Grebe A, Bakke S, Bode N, Halvorsen B, Ulas T, Skjelland M, De Nardo D, Labzin L, Kerksiek A, Hempel C, Heneka M, Hawxhurst V, Fitzgerald M, Trebicka J*, et al.* Cyclodextrin promotes atherosclerosis regression via macrophage reprogramming. Science Translational Medicine 2016;8(333):333ra350.
196. Hanson L, Frey W. Intranasal delivery bypasses the blood-brain barrier to target therapeutic agents to the central nervous system and treat neurodegenerative disease. BMC Neuroscience 2008;9(Suppl 3):S5.
197. Taegoankar S, Mishra P. Intranasal delivery: an approach to bypass the blood brain barrier. Indian Journal of Pharmacology 2004;36(3):140-147.
198. Chugh Y, Kapoor P, Kapoor A. Intranasal drug delivery: a novel approach. Indian Journal of Otolaryngol Head Neck Surgery 2009;61(2):90-94.
199. Hsu A, Piboolnurak P, Floyd A, Yu Q, Wraith J, Patterson M, Pullman S. Spiral analysis in Niemann-Pick disease type C. Movement Disorders 2009;24(13):1984-1990.
200. Lopez C, de Vries A, Marrink S. Molecular mechanism of cyclodextrin mediated cholesterol extraction. PLoS Computational Biology 2011;7(3):e1002020.
201. Atger V, de la Llera Moya M, Stoudt G, Rodrigueza W, Phillips M, GH R. Cyclodextrins as catalysts for the removal of cholesterol from macrophage foam cells. Journal of Clinical Investigation 1997;99(4):773-780.
202. Liu B. Therapeutic potential of cyclodextrins in the treatment of Niemann–Pick type C disease. Clinical Lipidology 2012;7(3):289-301.
203. Demais V, Barthelemy A, Perraut M, Ungerer N, Keime C, Reibel S, Pfrieger F. Reversal of pathologic lipid accumulation in NPC1-deficient neurons by drug-promoted release of LAMP1-coated lamellar inclusions. The Journal of Neuroscience 2016;36(30):8012-8025.
204. Tilloy S, Monnaert V, Fenart L, Bricout H, Cecchelli R, Monflier E. Methylated β-cyclodextrin as P-gp modulators for deliverance of doxorubicin across an in vitro model of blood–brain barrier. Bioorganic & Medicinal Chemistry Letters 2006;16:2154-2157.

Appendix Table 1

YGR140W	CBF2	/	bud neck	cytoplasm	Essential kinetochore protein; component of the CBF3 multisubunit complex that binds to the CDEIII region of the centromere; Cbf2p also binds to the CDEII region possibly forming a different multimeric complex,
YPR124W	CTR1	/	cell periph	punctate	High-affinity copper transporter of the plasma membrane; mediates nearly all copper uptake under low copper conditions; transcriptionally induced at low copper levels and degraded at high copper levels
YIL052C	RPL34B		cytoplams	ER	Ribosomal 60S subunit protein L34B
YDR080W	VPS41	VPS41	cytoplasm	ER (?)	Vacuolar membrane protein that is a subunit of the HOPS complex; essential for membrane docking and fusion at the Golgi-to-endosome and endosome-to-vacuole stages of protein transport
YGL161C	YIP5	PSMD14	cytoplasm	more punctate staining	Protein that interacts with Rab GTPases; localized to late Golgi vesicles; computational analysis of large-scale protein-protein interaction data suggests a possible role in vesicle-mediated transport
YMR176W	ECM5	/	cytoplasm	varied	Subunit of the Snt2C complex; also colocalizes with Snt2p, independently of Rpd3p, to promoters of stress response genes in response to oxidative stress; contains ATP/GTP-binding site motif A;
YGR061C	ADE6	/	cytoplasm	nucleus	Formylglycinamidine-ribonucleotide (FGAM)-synthetase; catalyzes a step in the 'de novo' purine nucleotide biosynthetic pathway
YOR035C	SHE4		cytoplasm	nucleus	Protein containing a UCS (UNC-45/CRO1/SHE4) domain; binds to myosin motor domains to regulate myosin function; involved in endocytosis, polarization of the actin cytoskeleton, and asymmetric mRNA localization
YLR398C	SKI2	SKIV2L	cytoplasm	nucleus	Ski complex component and putative RNA helicase; mediates 3'-5' RNA degradation by the cytoplasmic exosome;
YGR125W	/	/	cytoplasm	periphery / bud neck	Putative protein of unknown function; deletion mutant has decreased rapamycin resistance but normal wormannin resistance; green fluorescent protein (GFP)-fusion protein localizes to the vacuole
YGL089C	MF(α)2	/	cytoplasm	punctate / actin (?)	Mating pheromone alpha-factor, made by alpha cells; interacts with mating type a cells to induce cell cycle arrest and other responses leading to mating;
YMR185W	RTP1	TMCO7	cytoplasm	punctate / lipid particles	Protein required for the nuclear import and biogenesis of RNA pol II;
YPL030W	TRM44	/	cytoplasm	vacoule / ER	tRNA(Ser) Um(44) 2'-O-methyltransferase; TRM44 is a non-essential gene
YKL002W	DID4	CHMP2a	endosome	less punctate staining	Class E Vps protein of the ESCRT-III complex; required for sorting of integral membrane proteins into lumenal vesicles of multivesicular bodies, and for delivery of newly synthesized vacuolar enzymes to the vacuole, involved in endocytosis
YMR030W	RSF1		Er/ mito	ER only	Protein required for respiratory growth; localized to both the nucleus and mitochondrion; may interact with transcription factors to mediate the transition to respiratory growth and activate transcription of nuclear and mitochondrial genes
YLR100W	ERG27	HSD17B7	lipid particle	less punctate staining	3-keto sterol reductase; catalyzes the last of three steps required to remove two C-4 methyl groups from an intermediate in ergosterol biosynthesis; mutants are sterol auxotrophs
YER025W	GCD11	/	little staining / mito	mito	Gamma subunit of the translation initiation factor eIF2; involved in the identification of the start codon; binds GTP when forming the ternary complex with GTP and tRNAi-Met; mutations in human ortholog cause X-linked intellectual disability (XLID)
YML030W	RCF1	RCF1a/b	mito	cytoplasm	Cytochrome c oxidase subunit; required for assembly of the Complex III-Complex IV supercomplex, and for assembly of Cox13p and Rcf2p into cytochrome c oxidase; required for late-stage assembly of the Cox12p and Cox13p subunits and for cytochrome c oxidase activity; required for growth under hypoxic conditions
YNL122C	/	/	mito	ER	Putative protein of unknown function; green fluorescent

					protein (GFP)-fusion protein localizes to mitochondria; YNL122C is not an essential gene
YGR012W	MCY1	/	mito	more periph than mitocho	Putative cysteine synthase; localized to the mitochondrial outer membrane
YOR150W	MRPL23	MRPL13	mito	non specific	Mitochondrial ribosomal protein of the large subunit; localizes to vacuole in response to H2O2
YMR064W	AEP1	/	mito	peroxisomes (?)	Protein required for expression of the mitochondrial OLI1 gene; mitochondrial OLI1 gene encodes subunit 9 of F1-F0 ATP synthase
YOL096C	COQ3	COQ3	mito	punctate / actin (?)	O-methyltransferase; catalyzes two different O-methylation steps in ubiquinone (Coenzyme Q) biosynthesis; component of a mitochondrial ubiquinone-synthesizing complex; phosphoprotein
YDR194C	MSS116	/	mito	spindles (?)	Mitochondrial transcription elongation factor; required for efficient splicing of mitochondrial Group I and II introns; promotes RNA folding by stabilizing an early assembly intermediate
YLR382C	NAM2	LARS2	mito / cytoplasm	cytoplasm	Mitochondrial leucyl-tRNA synthetase; direct role in splicing of several mitochondrial group I introns; indirectly required for mitochondrial genome maintenance
YFR026C	ULI1	/	not specific	ER	Putative protein of unknown function; involved in and induced by the endoplasmic reticulum unfolded protein response (UPR)
YKL045W	PRI2	PRIM2	nucleus	bud neck/ periphery	Subunit of DNA primase; DNA primase is required for DNA synthesis and double-strand break repair
YIL143C	SSL2	ERCC3	nucleus	cytoplasm	Component of RNA polymerase transcription factor TFIIH holoenzyme; required for unwinding promoter DNA; interacts functionally with TFIIB and has roles in transcription start site selection and gene looping to juxtapose initiation and termination regions; involved in DNA repair
YAL059W	ECM1	/	nucleus	cytoplasm	Pre-ribosomal factor involved in 60S ribosomal protein subunit export; associates with the pre-60S particle; shuttles between the nucleus and cytoplasm
YEL073C	/	/	nucleus	cytoplasm	Putative protein of unknown function; located adjacent to ARS503 and the telomere on the left arm of chromosome V; regulated by inositol/choline
YBL087C	RPL23A	RPL23A	nucleus	cytoplasm	Ribosomal 60S subunit protein L23A; homologous to mammalian ribosomal protein L23 and bacterial L14
YGL070C	RPB9	/	nucleus	cytoplasm	RNA polymerase II subunit B12.6; contacts DNA; mutations affect transcription start site selection and fidelity of transcription
YCR096C	HMRA2	/	nucleus	cytoplasm	required along with a1p for inhibiting expression of the HO endonuclease in a/alpha HO/HO diploid cells with an active mating-type interconversion system
YLR095C	IOC2	/	nucleus	vac memb	exhibits nucleosome-stimulated ATPase activity and acts within coding regions to coordinate transcription elongation with termination and processing
YJL079C	PRY1	GLIPR2	nucleus / (?)	cytoplasm	Sterol binding protein involved in the export of acetylated sterols; secreted glycoprotein and member of the CAP protein superfamily (cysteine-rich secretory proteins (CRISP), antigen 5, and pathogenesis related 1 proteins)
YLR129W	DIP2	/	nucleus / vac memb	vac memb	Nucleolar protein; specifically associated with the U3 snoRNA, part of the large ribonucleoprotein complex known as the small subunit (SSU) processome
YJR041C	URB2	/	nucleus/nucleolus	cytoplasm	Protein required for normal metabolism of the rRNA primary transcript; nucleolar protein; proposed to be involved in ribosome biogenesis
YNL214W	PEX17	/	peroxisome	less punctate	Membrane peroxin of the peroxisomal importomer complex; complex facilitates the import of peroxisomal matrix proteins; required for peroxisome biogenesis
YIL095W	PRK1	/	punctate / actin	vac memb	Protein serine/threonine kinase; regulates the organization and function of the actin cytoskeleton and reduces endocytic ability of cell through the phosphorylation of the Pan1p-Sla1p-End3p protein complex;
YOR109W	INP53	/	punctate	more punctate staining	Polyphosphatidylinositol phosphatase; dephosphorylates multiple phosphatidylinositol phosphates; involved in trans Golgi network-to-early endosome pathway;

					hyperosmotic stress causes translocation to actin patches; contains Sac1 and 5-ptase domains;
YPL180W	TCO89	/	vac memb	mitochondria / vac memb	Subunit of TORC1 (Tor1p or Tor2p-Kog1p-Lst8p-Tco89p); regulates global H3K56ac; TORC1 complex regulates growth in response to nutrient availability; cooperates with Ssd1p in the maintenance of cellular integrity;
YFL026W	STE2	/	vac memb	cytoplasm	Receptor for alpha-factor pheromone; seven transmembrane-domain GPCR that interacts with both pheromone and a heterotrimeric G protein to initiate the signaling response that leads to mating between haploid a and alpha cells
YML013W	SEL1	/	Vac memb	cytoplasm	Bridging factor involved in ER-associated protein degradation (ERAD); redistributes from the ER to lipid droplets during the diauxic shift and stationary phase; required for the maintenance of lipid homeostasis
YGL167C	PMR1	ATP2C1	various	periphery	High affinity Ca2+/Mn2+ P-type ATPase; required for Ca2+ and Mn2+ transport into Golgi; involved in Ca2+ dependent protein sorting and processing; mutations in human homolog ATP2C1 cause acantholytic skin condition Hailey-Hailey disease

Appendix Table 1. *GFP protein mislocalization screen hits*. Compared Δncr1 yeast crossed with single GFP labelled protein with WT yeast crossed with same single GFP labelled protein for the entire yeast genome. Proteins that were found to be mislocalized in the mutant Δncr1 yeast are included, proteins that are common false-positives have been removed, as have all dubious open reading frames genes.

Appendix Table 2

Orf	yeast gene	mammalian	Description
YHR161C	YAP1801	/	Protein of the AP180 family, involved in clathrin cage assembly; binds Pan1p and clathrin; YAP1801 has a paralog, YAP1802, that arose from the whole genome duplication
YAL028W	FRT2	/	Tail-anchored ER membrane protein of unknown function; promotes growth in conditions of high Na+, alkaline pH, or cell wall stress, possibly via a role in posttranslational translocation;
YLR027C	AAT2	GOT1	Cytosolic aspartate aminotransferase, involved in nitrogen metabolism; localizes to peroxisomes in oleate-grown cells
YBR196C-A	/	/	Putative protein of unknown function; identified by fungal homology and RT-PCR
YHL011C	PRS3	PRPS2	5-phospho-ribosyl-1(alpha)-pyrophosphate synthetase, synthesizes PRPP, which is required for nucleotide, histidine, and tryptophan biosynthesis; one of five related enzymes, which are active as heteromultimeric complexes
YDR448W	ADA2	TADA2A	Transcription coactivator, component of the ADA and SAGA transcriptional adaptor/HAT (histone acetyltransferase) complexes
YOR128C	ADE2	/	Phosphoribosylaminoimidazole carboxylase, catalyzes a step in the 'de novo' purine nucleotide biosynthetic pathway; red pigment accumulates in mutant cells deprived of adenine
YAL065C	/	/	Putative protein of unknown function; has homology to FLO1; possible pseudogene
YEL059C-A	SOM1	/	Subunit of the mitochondrial inner membrane peptidase (IMP); IMP is required for maturation of mitochondrial proteins of the intermembrane space; Som1p facilitates cleavage of a subset of substrates; contains twin cysteine-x9-cysteine motifs
YGL246C	RAI1	DXO / DOM3Z	Nuclear protein with decapping endonuclease activity targeted toward mRNAs with unmethylated 7-methylguanosine cap structures; binds to and stabilizes the exoribonuclease Rat1p; required for pre-rRNA processing;
YKL081W	TEF4	/	Gamma subunit of translational elongation factor eEF1B, stimulates the binding of aminoacyl-tRNA (AA-tRNA) to ribosomes by releasing eEF1A (Tef1p/Tef2p) from the ribosomal complex
YBR181C	RPS6B	RPS6	Protein component of the small (40S) ribosomal subunit; homologous to mammalian ribosomal protein S6
YMR191W	SPG5	/	Protein required for proteasome assembly during quiescence; binds to base of the proteasome regulartory particle; required for survival at high temperature during stationary phase;
YCL025C	AGP1	/	Low-affinity amino acid permease with broad substrate range; involved in uptake of asparagine, glutamine, and other amino acids; expression regulated by SPS plasma membrane amino acid sensor system (Ssy1p-Ptr3p-Ssy5p);
YGL080W	FMP37	MPC1	Highly conserved subunit of the mitochondrial pyruvate carrier; a mitochondrial inner membrane complex comprised of Fmp37p/Mpc1p and either Mpc2p or Fmp43p/Mpc3p mediates mitochondrial pyruvate uptake
YOR221C	MCT1	/	Predicted malonyl-CoA:ACP transferase, putative component of a type-II mitochondrial fatty acid synthase that produces intermediates for phospholipid remodeling
YCR034W	FEN1	ELOVL5	Fatty acid elongase, involved in sphingolipid biosynthesis; acts on fatty acids of up to 24 carbons in length; mutations have regulatory effects on 1,3-beta-glucan synthase, vacuolar ATPase, and the secretory pathway;
YNL252C	MRPL17	/	Mitochondrial ribosomal protein of the large subunit
YGR206W	MVB12		ESCRT-I subunit required to stabilize oligomers of the ESCRT-I core complex (Stp22p, Vps28p, Srn2p), which is involved in ubiquitin-dependent sorting of proteins into the endosome;
YGR159C	NSR1	/	Nucleolar protein that binds nuclear localization sequences, required for pre-rRNA processing and ribosome biogenesis
YPL189C-A	COA2	/	Cytochrome oxidase assembly factor; null mutation results in respiratory deficiency with specific loss of cytochrome oxidase activity; functions downstream of assembly factors Mss51p and Coa1p and interacts with assembly factor Shy1p
YGL141W	HUL5	/	Multiubiquitin chain assembly factor (E4); proteasome processivity factor that elongates polyUb chains on substrates, opposing Ubp6p, a branched polyubiquitin protease; required for retrograde transport of misfolded proteins during ERAD
YLR089C	ALT1	GPT2	Alanine transaminase (glutamic pyruvic transaminase); involved in alanine biosynthesis and catabolism; TOR1-independent role in determining chronological lifespan; repression is mediated by Nrg1p;
YPR020W	ATP20	/	Subunit g of the mitochondrial F1F0 ATP synthase; reversibly phosphorylated on two residues; unphosphorylated form is required for dimerization of the ATP synthase complex
YJR118C	ILM1	/	Protein of unknown function; may be involved in mitochondrial DNA maintenance; required for slowed DNA synthesis-induced filamentous growth
YNR010W	CSE2	/	Subunit of the RNA polymerase II mediator complex; associates with core polymerase subunits to form the RNA polymerase II holoenzyme; required for regulation of RNA polymerase II activity
YDR500C	RPL37B	RPL37	Ribosomal 60S subunit protein L37B; protein abundance increases in response to DNA replication stress;
YPL263C	KEL3	/	Cytoplasmic protein of unknown function

YIL128W	MET18	MMS19	Component of cytosolic iron-sulfur protein assembly (CIA) machinery that directs Fe-S cluster incorporation into a subset of proteins involved in methionine biosynthesis, DNA replication and repair, transcription, and telomere maintenance;
YPR047W	MSF1	FARS2	Mitochondrial phenylalanyl-tRNA synthetase, active as a monomer, unlike the cytoplasmic subunit which is active as a dimer complexed to a beta subunit dimer; similar to the alpha subunit of E. coli phenylalanyl-tRNA synthetase
YNL254C	RTC4	/	Protein of unknown function; null mutation suppresses cdc13-1 temperature sensitivity; (GFP)-fusion protein localizes to both the cytoplasm and the nucleus
YDR443C	SSN2	/	Subunit of the RNA polymerase II mediator complex; associates with core polymerase subunits to form the RNA polymerase II holoenzyme; required for stable association of Srb10p-Srb11p kinase; essential for transcriptional regulation
YKL155C	RSM22	/	Mitochondrial ribosomal protein of the small subunit; also predicted to be an S-adenosylmethionine-dependent methyltransferase
YGR008C	STF2	/	Protein involved in resistance to dessication stress; Stf2p exhibits antioxidant properties, and its overexpression prevents ROS accumulation and apoptosis; binds to F0 sector of mitochondrial F1F0 ATPase in vitro and may modulate the inhibitory action of Inh1p and Stf1p; protein abundance increases in response to DNA replication stress;
YNL241C	ZWF1	G6DP	Glucose-6-phosphate dehydrogenase (G6PD); catalyzes the first step of the pentose phosphate pathway; involved in adapting to oxidatve stress;
YMR021C	MAC1	/	Copper-sensing transcription factor involved in regulation of genes required for high affinity copper transport
YHR067W	HTD2	/	Mitochondrial 3-hydroxyacyl-thioester dehydratase involved in fatty acid biosynthesis, required for respiratory growth and for normal mitochondrial morphology
YBR179C	FZO1	MFN1/2	Mitofusin; integral membrane protein involved in mitochondrial outer membrane tethering and fusion; role in mitochondrial genome maintenance; targeted for destruction by SCF-Mdm30p and the cytosolic ubiquitin-proteasome system
YML024W	RPS17A	RPS17	Ribosomal protein 51 (rp51) of the small (40s) subunit;
YHR064C	SSZ1	HSP70	Hsp70 protein that interacts with Zuo1p to form a ribosome-associated complex that binds the ribosome via the Zuo1p subunit; also involved in pleiotropic drug resistance via sequential activation of PDR1 and PDR5; binds ATP
YCR045C	RRT12	/	Probable subtilisin-family protease with a role in formation of the dityrosine layer of spore walls; localizes to the spore wall and also the nuclear envelope and ER region in mature spores
YDR004W	RAD57	/	Protein that stimulates strand exchange by stabilizing the binding of Rad51p to single-stranded DNA; involved in the recombinational repair of double-strand breaks in DNA during vegetative growth and meiosis;
YBR189W	RPS9B	RPS9	Protein component of the small (40S) ribosomal subunit
YDR226W	ADK1	AK2	Adenylate kinase, required for purine metabolism; localized to the cytoplasm and the mitochondria; lacks cleavable signal sequence; protein abundance increases in response to DNA replication stress
YML115C	VAN1	/	Component of the mannan polymerase I, which contains Van1p and Mnn9p and is involved in the first steps of mannan synthesis;
YGL133W	ITC1	Acf1p	Subunit of ATP-dependent Isw2p-Itc1p chromatin remodeling complex; required for repression of a-specific genes, repression of early meiotic genes during mitotic growth, and repression of INO1
YGR157W	CHO2	EBP	Phosphatidylethanolamine methyltransferase (PEMT), catalyzes the first step in the conversion of phosphatidylethanolamine to phosphatidylcholine during the methylation pathway of phosphatidylcholine biosynthesis
YNL025C	SSN8	/	Cyclin-like component of the RNA polymerase II holoenzyme, involved in phosphorylation of the RNA polymerase II C-terminal domain; involved in glucose repression and telomere maintenance
YDL224C	WHI4	/	Putative RNA binding protein; regulates the cell size requirement for passage through Start and commitment to cell division;
YPL183W-A	RTC6	/	Protein involved in translation; mutants have defects in biogenesis of nuclear ribosomes; may be a mitochondrial ribosomal protein; protein abundance increases in response to DNA replication stress
YLR170C	APS1	AP1S2	Small subunit of the clathrin-associated adaptor complex AP-1, involved in protein sorting at the trans-Golgi network;
YKL134C	OCT1	MIPEP	Mitochondrial intermediate peptidase, cleaves destabilizing N-terminal residues of a subset of proteins upon import, after their cleavage by mitochondrial processing peptidase (Mas1p-Mas2p); may contribute to mitochondrial iron homeostasis
YER040W	GLN3	/	Transcriptional activator of genes regulated by nitrogen catabolite repression (NCR), localization and activity regulated by quality of nitrogen source

Appendix Table 2. *Synthetic lethality screen hits*. Synthetic lethal screens can find genetic interactions in which the combination of two non-lethal mutations result in lethality. Screen of all single mutations on a Δncr1 background and if colony was reduced by over 50% compared to the single mutation on a WT background it was included as a hit. Proteins that are common false-positives have been removed, as have all dubious open reading frames genes.

Appendix Table 3

Gene names	Fold Change Het vs WT	Fold Change Hom vs WT	Fold Change Hom vs Het		Protein Summary
Abhd4	0.6689	0.6694	1.0347	Het vs WT Hom vs WT	Lysophospholipase selective for N-acyl phosphatidylethanolamine (NAPE). Contributes to the biosynthesis of N-acyl ethanolamines,
Anln	0.7720	0.4874	0.6504	Hom vs WT Hom vs Het	Required for cytokinesis. Essential for the structural integrity of the cleavage furrow and for completion of cleavage furrow ingression
Apoe	0.9495	1.5519	1.6725	Hom vs WT Hom vs Het	Mediates the binding, internalization, and catabolism of lipoprotein particles.
Asah1	0.9378	1.7253	1.8088	Hom vs WT Hom vs Het	Hydrolyzes the sphingolipid ceramide into sphingosine and free fatty acid.
Bpgm	1.1312	0.5580	0.6862	Hom vs WT	Plays a major role in regulating hemoglobin oxygen affinity by controlling the levels of its allosteric effector 2,3-bisphosphoglycerate (2,3-BPG). Also exhibits mutase (EC 5.4.2.1) and phosphatase (EC 3.1.3.13) activities.
Brox	1.3734	1.6040	1.1694	Hom vs WT	Interacts with CHMP4B; lipid anchor?
Cd82	0.7933	0.6293	0.7806	Hom vs WT	Associates with CD4 or CD8 and delivers costimulatory signals for the TCR/CD3 pathway.
Cldn11	0.9425	0.6297	0.6648	Hom vs WT Hom vs Het	Plays a major role in tight junction-specific obliteration of the intercellular space, through calcium-independent cell-adhesion activity.
Cnot2	1.3441	2.3838	1.5178	Hom vs WT Hom vs Het	Component of the CCR4-NOT complex which is one of the major cellular mRNA deadenylases and is linked to various cellular processes including bulk mRNA degradation, miRNA-mediated repression, translational repression during translational initiation and general transcription regulation.
Cnp	0.8705	0.6631	0.7692	Hom vs WT	May participate in RNA metabolism in the myelinating cell, CNP is the third most abundant protein in central nervous system myelin.
Col1a1	1.1677	1.7607	1.2410	Hom vs WT	Type I collagen is a member of group I collagen (fibrillar forming collagen).
Cpm	0.9072	0.6594	0.7504	Hom vs WT	Specifically removes C-terminal basic residues (Arg or Lys) from peptides and proteins. It is believed to play important roles in the control of peptide hormone and growth factor activity at the cell surface, and in the membrane-localized degradation of extracellular proteins
Cr1l	1.2960	1.4765	1.1332	Hom vs WT	Acts as a cofactor for complement factor I, a serine protease which protects autologous cells against complement-mediated injury by cleaving C3b and C4b deposited on host tissue.
Ctsa	0.9713	1.5356	1.4788	Hom vs WT Hom vs Het	Protective protein appears to be essential for both the activity of beta-galactosidase and neuraminidase, it associates with these enzymes and exerts a protective function necessary for their stability and activity.

Ctsb	0.9678	1.5365	1.6251	Hom vs WT Hom vs Het	Thiol protease which is believed to participate in intracellular degradation and turnover of proteins. Has also been implicated in tumor invasion and metastasis.
Ctsd	0.9357	1.5324	1.6625	Hom vs WT Hom vs Het	Acid protease active in intracellular protein breakdown.
Ctsf	0.5214	1.7991	2.6119	Het vs WT Hom vs WT Hom vs Het	Thiol protease which is believed to participate in intracellular degradation and turnover of proteins. Has also been implicated in tumor invasion and metastasis.
Ctsz	1.4834	2.4883	1.6828	Het vs WT Hom vs WT Hom vs Het	Exhibits carboxy-monopeptidase as well as carboxy-dipeptidase activity
D17Wsu104e	1.3737	1.5695	1.1555	Hom vs WT	Bone marrow-derived monocyte and paracrine-acting protein that promotes cardiac myocyte survival and adaptive angiogenesis for cardiac protection and/or repair after myocardial infarction (MI). Stimulates endothelial cell proliferation through a MAPK1/3-, STAT3- and CCND1-mediated signaling pathway. Inhibits cardiac myocyte apoptosis in a PI3K/AKT-dependent signaling pathway.
Dner	1.0774	1.5881	1.4372	Hom vs WT	Mediates neuron-glia interaction during astrocytogenesis. May promote differentiation of Bergmann glia during cerebellar development by activating DELTEX-dependent NOTCH1 signaling
Edil3	0.8495	1.9472	2.0252	Hom vs WT Hom vs Het	Promotes adhesion of endothelial cells through interaction with the alpha-v/beta-3 integrin receptor. Inhibits formation of vascular-like structures. May be involved in regulation of vascular morphogenesis of remodeling in embryonic development.
Elac2	0.7116	0.5594	0.9113	Hom vs WT	Zinc phosphodiesterase, which displays mitochondrial tRNA 3'-processing endonuclease activity. Involved in tRNA maturation, by removing a 3'-trailer from precursor tRNA
Enpp6	0.7858	0.6158	0.7600	Hom vs WT	Choline-specific glycerophosphodiester phosphodiesterase. The preferred substrate may be lysosphingomyelin
Ermn	0.7924	0.6600	0.8237	Hom vs WT	Plays a role in cytoskeletal rearrangements during the late wrapping and/or compaction phases of myelinogenesis as well as in maintenance and stability of myelin sheath in the adult. May play an important role in late-stage oligodendroglia maturation, myelin/Ranvier node formation during CNS development, and in the maintenance and plasticity of related structures in the mature CNS
Fyco1	1.1006	1.8994	1.5029	Hom vs WT Hom vs Het	May mediate microtubule plus end-directed vesicle transport.
Gba	1.4032	0.4960	0.3493	Hom vs WT	Non-lysosomal glucosylceramidase that catalyzes the conversion of glucosylceramide (GlcCer) to free glucose and ceramide. Involved in sphingomyelin generation and prevention of glycolipid accumulation. Required for proper formation of motor neuron axons

Gfap	0.5510	1.2113	2.3004	Het vs WT Hom vs Het	GFAP, a class-III intermediate filament, is a cell-specific marker that, during the development of the central nervous system, distinguishes astrocytes from other glial cells.
Gltp	0.7888	0.6386	0.7859	Hom vs WT	Accelerates the intermembrane transfer of various glycolipids. Catalyzes the transfer of various glycosphingolipids between membranes but does not catalyze the transfer of phospholipids. May be involved in the intracellular translocation of glucosylceramides
Gns	0.9718	1.4754	1.5427	Hom vs WT Hom vs Het	Hydrolysis of the 6-sulfate groups of the N-acetyl-D-glucosamine 6-sulfate units of heparan sulfate and keratan sulfate.
Grn	1.0476	2.9206	2.7223	Hom vs WT Hom vs Het	Granulins have possible cytokine-like activity. They may play a role in inflammation, wound repair, and tissue remodeling.
Hexa	0.8865	1.8849	2.0730	Hom vs WT Hom vs Het	Responsible for the degradation of GM2 gangliosides, and a variety of other molecules containing terminal N-acetyl hexosamines, in the brain and other tissues
Hexb	0.9368	2.1072	2.4352	Hom vs WT Hom vs Het	Responsible for the degradation of GM2 gangliosides, and a variety of other molecules containing terminal N-acetyl hexosamines, in the brain and other tissues.
Irf2bpl	1.2965	1.6010	0.9900	Hom vs WT	May contribute to the control of female reproductive function. May play a role in gene transcription by transactivating GNRH1 promoter and repressing PENK promoter
Itm2b	1.2046	1.4985	1.3391	Hom vs WT	Plays a regulatory role in the processing of the beta-amyloid A4 precursor protein (APP) and acts as an inhibitor of the beta-amyloid peptide aggregation and fibrils deposition. Plays a role in the induction of neurite outgrowth.
Itm2c	1.4767	1.8409	1.2641	Hom vs WT	Negative regulator of beta amyloid peptide production. May inhibit the processing of APP by blocking its access to alpha- and beta-secretase. May play a role in TNF-induced cell death and neuronal differentiation.
Lamp1	0.9689	2.6616	2.7646	Hom vs WT Hom vs Het	Presents carbohydrate ligands to selectins. Also implicated in tumor cell metastasis.
Lamtor1	0.8972	1.5399	1.7666	Hom vs WT Hom vs Het	Part of the Ragulator complex involved in activation of mTORC1. Responsible for anchoring the Ragulator complex to membranes, required for late endosomes/lysosomes biogenesis. May regulate recycling of receptors through endosomes and the MAPK signaling pathway through recruitment of some of its components to late endosomes. May be involved in cholesterol homeostasis regulating LDL uptake and cholesterol release from late endosomes/lysosomes.
Lamtor2	0.9496	1.6788	1.8285	Hom vs WT Hom vs Het	Part of the Ragulator complex it is involved in amino acid sensing and activation of mTORC1. Adapter protein that enhances the efficiency of the MAP kinase cascade facilitating the activation of MAPK2.

Lamtor3	0.9577	1.5992	1.6312	Hom vs WT Hom vs Het	Part of the Ragulator complex it is involved in amino acid sensing and activation of mTORC1. Adapter protein that enhances the efficiency of the MAP kinase cascade facilitating the activation of MAPK2.
Lamtor5	1.0892	1.8251	1.6669	Hom vs WT Hom vs Het	Part of the Ragulator complex it is involved in amino acid sensing and activation of mTORC1. When complexed to BIRC5, interferes with apoptosome assembly, preventing recruitment of pro-caspase-9 to oligomerized APAF1, thereby selectively suppressing apoptosis initiated via the mitochondrial/cytochrome c pathway
Mbp	0.7357	0.4883	0.6694	Hom vs WT Hom vs Het	The classic group of MBP isoforms (isoform 4-isoform 13) are with PLP the most abundant protein components of the myelin membrane in the CNS. They have a role in both its formation and stabilization.
Mcfd2	1.3407	1.7746	1.3237	Hom vs WT	The MCFD2-LMAN1 complex forms a specific cargo receptor for the ER-to-Golgi transport of selected proteins.
Mog	0.8134	0.5513	0.6852	Hom vs WT	Minor component of the myelin sheath. May be involved in completion and/or maintenance of the myelin sheath and in cell-cell communication.
Myo1d	0.8588	0.6469	0.7755	Hom vs WT	Myosins are actin-based motor molecules with ATPase activity. Unconventional myosins serve in intracellular movements.
Naaa	1.1691	2.0112	1.9058	Hom vs WT Hom vs Het	Degrades bioactive fatty acid amides to their corresponding acids, with a preference for N-palmitoylethanolamine.
Opalin	0.8402	0.5665	0.6643	Hom vs WT Hom vs Het	Oligodendrocytic myelin paranodal and inner loop protein expressed specifically in oligodendrocytes of the brain.
Phlpp1	1.3620	1.4818	1.1416	Hom vs WT	Protein phosphatase that mediates dephosphorylation of 'Ser-473' of AKT1, 'Ser-660' of PRKCB, and 'Ser-657' of PRKCA. AKT1 regulates the balance between cell survival and apoptosis through a cascade that primarily alters the function of transcription factors that regulate pro- and antiapoptotic genes.
Pla2g7	1.0655	1.5377	1.6898	Hom vs WT Hom vs Het	Modulates the action of platelet-activating factor (PAF) by hydrolyzing the sn-2 ester bond to yield the biologically inactive lyso-PAF.
Ppapdc2	2.0456	0.9431	0.5312	Het vs WT Hom vs Het	Phosphatase that dephosphorylates presqualene diphosphate (PSDP) into presqualene monophosphate (PSMP), suggesting that it may be indirectly involved in innate immunity.
Ppp1r14a	0.8156	0.6480	0.8315	Hom vs WT	regulates the phosphorylation status of PPP1CA substrates and smooth muscle contraction
Ppt1	0.8853	2.4133	2.7563	Hom vs WT Hom vs Het	Removes thioester-linked fatty acyl groups such as palmitate from modified cysteine residues in proteins or peptides during lysosomal degradation.

Ptgds	1.1765	2.1370	1.8019	Hom vs WT Hom vs Het	Involved in a variety of CNS functions, such as sedation, NREM sleep and PGE2-induced allodynia, and may have an anti-apoptotic role in oligodendrocytes.
Rapgef5	1.3308	1.4689	1.0917	Hom vs WT	Guanine nucleotide exchange factor (GEF) for RAP1A, RAP2A and MRAS/M-Ras-GTP. Its association with MRAS inhibits Rap1 activation
Rnf114	1.2339	1.5231	1.3023	Hom vs WT	This protein is involved in the pathway protein ubiquitination, which is part of Protein modification.
Rragc	0.9918	1.6399	1.6369	Hom vs WT Hom vs Het	Guanine nucleotide-binding protein forming heterodimeric Rag complexes required for the amino acid-induced relocalization of mTORC1 to the lysosomes and its subsequent activation by the GTPase RHEB. This is a crucial step in the activation of the TOR signaling cascade by amino acids
Scamp5	0.4933	0.4586	1.0574	Het vs WT Hom vs WT	Required for the calcium-dependent exocytosis of signal sequence-containing cytokines such as CCL5. Probably acts in cooperation with the SNARE machinery
Scarb2	1.0738	3.2547	2.7460	Hom vs WT Hom vs Het	Acts as a lysosomal receptor for glucosylceramidase (GBA) targeting.
Sdhd	1.4491	1.5790	1.0606	Hom vs WT	This protein is involved in the pathway tricarboxylic acid cycle, which is part of Carbohydrate metabolism.
Serinc1	1.1201	1.8276	1.6135	Hom vs WT Hom vs Het	Enhances the incorporation of serine into phosphatidylserine and sphingolipids.
Sparc	1.0952	1.5623	1.4530	Hom vs WT	Appears to regulate cell growth through interactions with the extracellular matrix and cytokines. Binds calcium and copper
Spock1	1.3020	1.4835	1.2136	Hom vs WT	May contribute to various neuronal mechanisms in the central nervous system.
Stx8	1.0460	1.8384	1.7664	Hom vs WT Hom vs Het	Vesicle trafficking protein that functions in the early secretory pathway, possibly by mediating retrograde transport from cis-Golgi membranes to the ER.
Sult4a1	1.3945	1.6960	1.0834	Hom vs WT	May have a role in the metabolism of drugs and neurotransmitters in the CNS.
Tmem175	1.1948	2.2087	1.8199	Hom vs WT Hom vs Het	Multi-pass membrane protein on lysosomal membrane
Tpp1	0.9453	3.1593	3.2461	Hom vs WT Hom vs Het	Lysosomal serine protease with tripeptidyl-peptidase I activity.
Tspan2	0.7810	0.6737	0.7883	Hom vs WT	May play a role in signalling in oligodendrocytes in the early stages of their terminal differentiation into myelin-forming glia and may also function in stabilizing the mature sheath.
Ugt8	0.8211	0.6468	0.8357	Hom vs WT	Catalyzes the transfer of galactose to ceramide, a key enzymatic step in the biosynthesis of galactocerebrosides, which are abundant sphingolipids of the myelin membrane of the central nervous system and peripheral nervous system.

Vps18	1.3016	1.8566	1.2307	Hom vs WT	May play a role in vesicle-mediated protein trafficking to lysosomal compartments and in membrane docking/fusion reactions of late endosomes/lysosomes.
Vps28	1.1120	1.4779	1.4666	Hom vs WT	Component of the ESCRT-I complex, a regulator of vesicular trafficking process.
Vti1b	1.0396	1.6238	1.3431	Hom vs WT	V-SNARE that mediates vesicle transport pathways through interactions with t-SNAREs on the target membrane. These interactions are proposed to mediate aspects of the specificity of vesicle trafficking and to promote fusion of the lipid bilayers.

Appendix Table 3: *Quantitative proteomic screen hits in Npc1$^{-/-}$, Npc1$^{+/-}$, and Npc1$^{+/}$ cerebellum.* Lysosomal proteins indicated in blue, proteins of the myelin sheath in red, and proteins belonging to mTOR nutrient-sensing pathay in green.

Appendix Table 4

Gene names	Fold Change Het vs WT	Fold Change Hom vs WT	Fold Change Hom vs Het		
Aatk	0.372	0.402	1.075	Het vs WT Hom vs WT	May be involved in neuronal differentiation.
Abi1	2.629	1.952	0.776	Het vs WT Hom vs WT	Involved in cytoskeletal reorganization and EGFR signaling. In brain, seems to regulate the dendritic outgrowth and branching as well as to determine the shape and number of synaptic contacts of developing neurons.
Add1	2.100	5.152	2.456	Het vs WT Hom vs WT Hom vs Het	Membrane-cytoskeleton-associated protein that promotes the assembly of the spectrin-actin network. Binds to calmodulin.
Add1	0.106	0.087	0.847	Het vs WT Hom vs WT	
Aftph	4.507	4.723	1.066	Het vs WT Hom vs WT	clathrin binding
Ank2	3.092	4.925	1.566	Het vs WT Hom vs WT	potassium channel regulator activity
Ank2	0.520	0.497	1.010	Het vs WT Hom vs WT	
Ank2	0.408	0.360	0.872	Het vs WT Hom vs WT	
Ank2	0.395	0.351	0.888	Het vs WT Hom vs WT	
Ap3b1	2.303	2.811	1.337	Het vs WT Hom vs WT	Subunit of non-clathrin- and clathrin-associated adaptor protein complex 3 (AP-3) that plays a role in protein sorting in the late-Golgi/trans-Golgi network (TGN) and/or endosomes.
Arhgef12	1.041	0.324	0.314	Hom vs WT Hom vs Het	May play a role in the regulation of RhoA GTPase by guanine nucleotide-binding alpha-12 (GNA12) and alpha-13 (GNA13).
Arhgef7	0.189	0.454	2.425	Het vs WT Hom vs WT Hom vs Het	Acts as a RAC1 guanine nucleotide exchange factor (GEF) and can induce membrane ruffling. May function as a positive regulator of apoptosis.
Arrb1	4.828	5.077	1.076	Het vs WT Hom vs WT	Functions in regulating agonist-mediated G-protein coupled receptor (GPCR) signaling by mediating both receptor desensitization and resensitization processes.
Atp2b1	2.406	1.883	0.818	Het vs WT Hom vs WT	This magnesium-dependent enzyme catalyzes the hydrolysis of ATP coupled with the transport of calcium. Involved in bone homeostasis.
Atp2b2	2.406	1.883	0.818	Het vs WT Hom vs WT	This magnesium-dependent enzyme catalyzes the hydrolysis of ATP coupled with the transport of calcium out of the cell. Plays a role in maintaining balance and hearing.
Atp8a1	4.075	9.575	2.333	Het vs WT Hom vs WT Hom vs Het	phospholipid-translocating ATPase activity
Atp8a1	4.075	9.575	2.333	Het vs WT	

				Hom vs WT Hom vs Het	
Atp8a1	4.075	9.575	2.333	Het vs WT Hom vs WT Hom vs Het	
Atxn2	0.297	0.307	1.020	Het vs WT Hom vs WT	Involved in EGFR trafficking, acting as negative regulator of endocytic EGFR internalization at the plasma membrane.
Bclaf1	9.151	11.290	1.342	Het vs WT Hom vs WT	Death-promoting transcriptional repressor. May be involved in cyclin-D1/CCND1 mRNA stability through the SNARP complex which associates with both the 3'end of the CCND1 gene and its mRNA
Canx	1.857	4.109	2.541	Het vs WT Hom vs WT Hom vs Het	Calcium-binding protein that interacts with newly synthesized glycoproteins in the endoplasmic reticulum. It may act in assisting protein assembly and/or in the retention within the ER of unassembled protein subunits. It seems to play a major role in the quality control apparatus of the ER by the retention of incorrectly folded proteins
Canx	1.834	4.031	2.514	Het vs WT Hom vs WT Hom vs Het	
Cenpv	2.355	2.197	0.939	Het vs WT Hom vs WT	Required for distribution of pericentromeric heterochromatin in interphase nuclei and for centromere formation and organization, chromosome alignment and cytokinesis.
Cnp	0.329	0.249	0.749	Het vs WT Hom vs WT	May participate in RNA metabolism in the myelinating cell, CNP is the third most abundant protein in central nervous system myelin.
Dlgap1	2.050	2.257	1.146	Het vs WT Hom vs WT	Part of the postsynaptic scaffold in neuronal cells.
Dync1li1	2.224	1.846	0.826	Het vs WT Hom vs WT	Acts as one of several non-catalytic accessory components of the cytoplasmic dynein 1 complex that are thought to be involved in linking dynein to cargos and to adapter proteins that regulate dynein function.
Eif3b	2.158	3.048	1.397	Het vs WT Hom vs WT	Component of the eukaryotic translation initiation factor 3 (eIF-3) complex, which is required for several steps in the initiation of protein synthesis.
Eif3b	2.158	3.048	1.397	Het vs WT Hom vs WT	
Epb41l3	2.786	3.779	1.379	Het vs WT Hom vs WT	Tumor suppressor that inhibits cell proliferation and promotes apoptosis.
Epb41l3	2.487	4.585	1.875	Het vs WT Hom vs WT Hom vs Het	
Fam131b	0.132	0.160	1.150	Het vs WT Hom vs WT	Activation of mitophagy in response to mitochondrial depolarization
Fam21	0.083	0.089	1.054	Het vs WT Hom vs WT	Acts at least in part as component of the WASH core complex; retrograde transport, endosome to Golgi
Fam21	0.094	0.099	1.064	Het vs WT Hom vs WT	
Garnl3	2.345	2.150	0.926	Het vs WT	GTPase activator activity

				Hom vs WT	
Garnl3	2.345	2.150	0.926	Het vs WT Hom vs WT	
Gpm6a	1.848	1.887	1.072	Het vs WT Hom vs WT	Involved in neuronal differentiation, including differentiation and migration of neuronal stem cells. Gpm6a-induced filopodia formation involves mitogen-activated protein kinase (MAPK) and Src signaling pathways. May be involved in regulation of endocytosis and intracellular trafficking of G-protein-coupled receptors (GPCRs)
Hsp90ab1	3.142	7.710	2.753	Het vs WT Hom vs WT Hom vs Het	Molecular chaperone that promotes the maturation, structural maintenance and proper regulation of specific target proteins involved for instance in cell cycle control and signal transduction.
Klc2	2.167	4.664	2.151	Het vs WT Hom vs WT Hom vs Het	microtubule motor activity
Leo1	2.224	2.764	1.266	Het vs WT Hom vs WT	Component of the PAF1 complex (PAF1C) which has multiple functions during transcription by RNA polymerase II and is implicated in regulation of development and maintenance of embryonic stem cell pluripotency.
Lrrc16a	4.585	3.004	0.658	Het vs WT Hom vs WT	protein complex binding
Map1a	0.519	0.510	1.004	Het vs WT Hom vs WT	Structural protein involved in the filamentous cross-bridging between microtubules and other skeletal elements. LC2 is generated from MAP1A by proteolytic processing.
Map1a	0.460	0.475	1.042	Het vs WT Hom vs WT	
Mllt4	0.502	0.385	0.765	Het vs WT Hom vs WT	Belongs to an adhesion system, probably together with the E-cadherin-catenin system, which plays a role in the organization of homotypic, interneuronal and heterotypic cell-cell adherens junctions (AJs).
Nefh	2.249	2.503	1.343	Het vs WT Hom vs WT	Neurofilaments usually contain three intermediate filament proteins: L, M, and H which are involved in the maintenance of neuronal caliber. NF-H has an important function in mature axons that is not subserved by the two smaller NF proteins.
Nefh	2.249	2.503	1.343	Het vs WT Hom vs WT	
Nefh	0.167	0.187	1.222	Het vs WT Hom vs WT	
Nefm	3.267	3.867	1.176	Het vs WT Hom vs WT	Neurofilaments usually contain three intermediate filament proteins: L, M, and H which are involved in the maintenance of neuronal caliber.
Nudc	2.727	5.864	2.122	Het vs WT Hom vs WT Hom vs Het	Plays a role in neurogenesis and neuronal migration. Necessary for correct formation of mitotic spindles and chromosome separation during mitosis
Palm	2.758	2.204	0.876	Het vs WT Hom vs WT	Involved in plasma membrane dynamics and cell process formation.
Pde4b;Pde4d	1.842	4.007	2.345	Het vs WT Hom vs WT	metal ion binding
Plvap;Hnrnpm	2.396	4.336	1.823	Het vs WT Hom vs WT	Involved in the formation of stomatal and fenestral diaphragms of caveolae. May function in microvascular permeability

Prkab1	1.948	3.790	1.909	Het vs WT Hom vs WT Hom vs Het	Non-catalytic subunit of AMP-activated protein kinase (AMPK), an energy sensor protein kinase that plays a key role in regulating cellular energy metabolism. I
Prpf4b	1.964	2.015	1.183	Het vs WT Hom vs WT	Has a role in pre-mRNA splicing. Phosphorylates SF2/ASF.
Rbm33	2.302	3.248	1.432	Het vs WT Hom vs WT	X
Sh3kbp1	0.352	0.372	1.032	Het vs WT Hom vs WT	Adapter protein involved in regulating diverse signal transduction pathways. Involved in the regulation of endocytosis and lysosomal degradation of ligand-induced receptor tyrosine kinases, including EGFR and MET/hepatocyte growth factor receptor, through a association with CBL and endophilins.
Sik3	0.413	0.413	1.010	Het vs WT Hom vs WT	cartilage development involved in endochondral bone morphogenesis
Slc12a5	0.451	0.325	0.760	Het vs WT Hom vs WT	Mediates electroneutral potassium-chloride cotransport in mature neurons.
Slc4a1ap	1.978	3.344	1.704	Het vs WT Hom vs WT	X
Slc6a5	0.399	0.351	0.882	Het vs WT Hom vs WT	Terminates the action of glycine by its high affinity sodium-dependent reuptake into presynaptic terminals.
Slc9a3r1	1.957	1.988	0.997	Het vs WT Hom vs WT	Scaffold protein that connects plasma membrane proteins with members of the ezrin/moesin/radixin family and thereby helps to link them to the actin cytoskeleton and to regulate their surface expression.
Thrap3	18.666	6.791	0.362	Het vs WT Hom vs WT Hom vs Het	Involved in pre-mRNA splicing.
Thrap3	2.005	2.627	1.323	Het vs WT Hom vs WT	
Vps13c	0.299	0.271	0.916	Het vs WT Hom vs WT	protein retention in Golgi apparatus
Vps13c	0.470	0.331	0.703	Het vs WT Hom vs WT	
Xkr7	0.507	0.311	0.611	Het vs WT Hom vs WT	X

Appendix Table 4. *Quantitative phosphoproteomic screen hits in Npc1$^{-/-}$, Npc1$^{+/-}$, and Npc1$^{+/}$ cerebellum.* Deregulated phosphorylation of proteins involved in cytoskeletal transport indicated in blue, calcium transporters in red, transport protein in green, and cell cycle regulation proteins in orange.

Appendix Table 5

Parameter	Definition	Observed in *Npc1*$^{-/-}$ vs WT
Stand Mean	Average duration (sec) of paws in contact with glass plate	+
Step Cycle	Duration (sec) between two consecutive contacts of the same paw	+
Duty Cycle	Percentage of time paws in contact with plate compared with time to complete a step cycle	+
Step Sequence (AB)	Percentage of time spent walking in LF-RH-RF-LH alternating pattern	-
Cadence	Steps per second in a trial	-
Diagonal Support	Percentage of time with simultaneous contact of diaganol paws with the glass plate [RF&LH or RH&LF]	-

Appendix Table 5. *Definition of gait parameters examined on CatWalk system and the differences in each parameter between Npc1*$^{-/-}$ *and wild type mice.* As the disease progresses, untreated *Npc1*$^{-/-}$ mice have increased stand mean, step cycle, and duty cycle values, and decreased AB step sequence, cadence, and diagonal support values.

Publications

Platt FM, Wassif C, **Colaco A**, Dardis A, Lloyd-Evans E, Bembi B, Porter FD. Disorders of cholesterol and their unanticipated convergent mechanisms of disease. Annu Rev Genomics Hum Genet. 2014. 15: 173-194

Bradbury AM, Gray-Edwards HL, Shirley JL, McCurdy VJ, **Colaco AN**, Randle AN, Christopherson PW, Bird AC, ohnson AK, Wilson DU, Hudson JA, De Pompa NL, Sorjonen DC, Brunson BL, Jeyakumar M, Platt FM, Baker HJ, Cox NR, Sena-Esteves M, Martin DR. Biomarkers for disease progression and AAV therapeutic efficacy in feline Sandhoff disease. Exp Neurol. 2015. 263: 102-112

Platt N, Speak AO, **Colaco A**, Gray J, Smith DA, Williams IM, Wallom KL, Platt FM. Immune dysfunction in Niemann-Pick disease type C. J Neurochem. 2016. 136 Suppl 1: 74-80

Sezgin E, Can FB, Schneider F, Clausen MP, Galiani S, Stanly TA, Waithe D, **Colaco A**, Honigmann A, Wustner D, Platt F, Eggeling C. A comparative study on fluorescent cholesterol analogs as versatile cellular reporters. J Lipid Res. 2016. 57 (2): 299-309